

Universiteit
Leiden
The Netherlands

Dusty perspectives on the cradles of planets

Guerra Alvarado, O. M.

Citation
Guerra Alvarado, O. M. (2026, February 6). *Dusty perspectives on the cradles of planets*. Retrieved from https://hdl.handle.net/1887/4289494

Version:	Publisher's Version
License:	Licence agreement concerning inclusion of doctoral thesis in the Institutional Repository of the University of Leiden
Downloaded from:	https://hdl.handle.net/1887/4289494

Note: To cite this publication please use the final published version (if applicable).

Dusty perspectives on the cradles of planets

Proefschrift

ter verkrijging van
de graad van doctor aan de Universiteit Leiden,
op gezag van waarnemend rector magnificus,
volgens besluit van het college voor promoties
te verdedigen op vrijdag 6 februari 2025
klokke 10:00 uur

door

Osmar Manuel Guerra Alvarado
geboren te Colorado Springs, Colorado, United States of America
in 1994

Promotor:	Prof. dr. Hogerheijde	
Co-promotor:	Dr. van der Marel	
Promotiecommissie:	Prof. dr. Snellen	
	Dr. Kenworthy	
	Prof. dr. Birnstiel	(Ludwig-Maximilians-Universitat Munich)
	Prof. dr. Jørgensen	(University of Copenhagen)
	Dr. McClure	

Cover design and layout by Nina Breck

Table of Contents

1 Introduction **1**

1.1 The beginning and evolution of protoplanetary disks 1

1.1.1 Interstellar dust and its influence in protoplanetary disks 3

1.1.2 Dust evolution: Radial Drift 6

1.1.3 Dust evolution: Settling and turbulent mixing 8

1.2 Protoplanetary disks in the modern era with ALMA 9

1.2.1 Gas and ice content of protoplanetary disks 10

1.2.2 Complex organic molecules in YSOs 12

1.2.3 Early disk formation and spatial distribution of dust and COMs 14

1.2.4 Substructures in protoplanetary disks 16

1.3 The current problems in planet formation 17

1.3.1 Early substructure formation and unsettled Disks in YSOs 17

1.3.2 Exoplanet demographics vs protoplanetary disks surveys 19

1.4 This thesis 22

1.4.1 Analysis tools 23

1.4.2 Main conclusions 29

1.4.3 Future science 30

2 IRAS4A1: Multiwavelength continuum analysis of a very flared Class 0 disk **32**
2.1 Introduction 35
2.2 Observations 37
2.3 Results 41
2.3.1 Multiwavelength analysis of a Class 0 young stellar object. 44
2.3.2 Generic gap models with large scale heights. 52
2.3.3 Large scale height and very flared disk models of IRAS4A1 56
2.4 Discussion 59
2.5 Summary and conclusions 60
Appendix A: Faint Emission Between A1 and A2 63

3 From large-scale outflows to compact line emission in IRAS4A2 **64**
3.1 Introduction 67
3.2 Observations 68
3.3 Results 70
3.3.1 Analysis and line detection with CASSIS 70
3.3.2 Outflows, extended emission and compact emission in IRAS4A2 73
3.4 Discussion 79
3.4.1 Spatial scales of the dust and gas of IRAS4A2 79
3.4.2 Accretion Shocks 86
3.4.3 High mass star forming regions vs IRAS4A2 87
3.4.4 Outflows and misaligned velocity fields 89
3.5 Summary and conclusions 90
Appendix A: IRAS4A2 Molecules in spectra 93
Appendix B: IRAS4A2 Moment 0 maps 95

4 Into the thick of it: ALMA 0.45 mm observations of HL Tau at a resolution of 2 au **96**
4.1 Introduction 99

4.2 Observations 101
4.3 Results 104
4.4 Discussion 107
4.4.1 Modeling of the dust properties 107
4.4.2 Azimuthally asymmetric emission in the inner disk . 114
4.4.3 Substructure in the inner disk: Possible sign of the traffic-jam effect 121
4.5 Summary and conclusions 124
Appendix A: Markov chain Monte Carlo model versus observations: VLA fitting 127

5 A high-resolution survey of protoplanetary disks in Lupus and the nature of compact disks 129
5.1 Introduction 132
5.2 Observations 135
5.3 Results 138
5.3.1 Dust continuum images 138
5.3.2 Visibility modeling 140
5.3.3 Disk size and substructure distribution 145
5.3.4 Radiative transfer modeling 149
5.3.5 Dust mass estimates 152
5.3.6 The exoplanet population in the Lupus substructures 155
5.4 Discussion 159
5.4.1 New insights into the substructures and origin of compact disks 159
5.4.2 Size-luminosity relation 163
5.4.3 Dust masses and optical depths 164
5.4.4 Impact of compact disks in the exoplanet population 165
5.5 Summary and conclusions 167
Appendix A: ALMA image characteristics 170
Appendix B: GALARIO fitting results 171
Appendix C: Lupus stellar parameters 172

Appendix D: Visibility models 174

Introduction

Studying the origins of life on planet Earth has always been one of the most prominent pursuits in human history. With the increasing advances in astronomy, we began observing other stellar systems closely and discovered that they host a variety of planets with different compositions and sizes. This led to the study of planet formation, aiming to understand how planetary systems like our own and those around other stars originate. By doing so, we hope to uncover not only how Earth and the Solar System formed but also whether life exists elsewhere in the universe or not. Today it is known to be a fact that the process of planet formation begins in the early stages of what are known as protoplanetary disks.

1.1 The beginning and evolution of protoplanetary disks

Classification of young stellar objects

Before discussing the current challenges in studying protoplanetary disks and planet formation, it is important to first consider how far our understanding of their origins has come. The formation of stars and, eventually, planets begins in what is known as a molecular cloud (e.g., Ballesteros-Paredes et al. 2007). These molecular clouds originate from the atomic gas found in the interstellar medium (ISM), the gas and dust that fill the space between stars in galaxies such as our own Milky Way.

As regions within this gas become denser, they reach the physical conditions necessary for molecule formation (Glover & Mac Low 2007; Valdivia et al. 2016; Ballesteros-Paredes et al. 2020), where these dense, molecule-rich regions are the birthplaces of stars and what we call molecular clouds. Initially, the material in these clouds is concentrated in a localized region called a core, but as the system evolves, it begins to evolve away from simple spherical symmetry. Through a process known as accretion, the material (gas and dust) is channeled inward via a rotating disk structure, feeding the growing central protostar (Zhao et al. 2020b), forming the disk that we refer to as a protoplanetary disk. One of the earliest, and still used, observational classifications for Young Stellar Objects (YSOs) was introduced by Lada (1987), dividing them into three categories: Class I, Class II, and Class III sources. This classification was based on spectral energy distribution (SED) observations of these protostars at infrared wavelengths (between 2 and 25 μm, see Fig 1.1). As observational techniques improved and became more sensitive, the classification was extended to include Class 0 objects (Andre et al. 1993). While these classifications have some limitations, they remain widely used today to categorize the evolutionary stages of protoplanetary disks and their host stars.

The evolutionary transition from the initial collapse and disk formation phase (Class 0/I) to the Class II stage occurs very quickly, within approximately 0.5 Myr (Evans et al. 2009). Class II objects, however, persist for a longer period, with median lifetimes between 2–3 Myr, though they can last up to 10 Myr (Fedele et al. 2010; Michel et al. 2021). Although each phase of star evolution presents its own details and challenges, throughout these evolutionary stages, one crucial component shapes the evolution of protoplanetary disks in ways beyond planet formation alone. This component will be studied in detail in this thesis: the interstellar dust grains.

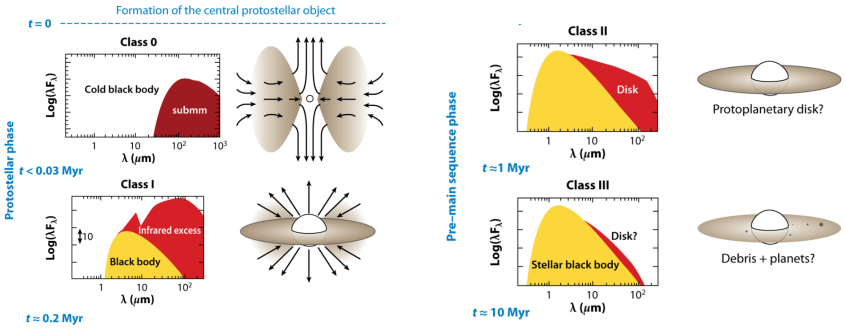


Figure 1.1: Star and disk formation stages classified based on the spectral energy distribution (SED) at micrometer wavelengths, adapted from Dauphas & Chaussidon (2011).

1.1.1 Interstellar dust and its influence in protoplanetary disks

Dust grains significantly influence the composition of the ISM, the appearance of galaxies, and the process of star formation. The term dust grains or interstellar dust is commonly understood, following Draine (2003), as solid particles consisting of tens or more atoms. Although this includes large molecular structures, dust grains are typically larger in size and possess more complex compositions, often involving silicates, carbonaceous materials, and ices. The origin of this dust is believed to be primarily from stellar outflows of red giants, giant stars, and planetary nebulae (stardust). However, it is important to note that the majority of interstellar dust is not pristine stardust; rather, its composition and properties are largely shaped and altered by various physical and chemical processes that occur within the ISM (Draine 2003). The exact composition of these small dust grains remains somewhat controversial, as it can only be inferred indirectly through e.g. spectral emission features, scattered light or optical extinction. These three processes can be explained as follows: Extinction refers to the dimming of optical and near-infrared starlight as it passes

through dust. Scattering is the process where light is redirected in multiple directions as it encounters the surface of a dust grain, and emission occurs when dust grains absorb energy from different sources and then re-emit this energy at longer wavelengths, predominantly in the infrared. From observations of these spectral features, the main probable components of interstellar dust have been narrowed down to the following:

- Silicates: Infrared extinction curves show a strong absorption feature peaking at approximately 9.7 μm, associated with silicate minerals. It is well established that a large fraction of the ISM dust mass is in silicates, with at least 95% of it being amorphous (Li & Draine 2002).

- Carbonaceous materials: A broad spectral feature in the dust extinction curve centered near 0.21 μm is typically attributed to carbon-rich materials, such as graphite or diamond-like carbon.

- Silicon Carbide (SiC): SiC is commonly detected in meteorites and as an emission feature in the spectra of many carbon stars (Treffers & Cohen 1974; Blanco et al. 1998). Although SiC is a confirmed part of interstellar dust grains, its abundance is estimated to be less than 5% that of silicates (Whittet et al. 1990).

- Carbonates: Some carbonates have been detected around dusty disks (Kemper et al. 2002), but these exist only in very small quantities and are not considered a major component of interstellar dust.

Regarding grain sizes, Mathis et al. (1977) showed that the observed extinction curve in the ISM can be reproduced by assuming a grain size distribution following a power law, $dn/da \propto a^{-3.5}$, with grain sizes ranging from 5 nm to 0.25 μm, consisting mainly of graphite and silicate grains. Since then, various modifications have been made to the assumed composition, opacities, and size distributions of dust grains present in

protostellar objects. Despite these refinements, the detailed size distribution in these systems remains uncertain and although larger dust grains are expected in protoplanetary disks (from 5 nm to 1 mm and even cm, Testi et al. (2014)), many assumptions about dust in disks are still based on the properties derived for the ISM.

While it constituting only about 1% of the total YSO mass, dust plays an indispensable role in numerous pathways and aspects of disk and planet formation (e.g., Birnstiel 2024). For example, the continuum dust opacity plays a critical role in regulating disk heating and photodissociation, shaping the disk's structure (Jonkheid et al. 2004; Aikawa & Nomura 2006). Additionally, dust traces the hydrostatic structure of disks, as small dust particles absorb and emit stellar radiation, heating the disk and influencing the thermal balance (Gorti & Hollenbach 2009; Woitke et al. 2009). Dust grains also provide the surface area for the formation of volatile and complex organic molecules (COMs) (e.g., Garrod & Herbst 2006), which are considered precursors to prebiotic chemistry and their formation in early star-forming regions may determined the potential habitability of new forming planets. Moreover, depending on the disk's dynamics and the locations where molecules freeze-out or form, dust contributes to the redistribution and structural variation of chemical abundances (e.g., Cyr et al. 1998; Ciesla & Cuzzi 2006; Krijt et al. 2016; Stammler et al. 2017) which may set a diversity in the atmospheric conditions of exoplanets.

Observationally, dust can be traced in both scattered light and thermal dust emission. Scattered light originates from small dust particles in the upper layers, whereas thermal dust emission ranges from optically thick continuum emission in the infrared to optically thin continuum emission at millimeter wavelengths. Modern telescopes such as the Atacama Large Millimeter Array (ALMA) can detect this millimeter emission, offering valuable insights of the disk structure, but more importantly of the disk's mid-plane where it is believed that dust grows, collides, accumulates, migrates, and eventually leads to the formation of planets (Brauer et al. 2008). This underscores the crucial role of dust in shaping not only

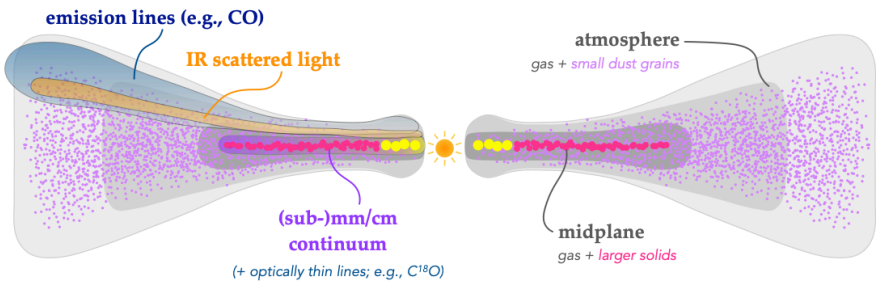


Figure 1.2: Protoplanetary disk structures as traced by emission lines, infrared scattered light (small dust grains), and sub-mm/cm continuum emission (large dust grains), adapted from Andrews (2020).

planet formation, but also the overall structure, evolution, and chemical composition of protoplanetary disks, by both tracing and influencing different regions within them. Figure 1.2 illustrates the current understanding of disk structure. Infrared scattered light traces small dust grains in the upper, flared surface layers of the disk. Sub-millimeter continuum emission, probes larger, millimeter-sized grains that have settled closer to the mid-plane. Meanwhile, molecular line emission, such as CO and its isotopologues, traces the gas component across different vertical layers. Together, these tracers provide a more complete view of the physical and chemical environment within protoplanetary disks that will be studied in this thesis.

1.1.2 Dust evolution: Radial Drift

To understand how dust evolves in protoplanetary disks, it is essential to comprehend the drag forces that enable various interactions between these dust particles, including collisions, sticking, fragmentation, and growth. These interactions are the building blocks of dust dynamics in protoplanetary disks (Brauer et al. 2008; Birnstiel et al. 2010; Zsom et al. 2010; Windmark et al. 2012). In particular, drag forces occur due to

the interaction between dust particles and the surrounding gas, which depends on the relative motion between them and the particle size (e.g., Testi et al. 2014).

The most important consequence of drag forces is the dust radial drift (Whipple 1972; Adachi et al. 1976; Weidenschilling 1977). In a disk with gas, where centrifugal forces, gravitational forces, and pressure gradients are in balance, the gas orbits at a slightly sub-Keplerian speed, caused by an outward pressure gradient. Dust particles, however, depending on their degree of coupling to the gas, are primarily influenced by gravitational and centrifugal forces and, as a result, they tend to move at Keplerian velocities. This slight difference in orbital velocities between the gas and dust leads to the dust experiencing a headwind, which results in dust particles eventually slowing down and spiraling inward towards the star. The rate of radial drift then depends on how strongly the dust is coupled to the gas, which is quantified by the dimensionless Stokes number, $St = t_{stop}\Omega_K$ (Cuzzi et al. 2001). This number relates the stopping time to the orbital timescale, and depends on particle size and composition, meaning that particles of different sizes drift at varying speeds in different regions of the disk (Testi et al. 2014).

One of the main unresolved issues that will be mentioned throughout this thesis is that, unless the disk is exceptionally massive (which is unlikely), large dust particles on the order of mm to cm in size will spiral into the star very quickly, within a short fraction of the disk's lifetime. This rapid inward motion makes it difficult for dust to interact, grow, and finally, form planetesimals or planets. Numerous studies were conducted to understand and solve the problem of radial drift (e.g., Whipple 1972; Weidenschilling 1977; Youdin & Shu 2002; Brauer et al. 2007). Even then, a proposed solution to this problem was an inversion of the pressure gradient in the disk to help halt radial drift (Nakagawa et al. 1986; Pinilla et al. 2012b), though observational capabilities were limited at the time, and results were primarily theoretical.

1.1.3 Dust evolution: Settling and turbulent mixing

In addition to radial drift, there is another important type of drag force that exist in protoplanetary disks and shapes the pathway of planet formation: Turbulent mixing and settling. Under the influence of gravitational force, dust particles were initially thought to follow inclined orbits, oscillating vertically and constantly through the mid-plane. However, due to strong gas drag-forces, these particles tend to gradually settle toward the mid-plane over timescales of a few hundred thousand years (Goldreich & Ward 1973; Weidenschilling 1980; Nakagawa et al. 1986; Dullemond & Dominik 2004). Understanding vertical settling is vital, as it directly shapes and regulates the concentration of dust in the disk mid-plane, that allows dust to gather and grow. This process, however, does not occur unimpeded. Turbulent mixing, which is often attributed to instabilities such as the Magneto-Rotational Instability (MRI) or other hydrodynamic instabilities, counteracts settling by stirring particles upward, preventing excessive dust accumulation at the mid-plane. This process typically acts within a specific vertical region of the disk: above a certain height, vertical settling can proceed efficiently, causing small grains to settle rapidly and disappear from the upper layers; below that, turbulence maintains the balance within a more uniform dust distribution for grains of certain sizes and establishing a balance that defines the vertical distribution of solids (Dullemond & Dominik 2004). In this context, Dubrulle et al. (1995) was able to calculate the vertical structure of the dust layer by solving the equilibrium between the effects of settling and turbulent mixing, which defines the dust scale height.

Settling has profound implications for the observational appearance of disks. It can lead to the formation of a thin mid-plane layer of large grains (e.g., pebbles). Additionally, settling alters the disk's optical depth and temperature structure, affecting the emission and scattering properties observable in infrared and millimeter wavelengths (Chiang et al. 2001; D'Alessio et al. 2001; Dullemond & Dominik 2004). High-resolution obser-

vations of edge-on protoplanetary disks at both millimeter and infrared wavelengths have confirmed a certain degree of settling by measuring the vertical extent of the dust continuum emission at different wavelengths (e.g., Villenave et al. 2019, 2020, 2022).

Both drag forces (radial drift and vertical settling), shape the appearance of protoplanetary disks and influence their observational signatures (Fig. 1.2). In this thesis, understanding these processes is key to interpreting the emission observed from such disks with one of the most advanced astronomical instruments of our era.

1.2 Protoplanetary disks in the modern era with ALMA

The Atacama Large Millimeter/submillimeter Array (ALMA) is a state-of-the-art telescope located on the Chajnantor Plateau in the Chilean Andes. It was built by the collaboration between the European Southern Observatory (ESO), the National Radio Astronomy Observatory (NRAO) and the National Astronomical Observatory of Japan (NAOJ) to study the universe in unprecedented detail. One of ALMA's primary goals is to observe the coldest objects in the universe, such as molecular gas and dust, which emit radiation at millimeter and submillimeter wavelengths.

ALMA consists of 66 individual antennas, each operating at wavelengths ranging from 0.32 to 3.6 millimeters at high sensitivity. It functions as an interferometer, meaning the signals from multiple antennas are combined to simulate a much larger telescope, with the resolution of such an array being comparable to that of a single dish with a diameter equal to the maximum separation between antennas. The main array includes fifty 12-meter antennas, complemented by an additional four 12-meter and twelve 7-meter antennas in the Atacama Compact Array (ACA). The distance between antennas can be adjusted from 150 meters up to 16 kilometers, allowing ALMA to achieve some of the highest angular

resolutions ever achieved to study the universe.

Over the last decade, the capabilities of ALMA have significantly advanced our understanding of protoplanetary disks, not only in terms of dust evolution and continuum emission at sub-millimeter wavelengths, but also concerning molecular line emission and the gas structure within these disks.

1.2.1 Gas and ice content of protoplanetary disks

The chemical composition of protoplanetary disks depends on two main factors: the chemical processes occurring within the disk itself and the chemical inheritance passed down from the interstellar cloud (e.g., Visser et al. 2009). While the first molecules form in the interstellar cloud, most remain frozen in icy mantles on the dust grains. During the protostellar phase, however, more complex molecules form in the ice through processes such as hydrogenation and irradiation. These molecules, along with pre-existing volatiles, then sublimate before being incorporated into the disk (e.g., Öberg et al. 2023).

The gas and chemical structure in the disk also experiences redistribution, similar to dust, and is influenced by processes such as advection, turbulent diffusion, and disk winds. One of the most important factors affecting the gas distribution in disks is the location of condensation fronts, or snowlines (e.g., Öberg et al. 2023), which impact the chemistry in both radial and vertical direction. Snowlines mark the regions where molecules freeze out in the disk, depending on the vertical and radial temperature gradients. It is believed that these snowlines play a critical role in planet formation (e.g., Hayashi 1981) for three main reasons:

- The surface density of dust particles is thought to be enhanced beyond the snowlines, meaning that outward past a snowline, gas-phase molecules freeze onto grains, increasing their mass and surface density (Zhang 2024).

- Depending on the local temperature, snowlines could facilitate

the formation of planetesimals since the fragmentation thresholds (maximum velocity at which dust particles can collide without breaking apart) and sticking properties of the dust change given their icy composition or lack thereof after crossing a snowline. (Gundlach & Blum 2015; Gundlach et al. 2018)

- Snowlines create distinct regions within the disk that have different elemental ratios, as various molecules freeze out at different distances from the central star depending on the temperature. The classical picture suggests that measuring elemental ratios in planetary atmospheres can reveal their formation locations within the disk (Öberg et al. 2011). However, more recent studies have shown that in reality, the elemental ratios are more complicated due to effects of dust transport (e.g., Krijt et al. 2023).

Although chemical characterization of disks has been conducted observationally across a wide range of frequencies and energy scales, from UV to millimeter wavelengths observations, our focus on this thesis will be on submillimeter and millimeter observations, which probe the cold gas, the bulk of the disk's gas reservoir (e.g., Öberg et al. 2023). Depending on dust optical depth and the specific spectral lines observed, it is possible to trace gas from the disk's upper layers down to the mid-plane regions of protoplanetary disks. More specifically, with ALMA's long baselines and sensitivity, rarer molecules can be detected, enabling high spatial resolution studies of disk chemistry on scales smaller than 10 au (Öberg et al. 2015; Huang et al. 2018a). To date, 31 molecules have been detected in Class II protoplanetary disks (McGuire 2022; Booth et al. 2021; Canta et al. 2021; Phuong et al. 2021; Brunken et al. 2022), yet more complex molecules are still being observed and discover within the earlier stages of disk formation.

1.2.2 Complex organic molecules in YSOs

The study of molecular emission in YSOs has progressed significantly in recent years, particularly with the discovery of several complex molecular species from within the interstellar medium (ISM) to the core of protoplanetary disks. According to Herbst & van Dishoeck (2009), a complex organic molecule (COM) is defined as a carbon-bearing molecule containing at least six atoms, the term COM (or COMs) has become widely adopted in the literature. Although other nomenclature exists, for the purposes of this thesis, we will consistently use the term COM. Understanding the abundances and distributions of COMs in YSOs and how they eventually make their way into protoplanetary disks is crucial, as these COMs in the Solar Nebula were potential building blocks for life (Zhang 2024).

Advancements made possible by ALMA and other facilities have greatly expanded our understanding of COMs. Initially, they were only identified in the ISM or in high-mass star-forming regions. However, more recent observations have shown that most of the same COMs are also present in low-mass star-forming regions, with no clear difference in abundances ratios and therefore chemical complexity between high- and low-mass environments (Jørgensen et al. 2020).

As the number of observational samples has increased, the number of open questions has increased as well. For instance, Bisschop et al. (2007) studied COM emission in seven high-mass YSOs and found that the molecules fell into two distinct groups: one tracing hot gas ($T > 100$ K) and the other associated with cold gas ($T < 100$ K). While several subsequent studies attempted to establish some chemical patterns between these sources, their efforts were often limited by insufficient spatial resolution, the number of detectable COMs, and different spectral coverage (e.g., Calcutt et al. 2014; Suzuki et al. 2018; Taniguchi et al. 2018).

Despite these limitations, these early studies were fundamental and critically important, as they allowed researchers to begin distinguishing between different physical regions and processes in young stellar objects.

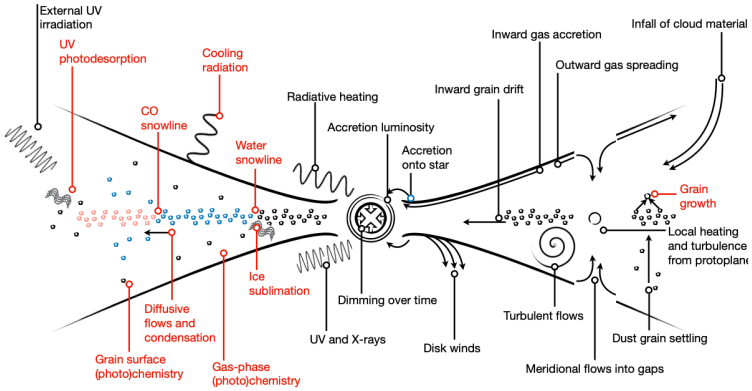


Figure 1.3: An overview of all the chemical processes occurring in protoplanetary disks taken from Öberg et al. (2023). In this schematic, processes shown in black are stellar and dynamical ones, while those in red correspond to chemical processes that directly depend on the disk's chemical composition.

For example, in the case of the young high-mass YSO G328.2551–0.5321, ALMA observations at small spatial scales (a few hundred AU) revealed clear chemical differentiation (Csengeri et al. 2018, 2019). This was interpreted as evidence of accretion shocks combined with a rotational pattern. From a theoretical perspective, the formation of a circumstellar disk is thought to be closely tied to the presence of such accretion shocks, where infalling material transitions into the disk structure (e.g., Cassen & Moosman 1981; Neufeld & Hollenbach 1994). These findings underscore the importance of high-resolution chemical studies in unraveling the physical mechanisms that govern disk formation and early stellar evolution. However, this is only a brief overview, and it is important to acknowledge the wide range of processes involved in the chemistry of protoplanetary disks and the distribution of complex organic molecules (COMs), as illustrated in Fig. 1.3.

1.2.3 Early disk formation and spatial distribution of dust and COMs

Observations with ALMA and other sub-millimeter facilities have gradually revealed the presence of Keplerian disks in embedded objects or Class I protostars, confirming their existence (e.g., Harsono et al. 2014; Yen et al. 2015a; Artur de la Villarmois et al. 2019b), including in some Class 0 sources (Tobin et al. 2012; Murillo et al. 2013; Yen et al. 2017). However, there are also notable cases where no clear signs of Keplerian rotation are detected, even down to 10 au scales (e.g., Yen et al. 2015b; Jacobsen et al. 2019).

Despite the non-detections, these youngest circumstellar disks provide a crucial link between the complex organic molecules (COMs) observed in warm gas regions and the initial conditions for subsequent dust evolution and planet formation. As noted by Harsono et al. (2018), many embedded disks may already harbor millimeter-sized dust grains, which can lead to optically thick dust that obscures the underlying gas emission. Consequently, careful interpretation is required when analyzing the spatial differentiation between molecular species and dust emission at these scales. Even in the absence of large grains, high continuum optical depths can significantly affect the observed gas emission.

The exact distribution and origin of complex organic molecules (COMs) around Class 0/I protostellar sources remains an open question. Observations from the ALMA Ophiuchus survey suggest that CH_3OH is very limited in spatial extent toward certain protostars (Artur de la Villarmois et al. 2019a). Additionally, Lee et al. (2017) conducted an in-depth study of the HH 212 protostellar system in the L1630 cloud of Orion, leading to the suggestion that some COM species may reside in the "atmosphere" of the disk. These molecules may either originate from cold regions on larger scales, sublimating upon heating in the disk atmosphere, or form in situ through rapid gas-phase reactions under high-temperature conditions.

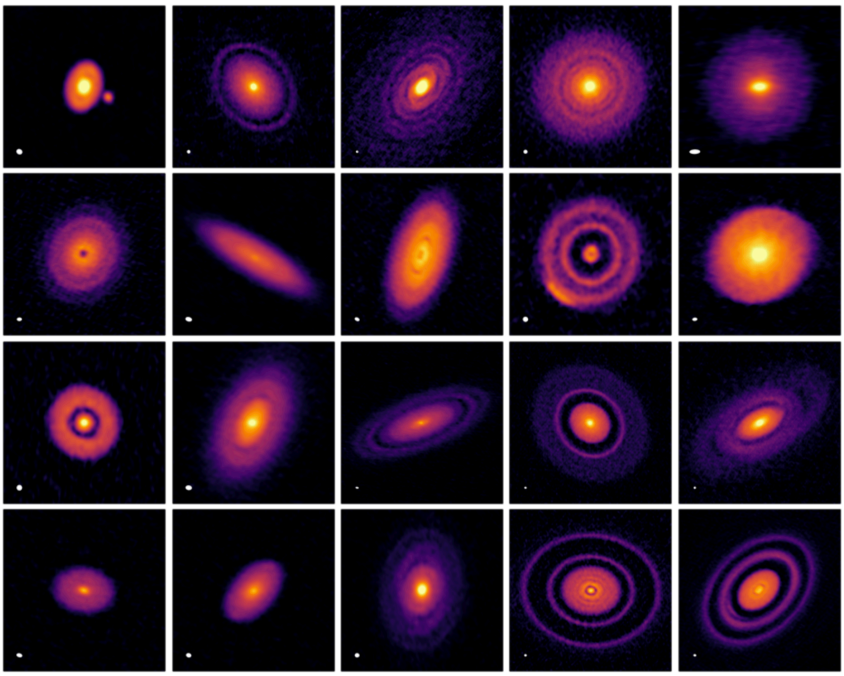


Figure 1.4: ALMA observations at 240 GHz from the DSHARP survey (Andrews et al. 2018a) revealing a variety of substructures in the dust continuum emission, indicating a more complex dust surface density distribution.

Nevertheless, this investigation is ongoing, and to properly constrain the spatially resolved abundance profiles of COMs in protostellar envelopes, high-sensitivity ALMA observations are essential. Such studies should be extended to larger, statistically significant samples of young stellar objects. This is the only way to robustly test the predictions of astrochemical models, derive accurate molecular abundances, and identify systematic patterns in the chemical structure and distribution of COMs during the earliest stages of star and planet formation (Jørgensen et al. 2020).

1.2.4 Substructures in protoplanetary disks

Regarding more evolved disks, early high-resolution, high-sensitivity ALMA observations (e.g., ALMA Partnership et al. 2015; Andrews et al. 2016; Isella et al. 2016) revealed that Class II disk density distributions are not as smooth as once thought, but instead exhibit distinct radial structures and variations. These findings supported the idea that pressure gradients, originally proposed as a solution to the efficiency of radial drift as mentioned before, may indeed be present and play a role in dust trapping, bringing us closer to understanding planet formation.

Subsequent studies showed that the most common substructures in these disks appear as bright rings and deep gaps, while less frequently observed features include spiral arms and asymmetries. (e.g., Pérez et al. 2016; Dong et al. 2018; Andrews et al. 2018a), as shown in Figure 1.4. Despite these observations, how and when these substructures originate remains an open question. Among some of the proposed mechanisms, the most widely accepted explanation involves planet-disk interactions (e.g., Zhu et al. 2014; Bae et al. 2017; Zhang et al. 2018). However, while planets can create the substructures needed to halt radial drift, such structures may also be necessary to grow dust and form planets themselves creating a chicken and egg problem.

Moreover, the increasing number of substructures detected in protoplanetary disks without any clear planetary signatures has motivated alternative theories. These include zonal flows and MHD-induced pressure bumps, gravitational instabilities, condensation fronts such as snow lines, and other dust evolution processes like sintering (Zhang et al. 2015b; Flock et al. 2015; Okuzumi et al. 2016; Dong et al. 2018).

Given this paradigm, determining when exactly these substructures emerge, particularly during the early, embedded Class 0/I phases, is critical for interpreting the substructures observed in more evolved, Class II disks.

1.3 The current problems in planet formation

While significant advances in planet and disk formation since the early ALMA years have been made, several key challenges remain. In this section, we highlight two of these unresolved issues that are particularly relevant to this thesis. These problems will be introduced here and discussed in greater detail in the following chapters.

1.3.1 Early substructure formation and unsettled Disks in YSOs

Ohashi et al. (2023) conducted high-resolution ALMA observations of several Class 0/I disks, revealing a strong connection between the physical structure, chemical composition, and evolution of young stars and their surrounding disks. Despite the remarkable resolution of these observations, most of the YSO disks showed little to no substructure in the dust continuum at 1.3 mm, at least at the wavelength at which the data was taken (see Fig. 1.5). This raised several questions about the true origin and timing of substructure formation in disks. The authors suggested that the apparent absence of substructures may be either due to high optical depths obscuring them or that the substructures that we commonly observed in Class II disks form very quickly during the transition from Class I to Class II, which would support scenarios involving early and thus rapid planet formation.

For optical depth to effectively obscure substructures, the disk must exhibit significant vertical structure. This requires a degree of stratification, where smaller grains trace upper layers of the disk, while larger grains, and substructures, reside closer to the mid-plane. In fact, studies of edge-on Class I protoplanetary disks by Villenave et al. (2020, 2023) show that disk layers probed by infrared scattered light have a much larger vertical extent than those traced by ALMA at millimeter wavelengths. Also in more evolved Class II disks, several observations show that the scale height increases with decreasing wavelength (Villenave et al. 2020). While

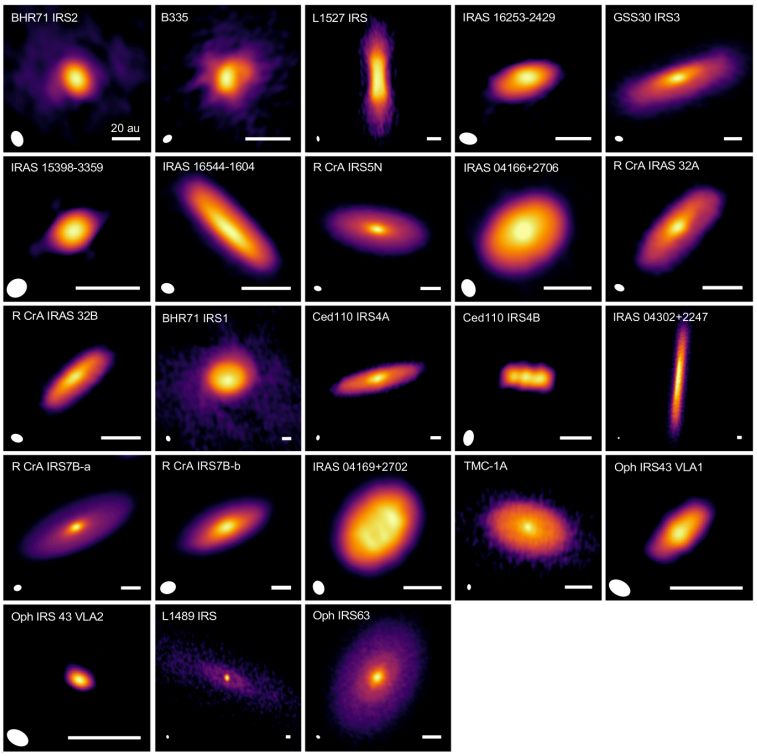


Figure 1.5: ALMA observations of protoplanetary disks around Class 0/I sources by Ohashi et al. (2023), revealing that most of these disks exhibit little to no substructure.

this stratification depends on the optical depth at the observe wavelengths and the structure of the disk itself, not all dust grains appear to be fully settled, particularly those traced at the shortest sub-millimeter wavelengths with ALMA, where the emission is expected to be optically thick.

These optically thick observations often provide very limited insight into disk substructures and, therefore, into potential signs of planet formation. Such observations, however, may contain information about the vertical structure of disks and the degree of dust settling. Understanding the settling and the vertical distribution of solids in disks is just as important as understanding radial drift. Settling governs how much dust

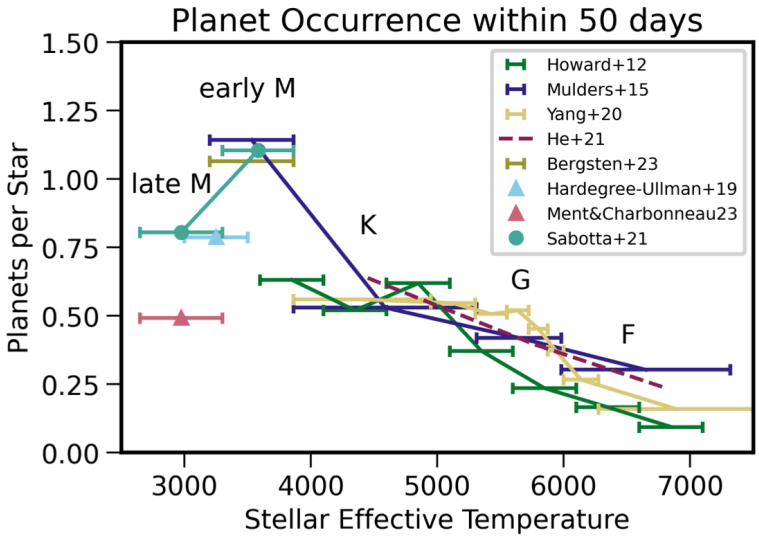


Figure 1.6: The occurrence rate of sub-Neptunes with orbital periods of less than 50 days as a function of stellar spectral type, source from Mulders (2018).

accumulates in the mid-plane, where grain growth and planet formation take place. Ignoring the vertical structure (scale height) of dust in protoplanetary disks risks overlooking a critical mechanism that could replenish the mid-plane with material that allows for planet formation to happen.

1.3.2 Exoplanet demographics vs protoplanetary disks surveys

Another challenge in planet formation studies has been the reconciling of the growing exoplanet catalog with the structures observed in Class II protoplanetary disks. Since the discovery of the first exoplanet, thousands of planets have been identified, with many exciting findings, such as the relation between the occurrence rate of giant planets and stellar mass (e.g., Johnson et al. 2010). However, the majority of giant exoplanets are detected at orbital radii between 1 and 10 au (Fernandes et al. 2019;

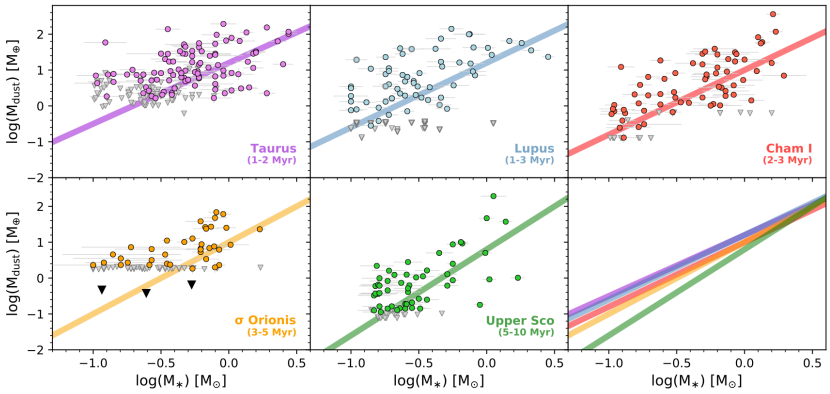


Figure 1.7: Stellar masses vs dust masses of protoplanetary disks, derived from various ALMA observations across multiple star-forming regions (Ansdell et al. 2017).

Fulton et al. 2021), which doesn't align well with the large-scale substructures seen in Class II disks. If these planets indeed formed in the outer disk regions (in association with these substructures), significant inward migration must have occurred during their evolution.

Second, super-Earths, which vastly outnumber giant gas planets, are much more commonly found around M-type stars after their formation (Howard et al. 2010, 2012). This trend is inversely correlated with stellar mass (see Fig. 1.6). van der Marel & Mulders (2021) compared the occurrence of disks with and without substructure and the known exoplanetary systems. They proposed that in systems without large-scale substructures, indicating that giant planets have not formed at wide orbits early in the disk lifetime, radial drift leads to the formation of a compact disk. These compact disks would experience a high influx of large dust grains (pebbles) in the inner regions of the disk to form the most common type of exoplanet, the close-in super-Earths with masses < 20 $M_\oplus$, potentially resolving the apparent discrepancy between observed disk structures and exoplanet demographics. This idea is supported by observational trends, where compact disks and close-in super-Earths are both more frequently

found around M-dwarf stars (e.g., Mulders et al. 2018).

Although demographic surveys of protoplanetary disks have already provided valuable insights into disks properties and dust evolution, such as the correlation between stellar mass and dust mass, and the observed decrease in dust mass in older star-forming regions (see Fig. 1.7) (~0.25", Ansdell et al. 2016; Barenfeld et al. 2016; Cieza et al. 2019). These studies have generally been conducted at relatively low angular resolution, especially when looking at complete star-forming regions. As a result, key properties of compact disks, such as their true sizes and dust content, remain poorly constrained. Most high-resolution ALMA observations to date have focused on the brightest and therefore largest disks and only a limited number of compact disks have been observed at high resolution in recent years (Facchini et al. 2019; Long et al. 2019; Kurtovic et al. 2021; van der Marel et al. 2022; Miley et al. 2024; Shi et al. 2024). While these studies were novel, the exact connection between compact disks and the formation of super-Earths remained inconclusive.

1.4 This thesis

While it is now believed that substructures in protoplanetary disks are, directly or indirectly, essential for planet formation, their exact origin remains unclear. In this thesis, we aim to address questions about these substructures and how they relate to planet formation and dust growth. Specifically, we want to investigate how and when these substructures form by studying young disk systems such as IRAS4A and HL Tau, as well as those in a nearby star-forming region like Lupus. Can substructures be detected in optically thick environments, and even at optically thick wavelengths, assuming they are deep enough? Does the chemical structure in these embedded disks show signs of dust evolution? Are substructures only common in large, massive disks, or is their absence in the most compact disks simply a matter of resolution? And if compact disks truly lack substructures, do they still have the conditions necessary to trigger planet formation, particularly for planets like super-Earths? We will use ALMA and VLA observations at several wavelengths (8, 2.1, 1.3, 0.9, and 0.45 mm) to study these questions of protoplanetary disks. We will first focus on optically thick observations of two systems at different evolutionary stages: the Class 0 source IRAS4A and the Class I source HL Tau. We aim to constrain the dust properties and vertical structure (scale height) of both disks to better understand the dust distribution and its role in dust evolution and disk substructures. For IRAS4A, we will also analyze molecular line emission to further constrain the dust distribution and provide insights into its evolutionary stage. Finally, we will study all protoplanetary disks, including the faintest ones, at high angular resolution of 0.025" in the Lupus star-forming region, aiming to determine their true dust sizes and explore the implications for dust evolution and the formation of the most common exoplanets: super-Earths.

1.4.1 Analysis tools

For the work in this thesis, we primarily used three publicly available software packages: RADMC-3D (Dullemond et al. 2012), GALARIO (Tazzari et al. 2018), and CASSIS (developed by IRAP-UPS/CNRS (https://cassis.irap.omp.eu)). These tools were employed to analyze observations from the telescopes at sub-mm wavelengths (ALMA or VLA), using the visibility data or the molecular and continuum emission.

RADMC-3D is a publicly available radiative transfer code widely used in astrophysics and astronomy. It is primarily designed to simulate the thermal and radiative properties of environments such as protoplanetary disks, molecular clouds, and circumstellar envelopes. The code calculates the dust temperature using a Monte Carlo radiative transfer method, producing realistic dust continuum emission. For gas, line radiative transfer is performed under the assumption of local thermodynamic equilibrium (LTE). RADMC-3D acts as a post-processing tool, allowing users to generate synthetic images, spectra, and spectral energy distributions (SEDs) based on parametric input models of gas and dust density and a stellar radiation field. One of its key strengths is its flexibility: it supports fully three-dimensional geometries, making it ideal for modeling complex disk structures. Because the models are user-defined, RADMC-3D offers significant freedom in setting up custom simulations. Its output can be directly compared with observational data, such as those obtained from the ALMA telescope.

GALARIO (GPU Accelerated Library for Analyzing Radio Interferometer Observations) is a library package designed to accelerate the comparison between model predictions and observed visibilities from radio interferometric telescopes. With the rapid advancement of interferometric techniques and the increasing volume of data across a wide range of spatial frequencies, fast and efficient computational tools like GALARIO are essential. Rather than working with reconstructed images, GALARIO operates directly in the Fourier (uv) plane, preserving the full spatial in-

formation and avoiding biases introduced during image deconvolution. GALARIO is particularly well suited for fitting disk models, comparing visibility profiles of disks with and without substructure with observations. It is especially useful in high-resolution studies of protoplanetary disks, where exploring parameter spaces directly in the uv-plane enables robust constraints on disk geometry and emission profiles.

CASSIS is a publicly available software tool for identifying molecular transitions and modeling spectra from astronomical observations. It is valuable for interpreting data from sub-millimeter observations from radio telescopes like ALMA. CASSIS allows users to visualize, analyze and identify molecular emission lines using spectral catalogs such as CDMS and JPL. It supports both LTE modeling and non-LTE analysis through integration with RADEX. CASSIS is particularly useful in the study of protoplanetary disks, where it helps extract key physical parameters, such as gas temperature, column density, and velocity structures—from observed molecular line emission.

Chapter 2: IRAS4A1: Multiwavelength continuum analysis of a very flared Class 0 disk.

In this chapter, we analyze the continuum dust emission of the protobinary system NGC1333-IRAS4A (IRAS4A), a well-studied Class 0 system located in the Perseus molecular cloud at a distance of 293 parsecs (Zucker et al. 2018). IRAS4A consists of two Class 0 protostars, IRAS4A1 and IRAS4A2, with a separation of 1.8" (Tobin et al. 2018). We obtained high-resolution ALMA and VLA observations (78 mas) of this protobinary system, which allowed us to create dust continuum images of IRAS4A1. From these images, we derived radial profiles of the spectral index and brightness temperature. Our analysis focuses exclusively on IRAS4A1, as IRAS4A2 remains unresolved at the resolution of our current dataset.

We modeled and fitted the emission at each wavelength using radiative transfer equations and Markov Chain Monte Carlo (MCMC) methods

to infer the dust properties that better reproduce the observed brightness temperatures across the disk. Our results suggest that, while IRAS4A1 is significantly more massive than typical Class II disks, the characteristic dust grain sizes are already of millimeter sizes.

To investigate the presence of substructures in IRAS4A1, we used the radiative transfer code RADMC-3D to simulate disks with varying scale heights and flaring angles. Our models show that substructures, such as rings or gaps, can remain hidden in optically thick disks if the vertical scale height is large and the disk is moderately inclined. Using the mass estimates derived from our dust parameters, we specifically modeled IRAS4A1 and found that certain features in the emission, such as shoulders, could only be reproduced by introducing substructures into the models. This suggests that substructures could indeed be present at these early stages but remain concealed within optically thick regions, a scenario that could plausibly extend to other Class 0 sources as well.

Chapter 3: From large-scale outflows to compact line emission in IRAS4A2.

In Chapter 3, we focus our analysis on IRAS4A2, as unlike IRAS4A1, its molecular content is not hidden by optically thick dust. Although a multi-wavelength continuum analysis could not be performed for this source, IRAS4A2 is believed to be more evolved than IRAS4A1. This motivated a comprehensive study of its molecular emission and what it reveals about dust distribution and the embedded disk conditions.

IRAS4A2 is one of the first hot corinos ever discovered (Bottinelli et al. 2004). As previously mentioned, it is part of a binary system that shows significant interaction in both the millimeter continuum and line outflow emission. Its molecular content has been extensively studied (e.g., Taquet et al. 2015; López-Sepulcre et al. 2017; De Simone et al. 2017), although only very recently at high resolution of 0.2" (Frediani et al. 2025). Here, we present observations at even higher angular resolution (~0.15") and over a

broader frequency range (140.7319–140.8512 GHz and 265.8214–267.6103 GHz).

Our observations revealed that the molecular environment spans from large-scale outflows, traced by HCN, H_2CO, and HCO^+, to the innermost regions of the IRAS4A2 system. Using CASSIS, a spectral analysis tool (Vastel et al. 2015), we detected numerous complex organic molecules (COMs), confirming the presence of at least 4 (e.g., $C_2H_3CN_{v=0}$, $CH_2(OH)CHO$, CH_3OCHO, and $CH_3C^{15}N$), with several additional tentative detections. These molecules appear to trace multiple components of the system simultaneously, increasing the challenge of the analysis.

Through analysis of the zero-moment maps (integrated emission of the molecules), we identified four distinct regions: the bipolar outflows, a large flattened envelope structure, a disk, and a warm inner envelope. Some emission lines also show strong absorption, particularly in the regions associated with the warm inner envelope.

Position–velocity (PV) diagrams, combined with upper-state energy levels and emission area estimates, indicate that many molecules, including sulfur-bearing species that are likely tracing accretion shocks too, trace stratified layers in the disk, as well as mid-plane emission near the central star. The mid-plane emission appears to be partially absorbed for many molecules, though not for all, suggesting that the envelope has either dissipated in the outer regions, has become optically thin in most areas, or has shrunk and moved closer to the star and the mid-plane, pointing towards settling processes still ongoing. This, combined with continuous dust radial drift, affects the location at which sublimation temperatures for different COMs are reached, altering both the radius and scale height where they are observed. These findings indicate that the radial and vertical chemical structure and emission in young stellar objects are more complex than previously anticipated and that the dust keeps rapidly evolving within the system.

Chapter 4: Into the thick of it: ALMA 0.45 mm observations of HL Tau at a resolution of 2 au.

In Chapter 4, we analyzed the protostellar system of HL Tau, one of the most well-known and extensively studied protoplanetary disks. HL Tau is a young stellar object located in the Taurus-Auriga molecular cloud (~147 pc; Galli et al. 2018). It is classified as a Class I disk transitioning to Class II (Furlan et al. 2008), with an estimated age of less than 1 Myr (Liu et al. 2017). HL Tau was among the first protoplanetary disks observed at high resolution with ALMA that revealed bright and dark ring features (ALMA Partnership et al. 2015).

For this work, we analyze optically thick emission using ALMA Band 9 observations. Despite the high optical depth, Band 9 data offers valuable insights due to its unprecedented angular resolution. In the case of HL Tau, we achieved a resolution of 13 milliarcseconds, the highest ever obtained for a protoplanetary disk with ALMA. This unprecedented resolution allowed us to probe the innermost regions of the disk, where we identified a previously undetected substructure at ~2.5 au. This feature, shown as an increase in the brightness temperature, is likely caused by an increase in the surface density of small dust particles, potentially linked to the effects of the water snowline.

Additionally, we identified a notable asymmetry within the inner 32 au of the disk. We argue that this asymmetry arises from a combination of optically thick emission, a significant dust scale height, and a certain disk inclination. Using radiative transfer modeling, we found that the HL Tau disk exhibits a dust dimensionless scale height (h/r) of approximately 0.08 at the observed wavelengths, and that the observed asymmetry is degenerate with the dust mass. This suggests that millimeter-sized grains may be less settled than previously assumed, and that the dust scale height may vary with radius in protoplanetary disks.

Finally, we revisited the multi-wavelength analysis from Carrasco-González et al. (2019), this time incorporating the optically thick Band

9 data. The addition of this high-frequency dataset allowed us to better constrain the dust temperature profile, which in turn influenced all other model parameters. We derived grain sizes up to an order of magnitude larger within 60 au, along with consistently lower dust temperatures at all radii.

Altogether, this work emphasizes the importance of studying the smallest observable wavelengths with ALMA. Despite observational challenges, these data are essential for revealing the detailed dust properties and structures within protoplanetary disks, demonstrating that deep substructures can still exist in optically thick and unsettled environments.

Chapter 5: A high-resolution survey of protoplanetary disks in Lupus and the nature of compact disks.

To better understand planet formation and its connection to protoplanetary disks, specifically around M-dwarfs, we obtained high-resolution observations of all Class II disks in the Lupus star-forming region. Lupus is a nearby (~160 pc; Lombardi et al. 2008; Galli et al. 2020), young (1–2 Myr), low-mass star-forming region in the Scorpius-Centaurus association, comprised of several molecular cloud complexes (Lupus 1–9).

With resolved observations of nearly all disks within this single region, we constructed a comprehensive image gallery of Lupus disks at high resolution, gathering data from both our observations and existing literature. This enabled a complete analysis of the full sample of 74 Class II disks around low-mass (M-type) stars.

We found that 67% of the disks in Lupus are compact, with dust radii smaller than 30 au. Notably, we measured dust sizes down to 0.58 au and discovered previously undetected substructures, primarily cavities, in 11 of these compact disks.

By plotting the size–luminosity relation, we found that the majority of disks follow a trend consistent with a drift-dominated evolutionary scenario. Through radiative transfer modeling, we estimated the dust

masses of the compact disks to be relatively low (ranging from 0.3 to 26.3 $M_{\oplus}$), corresponding to optically thin emission in most cases. This suggests either that current observations probe only a surface layer of the total dust mass or that we are witnessing the remnants of dust material left after the bulk of planet formation has already taken place.

Finally, our results show that one-third of the total disk population in Lupus is smooth, and only large disks commonly show substructure at the current resolution. Taken together, these findings highlight compact disks as promising birthplaces with the ideal conditions for forming super-Earths, the most common type of exoplanet observed.

1.4.2 Main conclusions

- By showing the possibility of substructures in a system like IRAS4A1 and the chemical distribution in IRAS4A2, we suggest that planet formation may already be well underway, or even completely finished by the Class II phase in protoplanetary disks. This suggests that it must begin very early in the disk lifetime, during the Class 0/I phase, or happen rapidly during the transition from Class 0/I to Class II. Understanding these early formation stages is therefore critical for constraining planet formation mechanisms. One way to investigate this is by exploring the connection between disk substructures and the occurrence of planets. By identifying substructures in the earliest stages of disk evolution or linking their presence, or absence, to known and distinct types of exoplanets, these studies can provide valuable insights into how and when planets are most likely to form.

- There is much scientific value in looking beyond the more common wavelengths of 0.8-1.3mm with ALMA and the brightest protoplanetary disks. Small disks and optically thick regions with ALMA can offer equally valuable insights about disk structure and evolution. Moreover, high-resolution molecular line observations, combined with dust continuum data, are essential to fully understand the dis-

tribution of solids and the conditions that drive planet formation. Future efforts should focus on studying the most common disks in our galaxy, compact disks, as they are crucial for building a more representative and comprehensive picture of protoplanetary disk evolution.

- The vertical distribution of dust (i.e., dust settling) is just as important as the radial distribution (i.e., radial drift) in shaping protoplanetary disk structure. These processes must be studied together to gain a comprehensive understanding of disk evolution. Furthermore, radial variations in the vertical structure of disks appear to be more common than previously thought, and their characterization in disk substructures may hold the key to understanding the initial conditions for planet formation.

- Most disks in low-mass star-forming regions are compact (less than 30 au), with substructures commonly observed only in larger disks. However, substructures may remain hidden in the innermost regions of these compact protoplanetary disks, or some other mechanism, still unknown, might be slowing down radial drift. The fact that most compact disks have relatively low dust masses and optically thin emission could also suggest, again, very early planet formation (during Class 0/I), with ideal conditions for forming the most common exoplanet, super-Earths.

1.4.3 Future science

Despite the remarkable progress made in recent years, there is still much to uncover with ALMA using its current capabilities. Investigating dust and CO emission at high resolution in older star-forming regions, such as Upper Scorpius, will provide valuable insights into the evolution of dust and gas, helping us build a more complete picture of disk evolution in the latter stages of protoplanetary disks. Moreover, one major instrument upgrade is on the horizon for ALMA. The Wideband Sensitivity Upgrade will

increase the spectral bandwidth by a factor of four without compromising spectral resolution. This will come with a full upgrade of ALMA's receivers and digitizers, which will significantly increase its overall sensitivity as well as much wider bandwidth for simultaneous line observations. These upgrades will improve our ability to study dust and molecular emission in compact disks by making such observations much less time-consuming.

The arrival of JWST was a groundbreaking moment for astronomy, offering a revolutionary view of the universe. Many new opportunities have arisen with this powerful telescope in many fields, including in the study of protoplanetary disks. In particular, future observations of compact protoplanetary disks with JWST are expected to uncover their inner chemical compositions and provide a detailed infrared perspective of these small, faint systems.

Looking ahead, the next-generation Very Large Array (ngVLA) will define the future of radio astronomy (expected 2035). With unprecedented angular resolution down to 1 milliarcsecond and sensitivity an order of magnitude greater than the current Jansky VLA, the ngVLA will allow us to observe the innermost regions of protoplanetary disks and some of the most compact ones, with exceptional detail. Operating over a frequency range from 1.2 GHz (21 cm) to 116 GHz (2.6 mm), the ngVLA will probe the optically thin regions of disks where the largest dust grains and the fundamental building blocks of planet formation (dust growth) are found. The advanced capabilities of ngVLA will also make it possible to detect new COMs, which are those predicted but not yet observed. This will provide clues about the chemical initial conditions of many planetary systems.

IRAS4A1: Multiwavelength continuum analysis of a very flared Class 0 disk

O. M. Guerra-Alvarado, N. van der Marel, J. Di Francesco, L. W. Looney, J. J. Tobin, E. G. Cox, P. D. Sheehan, D. J. Wilner, E. Macías, C. Carrasco-González.

Astronomy & Astrophysics, Volume 681, Article A82, 2024.

Abstract

Context. Understanding the formation of substructures in protoplanetary disks is vital for gaining insights into dust growth and the process of planet formation. Studying these substructures in highly embedded Class 0 objects using the Atacama Large Millimeter-submillimeter Array (ALMA), however, poses significant challenges. Nonetheless, it is imperative to do so to unravel the mechanisms and timing behind the formation of these substructures.

Aims. In this study, we present high-resolution ALMA data at Bands 6 and 4 of the NGC1333 IRAS4A Class 0 protobinary system. This system consists of two components, A1 and A2, which are separated by 1.8" and located in the Perseus molecular cloud at a distance of ~293 pc.

Methods. To gain a comprehensive understanding of the dust properties and formation of substructures in the early stages, we conducted a multiwavelength analysis of IRAS4A1. Additionally, we sought to address whether the lack of observed substructures in very young disks could be attributed to factors such as high degrees of disk flaring and large scale heights. To explore this phenomenon, we employed radiative transfer models using RADMC-3D. We employed different approaches and compared the model outcomes with our observational data. This comparison allowed us to gain insights into the challenges in detecting substructures in nascent disks and shed light on the potential influence of the dust scale height on observations of protoplanetary disks.

Results. The continuum data revealed the presence of two disks-envelopes around A1 and A2, along with structure connecting the two sources. Furthermore, spectral index measurements indicate lower optical depth within the A2 disk compared to the A1 disk. Our multiwavelength analysis of A1 discovered characteristics such as high dust surface density, substantial dust mass within the disk, and elevated dust temperatures. These findings suggest the presence of large dust grains compared to the ones in the interstellar medium (ISM), greater than 100 microns in size within the

region. By employing RADMC-3D, we confirmed that increasing the scale height creates the appearance of an asymmetry in protoplanetary disks. Our findings indicate that a scale height of at least 0.3 (H/R) is necessary to produce this observed asymmetry. Furthermore, while there's no direct detection of any substructure, our models indicate that some substructure, such as a small gap, must be present. However, reproducing the intensity profile along the major and minor axes necessitates considering other processes that may be occurring within the IRAS4A1 disk.
Conclusions. The result implies that disk substructures may be masked or obscured by a large scale height in combination with a high degree of flaring in Class 0 disks.

2.1 Introduction

Recent studies of young stellar objects (YSOs) have concluded that dust growth from small particles to planetesimals may occur very early in the lifetime of protoplanetary disks (Tychoniec et al. 2020; Drążkowska et al. 2023). To stop the radial drift of dust particles and allow growth to happen, dust evolution models require dust particles to be trapped within disk substructures. This requirement implies that the formation of these substructures should be well underway during the Class 0-I phase of disk evolution. While such substructures have been detected in the disks of some Class I objects (Sheehan 2020; Segura-Cox et al. 2020), these are still very limited in number. Moreover, they have not yet been observed in Class 0 protoplanetary disks. High-resolution studies of more evolved (Class II) protoplanetary disks, however, have revealed that substructures are common (ALMA Partnership et al. 2015;Andrews et al. 2018a;Isella et al. 2016; Long et al. 2018). These substructures, such as gaps, rings, arcs in cavities, and spiral arms (e.g., Casassus et al. 2013; van der Marel et al. 2013, Pérez et al. 2016; Huang et al. 2018b), have proven crucial in reconciling the timescales for dust drift and planet formation, allowing larger dust particles to decelerate and grow further (Pinilla et al. 2012b).

Many authors have suggested that disk substructures form due to interactions between the disk and forming planets (Dong et al. 2015; Zhang et al. 2018). Other processes, however, may also contribute to their presence (Flock et al. 2015; Zhang et al. 2015a; Okuzumi et al. 2016; Takahashi & Muto 2018). The presence of substructures in evolved disks raises questions about when these substructures form and how are they linked to planet formation. The origin of these substructures, however, remains a subject of debate.

In addition to radial drift, vertical settling is another crucial process that significantly influences the evolution of dust particles in protoplanetary disks allowing them to grow and move into the mid-plane. This settling refers to the vertical motion of particles within the protoplane-

tary disk, driven by the balance between the gravitational force from the central star and the gas drag experienced by the particles. This settling process is influenced by several factors, including the turbulence of the disk and the sizes of the dust grains (Dullemond & Dominik 2004). Larger dust grains are generally more efficient in settling due to their greater inertia decoupling from the gas and moving into the mid-plane where they can grow further while smaller grains experience stronger gas drag and tend to stay more mixed with the gas in higher layers of the disk (Barrière-Fouchet et al. 2005). Vertical settling is expected to occur faster than radial drift and can be particularly pronounced in the inner regions of disks (Laibe et al. 2014).

In evolved Class II disks, some studies have observed that the larger dust particles are already primarily located at the mid-plane, indicating that settling has already occurred (Pinte et al. 2016). On the other hand, the larger dust particles in younger disks may not have had enough time to settle completely, and the settling process may be ongoing in Class I disks with larger vertical extensions (Villenave et al. 2020, 2023).

Furthermore, previous studies have provided enough evidence supporting the occurrence of grain growth in Class 0 young sources, as indicated by their low millimeter spectral indices. Notably, these studies have shown that the spectral index values are larger (ranging from 3.5 to 5) within the envelope at scales extending beyond 2000 au compared to the values (< 3.5) at smaller scales (<200 au) (Kwon et al. 2009;Jørgensen et al. 2007).

More recent findings suggest that young objects, particularly Class 0 YSOs, exhibit significant degrees of flaring and have considerable scale heights (Sheehan et al. 2022; Michel et al. 2022). This flaring and large scale height, irrespective of resolution or optical depth considerations, may conceal substructures in these systems or even prevent their formation. As a result, the settling of large particles is still ongoing, and much material remains in higher layers of the disk. More recently, a large study was performed in the eDisk survey (Ohashi et al. 2023) of Class 0-I objects

with several new findings about their young disks. Understanding the dust properties, vertical structures, and evolution of substructures from the early disk stages is crucial for comprehending the onset and progression of planet formation, as dust evolution and grain growth play vital roles in that process.

In this study, we investigated the protobinary system NGC1333-IRAS4A (IRAS4A), which is situated in the Perseus molecular cloud at a distance of 293 parsecs (pc) (Zucker et al. 2018). The system consists of two Class 0 protostars, namely IRAS4A1 and IRAS4A2, which are separated by an angular distance of 1.8" (Tobin et al. 2018). Both IRAS4A1 and IRAS4A2 are surrounded by an envelope with a total mass of approximately 8 $M_{\odot}$ and a total luminosity of around 5 $L_{\odot}$ (Maury et al. 2019). Both objects have very well-distinguished outflows (Santangelo et al. 2015). We present here the continuum emission of both A1 and A2. We aim to study the structure of IRAS4A1 and investigate the absence of substructures in this component using radiative models. Additionally, in a separate paper, we will discuss the line emission and the presence of complex organic molecules in the IRAS4A system, as well as the continuum analysis of IRAS4A2.

2.2 Observations

The observations used in this paper were obtained using the Atacama Large Millimeter-submillimeter Array (ALMA). Band 4 (1.2 mm) and Band 6 (2.1 mm) data were taken as part of the project code 2018.1.00510.S (PI: James Di Francesco). The calibration of the data was performed by the ALMA staff and was restored by the allegro team at Leiden University. For Band 4, the observations were carried out in five execution blocks spanning from October 16, 2018, to September 12, 2021. Band 6 data were acquired in four execution blocks from November 19, 2018, to September 30, 2019. The total observing time on source for Band 4 was 3.34 h, while Band 6 had a total observing time of 2.88 h. Table 2.1 provides additional

Table 2.1: Observations characteristics of IRAS4A.

Project Code	P.I	ALMA Band	Repr. Frequency (GHz)	ToS (s)	Array	Sensitivity (mJy)	Rms (mJy)	Min BL (m)	Max BL (m)	BW (GHz)
Long baseline observations										
2018.1.00510.S	James Di Francesco	6	265.88	7111	TM1(C43-8)	0.0220	0.10	92.1	8547.6	248-268
2018.1.00510.S	James Di Francesco	4	140.84	8913	TM1(C43-9)	0.017	0.013	83.1	16196.3	136-154
Short baseline observations										
2018.1.00510.S	James Di Francesco	6	265.88	3267	TM2 (C43-5)	0.04690	0.02050	15.1	2617.4	248-268
2018.1.00510.S	James Di Francesco	4	140.84	3125	TM2 (C43-6)	0.037	0.045	15	2516.9	136-154

Table 2.2: IRAS4A intrinsic continuum images characteristics.

Band	Central Frequency (GHz)	Central Wavelength (mm)	Synthesized beam Major × minor (mas × mas)	Beam P.A. (deg)	rms (μJy/beam)	Peak flux A1 (mJy/beam)	Peak flux A2 (mJy/beam)	Robust	Peak S/N
6	256.994	1.2	78 × 31	20.82	135.299	14.04	19.92	0.0	147.5
4	145.009	2.1	47×29	5.79	26.27	3.13	2.63	0.0	120.4
VLA Ka	32.95	9.1	75×54	79.94	9.773	0.719	0.306	0.5	80

Table 2.3: IRAS4A tapered continuum images characteristics.

Band	Synthesized beam Major × minor (mas × mas)	rms (μJy/beam)	Peak flux A1 (mJy/beam)	Peak flux A2 (mJy/beam)
6	78×78	370.5	33.94	40.01
4	78×78	62.53	13.09	8.17
VLA Ka	78×78	9.89	0.943	0.355

information regarding the characteristics of the data utilized in this study.

The data reduction process was carried out using the Common Astronomy Software Applications (CASA, (McMullin et al. 2007)) version 5.7.0. The continuum spectral windows were separated from the line spectral windows and then averaged into eight channels for both data sets. Band 6 has 12 spectral windows centered at 264 Ghz, 252 GHz, and 250 Ghz with a total bandwidth of 2 GHz each. Band 4 has 15 spectral windows centered at 138 GHz, 150 Ghz, and 152 GHz with a total bandwidth of 2 GHz each. The flux calibration errors are set to the nominal values of 5% at Bands 4 and 6.

Self-calibration techniques were employed for each spectral window individually using solution intervals of inf, 60s, and 30s. Initially, we performed phase-only self-calibration to the short baseline data, which resulted in significant improvements for Band 4 data (signal-to-noise ratio,

from 88 to 380). For Band 6 data, however, only an increase in the signal-to-noise ratio (S/N) from 61 to 69 was achieved. In any case, sufficient self-calibration solutions were found, leading to enhanced data quality. Amplitude self-calibration was also performed, but we stopped after a single step for most of the spectral windows as it did not yield substantial improvements in the signal-to-noise ratio. For the long baseline data, we also performed phase self-calibration, although the improvement observed was comparatively less significant than in the short baseline data (Band 4 S/N from 42 to 86 and Band 6 S/N from 16 to 19). The reason for the lesser improvement in long baselines compared to short baselines could be attributed to a higher frequency of returns to the phase calibrator source during the long-baseline observations. Additionally, since self-calibration was exclusively applied in the same configuration, the cleaning process for long-baseline data often struggles to model the largest angular scales, even though they are present. This limitation affects the visibility data, especially considering the substantial amount of large-scale emission present in these data. Amplitude self-calibration was only applied to a few specific spectral windows due to minimal enhancements in the S/N. The final data sets were obtained after concatenating all the spectral windows in which no alignment was needed for any of them.

Moreover, Very Large Array (VLA) data of IRAS4A were obtained from the VLA Nascent Disk and Multiplicity (VANDAM) survey (Tobin et al. 2016) conducted in the Perseus molecular cloud. The observations took place on October 21, 2013, employing the B-array configuration. For the correlator setup, two basebands with a total bandwidth of 4 GHz were utilized. These basebands were centered at frequencies of 36.9 GHz and 28.5 GHz, respectively. The setup was then further divided into 32 spectral windows each having a bandwidth of 128 MHz. The VLA Ka-band data in B-configuration has a shortest baseline length of 210 m and an estimated amplitude calibration uncertainty of ~10%.

The final continuum images were created using task *tclean* in CASA. In addition, we used the MTMFS deconvolver (Rau & Cornwell 2011) with

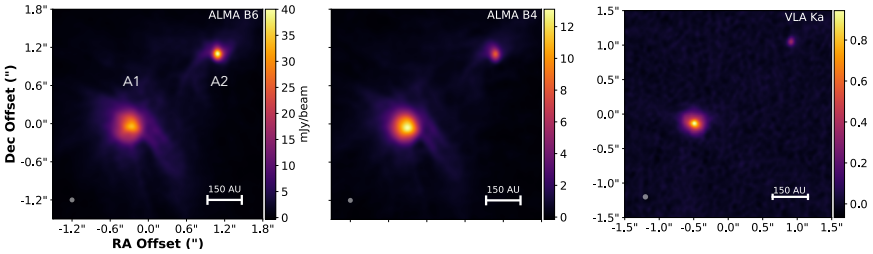


Figure 2.1: Images of IRAS4A at 1.2 mm, 2.1 mm, and 9.1 mm imaged at 78 mas resolution. The central RA and Dec positions for Band 4 and Band 6 are 03:29:10.510 and +31.13.31.010, respectively. For the VLA image, the central Dec position is 03:29:10.502 and the central RA position remains the same, aligning with +31.13.31.010. Both sources are visible at a separation of 1.8", with some surrounded leftover emission seen between them at 1.2 and 2.1 mm but not at 9.1 mm (see Appendix A.1, where the image color scale was changed to show the extended emission). Moreover, the peak emission of IRAS4A2 is larger than that of IRAS4A1 at 1.2 mm. The emission of both sources in the VLA image is more radially compact, though it is very faint for IRAS4A2.

nterms=2, with scales of 0, 10, 30, and 50 times the pixel size (0.003" and 0.01" for ALMA and VLA images, respectively). Briggs weighting was found to be optimal for the purpose of this project as it provided the best compromise between sensitivity and resolution, and several Robust values were explored when making the final images. Furthermore, for the Band 4 data the uv range was modified to decrease the resolution. A smooth tapering was applied by setting *uvtaper* to 0.058". Both the Band 4 and Band 6 images were convolved to have the same 78 (milliarcsecond) beam. This common resolution allowed for a consistent analysis alongside the Very Large Array (VLA) data at 9.1 mm. Table 2.2 and Table 2.3 provide an overview of the characteristics of the images for Band 4 and Band 6, along with the VLA image obtained from the VANDAM survey.

We acknowledge that the ALMA data for IRAS4A at Band 4, with its high resolution, time on source, and rms, can be favorably compared to the

data obtained in the ALMA 2014 Long Baseline Campaign (LBC) Science Verification (SV) data of HL Tau at Band 6 (ALMA Partnership et al. 2015). The data for HL Tau was specifically designed to search for substructures, a goal in common with the observation of IRAS4A1. The IRAS4A data set has a resolution of 47 mas, a time on source of 3.34 h, and an rms of 13 μJy, while the HL Tau data had a resolution of 35 mas, a time on source of 4.5 h, and an rms of 11 μJy. Given the numerous substructures identified in the HL Tau disk and the comparable nature of the data, one would expect these observations to be sufficient for detecting substructures in the IRAS4A1 disk.

2.3 Results

Figure 2.1 displays the continuum images obtained from the observations. IRAS4A1 and IRAS24A2 are well resolved in both the Band 4 and Band 6 images. The majority of the submillimeter emission originates from within each of these two sources. There is, however, additional faint emission observed between and surrounding A1 and A2, indicating some form of structure between the two sources. This structure is particularly evident at 2.1 mm and 1.2 mm wavelengths, but not at 9.1 mm, which might be related to the lower sensitivity to thermal dust emission at 9.1 mm (see Appendix A.1). The origin of this extended emission remains unknown, but the material could potentially be associated with the surrounding molecular cloud or with some diffuse envelope-core material at these scales. In contrast, the emission surrounding A1 or A2 is likely originating from the inner envelope or a very optically thick flared disk. Moreover, the brightness peak emission from A1 is lower than that from A2 at 1.2 mm, contrary to what is observed at 2.1 mm and 9.1 mm (see Section 2.2 for the flux values). One possible explanation for this discrepancy could be that both sources have different scale heights and different optical depths. Despite the objects' similar age, Band 6 may be tracing different layers in A1 and A2, possibly not corresponding to the mid-plane.

Furthermore, our ALMA images have been thoroughly examined, and no additional compact objects, such as low-mass companions or distant galaxies, have been detected within the field of view ($> 3\sigma$). Due to the high sensitivity and resolution of our data, it is highly improbable that any such objects have been missed. This suggests that A1 and A2 are unlikely to be part of a binary with a separation greater than 20 au, which is the long axis of the beam. However, is important to note that our data are not sensitive enough to detect a star lacking a circumstellar disk.

Lastly, a distinct asymmetry is observed for A1 in the 1.2 mm image, which is not apparent in the 2.1 mm and 9.1 mm images. The cause of this asymmetry warrants further investigation as it may provide valuable insights into the vertical structure of its Class 0 protoplanetary disk.

The radial profiles from these images were obtained by averaging the emission in elliptical rings for both sources, and the central position of the radial profile of A2 was determined based on the peak emission in the respective images. Since there is an asymmetry in the A1 source, the central position of the radial profiles was determined by a Gaussian fit using *imfit*. Although a slight bias might remain in the Gaussian fit, it was considerably less pronounced than that seen when using the peak emission center. Consequently, the center from the Gaussian fit is likely much closer to the actual center of the source. For A1, the inclination and position angle values were set to 20 degrees and 96 degrees (NE direction, from the north axis moving towards the east), respectively, as reported for the outflow in Ching et al. 2016. On the other hand, for A2 we took the inclination to be 14 degrees (Ching et al. 2016), while the position angle was taken from measurements on the inner outflow (Chuang et al. 2021) (122 degrees NE). Finally, the brightness temperature values were calculated by applying the full Planck equation to the radial intensity profiles as indicated by Rybicki & Lightman (1979); the concept refers to the temperature of a blackbody with the same brightness at that specific frequency. Moreover, two additional radial profiles were generated, representing the spectral indices between 9.1 mm and 2.1

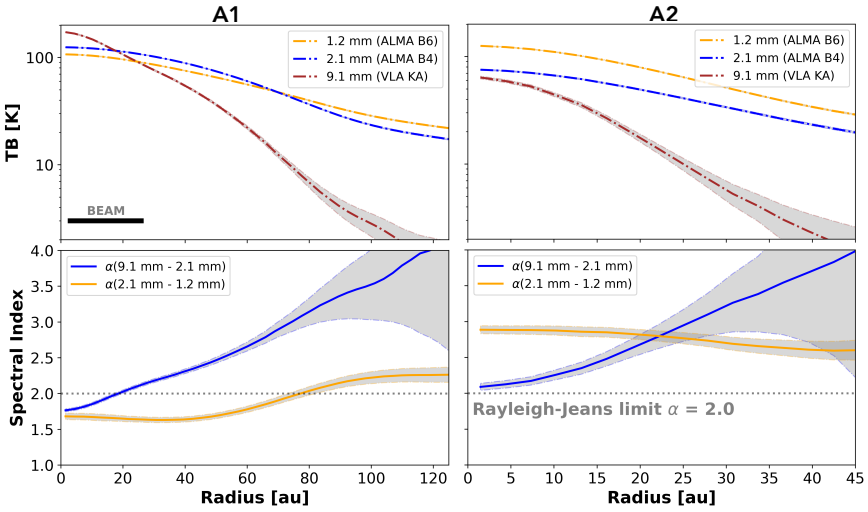


Figure 2.2: Brightness temperatures and spectral indices across the entire radius of A1 and A2, illustrating their emission patterns. Upper right and left panels: Brightness temperatures at 1.2 mm, 2.1 mm, and 9.1 mm of A1 and A2, respectively. Lower right and left panels: Spectral indices between 9.1 mm - 2.1 mm and 2.1 mm - 1.2 mm of A1 and A2, respectively. In the inner parts of the A1 source, some free-free emission might be present at 9.1 mm. Moreover, the brightness temperature in A1 at 1.2 mm is lower than that at 2.1 mm, which, as seen from the spectral index, might indicate very optically thick emission at those wavelengths and small dust particles (<1 mm). We only considered the statistical uncertainties for the brightness temperature and spectral index.

mm, as well as between 2.1 mm and 1.2 mm. Figure 2.2 displays both the brightness temperature profiles and the spectral indices for A1 and A2. By examining Figure 2.2, we can observe the behavior of the spectral indices for A1 and A2. For A1, the spectral indices are very low at the center of the source. As the radius increases, however, these indices gradually become larger. This continues until the noise of the 9.1 mm image starts to dominate the emission. Comparing the spectral index between 2.1 mm and 1.2 mm for A1 with that of A2, we find that the index for A1 remains consistently below two across most radii. On the other hand, the

spectral indices for A2 are consistently above two throughout the range of radii considered. This discrepancy suggests that the emission from A1 is significantly more optically thick than that from A2 at these wavelengths. The difference in spectral indices between A1 and A2 implies differences in the physical properties of the two sources. For example, A1 may have a denser and more optically thick environment, which affects the observed spectral behavior. Furthermore, dust self-scattering might be affecting the inner regions of the IRAS4A1 disk. Additionally, some free-free emission might be increasing the brightness temperature in the inner regions of the A1 VLA image, affecting the spectral index from 9.1 mm - 2.1 mm.

In the recent study conducted by Galametz et al. (2019) using independent measurements from the CALYPSO sample at 1.3 and 3.2 mm, the authors reported discovering remarkably low values of spectral indices (<2.0) within the inner regions of the IRAS4A1 envelope, specifically at distances of less than 200 au. This is in agreement with our spectral index values of the IRAS4A1 inner regions. Additionally, Galametz et al. (2019) also observed higher spectral index values extending up to 2000 au, which was attributed to grain growth processes occurring within the envelope. It is crucial to acknowledge that our high-resolution image might be causing the extended component of the envelope to be resolved out, thereby making it difficult to measure the spectral index of this particular component. Jørgensen et al. (2007) previously pointed out that when extracting emission from the envelope, the spectral index of compact components would be flattened. Then, spectral index values below 3.5 at smaller radii could be indicative of the presence of another component, most likely a disk.

2.3.1 Multiwavelength analysis of a Class 0 young stellar object.

In this study, we adopted the hypothesis that the emission detected in our high-resolution images originates primarily from a disk rather than the envelope. The reason behind this is that the high resolution of our

imaging may result in the loss of most of the emission from the extended components (envelope) and that, as mentioned before, our findings of low values of the spectral indices in Figure 2.2 further support the notion of a disk scenario. Of course, it needs to be noted that some emission coming from the inner envelope might still be contributing to the total emission. While there might still be some confusion within the envelope, we unfortunately did not account for a dynamical distinction. Separating the continuum from the envelope is challenging, and due to the optical depth, analyzing the lines becomes quite limited. Additionally, to be aligned with previous research, we also consider the disk to be flared, similarly to observations and results found in Class 0 young stellar objects (YSOs) using ALMA data (Sheehan et al. 2022;Michel et al. 2022) and as suggested by edge-on observations (Villenave et al. 2020, 2023) and, recently, the eDisk survey (Ohashi et al. 2023).

Protoplanetary disks are commonly expected to have millimeter- or even centimeter-sized dust particles. Because of such grain growth, the albedo of the dust can be high at millimeter wavelengths, indicating that scattering plays a significant role in the opacity of the dust emission. When scattering is a dominant factor, the spectral index of the dust emission can no longer be directly associated with a spectral index of the dust opacity (i.e., β; e.g., Sierra & Lizano 2020; Zhu et al. 2019). To analyze the spectral energy distribution (SED) of protoplanetary disks properly, it is crucial to consider both absorption and scattering effects in the dust opacity. To include the scattering effect, we can write the source function in the radiative transfer equation as

$$S_\nu(T) = \omega_\nu J_\nu + (1-\omega_\nu) B_\nu(T), \tag{2.1}$$

where J_ν is the local mean intensity and ω_ν is the albedo, defined by the scattering coefficient and the absorption coefficient as $\omega_\nu = \frac{\sigma_\nu}{\kappa_\nu+\sigma_\nu}$. We can approximate this to the analytical solution found in Miyake & Nakagawa 1993 assuming a disk as a vertically isothermal slab and with isotropic

scattering:

$$J_\nu = B_\nu(T)[1 + f(t, \tau_\nu, \omega_\nu)], \tag{2.2}$$

where

$$f(t, \tau_\nu, \omega_\nu) = \frac{\exp(-\sqrt{3}\epsilon_\nu t) + \exp(\sqrt{3}\epsilon_\nu (t - \tau_\nu))}{\exp(-\sqrt{3}\epsilon_\nu \tau_\nu)(\epsilon_\nu - 1) - (\epsilon_\nu + 1)}; \tag{2.3}$$

t is the optical depth variable and $\tau_\nu = \Sigma_{dust}\chi_\nu$; both are measured perpendicular to the disk mid-plane. Also, $\epsilon_\nu = \sqrt{1-\omega_\nu}$. Considering inclination effects by correcting the optical depth by the inclination angle (i) of the disk, we reach the emergent specific intensity obtained by Sierra et al. 2019:

$$I_\nu = B_\nu(T)[(1 - \exp(\tau_\nu/\mu)) + \omega_\nu F(\tau_\nu, \omega_\nu)], \tag{2.4}$$

where

$$F(\tau_\nu, \omega_\nu) = \frac{1}{\exp(-\sqrt{3}\epsilon_\nu \tau_\nu)(\epsilon_\nu - 1) - (\epsilon_\nu + 1)} \text{X}$$
$$\left[\frac{1 - \exp(-(\sqrt{3}\epsilon_\nu + 1/\mu)\tau_\nu)}{\sqrt{3}\epsilon_\nu \mu + 1} + \frac{\exp(-\tau_\nu/\mu) - \exp(-\sqrt{3}\epsilon_\nu \tau_\nu)}{\sqrt{3}\epsilon_\nu \mu - 1}\right]. \tag{2.5}$$

It is important to mention that isotropic scattering is assumed for these equations, which may be an incorrect approximation for $2\pi a \geqslant \lambda$. To reduce the effect of the approximation, we replaced the scattering coefficient in all equations with an effective scattering coefficient in the following form (Ishimaru 1978, Birnstiel et al. 2018):

$$\sigma_\nu^{eff} = (1 - g_\nu)\sigma_\nu, \tag{2.6}$$

where g_ν is the asymmetry parameter, that is, the expectation value of cos θ, where θ is the scattering angle (e.g., Ishimaru 1978, Birnstiel et al. 2018). The values of g_ν depend on the dielectric properties of the dust particles.

For our calculations, the values obtained by Birnstiel et al. 2018 for σ_v^{eff} were used.

In our analysis, the particle size distribution is assumed to follow a power law with a slope ($n(a) \propto a^{-p}$), where p is commonly assumed to be 3.5 according to measurements of the ISM (Mathis et al. 1977). Also, the DSHARP opacity data (Birnstiel et al. 2018) were employed, which considers particles without porosity and a composition of 20 % water fraction by mass, 32.91 % astronomical silicates, 7.43 % troilite, and 39.66 % refractory organics.

Equation 2.5 then ultimately depends on only three free parameters: dust temperature (T_{dust}), surface density (Σ_{dust}), and particle size (a_{max}). With three or more observed wavelengths, it becomes possible to solve the equation and obtain estimates for the three free parameters (T_{dust}, Σ_{dust}, a_{max}).

It is important to note that this model assumes a single temperature at each radius within the disk. This assumption generally holds when most of the dust is settled in the disk's mid-plane. In cases where the emission is originating from an envelope or a flared disk involving different layers, however, this assumption may not be valid. So, it is worth noting that the temperature structure within protoplanetary disks can be complex, particularly if there are significant vertical temperature gradients or if different layers of the disk are contributing to the observed emission at different wavelengths. In these situations, a more sophisticated modeling approach that considers the vertical structure and temperature gradients within the disk would be necessary to interpret the observed SED.

A multiwavelength analysis similar to ours here was previously performed on HL Tau using four images between 8 mm and 0.9 mm (Carrasco-González et al. 2019) by simplifying the spectral behavior of the extinction coefficient using a power law. After that, it has been used in several other works (e.g., Macías et al. (2021), Sierra et al. (2021), and Guidi et al. (2022)), including the work presented in this paper, using the exact values of the dust opacity at each wavelength. This model is a first

approach in determining the dust properties around a Class 0 YSO such as A1.

A Bayesian approach was employed to obtain the posterior probability distributions of the model parameters (a_{max},T_{dust},Σ_{dust}) at each radius. To achieve this, a standard log-normal likelihood function was used, which is defined as follows:

$$\ln p(\bar{I}(r) \mid \Theta) = -0.5 \sum_i \left((\frac{\bar{I}_i - I_{m,i}}{\hat{\sigma}_{\bar{I},i}})^2 + \ln(2\pi\hat{\sigma}^2_{\bar{I},i}) \right), \tag{2.7}$$

where $\bar{I}$ is the azimuthally averaged intensity at radius r and at frequency ν_i, $I_{m,i}$ is the model intensity from different combinations of the three free parameters at a radius r, and Θ is the vector of the three free parameters. In addition, we assumed that the uncertainty $\hat{\sigma}_{\bar{I},i}$ at radius r is

$$\hat{\sigma}_{\bar{I},i} = \sqrt{\sigma^2_{\bar{I},i} + (\delta_i \bar{I}_i)^2}, \tag{2.8}$$

where $\sigma^2_{\bar{I},i}$ is the error of the mean, obtained from the azimuthally averaged intensity profiles (see Section 2.2), and δ_i is the flux calibration error at each frequency.

Figure 2.3 shows the analysis we performed; a model grid of intensities was created using various dust parameters. To infer the physical parameters of the dust particles, we compared the observed intensity at each radius with the expected spectral energy distribution (SED) derived from different combinations of the three free parameters in Equations 2.4 and 2.5 (a_{max} from 0.001 - 10 cm, T_{dust} from 0.1 - 250 K, Σ_{dust} from 0.1 - 1000 gcm^{-2}). In order to better match the observational data, the probability distribution of each parameter was plotted, along with the corresponding expected value (represented by the red curve in Figure 2.3). The expected value of each parameter was obtained by

$$E(X) = \frac{\sum_i X_i P(X_i|\bar{I}(r))}{\sum_i P(X_i|\bar{I}(r))}, \tag{2.9}$$

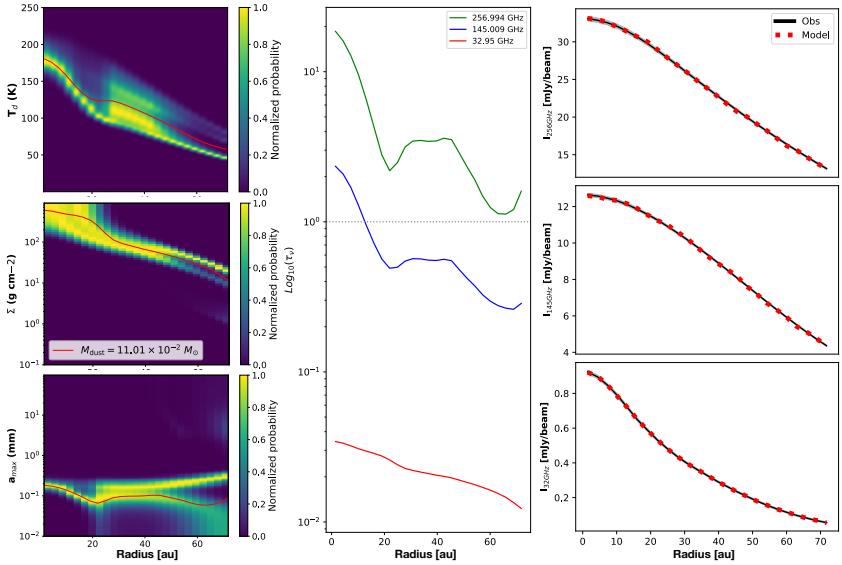


Figure 2.3: Multiwavelength analysis results of A1 Left panels: Probability distributions of dust parameters (a_{max},T_{dust},Σ_{dust}) of A1; the red line in each plot is the expected value of each of the dust parameters. Middle panel: Optical depths at each radius of the three different wavelengths used in this work. Right panels: Comparison of radial intensities from the observations and the model at each wavelength. The plots show very high temperatures and surface densities along the radius of the disk. Particle sizes have increased and are large in comparison with the ISM but still very small for the mid-plane of protoplanetary disks, in agreement with the expectation that not much settling has occurred in very young protoplanetary disks. Lastly, A1 shows optically thick emission at Bands 6 and 4 at the inner radii.

where X_i is each value in all the parameters inside our grid, and $P(X_i|\bar{I}(r))$ is the marginalized posterior probability of each parameter in every single cell of the grid.

Multiple equally likely solutions close to each other were found for the A1 source, which equally explained the observed intensity. All the possible solutions have similar Σ_{dust} and dust temperatures, which is explained in Zhang et al. (2023b) as there are no strong Mie interference patterns when

$2\pi a < \lambda$. Finally, the optical depth values were derived from the analysis to provide insights into the dust properties at different locations within the disk. Figure 2.3 shows the dust parameters, the optical depths at each wavelength, and the intensities of the observations compared with the ones obtained from the model.

From Figure 2.3, it is evident that the A1 disk exhibits high optical thickness at the inner radii of A1, which poses challenges in fitting the dust parameters accurately. This observation suggests that the disk is highly unstable and contains very small dust particles (hundreds of microns in size) relatively to dust grain sizes in protoplanetary disks. Notably, the derived temperature from the multiwavelength analysis in A1 appears to be higher compared to other Class II disks analyzed using similar methods (Macías et al. (2021), Sierra et al. (2021), Guidi (2019), and Carrasco-González et al. (2019)). This discrepancy may be attributed to the young age of the source and other processes occurring within the system, such as infalling material that can contribute to the elevated temperature of the dust particles, viscous heating or even back warming by the envelope (Natta 1993).

Furthermore, A1 displays a notably high dust surface density and mass in comparison to Class II disks. This result aligns with the notion that a significant portion of the material remains distributed as submillimeter particles surrounding the star rather than having settled and grown in the disk's mid-plane, where it cannot be detected by our observations due to high optical depths. The high mass inferred is expected for a very young source such as A1, which is likely to be very gravitationally unstable as it still has a substantial circumprotostellar mass not yet accreted by the central star. We note that the particle sizes found in other disk studies often vary significantly depending on the presence of substructures, which are not detectable in the A1 source. Moreover, the particle sizes observed in other Class II disks tend to be larger (centimeter-sized particles) compared to the 0.1 mm particles found in A1. This disparity can be attributed to the different evolutionary stages of the disks, with the dust in the other

disks having evolved and settled more in the mid-plane.

Figure 2.3 indicates that the material flowing in to form the disk already contains large dust particles (> 10 microns) compared to the average ISM dust sizes. This suggests widespread grain growth across the entire disk radius. However, as one approaches the mid-plane and the central star, particles tend to become larger. These large dust particles compared to the ISM particles imply that grain growth is not limited to the mid-plane and that it also occurs in the flared regions of the disk where infall is likely the process that triggers this growth. Additionally, the increase in error at the outer region of the A1 disk is a result of the spatial sensitivity of the VLA image.

We compared the temperature profile of A1 with other Class 0 sources and found that A1's temperature agrees with those derived from CO and H_2CO snow lines in IRAS04302 (Class I) and L1527 (Class I-O) by van 't Hoff et al. (2020). Comparing with models from Yang et al. (2017) on the Class 0 protostar BHR71, however, we note that the derived densities in A1 are at least an order of magnitude lower. This difference could potentially stem from the observations utilized by Yang et al. (2017) being of shorter wavelengths (*Herschel*) that are more sensitive to the cloud, the surrounding envelope, and smaller dust grains.

Concerning particle sizes, our analysis indicates that the inner disk of A1 comprises particles nearly 0.3 mm in size. This suggests that the dust size distribution in the disk is primarily characterized by larger particles when compared to typical interstellar medium (ISM) dust sizes. However, in comparison to pebbles found in more evolved disks, these particles are relatively small. This suggests that although some dust growth has already occurred, the process is still ongoing. Several studies focused on Class 0 objects have measured dust sizes in the envelope using low dust emissivity indices, revealing that grain growth might already happen in this Class 0 object, maybe even up to millimeter-sized particles (Jørgensen et al. (2009); Galametz et al. (2019)). More specifically, scattering measure-

ments from polarization observations in IRAS4A show the possibility of large millimeter-size particles within the system (Cox et al. 2015). These findings diverge from the multiwavelength analysis in our work that shows smaller dust particles in IRAS4A1.

The findings presented in Figure 2.3 do not provide a definitive explanation for the spectral index below two in Figure 2.2. The particle sizes around 0.1 mm align with what is expected for dust self-scattering, indicating the presence of low spectral indices (Liu 2019). Nevertheless, these observed values can also be rationalized by considering a highly optically thick disk within r<60 AU, where the inner layers are warmer than the outer layers. This scenario not only aligns with the observations but also corresponds to the outcomes illustrated in Figure 2.3, showcasing the high optical depth across all radii.

2.3.2 Generic gap models with large scale heights.

To explain the absence of observed substructures and the observed asymmetry in the IRAS4A1 disk, we employed radiative transfer models using RADMC-3D (Dullemond et al. 2012). For these models we assumed that instead of observing a highly optically thick envelope with an embedded disk, IRAS4A1 is actually a flared disk with a significant scale height (the surrounding envelope has been resolved out in these high-res images; see Section 2.3). When considering a greater scale height and flaring in the disk, it is crucial to differentiate between flared disks, which represent an equilibrium configuration of orbiting material, and an infalling model. In this study, we modeled the flared disk solely from the perspective of the dust continuum, without incorporating a dynamic approach such as infalling or rotational motions. This flaring effect can create an asymmetry in the disk and make it challenging to detect substructures, if they exist. The combination of disk inclination, large scale heights, and optically thick emission, even at Band 6, contribute to this effect. Evidence supporting the presence of a highly flared disk instead of an envelope has

been observed in the Class 0 Protostar L1527 IRS by Sheehan et al. (2022).

To test this assumption, a model of the dust continuum emission at 1.2 mm was constructed using RADMC-3D. Initially, "generic gap models" inspired by the disk of HD163296 were made to investigate the disappearance of substructures with increasing scale height. Subsequently, we developed a specific model to the IRAS4A1 disk to reproduce the observed asymmetry at 1.2 mm in combination with the absence of substructures. These radiative transfer models allowed us to perform a detailed examination of the disk's dust evolution and provide insights into its vertical structure.

For the generic gap models, we fixed certain parameters based on previous studies of HD163296. For the star, the parameters in Table 1 from (Andrews et al. 2018a) were used: M_* = 2.04 $M_\odot$, L_* = 17 $L_\odot$, T_* = 9332 K, and a distance of 101 pc. The positions of the two most prominent gaps were taken to be 49 and 86 au with a fixed width of 10 and 8 au, respectively.

The disk model was taken to have an inclination of i = 46.7°, a position angle of 133.3°, and a dust mass of $0.039_\odot$ from Dullemond et al. (2020). In addition, a size of 110 au for the disk was chosen. Inside RADMC-3D, a generic protoplanetary disk model was used, with the scale height varied in each model. To incorporate the DSHARP dust particle opacities, the optool software (Dominik et al. 2021) was utilized, allowing for their utilization within RADMC-3D. Finally for completeness, RADMC-3D calculated the dust temperature using the density distribution for the generic protoplanetary disk model as follows:

$$\rho(r,z) = \frac{\sum(r)}{H_p\sqrt{2\pi}} exp(-\frac{z^2}{2H_p^2}), \tag{2.10}$$

where r is the distance to the star from the disk, $\sum(r)$ is the dust surface density, and H_p is the scale height of the dust disk.

The scale height (H_p) in the generic protoplanetary disk model follows a power-law dependence on the radial distance as follows:

$$H_p = H_{100}(\frac{r}{100AU})^{1+\Psi}, \tag{2.11}$$

where Ψ is the flaring index, with a predefined value 0.14, and H_{100}, is the value of the scale height at a distance of 100 au from the central star.
The scale height parameter was increased in the generic gap models until the substructures disappeared due to shadowing, obscuration, and-or contrast effects. Figure 2.4 shows the images of these models together with a cut through their major and minor axes.

In Figure 2.4, it is evident that substructures present in young Class 0 disks are challenging to observe, if present, due to the large scale heights that these disks may exhibit. The cuts shown in Figure 2.4 provide additional insights into the behavior of the disk at different scale heights. Along the major axis, even at a low scale height of 0.05, a strong flattening effect on the rings and gaps is observed. This effect is highly dependent on the inclination and position angle of the disk. The intensity variations along the minor axis reveal another interesting aspect: in the SW part of the disk, a lack of intensity is observed, an asymmetry caused by a large vertical structure in the disk, also seen in other sources, such as Lee et al. (2021) and Lin et al. (2023b). The direction of this asymmetry is determined by the orientation of the modeled disk. Furthermore, as the scale height increases, both the depth of the gaps and the visibility of substructures begin to flatten along the minor axis too. Eventually, there is a point where substructures ($\leq$10 au) can no longer be distinguished. This example demonstrates the impact of a highly flared disk on the visibility and discernibility of substructures, if any, in a young protoplanetary disk.

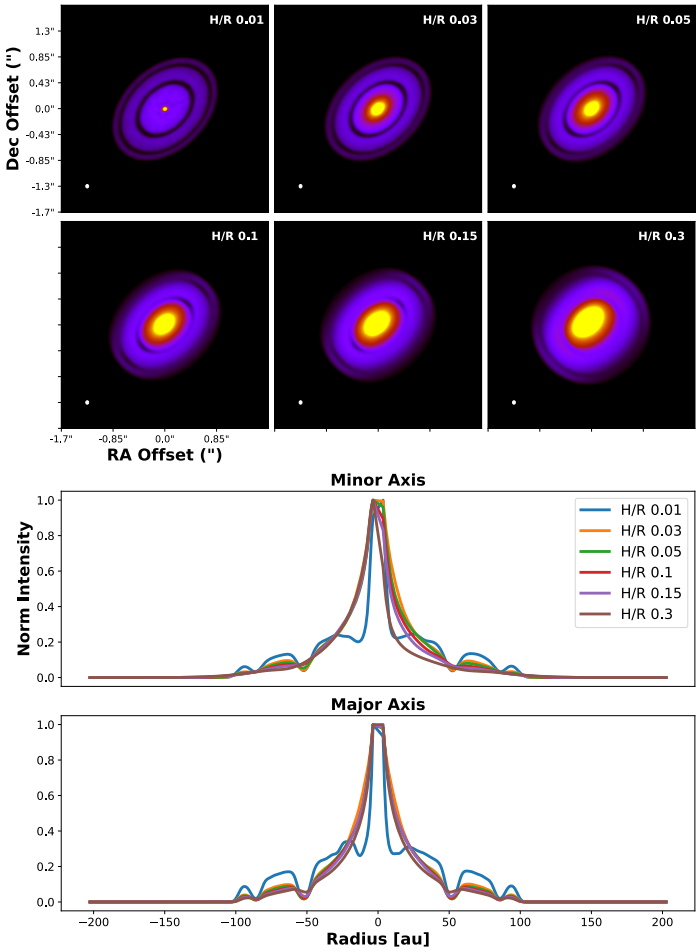


Figure 2.4: Generic gaps models using RADMC-3D, with cross-sections made along both the major and minor axes. Top panels: Generic gap models in RADMC-3D increasing the scale height up to H/R 0.3. Bottom panels: Normalized intensities of major axis and minor axis cuts of the generic gap models. An asymmetry in the minor axis of the disk becomes more prominent as the scale height increases. In both the minor and major axes, substructures start to flatten with increasing scale height, and after 0.3 they become barely visible.

2.3.3 Large scale height and very flared disk models of IRAS4A1

To investigate the asymmetry observed in the 1.2 mm image of the IRAS4A1 disk, additional modeling was performed in RADMC-3D. The objective was to determine whether or not the observed asymmetry could be reproduced in a large-scale-height flared-disk scenario. To set up the RADMC-3D models, we fixed specific parameters. Due to the difficulty of determining the stellar properties directly from the literature for a highly embedded Class 0 object such as IRAS4A1, average values of stellar properties in a number of Class I systems were obtained from Tables 1 and 2 in Fiorellino et al. (2023). These average values include the stellar mass (1.55 $M_{\odot}$), radius (2.1 $R_{\odot}$), and effective temperature (3700 K). The inclination and position angle of the disk were fixed at 20° and 99°, respectively. The dust mass in the disk was taken from the multi-wavelength analysis, resulting in a value of $0.11^{+0.08}_{-0.04}$ $M_{\odot}$. The scale height in the RADMC-3D models for the IRAS4A1 disk was initially set to H/R = 0.3, based on the appearance of asymmetry in the generic gap models. In addition to this base model, eight more models were created. three with a fixed scale height, three with a fixed high flaring index (Ψ = 1.3), and two models with reduced gap widths. This variety allowed us to explore different scale heights within the context of a consistently high flaring profile. Figure 2.5 shows the corresponding cuts through the major and minor axes in all eight models. The IRAS4A1 observation and the model that best reproduces its intensity along the major and minor axis are shown in Figure 2.6. By examining the outcomes of these various models, we can observe the influence of a gap presence, large flaring index, and large scale heights on the observed asymmetry and young Class 0 sources like the IRAS4A1 disk.

From the radiative transfer models of IRAS4A1, it is evident that an asymmetry is formed on the north (compared to south) part of the disk at large scale heights. The inclination and position angle in the models greatly influence the resulting asymmetry, emphasizing the uncertainties in these results. Furthermore, the simplicity of the model employed in

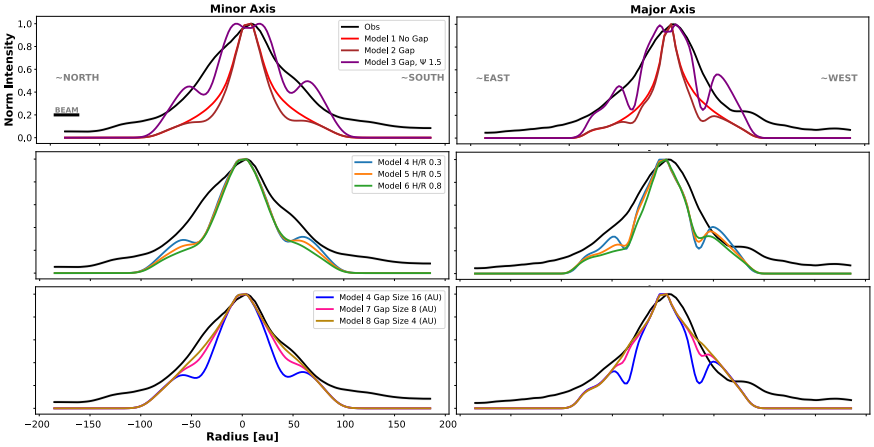


Figure 2.5: Normalized intensities of major axis and minor axis cuts of the IRAS4A1 RADMC-3D models. Top panels: Scale height of each model was fixed to H/R=0.3. Middle panels: Ψ flaring index values were fixed to 1.3 in the RADMC-3D models. Bottom panels: Scale height was fixed to 0.3 and flaring index to 1.3, but the gap width was reduced in each model. The "shoulder" shape and the asymmetry of the disk are better reproduced using a large scale height, a large flaring index, and a small gap width. Unfortunately, an excess of emission is found in the models and the small size of the gap needed cannot be observed at the current resolution.

this study may limit its ability to accurately reproduce the complexities of a Class 0 young stellar object such as IRAS4A1. Nevertheless, the intensity profiles along the major and minor axes suggest the presence of "substructures" or other unknown processes occurring in the actual observations, as most models appear flat unless a gap is included. In the upcoming paragraphs, we will speculate about the substructure scenario in the IRAS4A1 disk, although it is possible that something else is shaping the intensity profiles along the major and minor axis.

The models with a very small gap exhibit intensity profiles that more closely resemble the observed profile at 1.2 mm in both the major and minor axes. This difference may indicate that the gaps at these early stages

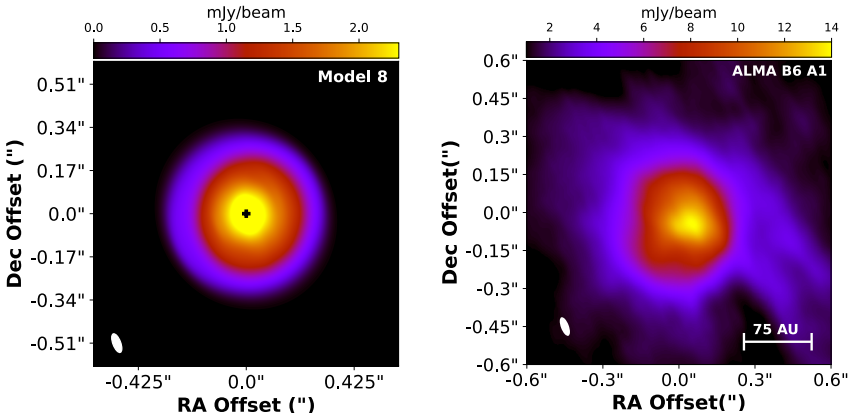


Figure 2.6: Comparison between the best-fit RADMC-3D model image and the ALMA observation at Band 6 of IRAS4A1. Left: RADMC-3D model 8 convolved with a 0.078" x 0.031" beam. Considering both the major and minor axis cuts, the substructures disappear in the major axis at a scale height of 0.3. The gap radial location is set at 40 au with a small width of 4 au. Right: ALMA continuum unconvolved emission image at 1.2 mm with a zoomed-in view of the A1 source. The respective intensities of each images is shown in the upper color bars.

are still forming and that we will need still higher resolution to see them. Regardless of whether IRAS4A1 is indeed a flared disk, a lower limit on the scale height for generating an asymmetry can be established (H/R > 0.3). We note that the intensity profiles in the figure are normalized, as the primary goal of this study is not to replicate the flux of the IRAS4A1 source precisely, but rather to provide insights into the earliest stages of disk and planet formation. Nevertheless, if our observations capture emission from higher layers in the disk, and if the emission remains highly optically thick, it may be challenging to detect substructures with ALMA at the available resolution.

2.4 Discussion

The inferred large scale height (H/R > 0.3) in IRAS4A1 has significant implications for planet formation. Despite the fast settling expected during the disk's lifetime, the optical thickness and asymmetry observed at Band 6 indicate the presence of material with varying grain sizes in higher layers of the disk. This result implies that settling is still ongoing for millimeter-sized particles. Indeed, this state is expected considering the settling timescales (<1 Myr, Dullemond & Dominik 2004) and the estimated dynamical age of the outflows in IRAS4A (around 0.01 Myr; Taquet et al. 2020). Furthermore, settling and radial drift are likely acting together during these early stages of dust evolution and growth in the disk.

The large scale height of the disk may also obscure young substructures, as suggested by models, particularly when combined with very narrow substructures measuring less than 4 au in size. While we are unable to directly resolve substructures (i.e., gaps) in the disk, our models suggest that some must be present to explain the observed bumps in the radial profile of IRAS4A1. These small-scale features are challenging to observe directly with current resolution capabilities (no substructures observed in IRAS4A1), but their presence at these early stages could indicate two possibilities. Firstly, if these substructures are caused by planet-disk interactions, it suggests that planets formed nearly instantaneously after the collapse of the molecular cloud. Furthermore, given sufficient time, substructures within protoplanetary disks are expected to widen, resembling those observed in other systems. This widening occurs as planets grow in size by accreting and carving out material from their surroundings.

We note that substructures can potentially arise from mechanisms other than planet-disk interaction. If this is the case, it introduces an intriguing possibility. In this scenario, the substructures initially form early on and are narrow, as indicated by the narrow gap width in the models. Given settling-induced growth of dust particles and other processes occur-

ring within these narrow substructures, substructure formation through alternative mechanisms may itself trigger planet formation within such gaps. Hence, planet formation could take place very early in the disk's evolution, following an evolutionary path similar to the first scenario.

An additional crucial aspect to consider is the large flaring index observed in IRAS4A1. If the "shoulder" position around the 20-40 AU range, which served as the basis for defining the gap position for the models, is pointing to a substructure, this substructure could be relatively close to the disk's mid-plane. For example, smaller scale heights may occur in the center of the disk, meaning that the closer to the center a substructure forms, the easier it would be to detect it in a very flared disk. Consequently, any mechanism responsible for carving out these substructures probably starts in the mid-plane and is unable to reach large scale heights, as seen in other protoplanetary disks when scattered light observations and submillimeter observations with ALMA are compared.

It is important to note, however, that the combination of large scale heights and a large flaring index could still hide further substructures in the outer radii of the IRAS4A1 disk. On the other hand, if there are no substructures in the flared disk of IRAS4A1, planet formation may then occur only at a later stage when larger particles have already settled in the disk's mid-plane, taking into account the timescales required for settling.

Recently, similar results including the "shoulders", asymmetries, and large scale heights were found in YSOs in studies by the eDisk survey team (Ohashi et al. 2023). Regardless of the specific dynamics within the IRAS4A1 disk, it is becoming evident that Class 0 YSOs exhibit flared disks with significant scale heights, providing valuable insights into the planet formation process.

2.5 Summary and conclusions

We have shown high-resolution ALMA images (78 mas) of the IRAS4A binary system in Bands 4 and 6. The key findings of this paper can be

outlined as follows:

- No substructures were detected in either A1 or A2 at the current resolution.
- Analysis of spectral indexes and brightness temperatures indicated that A1 is significantly more optically thick than A2.
- A multiwavelength image analysis was carried out showing the dust parameters in A1. The expected values of the dust parameters inferred high temperatures (>50 K), high surface densities (>10 gcm^{-2}), and large dust size particles (>30 μm) at all radii (< 60 au) in the IRAS4A1 disk. In addition, the analysis showed high optical depth in the inner disk in Band 6 and Band 4.
- Radiative transfer models using RADMC-3D have shown that a minimum scale height of H/R > 0.3 is adequate to render the substructures invisible and produce an asymmetry in the disks. Moreover, the models that incorporated a narrow gap around 34-50 au and increased flaring index, provided better matches to the observed intensity profiles, suggesting the presence of potential hidden substructures within a very flared disk in the IRAS4A1 system, even in these early stages of disk formation.

Observations with high resolution and sensitivity at centimeter wavelengths with the ngVLA can help unveil any substructure that might exist in IRAS4A1 and give us a better understanding of substructure formation in young protoplanetary disks.

acknowledgements. We thank the referee for the very constructive comments. We also thank Dominique M. Segura-Cox for the useful discussion. We acknowledge assistance from Allegro, the European ALMA Regional Centre node in the Netherlands. This paper makes use of the

following ALMA data: ADS/JAO.ALMA#2018.1.00510.S. ALMA is a partnership of ESO (representing its member states), NSF (USA) and NINS (Japan), together with NRC (Canada), MOST and ASIAA (Taiwan), and KASI (Republic of Korea), in cooperation with the Republic of Chile. The Joint ALMA Observatory is operated by ESO, AUI/NRAO and NAOJ. EGC acknowledges support from the National Science Foundation through the NSF MPS-Ascend Fellowship Grant number 2213275. L.W.L. acknowledges support from NSF AST-1910364 and NSF AST-2108794.

Appendix A: Faint Emission Between A1 and A2

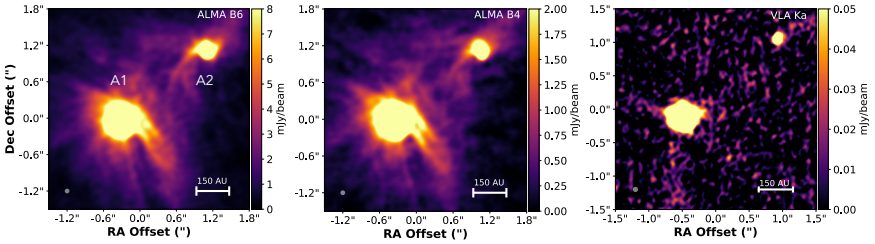


Figure A.1: Images of IRAS4A at 1.2 mm, 2.1 mm, and 9.1 mm imaged at 78 mas resolution. The color scale was changed to better observe the faint emission between the two targets at B6 and B4.

From large-scale outflows to compact line emission in IRAS4A2

Osmar M. Guerra-Alvarado, N. van der Marel, P. Nazari, J. Di Francesco, Ł. Tychoniec, L. W. Looney, E. G. Cox, D. J. Wilner, M. R. Hogerheijde.

Submitted to A&A

Abstract

Aims. Studying protostellar objects in their earliest stages, particularly during the Class 0 phase, provides key insight into the beginnings of planet formation and dust evolution. Disentangling the various components, such as the envelope, outflow, and nascent disk, to characterize and understand these young systems, however, is particularly challenging. High spatial and spectral resolution observations of molecular line emission with the Atacama Large Millimeter/submillimeter Array (ALMA) are therefore crucial for probing their complex environments.

Methods. In this work, we present high-resolution ALMA observations of the IRAS4A2 Class 0 system. We analyze the gas emission surrounding this young source, tracing it from the extended outflow to the most compact inner region and identifying emission lines using the spectral analysis tool CASSIS.

Results. We detected large, well-traced outflows in HCN, H_2CO, and HCO^+, as well as numerous complex organic molecules (COMs) within the system. Using moment maps, we analyzed the kinematics and spatial distributions of these molecules, finding that the emission spans a wide range of spatial scales, from large-scale outflows to compact regions within the IRAS4A2 core, with some molecular lines showing signatures of Keplerian rotation. In contrast, the primary IRAS4A1 exhibits little to no molecular emission, likely due to the strong absorption of the optically thick dust around it.

Conclusions. Our results indicate that the IRAS4A2 system consists of multiple components that are traced by different molecules. Most complex molecules seem to trace a warm inner envelope closer to the central star, while S-bearing molecules and outflow tracers follow a more extended layer with lower upper energy states around IRAS4A2. On the contrary, certain molecules exhibiting both extended and compact emission appear to trace multiple components or structures simultaneously, which suggests a more complex spatial distribution and chemical stratification

within IRAS4A2.

3.1 Introduction

Studying and understanding the evolution of protoplanetary disks from very embedded Class 0 objects to Class II disks is fundamental to unraveling the processes of planet formation. Protoplanetary disks emerge at very early evolutionary stages (Jørgensen et al. 2009; Harsono et al. 2014; Maury et al. 2019; Tobin et al. 2020), with evidence that suggests that planet formation may already be underway during these initial phases (Harsono et al. 2018; Tychoniec et al. 2020). Although many of these early-stage disks appear smooth in current observations (Hsieh et al. 2024), substructures such as rings, gaps, and spirals could already be forming but remain undetected or hidden due to resolution limitations, optical depth effects (Ohashi et al. 2023) and temperature effects (Nazari et al. 2025). Even though studying planet formation in Class 0/I sources remains a challenge, primarily because of the optically thick dust continuum emission, it is still possible to study the chemical composition of these young disks, which can provide crucial insights into their evolution.

In this context, numerous Class 0/I protostars have been identified with hot, dense environments known as hot corinos, which are analogs of the hot cores found in high-mass star-forming regions (Ceccarelli 2004). Many of these sources have been found to contain high abundances of Complex Organic Molecules (COMs), species with six or more atoms (Herbst & van Dishoeck 2009; Caselli & Ceccarelli 2012; Ceccarelli 2023). Most of these studies, however, have been conducted at low spatial resolution, limiting our ability to resolve the detailed structure and stratification of molecular species within these young disks.

With the unprecedented sensitivity and resolution of the Atacama Large Millimeter/submillimeter Array (ALMA) we are now able to investigate in more detail the molecular distribution of these hot corinos.

As of today, only a handful of Class 0 hot corino sources have been resolved at high angular resolution ($\sim$ 0.1") (IRAS 16293-2422 A (Maureira et al. 2022), SVS13-A (Bianchi et al. 2022), B335 (Okoda et al. 2022),

IRAS4A2 (Frediani et al. 2025), HH212 (Lee et al. 2022)) and L1448-mm (Nazari et al. 2024). Interestingly, in HH 212, Lee et al. (2022) revealed molecular stratification, which was attributed to the binding energies of the molecules (sublimation temperature), as the temperature is expected to increase closer to the host star. Studying these young protoplanetary disks, where molecules sublimate at specific temperatures in different regions, can provide insights into where planet formation and dust growth may already be occurring, which we aim to identify in IRAS4A2.

IRAS4A2 was identified as the second hot corino source ever by Bottinelli et al. (2004). It is located at a distance of 293 pc (Zucker et al. 2018) in the NGC1333 region in Perseus, and it is part of a binary Class 0 system, separated by 1.8" from its primary component, IRAS4A1 (Tobin et al. 2018). IRAS4A2 has been extensively studied before (Taquet et al. 2015; López-Sepulcre et al. 2017; De Simone et al. 2017), identifying several complex organic molecules and well-characterized outflows (Santangelo et al. 2015).

In this work, we present a detailed study of the IRAS4A2 hot-corino, from its large-scale outflows to its innermost compact emission. In Section 3.2, we describe the observations and the process to obtain the spectral line emission. Section 3.3 discusses our line identification method, along with the techniques used to create the images of the outflows and the extended and compact emission. Finally, in Section 3.4, we explore the possible spatial distribution of these molecules and their implications for IRAS4A2 in the context of dust, disk evolution, and planet formation.

3.2 Observations

The spatially resolved line observations for IRAS4A2 were obtained using the Atacama Large Millimeter/submillimeter Array (ALMA). Specifically, Band 4 and Band 6 data were gathered under the project code 2018.1.00510.S (PI: James Di Francesco). For a more comprehensive understanding of the observations, including details about data characteris-

tics, calibration, self-calibration, and imaging of the continuum emission, refer to Guerra-Alvarado et al. (2024)

Line spectral windows were separated from the continuum ones, and in this instance, no channel averaging was applied. The self-calibration tables were derived from the continuum analysis and subsequently used in the line spectral windows. In Band 6, observations were carried out using two spectral windows, which we refer to as O6B1 and O6B2 for simplicity. O6B1 has a rest frequency of 267.557 GHz and encompasses two spectral windows (SPWs), each featuring 960 channels. These SPWs have central frequencies of 267.568 GHz and 267.569 GHz, respectively. O6B2, on the other hand, has a rest frequency of 265.886 GHz with four SPWs, each with 960 channels and central frequencies of 265.874 GHz, 265.894 GHz, 265.896 GHz, and 265.898 GHz, respectively. In total, the Band 6 data of O6B1 and O6B2 cover frequency ranges from 265.8214 GHz to 265.9385 GHz and from 267.4925 GHz to 267.6103 GHz, respectively.

The Band 4 line data have a rest frequency of 140.839 GHz with two SPWs, each containing 1920 channels with a central frequency of 140.795 GHz and a frequency range between 140.7319 - 140.8512 GHz. Across all observations, the system velocity was assumed to be 6.95 km/s (Di Francesco et al. 2001), which was later used for the analysis.

The final data cubes were produced using the *tclean* task in CASA, with *specmode* set to "cube" and the deconvolver to "Multiscale." We used scale values of 0, 2.5, 10, and 20 times the pixel size, which was fixed at 0.02" for all line cubes, approximately ten times smaller than the beam size. The spectral resolution is 0.5 for Band 6 observations and 1 for Band 4. These values were selected to balance sensitivity with maintaining the highest possible spectral resolution. Briggs weighting with a robust parameter of 0.5 was adopted for both datasets, as it was found to be the optimal choice based on the cubes images and also in the continuum images presented in Guerra-Alvarado et al. (2024). It also provided the best resolution against other robust values for determining the spatial distribution of the molecular emission, without blurring or

Table 3.1: Data cubes characteristics

Observations	Rest Frequency (GHz)	Beam Size (")	Channel Width (km s^{-1})	RMS (mJy beam^{-1})
O6B1 short baseline	267.557	0.28 × 0.17	0.5	2.8
O6B2 short baseline	265.886	0.28 × 0.17	0.5	2.87
Band 4 short baseline	140.839	0.44 × 0.28	1	2.3
O6B1 long+short baseline	267.557	0.13 × 0.085	0.5	1.59
O6B2 long+short baseline	265.886	0.155 × 0.10	0.5	1.57
Band 4 long+short baseline	140.839	0.10 × 0.047	1	0.95

missing any large-scale structures or weaker lines. This approach was confirmed through comparison with images made via natural weighting. The final characteristics are shown in Table 3.1 with typical beam sizes of 0.1" and rms values of ∼1 mJy/beam per 1 km/s channel.

Finally, for the short baseline data, continuum subtraction was performed prior to imaging using the *uvcontsub* task in CASA, resulting in three short baseline cubes. For the concatenated data, which has higher resolution and greater sensitivity to small features, determining the continuum level was more challenging. To enhance the accuracy of continuum subtraction and better determine the continuum emission in the image cubes, the STATCONT tool Sánchez-Monge et al. 2018 was employed. STATCONT utilizes a 'corrected sigma-clipping algorithm' for determining continuum emission in line-rich sources like IRAS4A2. This method was applied to all concatenated cubes in the study, resulting in the creation of three other cubes. We used only the short-baseline data to account for the most extended emission, to study the large-scale outflows, and the concatenated (short plus large baseline) data to study the emission surrounding IRAS4A2.

3.3 Results

3.3.1 Analysis and line detection with CASSIS

We conducted an exploration of the spectral emission windows within the concatenated cubes and identified several emission lines originating from a small region near the center of IRAS4A2. Spectra from all of

our data were extracted within CARTA (Cube Analysis and Rendering Tool for Astronomy) (Comrie et al. 2018) by selecting a pixel as close as possible to the continuum peak, but still outside the region affected by absorption, located at Dec = 31:13:31.9791986 and RA = 3:29:10.4336922. Subsequently, these spectra were converted into brightness temperature and processed for analysis using the CASSIS spectral analysis tool version 5.1.1 (Vastel et al. 2015). Following the methodology outlined in Nazari et al. (2022), we assumed local thermodynamic equilibrium (LTE) conditions and employed a fitting-by-eye approach. Potential transitions were investigated within CASSIS, utilizing the Cologne Database for Molecular Spectroscopy (CDMS, Müller et al. (2001)) and the Jet Propulsion Laboratory (JPL) database (Pickett et al. 1998).

Commonly detected molecules and COMs were prioritized in the search, with upper energy state levels and Einstein coefficient limits set to $E_{up} \leq 800$ K and $A_{ul} \geq 9\text{x}10^{-6}$ s^{-1}. Since we extracted the spectra from single pixels, the source size parameter in CASSIS was uniformly set to 1000 for all lines, i.e., no non-unity beam filling factors were assumed. The Full Width at Half Maximum (FWHM) of each line was adjusted to fit the spectra better, and the V_{lsrk} was uniformly set to 6.95 km/s for all spectral cubes.

Our data revealed emission lines from SO_2, OCS, HCN, and H_2CO, along with several COMs (see Table A.1). These emission lines exhibit a variety of spatial components and kinematic structures. In the following section, we first describe the identification of the emission lines around IRAS4A2, we then characterize the spatial distribution of the integrated emission and analyze the kinematics, beginning with the outflow, followed by the extended emission, and concluding with the compact COM emission.

Following the criteria from (Pickett et al. 1998), a molecule was considered detected if at least three lines were found at 3-σ; otherwise, it was categorized as a 'tentative detection'. Figure 3.1 displays the observed spectra, where lines were identified, from our cubes in IRAS4A2 alongside

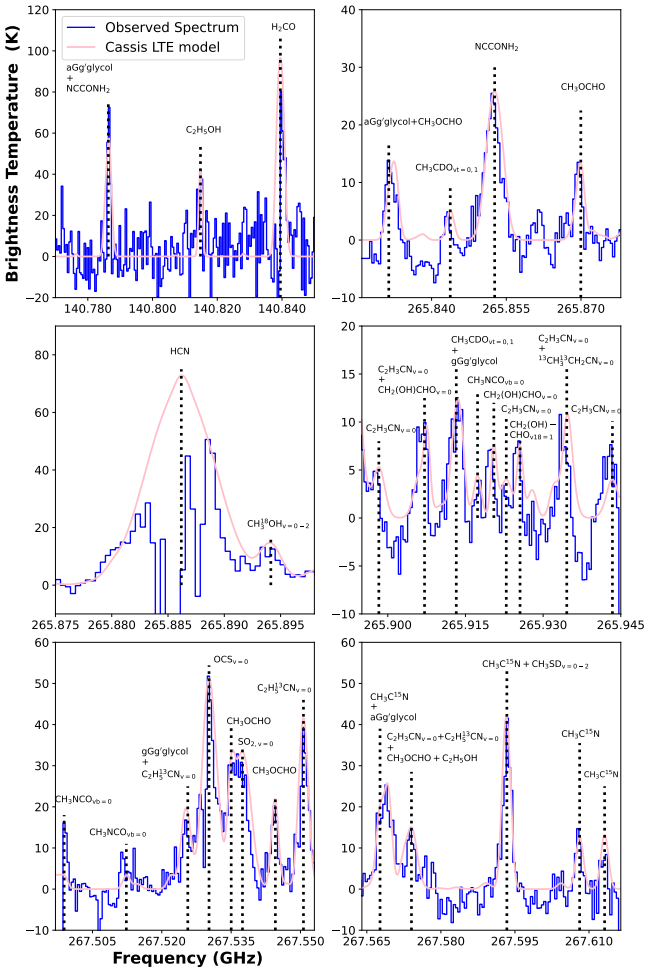


Figure 3.1: CASSIS models of the spectral lines in IRAS4A2 (pink) are compared with the observed spectra (blue) at frequencies where line emission is detected. The molecules are labeled in black

our CASSIS model of the lines. Additionally, Appendix A includes Table A.1, which provides detailed information on all identified molecular lines and their transitions, and Table A.2, which summarizes their morphologies and physical properties, including excitation temperatures and column densities.

The discovery of the numerous COMs around IRAS4A2 came as a surprise, especially when compared to the lack of emission lines around IRAS4A1, primarily attributed to the highly optically thick dust emission of the latter. Recent studies, such as De Simone et al. (2020), López-Sepulcre et al. (2017), and Guerra-Alvarado et al. (2024), have highlighted the differences in optical depth between the two sources. Despite the challenge in observing emission from IRAS4A1, analyzing the diverse species emanating from IRAS4A2 offers valuable insights into the early stages of Class 0 objects and the beginnings of protoplanetary disk formation.

Our IRAS4A2 CASSIS model confirmed the detection of four COMs: $C_2H_3CN_{v=0}$, $CH_2(OH)CHO$, CH_3OCHO, and $CH_3C^{15}N$. While we were unable to fully fit some of the emission around IRAS4A2, nearly all lines were covered within our frequency range. The aGa′ glycol line, while providing temperature and column density estimates, was consistently blended with other molecules. For $C_2H_5^{13}CN$, only one detection was made, but the model suggests the potential for two more if temperatures or densities around IRAS4A2 were higher. Finally, the higher frequency line of $CH_3NCO_{vb=0}$ is partially cut off in the frequency range, leading to underestimations of the associated excitation temperature and column densities. Despite comparable column densities with those found in López-Sepulcre et al. (2017) for different COMs, it has already been mentioned before that the high dust opacity in hot corinos results in underestimations of the abundances (De Simone et al. 2020).

3.3.2 Outflows, extended emission and compact emission in IRAS4A2

3.3.2.1 Outflows

We employed the code *bettermoments* for collapsing the concatenated spectral cube, generating moment maps of the outflows of the IRAS4A system (both components) and the emission lines around only IRAS4A2 (Teague & Foreman-Mackey 2018). For a comprehensive view of the large-

scale outflows, moment 0 and moment 1 images were generated for HCN, $HCO^+_{v=0,1,2}$, and H_2CO using the short baseline data. We present these in Figure 3.2, providing information about the spatial distribution and velocity structures of these outflows.

3.3.2.2 Extended emission

Four lines were identified as tracers of more extended emission in the concatenated data, each exhibiting its own distinct morphology. These molecules include SO_2, HCN, H_2CO, and OCS. In Figure 3.3 we present the moment 0 and 1 maps of these molecules, with white contours outlining the continuum dust emission at Band 6. For these specific spectral lines, we obtained position-velocity (P-V) diagrams to determine the nature of the observed emission, whether it was driven by infall motion, Keplerian rotation from a disk, or a rotating infalling flattened envelope. To analyze this, we used CARTA. We extracted a perpendicular P-V cut along the IRAS4A2 outflow region, specifically, perpendicular to the North-East (NE) to the South-West (SW) direction of the outflow (29 deg, Chahine et al. (2024)). After generating the fits file, we analyzed the image and manually selected points to fit the emission using the following models:

For infall motion, we adopt

$$v_{\text{infall}}(r) = \sqrt{2} \cdot \sqrt{\frac{GM}{|r|}}, \tag{3.1}$$

For Keplerian rotation, we use

$$v_{\text{Keplerian}}(r) = \sqrt{\frac{GM}{|r|}}, \tag{3.2}$$

and for a rotating infalling flattened envelope, following the methodology

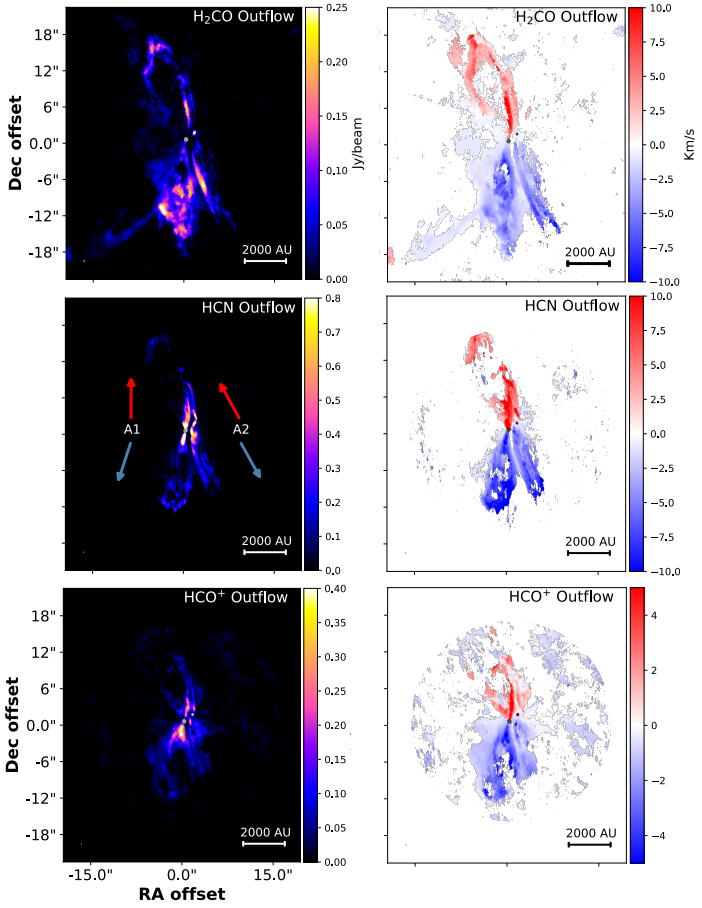


Figure 3.2: Integrated emission and velocity maps of the three main outflow tracers in our spectra: HCN, H_2CO, and HCO^+ generated using the short baseline line data for IRAS4A. The emission from the outflows of both sources, IRAS4A1 and IRAS4A2, is resolved and can be distinguished separately. In the figures, the dust continuum emission of IRAS4A1 and IRAS4A2 is outlined in small white contours, showing 5 σ and 10 σ. The beam is drawn in the lower left part of each panel, 0.28"×0.17" for HCN and HCO^+ and 0.44"×0.28" for H_2CO. The red and blue arrows in the middle-left panel indicate the outflow directions of IRAS4A1 (left) and IRAS4A2 (right)(Chahine et al. 2024), respectively.

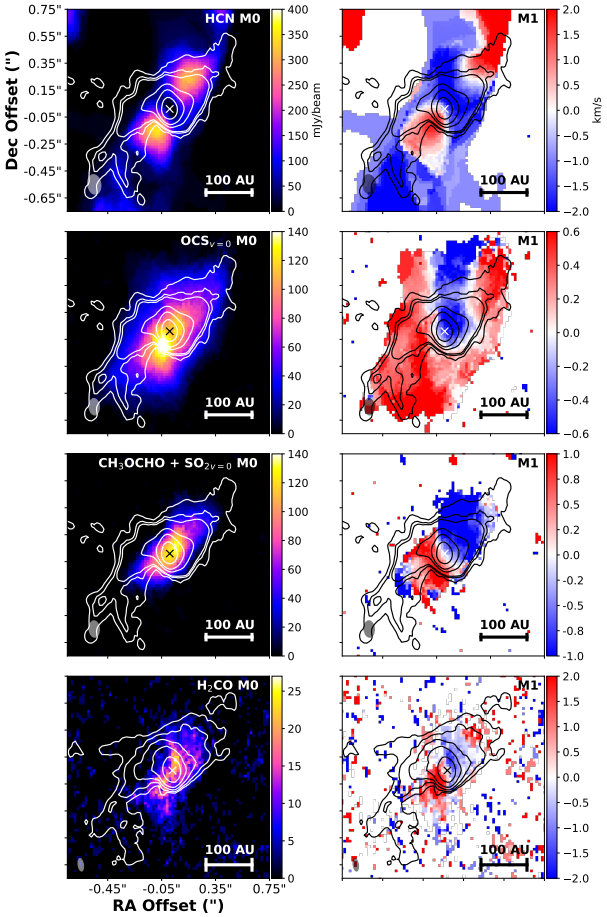


Figure 3.3: Integrated emission and velocity maps of SO_2, OCS, H_2CO and HCN using the long+short baseline data. These molecular lines trace a larger extended emission in IRAS4A2. We identified these features visually from the spectra as the most intense and spatially extended emission lines. The white and black contours represent the 6 to 60-σ levels of the continuum emission from the ALMA Band 6 and Band 4 data, highlighting the underlying dust distribution. The synthesized beam for all panels is shown in the lower-left corner.

in Sakai et al. (2014) and Lee et al. (2017), we adopt

$$v_r(r) = -\sqrt{\frac{2GM}{r} - \frac{l^2}{r^2}}, \tag{3.3}$$

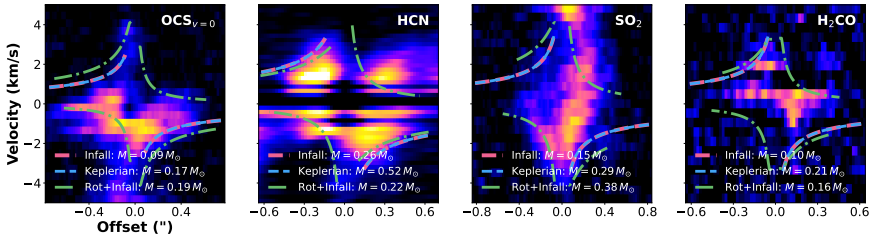


Figure 3.4: Position-velocity diagrams of SO_2, OCS, H_2CO, and HCN extracted along a cut perpendicular to the jet axis. The pink lines show the infall motion fit while the blue lines correspond to the Keplerian motion fit.

and,

$$v_\phi(r) = \frac{l}{r}, \tag{3.4}$$

where G is the gravitational constant, M is the mass of the central protostar, l is the specific angular momentum, and r is the distance from the central protostar.

In Figure 3.4, we present the P-V diagrams of the four extended molecules along with the Keplerian, infall, and the rotating infalling flattened envelope model fits, obtained using a non-linear least squares fitting procedure. While all four molecules tend to predict relatively low masses across the different models (see Figure 3.4), they exhibit variations in angular momentum, l, and centrifugal barrier (CB) radii, we show all this values in Table 3.2.

There are differences in the best fits of these four molecules that suggest different kinematic structures or physical origins. For OCS and H_2CO, the rotating infalling flattened envelope model reproduces the emission relatively well, although for H_2CO the model cannot reproduce the lower velocity emission. In contrast, for HCN and SO_2, the Keplerian and pure infall models better capture the observed emission patterns, but there is still significant emission that is not fit well by any of the models. Some possible contributing factors here are: absorption in certain velocity channels, that the molecules could be tracing multiple kinematic

components, or that the molecular lines fitted are blended with other molecules, particularly for SO_2, which is blended with CH_3OCHO.

3.3.2.3 Compact emission

Several COMs, like CH_3OCHO, $CH_3CDO_{vt=0-1}$, $C_2H_3CN_{v=0}$,$CH_3NCO_{vb=0}$, $CH_3{}^{18}OH_{v=0-2}$, and more, show much more compact emission, on scales of 20 to 50 au with a range of morphologies (see Fig B.1). We categorized these visually as the warm inner envelope (<20 au), disk (between 20 au and 40 au), and compact dust-absorbed emission (close to the warm inner envelope) molecules, following Tychoniec et al. (2021). As an illustration, Figure 3.5 displays the moment 0 maps generated by *bettermoments* for three representative molecules that were not blended with any other line emission, showcasing the three regions they trace within the IRAS4A2 system. In addition, Figure 3.5 includes the P-V diagram of $CH_3CDO_{vt=0-1}$, taken along a cut perpendicular to the outflow axis, and the moment 1 map of CH_3OCHO showing the velocity structure of this particular molecule.

To investigate the spatial distribution of molecular emission in IRAS4A2, we analyzed the emission radius using aperture photometry on the moment 0 maps. We applied a signal-to-noise ratio (SNR > 5) thresh-

Table 3.2: Derived properties for each molecule under different dynamical models. RIE stands for rotating infalling envelope.

Molecule	Model	M [$M_\odot$]	l [au·km·s^{-1}]	CB [au]
OCS	Keplerian	0.17 ± 0.07	–	–
	Infall	0.09 ± 0.03	–	–
	RIE	0.19 ± 0.04	38.5 ± 7.8	4.3 ± 2
HCN	Keplerian	0.52 ± 0.14	–	–
	Infall	0.26 ± 0.07	–	–
	RIE	0.22 ± 0.07	66.6 ± 13.5	11.2 ± 5.7
SO_2	Keplerian	0.29 ± 0.07	–	–
	Infall	0.15 ± 0.03	–	–
	RIE	0.38 ± 0.07	81.2 ± 10.8	9.87 ± 3.2
H_2CO	Keplerian	0.21 ± 0.04	–	–
	Infall	0.10 ± 0.02	–	–
	RIE	0.16 ± 0.03	44.4 ± 7.74	6.8 ± 2.7

old, masking all values below this limit, and then determined the 68% flux radius of the emission, r_{68}. We applied the methodology described in Appendix D of Podio et al. (2021), where we extract a cut perpendicular to the outflow axis going through the continuum peak to measure the spatial extent of the emission. We then assume the measured r_{68} corresponds to the FWHM/2 of the emission profile and deconvolve this value from the beam size to correct for beam smearing and avoid biases due to intensity variations across different molecular lines. Figure 3.6 shows the resulting radius plotted against the excitation temperature derived from CASSIS for molecules with available data. Using the same approach, Figure 3.6 also shows the measured emitting area of each molecule plotted against its respective upper energy levels.

It is important to note that many observed emission lines are blended with others, complicating the estimation of their emission radii and reducing accuracy. Furthermore, some molecular emission exhibits low signal-to-noise ratios or remains unresolved at the current spatial resolution. In these cases, we fixed the FWHM to the minimum beam size to avoid overestimating their spatial extent. Despite these concerns, we chose to proceed with the analysis, as even blended lines, when observed at high resolution, can still provide valuable insights into the chemical structure of young Class 0 objects like IRAS4A2. For a more precise determination of temperature and radius, multiple transitions of unblended molecular emission lines are required, as demonstrated in Frediani et al. (2025).

3.4 Discussion

3.4.1 Spatial scales of the dust and gas of IRAS4A2

3.4.1.1 Compact emission and the origin of the dust absorption

In IRAS4A2, the distributions of emission from COMs and other molecules appear to trace distinct physical processes. Identifying these at high

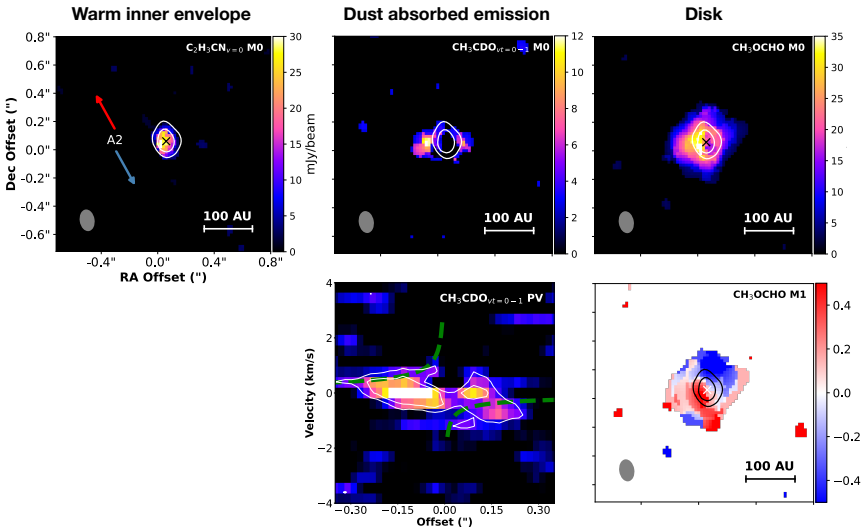


Figure 3.5: Integrated intensities of the three representative molecular lines that were not blended with any other, showcasing the three visually identified regions they trace within the IRAS4A2 disk: $C_2H_3CN_{v=0}$, $CH_3CDO_{vt=0-1}$ and CH_3OCHO. The top panels reveal three distinct morphologies of the compact emission: The left panel shows a warm inner envelope emission, the middle panel shows emission affected by dust absorption, and the right panel displays what seems to be a disk. The white contours show the 30 σ to 60 σ levels of the continuum emission, and the synthesized beams are indicated in the lower left corner of each image. The middle panel of the bottom row shows a P–V diagram of $CH_3CDO_{vt=0-1}$, extracted along a cut perpendicular to the outflow axis. The green dashed curve represents a Keplerian rotation model, while white contours indicate emission levels from 1.5 σ to 3 σ, based on the Band 6 line data. The bottom right panel shows the moment 1 (M1) map of CH_3OCHO, indicating the velocity structure across the emitting region.

resolution can reveal key regions where planet-forming and disk-forming processes occur, as well as the sublimation temperatures that dictate where certain molecules transition from solid to gas. In particular, around IRAS4A2, molecular emission extends from the warm inner envelope (~ 20 au) to large-scale outflows (~ 5300 au).

As previously discussed, Figure 3.5 reveals different morphologies. Some molecules, such as $C_2H_3CN_{v=0}$ and $CH_3^{18}OH_{v=0-2}$, exhibit very compact emission below 20 au, smaller than the beam radius (0.065"), suggesting they remain still very unresolved. In particular, despite the uncertainties introduced by absorption, the Keplerian model provides a good fit to the $CH_3CDO_{vt=0-1}$ emission in Figure 3.5. Combined with the fact that the emission is not aligned with the outflow direction, this could suggest that $CH_3CDO_{vt=0-1}$ may serve as a reliable tracer of the disk itself. The emission from CH_3OCHO also appears not to be along the outflow direction. Its moment 1 map reveals a velocity gradient perpendicular to the outflow axis, with similar rotation to the flattened envelope, which could indicate that emission from this molecule traces the base of a disk wind or the disk. Further investigation of these two molecules may provide valuable information about the embedded disk and the early conditions enabling planet formation.

Some of these compact regions appear to trace a warm inner envelope or the innermost part of the IRAS4A2 system, as shown in Figure 3.6, especially given that emission from a couple of molecules remains unresolved. Moreover, the sizes of the emitting areas appear to correlate with lower values of upper-state energy levels. This trend suggests that higher-energy transitions trace warmer and more compact regions of the disk located closer to the central protostar. In contrast, lower-energy transitions probe a wider range of regions across the system. The most compact emission among these low upper state energy level lines could likely originate from colder regions in higher layers of the disk if the temperatures are lower there than in the mid-plane (Zamponi et al. 2021), and if they are effectively shielded from the protostar's radiation. Further supporting this interpretation is the observation that some compact and extended molecular emission still exhibits absorption features around IRAS4A2, whereas many others do not. This contrast implies that the emitting and sublimation regions of certain molecules may lie in higher but closer and warmer layers of the disk structure, where the dust optically thick

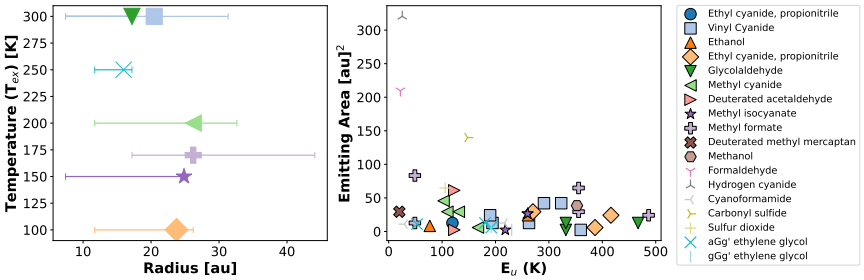


Figure 3.6: Left panel: Deconvolved radii of the emission plotted as a function of excitation temperature for the confirmed detected molecules in IRAS4A2. The error bars represent the minimum and maximum radii observed for all blended molecular lines, while the points indicate the median radius values. Right panel: The emission emitting area plotted against the upper state energy levels. Different colors and different figures represent emission from different molecules, as highlighted in the rightmost panel.

absorption appears to be now limited only to the innermost, with lower scale height regions. It is important to note that the protostellar envelope is normally related to an optically thick region at sub-mm wavelengths that absorbs the inner emission of Class 0/I objects (Galván-Madrid et al. 2018; Galametz et al. 2019) over a large extent. These absorption features have been observed and studied in other star-forming regions as well. For example, Lee et al. (2019) suggests that the absorption and reduction of line emission may be due to additional heating sources, which could be altering the temperature structure in the disk. This view comes from observations of systems experiencing accretion outbursts, similar to what has been observed in V883 Ori (Alarcón et al. 2024; Yamato et al. 2024). In the context of young stellar objects (YSOs), simulations by Baillié & Charnoz (2014) suggest that viscous heating could significantly impact the disk temperature beyond 20 au, affecting both the mid-plane and higher layers of the disk. Moreover, various hot spots have been identified in other protostellar sources, such as IRAS 16293-2422 A (Maureira et al. 2022). While the exact origin of these hot spots remains unclear, accre-

tion shocks, particularly those associated with infalling material along filamentary structures (streamers) from the extended envelope, are a primary candidate for generating such localized heating. As highlighted in Maureira et al. (2022), analyzing and identifying these diverse heating mechanisms is crucial for accurately modeling Class 0, and even Class I, protoplanetary disks as these systems have shown signs of late-stage accretion shocks (e.g., Garufi et al. 2022)

While additional heating processes may help explain some of the absorption features observed in IRAS4A2, an alternative explanation is continuum over-subtraction, an effect that arises when the optically thick continuum and the overlying gas have similar excitation temperatures, leading to absorption in the line profiles after subtraction of the continuum (see Nazari et al. 2024). Regardless of the underlying mechanism, this behavior is particularly clearly observed in the inner regions of IRAS4A2, very close to the central star. This behavior could suggest an evolutionary track, as previously mentioned, where strong absorption is now confined to the innermost regions for some molecules, in contrast to IRAS4A1 and some other regions, where much of its emission is still absorbed. This difference indicates that the optically thick dust or envelope has either dissipated in the outer regions, has become optically thin in most areas, or has shrunk and moved closer to the star and the mid-plane (as large dust grains are affected by settling and rapid radial drift). While these findings are intriguing, the absorbed emission may obscure critical details, preventing us from seeing the full picture with current observational capabilities. Furthermore, drawing conclusions about high-temperature and more compact molecular tracers remains challenging due to the limitations of both the CASSIS model and our spectral data (see Section 3.3), which explains the lack of a clear correlation between the excitation temperature and the radius of the emission.

3.4.1.2 Extended emission and its structure in IRAS4A2

Similarly, the extended emission in Fig.3.3 exhibits different morphologies, with some more complexity. First, H_2CO is a well-established tracer of the gas disk in YSOs (van't Hoff et al. 2020; Tychoniec et al. 2021). For $CH_3OCHO + SO_{2v=0}$, the emission would appear to originate from the same region as H_2CO, as they trace the same spatial extent, but it could also be tracing a potential disk wind (De Simone et al. 2024). Meanwhile, OCS appears to be an effective tracer of small grains, especially following the continuum emission bridge previously observed between IRAS4A1 and IRAS4A2 (as shown by the contours in Fig. 3.3 and in Guerra-Alvarado et al. (2024)). For both OCS and $SO_{2,v=0}$, it has been suggested that their extended emission in IRAS4A could originate from interactions between the outflow and the surrounding material (Taquet et al. 2020). The integrated emission maps further support the idea that both the grains and OCS are influenced by the S-shaped morphology of the IRAS4A2 outflow. A similar trend is observed for HCN, although in this case, its emission more clearly traces the disk continuum in the inner regions, suggesting it may be simultaneously tracing both the outflow and the gas component of the disk.

On the other hand, H_2CO and SO_2 do not fully align with the continuum emission. They are more compact and do not reach the outflow. This difference may arise from the fact that OCS transitions to the gas phase at lower temperatures than H_2CO and SO_2. Moreover, smaller dust grains, less affected by radial drift, tend to remain distributed over more extended colder regions, making OCS a suitable tracer of regions where only smaller dust grains are present. In contrast, the other two lines require higher temperatures, needing to be closer to the star to reach their sublimation temperatures, and therefore trace more evolved structures. Given this difference, one might expect that OCS and HCN trace a region with small dust grains, while H_2CO and SO_2 likely trace more inner structures, possibly those related to the gas disk. As shown in Fig. 3.4, however, while all

molecules yield reasonable mass estimates, both H_2CO and OCS emission is notably better fit by the rotational infalling envelope model. This commonality suggests that they may be tracing similar physical components. Nonetheless, it is important to note that the fit for H_2CO is not perfect and this interpretation may still involve uncertainties.

OCS, HCN, and H_2CO emission exhibits significant absorption by the dust continuum in the inner regions of the IRAS4A2 disk, near the warm inner envelope, with HCO^+ being completely absorbed.It is also worth noting that some of this molecular emission may be subject to self-absorption due to infalling material along the line of sight, which could either contribute to or even account for the observed absorption features, rather than dust absorption alone. In contrast, SO_2 shows little or no absorption compared to the other extended molecules, suggesting it may trace higher layers of the source, possibly the envelope. This behavior could indicate that HCN and H_2CO emission is likely tracing a more middle region, while HCO^+ emission, due to its strong absorption, may trace regions closer to the mid-plane of the source, where dust absorption from the shrinking envelope might still be significant. This stratification of molecular emission was also observed in HH212 by Lee et al. (2022), in IRAS4A2 by De Simone et al. (2024), and is consistent with findings in HD 163296, where emission from the same molecules were found to trace a similar vertical order (Paneque-Carreño et al. 2023).

In summary, the differences in characteristics between these molecules, such as H_2CO and SO_2 being more compact and not reaching the outflow, H_2CO and OCS having a common P-V diagram model and aligned masses, OCS, HCN, H_2CO, HCO^+ and SO_2 emission showing different absorption patterns, and the fact that HCN emission traces two components directly, suggest a discrepancy. These molecules may be tracing multiple components simultaneously, even at really small scales (in the warm inner envelope < 20 au) that vary in vertical distribution across radii and emission extent. Some of these interpretations, however, require further investigation to confirm which physical components these

molecules are actually tracing, and additional observations are needed to disentangle the potential chemical or structural stratification within IRAS4A2.

3.4.2 Accretion Shocks

OCS and SO_2 emission exhibits strong emission peaks that are outside of the continuum disk region (see Fig. 3.3). This observed emission pattern could be linked to shocks, as discussed in van Gelder et al. (2021), where sulfur-bearing molecules serve as tracers for material flowing from the envelope into the disk, likely originating from filaments formed by what are commonly referred to as streamers. The formation of SO and SO_2 typically occurs towards the end of a shock, suggesting that their emission is tracing such processes.

The origin of shocks in protostellar systems could be attributed to various mechanisms, including outflows (Persson et al. 2012), accretion shocks (Sakai et al. 2014; Garufi et al. 2022), or disk winds (Tabone et al. 2017). Notably, Artur de la Villarmois et al. (2022) identified SO_2 as the most reliable tracer of accretion shocks, while Maureira et al. (2022) suggested that such accretion shocks could be responsible for generating hot dust spots. Furthermore, OCS and SO_2 emission appears too extended to be solely associated with the envelope (Harsono et al. 2021).

In IRAS4A2, shocks are a plausible mechanism behind the observed emission of OCS and SO_2. Identifying a single, dominant origin for these shocks remains challenging, however, as they can arise in various contexts within the system. A key distinction lies between accretion shocks, which occur when infalling material decelerates upon impacting the disk surface, generating localized heating, and outflow-induced shocks, which result from the interaction between high-velocity outflows and the surrounding envelope, often producing more spatially extended emission with broader line profiles. Given the observations shown in Fig. 3.3, we propose that the compact, localized intensity peaks seen in OCS and SO_2 integrated

emission maps are most consistent with accretion shocks. Meanwhile, the more extended and broader emission features may instead be associated with outflow-driven shocks (Taquet et al. 2020), reinforcing the idea that emission from these molecules could be tracing multiple components of the system.

It is difficult to determine from the P-V diagrams whether or not SO_2 exhibits the symmetric Keplerian signature expected from a disk wind (Tabone et al. 2017). If the absorption feature in the OCS P-V diagram is ignored, however, a pattern emerges, resembling the expected kinematics (broad and slower than the jet) of a rotating disk wind. This could explain why OCS appears to trace the smallest grains and suggests that it is simultaneously probing multiple components, such as accretion shocks and the disk wind. Nonetheless, determining the precise origin of these emissions remains challenging, and it is still possible that these lines trace a different component than assumed here.

Finally, a secondary peak of OCS emission is identified just outside the continuum contour image of IRAS4A1, aligned with the southern outflow. This finding is consistent with Taquet et al. (2020), who previously detected this molecule in the IRAS4A binary within the same region.

3.4.3 High mass star forming regions vs IRAS4A2

To understand the origin of hot corinos, and in particular the one associated with IRAS4A2, it is valuable to compare their chemical composition with those of hot cores of other star-forming regions and identify both similarities and differences. Hot corinos have been proposed as low-mass analogs of the hot cores observed in high-mass star-forming regions, sharing comparable chemical signatures despite differences in mass and environmental conditions. In Fig. 3.7, we compare the molecular abundances relative to methanol for the species detected in IRAS4A2 with those reported in both high-mass and low-mass star-forming regions. The column densities of methanol were taken from Frediani et al. (2025), who

accounted for optical depth effects in their analysis. When necessary, isotopologue abundances were adjusted to reflect the main species using solar system isotopic ratios from Wilson & Rood (1994).

From Fig. 3.7, IRAS4A2 appears to exhibit molecular abundances similar to those of high-mass star-forming regions such as AFGL4176 and Sgr B2, at least for the molecules where direct comparisons are possible. In the case of $C_2H_5{}^{13}CN$, where we predict a high molecular abundance, we suspect the CASSIS fitting may be unreliable because only one unblended line is clearly detected in our spectra. The remaining lines are either heavily blended or faint, introducing significant uncertainty in the total molecular abundance of this molecule.

When comparing the molecular inventory of IRAS4A2 with that of the high-mass star-forming region AFGL 4176 in Bøgelund et al. (2019), we find that both regions share many molecular species, though AFGL 4176 exhibits a greater number of transitions and lines, probably due to its higher mass. Interestingly, the only molecules not identified in AFGL 4176 are $NCC(O)NH_2$ and $CH_3NCO_{vb=0}$. $CH_3NCO_{vb=0}$, however, has been detected in other high-mass star-forming regions, including Orion KL and Sgr B2(N) (Cernicharo et al. 2016; Belloche et al. 2017), and a tentative detection of $NCC(O)NH_2$ has recently been reported in Sgr B2(N) (Li et al. 2024). This absence is not entirely surprising, as previous studies have noted that AFGL 4176 is more comparable to the low-mass protobinary system IRAS 16293 (Jørgensen et al. 2016) than to other high-mass sources like Sgr B2(N) and Orion KL. In contrast, IRAS4A2 appears more aligned with the latter, supporting the idea that hot corinos may be low-mass analogs of the hot cores in high-mass star-forming regions, sharing similar complex chemistry but on a smaller scale.

Regarding the spatial distribution of these molecules, we observe several similarities with AFGL 4176 Bøgelund et al. (2019). First, emission from transitions with lower upper-state energies appears to be more spatially extended than that from higher upper-state energy transitions. Additionally, emission from sulfur-bearing molecules is among the most ex-

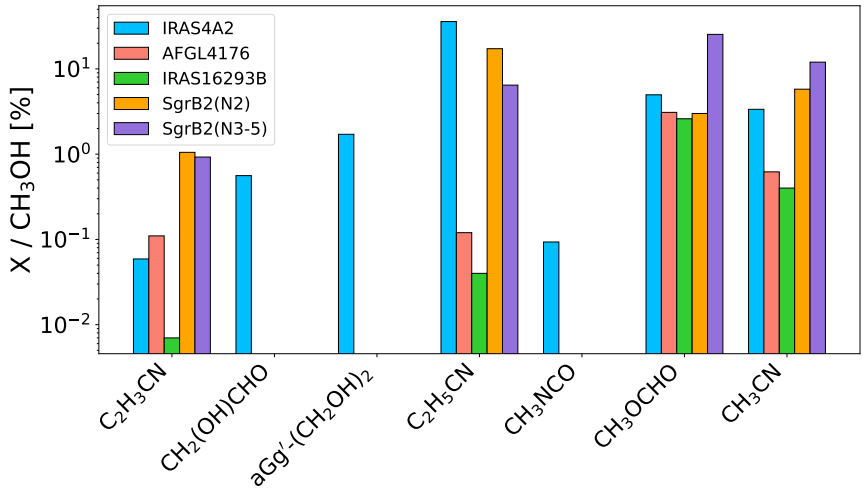


Figure 3.7: Normalized molecular abundance ratios relative to methanol, for the species detected in this work. The values are compared to those observed in both high-mass (AFGL4176 and SgrB2) and low-mass star-forming (IRAS16293B) regions.

tended compared to emission from other molecules, which aligns with detections in AFGL 4176 and our spatially resolved observations in IRAS4A2. Finally, we also observe a reverse trend with $C_2H_3CN_{v=0}$, like in AFGL 4176, with higher upper-state energy transitions corresponding to larger emitting areas. The reason for this reversal is still unclear and needs more investigation.

3.4.4 Outflows and misaligned velocity fields

The large-scale outflows observed in the IRAS4A region are from HCN, $HCO^+_{v=0,1,2}$, and H_2CO. These outflows extend to approximately 18" (~5300 AU). We resolve both outflows in all lines which allows for a clear distinction between the emission that originates from IRAS4A1 and IRAS4A2. We observed the distinctive S-shaped (observed in the moment 0 maps) pattern of the IRAS4A2 outflow, consistent with previous findings by Santangelo et al. (2015) and Chuang et al. (2021). This shape is

attributed to a misalignment between the initial core angular momentum vector and the magnetic field. It is suggested that this misalignment can happen if the Hall-induced magnetic field flips the angular momentum vector between the flattened envelope and the circumstellar envelope (Zhao et al. 2020a; Wurster et al. 2016).

By examining the moment 1 maps of the most extended molecular emission, we find that the velocity fields in the inner regions of HCN, H_2CO, OCS, and SO_2 are misaligned (flipped) with those of the outflow (see Fig. 3.3). In contrast, for the more compact COMs, it is difficult to determine a definitive rotation pattern due to SNR limitations. There are, however, hints that these species may also exhibit a rotational direction opposite to that of the outflow. This inversion of the velocity maps has been previously observed in various disks before, such as VLA 1623B (Ohashi et al. 2022), BHR71 (Tobin et al. 2019), and IRAS 16293-2422 (Zapata et al. 2013). Multiple origins for this inversion have been proposed, including interaction with the outflow, hydrodynamical interaction with the circumbinary disk, accretion shocks, and, more recently, material accelerated by the disk wind as it crosses the plane of the sky (De Simone et al. 2024). The exact cause of the inverted velocity gradient, however, remains incompletely understood and requires further investigation.

3.5 Summary and conclusions

We have studied the hot corino of IRAS4A2 at high resolution using ALMA, analyzing different spatial scales, from large-scale outflow-like emission down to a small warm inner envelope (~20 au) emission. Our findings indicate that:

- We confirm the detection of four complex molecules around IRAS4A2: $C_2H_3CN_{v=0}$, $CH_2(OH)CHO$, CH_3OCHO, and $CH_3C^{15}N$.
- Molecular emission appears to trace distinct regions within the IRAS4A2 system. Several species with small spatial extents and high

excitation temperatures are likely associated with a warm inner envelope or the innermost regions of IRAS4A2. In contrast, molecules such as $CH_3CDO_{v_t=0-1}$ and CH_3OCHO may serve as effective tracers of the disk structure, or a potential disk wind component. Further studies are necessary to determine the potential of these molecules for tracing the disk. If confirmed, however, these molecules could serve as key tracers for studying the disk during its earliest stages, when planet formation may have already begun.

- The extents of molecular emission observed in IRAS4A2 appear to correlate with lower upper-state energy levels. Given the inconsistencies between absorption features, kinematic signatures (e.g., P–V diagrams), and other observed properties, it is likely that extended emission is tracing multiple components simultaneously. These components include the outflow, envelope, disk, warm inner envelope, and possibly accretion shocks, outflow shocks and the disk wind, reflecting the complex and dynamic environment of this young protostellar system.

- The emission peaks observed in the OCS and SO_2 moment 0 maps are more consistent with signatures typically associated with shocks, particularly accretion shocks, which may be responsible for heating the dust in IRAS4A2. This hot dust could explain the prominent absorption features detected across the innermost regions of the spectra. In contrast, the more extended emission coming from the same molecules is better aligned with characteristics of outflow-driven shocks, suggesting that multiple shock mechanisms are contributing to the observed molecular emission.

- A comparison with high-mass star-forming regions such as AFGL 4176, Sgr B2(N), and Orion KL shows that these sources share mostly the same molecular species. This commonality suggests that hot corinos do not exhibit significant differences in molecular composi-

tion regardless of mass or environment. Furthermore, the spatial distribution of these molecules appears to be similar across different sources, but more studies at high resolution are needed to confirm this.

- We resolved the large-scale (~ 5300 au) outflows of HCN, $HCO^+_{v=0,1,2}$, and H_2CO, distinguishing the outflows from IRAS4A1 and IRAS4A2. We confirm the previously reported S-shaped morphology and the inverted velocity gradient observed in this region, between the outflow emission and other components of IRAS4A2.

acknowledgements. We thank J. Alejandro López-Vázquez, Annaëlle Maury, and Marta de Simone for their helpful discussions and insights. We acknowledge assistance from Allegro, the European ALMA Regional Centre node in the Netherlands. This paper makes use of the following ALMA data: ADS/JAO.ALMA#2018.1.00510.S. ALMA is a partnership of ESO (representing its member states), NSF (USA), and NINS (Japan), together with NRC (Canada), MOST and ASIAA (Taiwan), and KASI (Republic of Korea), in cooperation with the Republic of Chile. The Joint ALMA Observatory is operated by ESO, AUI/NRAO and NAOJ. P.N. acknowledges support from the ESO and IAU Gruber Foundation Fellowships.

Appendix A: IRAS4A2 Molecules in spectra

Table A.1: Line characteristics

Molecule	Name	Transition	Rest Frequency (GHz)	A_{ij} (s^{-1})	E_u (K)	g_u
HCN	Hydrogen cyanide	(3-2)	265.88618	8.42e-4	25.52	21
$C_2H_3CN_{v=0}$	Vinyl Cyanide	(28 6 23-27 6 22)	265.9347953	1.49e-3	262.77	171
$C_2H_3CN_{v=0}$	Vinyl Cyanide	(28 8 21-27 8 20)(28 8 20-27 8 19)	265.9062054	1.44e-3	323.06	171
$C_2H_3CN_{v=0}$	Vinyl Cyanide	(28 9 19-27 9 18)(28 9 20-27 9 19)	265.943385	1.40e-3	359.59	171
$C_2H_3CN_{v=0}$	Vinyl Cyanide	(29 1 29-28 1 28)	265.9228854	1.56e-3	194.36	177
$C_2H_3CN_{v=0}$	Vinyl Cyanide	(28 7 21-27 7 20)	265.8982758	1.47e-3	290.78	171
$C_2H_3CN_{v=0}$	Vinyl Cyanide	(28 1 27-27 1 26)	267.5746326	1.59e-3	189.95	171
$CH_3CDO_{vt=0,1}$	Deuterated acetaldehyde	(14 4 10 0-13 4 9 0)	265.91423	6.12e-4	122.84	29
$CH_3CDO_{vt=0,1}$	Deuterated acetaldehyde	(14 4 10 2-13 4 9 2)	265.843748	6.05e-4	122.83	29
$CH_2(OH)CHO_{v=0}$	Glycolaldehyde	(34 3 31 0-34 2 32 0)	265.9076199	1.51e-4	331.78	69
$CH_2(OH)CHO_{v=0}$	Glycolaldehyde	(34 4 31 0-34 3 32 0)	265.9204834	1.51e-4	331.78	69
$CH_2(OH)CHO_{v18=1}$	Glycolaldehyde	(18 11 7 1-18 10 8 1)	265.9255426	2.20e-4	466.95	37
$CH_3{}^{18}OH_{v=0-2}$	Methanol	(16 3 14 0-16 2 15 0)	265.894132	9.63e-5	352.57	132
$NCC(O)NH_2$	Cyanoformamide	(23 18 5-23 17 6)(23 18 6-23 17 7)	265.852665	3.14e-4	216.70	47
$NCC(O)NH_2$	Cyanoformamide	(11 4 7-10 3 8)	140.7863341	4.88e-5	29.71	23
$gGg' - (CH_2OH)_2$	gGg' ethylene glycol	(26 11 16 1-25 11 15 0)	265.9131258	1.42e-4	230.25	371
$gGg' - (CH_2OH)_2$	gGg' ethylene glycol	(27 3 24 1-26 4 23 1)	267.5258901	2.10e-4	191.86	385
$aGg' - (CH_2OH)_2$	aGg' ethylene glycol	(26 4 23 1-25 3 22 1)	265.8326715	2.06e-4	180.49	371
$aGg' - (CH_2OH)_2$	aGg' ethylene glycol	(26 6 20 0-25 6 19 1)	267.5692918	4.29e-4	192.05	371
$aGg' - (CH_2OH)_2$	aGg' ethylene glycol	(13 4 10 1-12 4 9 0)	140.7865974	6.02e-5	53.05	243
$^{13}CH_3{}^{13}CH_2CN$	Ethyl cyanide, propionitrile	(12 9 4-13 8 5)(12 9 3-13 8 6)	265.9346645	5.15e-6	119.36	25
$C_2H_5{}^{13}CN_{v=0}$	Ethyl cyanide, propionitrile	(30 8 23-29 8 22)	267.5506331	1.48e-3	270.05	61
$C_2H_5{}^{13}CN_{v=0}$	Ethyl cyanide, propionitrile	(30 14 17-29 14 16)(30 14 16-29 14 15)	267.5740406	1.25e-3	416.15	61
$C_2H_5{}^{13}CN_{v=0}$	Ethyl cyanide, propionitrile	(30 13 18-29 13 17)(30 13 17-29 13 16)	267.5248859	1.30e-3	386.33	61
$CH_3NCO_{vb=0}$	Methyl isocyanate	(31 0 0 1-30 0 0 1)	265.917341	9.14e-4	218.36	63
$CH_3NCO_{vb=0}$	Methyl isocyanate	(31 3 28 0-30 3 27 0)	267.512332	9.12e-4	260.16	63
$CH_3NCO_{vb=0}$	Methyl isocyanate	(31 3 29 0-30 3 28 0)	267.498881	9.12e-4	260.15	63
CH_3OCHO	Methyl formate	(7 7 0 0-6 6 1 0)(7 7 1 0-6 6 0 0)	265.869967	4.35e-5	49.05	30
CH_3OCHO	Methyl formate	(7 7 0 2-6 6 0 2)	265.831401	4.35e-5	49.07	30
CH_3OCHO	Methyl formate	(24 1 23 3-23 1 22 3)	267.544467	2.85e-4	355.60	98
CH_3OCHO	Methyl formate	(24 2 23 3-23 2 22 3)	267.535013	2.85e-4	355.60	98
CH_3OCHO	Methyl formate	(22 15 7 5-21 15 6 5)	267.572288	1.55e-4	486.69	90
$CH_3C^{15}N$	Methyl cyanide	(15 1-14 1)	267.608	1.66e-3	109.91	62
$CH_3C^{15}N$	Methyl cyanide	(15 3-14 3)	267.567	1.60e-3	167.16	124
$CH_3C^{15}N$	Methyl cyanide	(15 2-14 2)	267.593	1.63e-3	131.38	62
$CH_3C^{15}N$	Methyl cyanide	(15 0-14 0)	267.613	1.66e-3	102.76	62
HCO^+	Formyl ion	(3 0 0-2 0 0)	267.557526	1.45e-3	25.68	7
$CH_3SD_{v=0-2}$	Deuterated methyl mercaptan	(3 2 1 1-2 1 1 1)	267.599	2.56e-5	19.95	7
$SO2_{v=0}$	Sulfur dioxide	(13 3 11-13 2 12)	267.5374512	1.51e-4	105.82	27
$OCS_{v=0}$	Carbonyl sulfide	(22-21)	267.530219	5.57e-5	147.67	45
H_2CO	Formaldehyde	(2 1 2-1 1 1)	140.839502	5.30e-5	21.92	15
C_2H_5OH	Ethanol	(12 3 10 2-12 2 11 2)	140.81481	1.67e-5	76.93	25
C_2H_5OH	Ethanol	(15 9 6 1-16 8 8 0)	267.5732224	7.63e-6	260.82	31

Table A.2: Morphology and physical properties

Molecule	Name	Morphology	T_{ex} [K]	N_{Sp} [cm^{-2}]	FWHM [Km/s]
HCN	Hydrogen cyanide	Outflow and cold flattened envelope	-	-	7.5
$C_2H_3CN_{v=0}$	Vinyl Cyanide	Disk, blend	300 ± 4	1.77e15 ± 0.01e15	3
$C_2H_3CN_{v=0}$	Vinyl Cyanide	Disk, blend	300 ± 4	1.77e15 ± 0.01e15	3
$C_2H_3CN_{v=0}$	Vinyl Cyanide	Warm inner envelope	300 ± 4	1.77e15 ± 0.01e15	3
$C_2H_3CN_{v=0}$	Vinyl Cyanide	Upper side of the warm inner envelope	300 ± 4	1.77e15 ± 0.01e15	3
$C_2H_3CN_{v=0}$	Vinyl Cyanide	Warm inner envelope	300 ± 4	1.77e15 ± 0.01e15	3
$C_2H_3CN_{v=0}$	Vinyl Cyanide	Lower side of the warm inner envelope, blend	300 ± 4	1.77e15 ± 0.01e15	3
$CH_3CDO_{vt=0,1}$	Deuterated acetaldehyde	Disk, blend	-	-	2
$CH_3CDO_{vt=0,1}$	Deuterated acetaldehyde	Absorbed at the warm inner envelope	-	-	2
$CH_2(OH)CHO_{v=0}$	Glycolaldehyde	Disk, blend	300 ± 3	1.68e16 ± 0.1e16	1.5
$CH_2(OH)CHO_{v=0}$	Glycolaldehyde	Warm inner envelope	300 ± 3	1.68e16 ± 0.1e16	1.5
$CH_2(OH)CHO_{v18=1}$	Glycolaldehyde	Warm inner envelope	300 ± 3	1.68e16 ± 0.1e16	1.5
$CH_3{}^{18}OH_{v=0-2}$	Methanol	Warm inner envelope, part of disk	-	-	2.5
$NCC(O)NH_2$	Cyanoformamide	Disk	-	-	4
$NCC(O)NH_2$	Cyanoformamide	Warm inner envelope, blend	-	-	4
gGg′ – $(CH_2OH)_2$	gGg' ethylene glycol	Disk, blend	-	-	2.5
gGg′ – $(CH_2OH)_2$	gGg' ethylene glycol	Warm inner envelope, blend	-	-	2.5
aGg′ – $(CH_2OH)_2$	aGg' ethylene glycol	Disk, blend	250 ± 3	5.13e16 ± 0.02e16	2
aGg′ – $(CH_2OH)_2$	aGg' ethylene glycol	Warm inner envelope, blend	250 ± 3	5.13e16 ± 0.02e16	2
aGg′ – $(CH_2OH)_2$	aGg' ethylene glycol	Warm inner envelope, blend	250 ± 3	5.13e16 ± 0.02e16	2
$^{13}CH_3{}^{13}CH_2CN$	Ethyl cyanide, propionitrile	Disk, blend	-	-	2
$C_2H_5{}^{13}CN_{v=0}$	Ethyl cyanide, propionitrile	Disk	100 ± 0.3	1.21e16 ± 0.37e16	2.5
$C_2H_5{}^{13}CN_{v=0}$	Ethyl cyanide, propionitrile	Warm inner envelope, blend	100 ± 0.3	1.21e16 ± 0.37e16	2.5
$C_2H_5{}^{13}CN_{v=0}$	Ethyl cyanide, propionitrile	Warm inner envelope, blend	100 ± 0.3	1.21e16 ± 0.37e16	2.5
$CH_3NCO_{vb=0}$	Methyl isocyanate	Absorbed at the warm inner envelope	150 ± 4	2.8e15 ± 0.05e15	2
$CH_3NCO_{vb=0}$	Methyl isocyanate	Barely observed, warm inner envelope	150 ± 4	2.8e15 ± 0.05e15	2
$CH_3NCO_{vb=0}$	Methyl isocyanate	Warm inner envelope	150 ± 4	2.8e15 ± 0.05e15	2
CH_3OCHO	Methyl formate	Disk	170 ± 3	1.49e17± 0.09e17	2
CH_3OCHO	Methyl formate	Disk, blend	170 ± 3	1.49e17± 0.09e17	2
CH_3OCHO	Methyl formate	Disk	170 ± 3	1.49e17± 0.09e17	2
CH_3OCHO	Methyl formate	Cold flattened envelope, blend	170 ± 3	1.49e17± 0.09e17	2
CH_3OCHO	Methyl formate	Warm inner envelope, blend	170 ± 3	1.49e17± 0.09e17	2
$CH_3C^{15}N$	Methyl cyanide	Disk	200 ± 6	3.73e14 ± 0.2e14	2
$CH_3C^{15}N$	Methyl cyanide	Warm inner envelope, blend	200 ± 6	3.73e14 ± 0.2e14	2
$CH_3C^{15}N$	Methyl cyanide	Warm inner envelope, blend	200 ± 6	3.73e14 ± 0.2e14	2
$CH_3C^{15}N$	Methyl cyanide	Absorbed at the envelope	200 ± 6	3.73e14 ± 0.2e14	2
$HCO^+_{v=0,1,2}$	Formyl ion	Outflow	-	-	-
$CH_3SD_{v=0-2}$	Deuterated methyl mercaptan	Disk	-	-	2
$SO2_{v=0}$	Sulfur dioxide	Cold flattened envelope, blend	-	-	4.5
$OCS_{v=0}$	Carbonyl sulfide	Cold flattened envelope	-	-	3.5
H_2CO	Formaldehyde	Outflow and cold flattened envelope	-	-	5
C_2H_5OH	Ethanol	Warm inner envelope	-	-	2.5
C_2H_5OH	Ethanol	Warm inner envelope, blend	-	-	2.5

Appendix B: IRAS4A2 Moment 0 maps

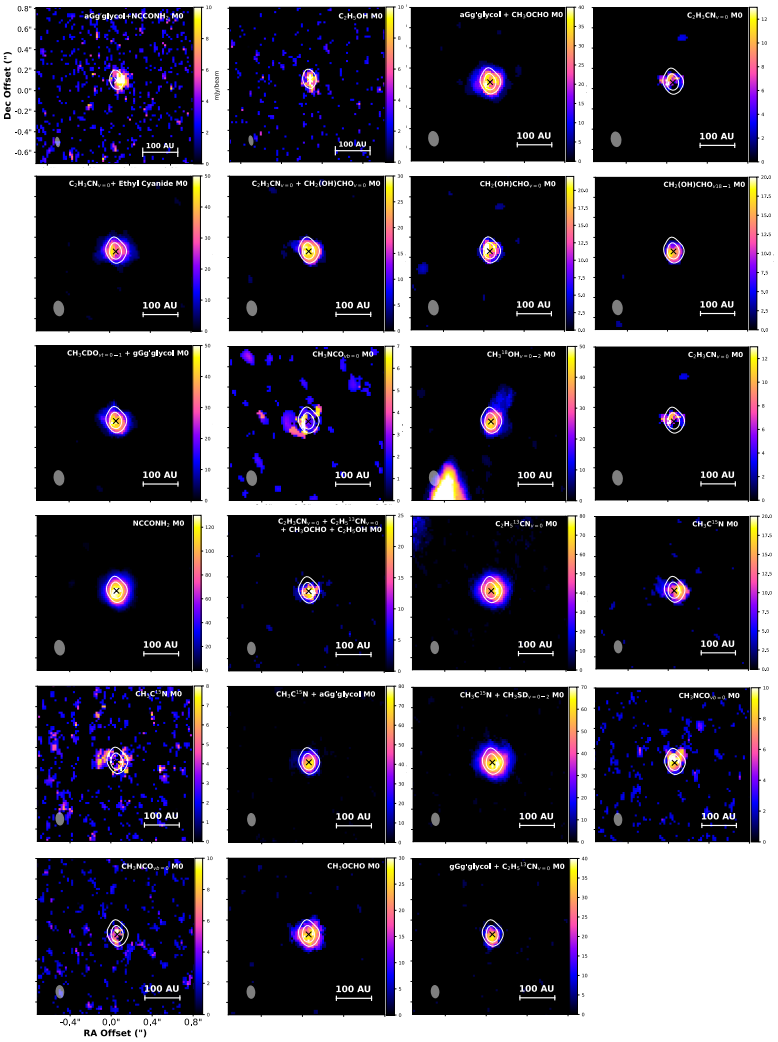


Figure B.1: Integrated emission (Moment 0) maps of all the remaining molecular lines identified in the ALMA Band 6 and Band 4 spectra of IRAS4A2.

Into the thick of it: ALMA 0.45 mm observations of HL Tau at a resolution of 2 au

Osmar M. Guerra-Alvarado, Carlos Carrasco-González, Enrique Macías, Nienke van der Marel, Adrien Houge, Luke T. Maud, Paola Pinilla, Marion Villenave, Yoshiharu Asaki Elizabeth Humphreys.

Astronomy & Astrophysics, Volume 686, Article A298, 2024.

Abstract

Aims. To comprehend the efficiency of dust evolution within protoplanetary disks, it is crucial to conduct studies of these disks using high-resolution observations at multiple wavelengths with the Atacama Large Millimeter/submillimeter Array (ALMA).

Methods. In this work, we present high-frequency ALMA observations of the HL Tau disk using its Band 9 centered at a wavelength of 0.45 mm. These observations achieve the highest angular resolution in a protoplanetary disk to date, 12 milliarcseconds (mas), allowing the study of the dust emission at scales of 2 au. We used these data to extend the previously published multiwavelength analysis of the HL Tau disk, constraining the dust temperature, dust surface density, and maximum grain size throughout the disk. We performed this modeling for compact solid dust particles as well as for porous particles.

Results. Our new 0.45 mm data mainly trace optically thick emission, providing a tight constraint to the dust temperature profile. We derive maximum particle sizes of ~ 1 cm from the inner disk to ~ 60 au. Beyond this radius, we find particles between 300 μm and 1 mm. The total dust mass of the disk is 2.1 M_J with compact grains, and it increases to 6.3 M_J assuming porous particles. Moreover, an intriguing asymmetry is observed at 32 au in the northeast inner part of the HL Tau disk at 0.45 mm. We propose that this asymmetry is the outcome of a combination of factors, including the optically thick nature of the emission, the orientation of the disk, and a relatively large dust scale height of the grains that is preferentially traced at 0.45 mm. To validate this, we conducted a series of radiative transfer models using the software RADMC-3D. Our models varying dust masses and scale heights successfully replicate the observed asymmetry in the HL Tau disk. If this scenario is correct, our measured dust mass within 32 au would suggest a dust scale height H/R> 0.08 for the inner disk. Finally, the unprecedented resolution allowed us to probe the dust emission down to scales of a few au for the first time. We observed an

increase in brightness temperature inside the estimated water snowline, and we speculate whether this might indicate a traffic-jam effect in the inner disk.

Conclusions. Our results show that 0.45 mm observations of protoplanetary disks can be used to robustly constrain the radial profile of their dust temperature. Additionally, the higher optical depths at this wavelength can be used to constrain the vertical scale height of the dust. Finally, these higher frequencies allow us to reach higher spatial resolutions, which have the potential to resolve the region within the water snowline in disks.

4.1 Introduction

Over the past ten years, the Atacama Large Millimeter/submillimeter Array (ALMA) has made significant contributions to our understanding of protoplanetary disks by revealing substructures within them. These studies (e.g., ALMA Partnership et al. 2015, Isella et al. 2016, and Long et al. 2018) have shown the frequent appearance of substructure in protoplanetary disks with different morphologies (van der Marel et al. 2013, Pérez et al. 2016, and Huang et al. 2018b). These substructures play a significant role in protoplanetary disks: They allow dust grains to accumulate and grow, facilitating the formation of planets by providing regions of higher dust density and trapping, and they slow down the radial drift of dust grains, which would otherwise hinder the planet formation process (Pinilla et al. 2012a).

Most ALMA studies of protoplanetary disks are performed at wavelengths of about 1 mm, where the dust emission is relatively bright and high angular resolutions of about 30 mas can be achieved. In some disks, similar studies have also been performed at longer wavelengths, where the emission is known to be optically thinner, up to 3 mm with ALMA (e.g., Tazzari et al. 2021, Cazzoletti et al. 2018,Long et al. 2020), but also up to 1 cm with the Very Large Array (VLA; e.g., Carrasco-González et al. 2016, Hashimoto et al. 2023). These observations at long wavelengths allow us to study the properties of the dust grains, but at the expense of angular resolution. Observations of protoplanetary disks with ALMA at shorter wavelengths provide the highest possible angular resolution with ALMA (~10 mas), but they are usually avoided because of the higher atmospheric opacity and turbulence, which lead to necessarily longer integration and calibration times. Moreover, dust emission is expected to be optically thick. However, complementary information can also be extracted from studies at these wavelengths. For instance, optically thick emission imposes better constraints on the temperature and on the albedo of the dust particles, which improves the results from multiwavelength modeling of

disks. Finally, observations at short wavelengths are the only way to explore the dust content in the gaps, whose emission is usually too optically thin to be detected at long wavelengths.

Recent multiwavelength analyses of Class II protoplanetary disks (Carrasco-González et al. 2019, Macías et al. 2021, Sierra et al. 2021, and Guidi et al. 2022) have measured dust properties within these substructures. The dust sizes determined from these observations are about 1 mm. However, there is a discrepancy with measurements obtained from polarization observations (Kataoka et al. 2017), which suggest dust sizes on the order of a few hundred micrometers. To reconcile these contradicting results, Kataoka et al. 2017 and Ohashi et al. 2020 have proposed the existence of two dust populations. The larger (millimeter) particles would experience more efficient vertical settling, become decoupled from the gas, and would gather toward the midplane of the disk. On the other hand, smaller particles would remain mixed with the gas in higher layers of the disk (Barrière-Fouchet et al. 2005). More recently, Zhang et al. 2023b proposed that large (larger than 1 mm) and porous (porosities higher than 70%) particles could reproduce both multiwavelength and polarization results. A very recent polarization multiwavelength study strongly supported the presence of porous particles in HL Tau (Lin et al. 2023a)

Pinte et al. 2016, Villenave et al. 2020, Doi & Kataoka 2021, Villenave et al. 2022, and Pizzati et al. 2023 have focused on understanding the vertical structure of protoplanetary disks. Although limited in number, these studies suggest that Class II disks exhibit significantly low dust scale heights, particularly at the longer wavelengths observed with ALMA. This is a consequence of the change in the distribution of dust grains in the vertical direction, which in turn is due to settling (Dullemond & Dominik 2004,Pinilla et al. 2021). Most constraints presented in these papers remain upper limits (except for HD163296), with suggestions such as H(100au) < 1 au. Additionally, Pizzati et al. 2023 discovered values < 4 au for certain disks from the Disk Substructures at High Angular Resolution Project (DSHARP), particularly those with less favorable orientations.

These findings were predominantly derived from the presence and depth of gaps and rings in the outer regions of the disks (outer 100 au), where the scale height in the inner regions remains mostly unknown.

In this work, we present high-resolution Band 9 observations of HL Tau, a young stellar object in the Taurus-Auriga molecular cloud (~ 147pc, Galli et al. 2018) with an estimated age younger than one million years (Liu et al. 2017). HL Tau is considered a Class I-II disk (Furlan et al. 2008), and it was the first protoplanetary disk in which dark and bright rings were discovered (ALMA Partnership et al. 2015). It was intensively observed in the last years with ALMA and VLA, and therefore, the currently available high-quality data cover a wide range of wavelengths between 0.9 mm and 1 cm (Carrasco-González et al. 2016, Carrasco-González et al. 2019). Several previous studies also modeled its continuum emission to infer the dust properties (e.g., Jin et al. 2016, Pinte et al. 2016, Liu et al. 2017). These studies clearly established that the dark rings are gaps in the dust distribution, that is, regions with a density lower than in the adjacent bright rings. The origin of the substructures is still debated, but the most promising suggestions are planet-disk interactions (e.g., Jin et al. 2016, Dipierro et al. 2016). Our new sensitive and high-resolution observations at 0.45 mm are combined with previous multiwavelength observations to analyze the dust properties in the disk. The addition of shorter-wavelength observations allowed us to improve previous modeling of the dust properties in the disk and also to obtain new insight into the dust temperature very close to the protostar and the vertical structure of the disk.

4.2 Observations

We analyzed archival observations obtained with the Atacama Large Millimeter/submillimeter Array (ALMA) at a wavelength of 0.45 mm. One of the archival data sets that we used was part of the test observations for the band-to-band calibration during the High-Frequency Long Baseline Campaign (Asaki et al. 2020), project code: 2011.0.00005.E). The observations

were taken during two execution blocks on November 3, 2017. The total observing time was 65 and 100 minutes for the first and second execution, respectively, which combined, gives a 45-minute on-source time for HL Tau. The final data has eight spectral windows, each of which covers a bandwidth of 2 GHz. We also used additional data at a lower resolution (project code: 2017.1.01178.S, PI: E. Humphreys) to complete the uv coverage at shorter baselines. These data have eight spectral windows covering frequencies from 646-662 GHz with a bandwidth of 1.875 GHz each. The observations were taken from October 2, 2018, to October 18, 2018, with a total observing time on-source of 95 minutes.

We calibrated the data by using the calibration pipeline and scripts provided by the ALMA staff. We used version 5.6.1 of Common Astronomy Software Applications (CASA); McMullin et al. 2007 for self-calibration and cleaning in both data sets. We identified and flagged the spectral lines that were found in both data sets. We also averaged channels for the low- and high-resolution data; the final self-calibrated data sets contain spectral windows of eight channels of 200 MHz each.

We performed phase-only and amplitude self-calibration in both data sets. First, self-calibration was performed on the short-baseline data. During the self-calibration process, we created the images using the task CLEAN in CASA. The MTMFS deconvolver (Rau & Cornwell 2011) was used with scales of 0, 1, 3, and 5 times the beam size. We also used a Briggs weighting with a robust parameter of 0.5. For the low-resolution data set, the self-calibration process resulted in a clear improvement in the image quality. We applied six iterations of phase-only self-calibration in which we decreased the time-solution interval to 18s. Furthermore, we were also able to apply two rounds of amplitude and phase self-calibration (`calmode=ap`) until no improvement in the signal-to-noise ratio was found. By the end of the whole self-calibration process, we achieved an increase in the S/N by a factor of ~17.4. We combined our short-baseline data together with the long-baseline data after aligning and correcting for proper motions and astrometric errors between our

data sets. This was done by applying a Gaussian fit using CASA in the high-resolution image and using the tasks FIXVIS and FIXPLANETS to apply shifts to the low-resolution data. After this, self-calibration was attempted on the combined dataset. We started with phase-only self-calibration, but due to the low S/N at the long baselines, no improvement was found.

Last, self-calibration separately on the long-baseline data was also attempted by using the model obtained from the self-calibrated low-resolution data, but no improvement was found either. Since not enough solutions were found with any method to improve the quality of the combined data set, the self-calibration process was stopped.

With our final data set at hand, we recalculated the weights using the task STATWT in CASA. For the final images, we used the TCLEAN task in CASA with the MTMFS deconvolver (Rau & Cornwell 2011) using nterms=1 and scales at 0, 1, 3, and 5 times the beam size. We used a pixel size that was ten times smaller than the beam size for all of the images. We explored different weightings: natural, uniform, and Briggs weighting, with different robust values. Finally, two images were used for this study. The first image was made by setting the parameter robust to 0 and using baselines shorter than 12 $k\lambda$ in length. This is a good compromise between resolution and sensitivity and was used to study the large-scale emission of the disk. This image has an rms noise of 270 μJy beam^{-1} and a beam size of ~23 mas. A second image was obtained by setting the parameter robust to -0.5, which resulted in a beam size of ~12 mas and an rms noise of 380 μJy beam^{-1}. The higher angular resolution of this image allowed us a detailed study of the innermost part of the disk ($\lesssim$20 au). Both images are shown in Figure 4.1.

In order to study the radial properties of the disk, we also obtained radial profiles of the emission and convolved the images to a round beam (robust 0, 24 mas, and robust -0.5, 13 mas). We used the known inclination and position angles of the disk for this, 46.72° and 138.02°, respectively (ALMA Partnership et al. 2015). However, due to the inclination of the disk, there is a loss in angular resolution in the NE-SW direction. Since the S/N

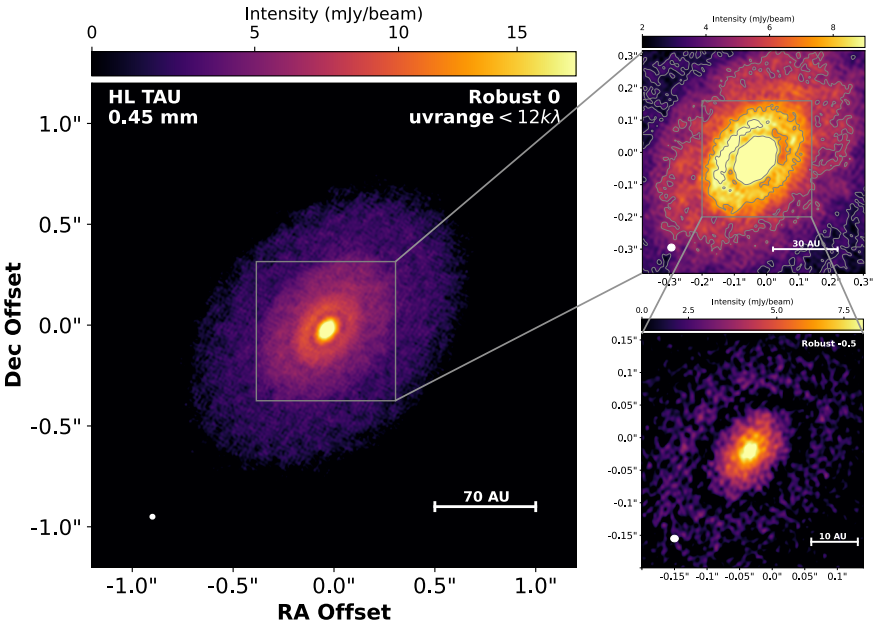


Figure 4.1: HL Tau Band 9 images. LEFT PANEL: Image using a robust parameter of 0 with a beam of 0.0226"× 0.021" TOP RIGHT PANEL: Zoom into the inner part of the HL Tau disk of the robust 0 images showing the asymmetry with gray contours at 11 times the rms and 33 times the rms. BOTTOM RIGHT PANEL: Inner HL Tau disk from the robust -0.5 image with a beam of 0.0116"× 0.010".

of the image is very high, we were able to avoid this loss in resolution by simply averaging the emission azimuthally within ±0.2 rad of the major axis of the disk. The radial profiles of the brightness temperature obtained from the intensity profiles of both images are shown in Figure 4.2.

4.3 Results

Figures 4.1 and 4.2 show that our images at 0.45 mm recover emission from the whole disk with a radius of ~1" or ~140 au, similar to previous ALMA images at longer wavelengths (see, e.g., Carrasco-González et al.

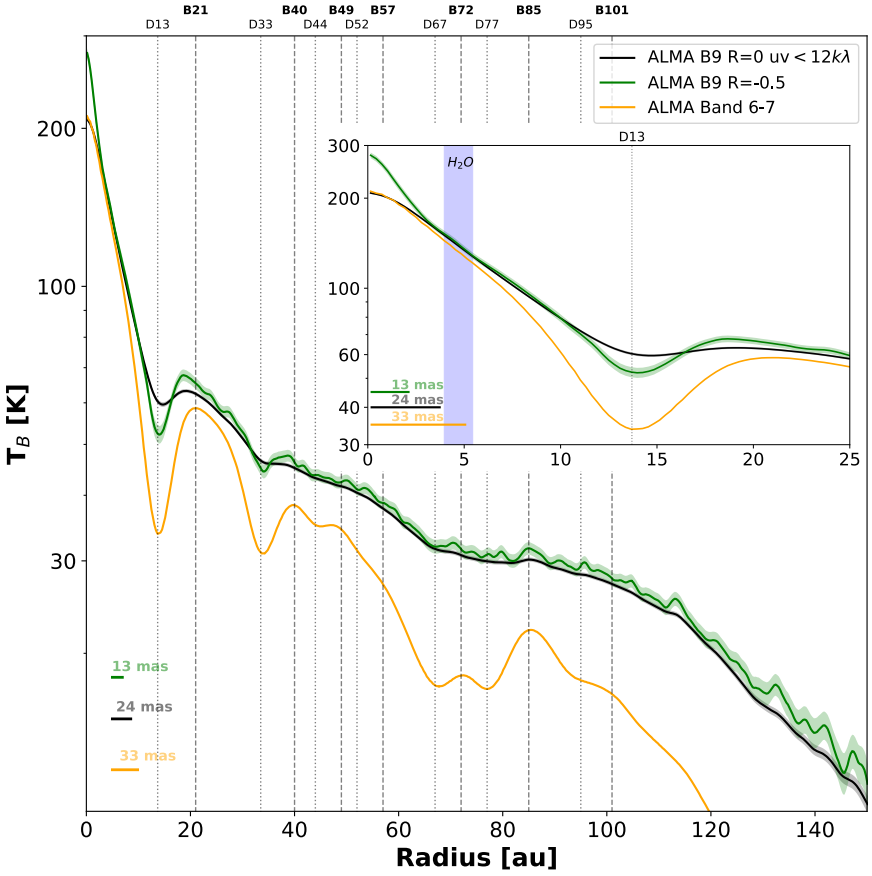


Figure 4.2: Comparison of the HL Tau Band 6-7 (ALMA Partnership et al. 2015) and the HL Tau Band 9 radial profiles of the brightness temperature. We plot the Band 6-7 ALMA image with the lowest resolution (33 mas, yellow), the Band 9 image with 22 mas (black), and the Band 9 image with 13 mas (green). The substructures are shallower in the radial brightness temperature for Band 9 than in the Band 6-7 image, and the emission from the Band 9 image extends up to 140 au. In the inset, we show the first 20 au of the HL Tau disk. We plot the brightness temperatures of the three images, and assuming that T_{disk}=T_B because of the optically thick regime, we display the position (in temperature) of the water snowline.

2019, ALMA Partnership et al. 2015). Our 0.45 mm image also shows some substructures, but as expected, substructures are detected with a lower

contrast between dark and bright rings because of the higher optical depth at this wavelength. This suggests that the gaps contain small particles traced by the 0.45 mm image. These particles are more strongly coupled with the gas and might fill the gaps more than the larger particles that are observed at longer wavelengths (Pinilla et al. 2012b,de Juan Ovelar et al. 2013). Furthermore, we observed a slight deviation in the positions of the gaps and rings at 0.45 mm when compared to the radial profiles at other wavelengths (see Figure 4.2), which suggests that there might be slight variations in the depth and width of the disk substructures at different wavelengths.

In the top right of Figure 4.1, we show a zoomed-in view of the inner 50 au. An asymmetry is visible in the 0.45 mm data that is not seen at longer wavelengths: the NE part of the first ring is more intense than the SW part of the ring.

In the bottom right panel of Figure 4.1, we show the image with the highest angular resolution, which allowed us to resolve the most internal part of the disk ($\lesssim$ 20 au) for the first time. This image shows the first ring and a very deep gap.

This first gap, centered at 13 au, shows some emission in the low-resolution 0.45 mm, but appears very dark in the image with the highest angular resolution (see Figures 4.1 and 4.2).

These observations provide a clearer view of the gap structure. They reveal that it is likely deeper and more depleted of dust particles than was initially observed with a lower resolution at 0.87 mm and 1.3 mm. Moreover, the very deep gap in the 0.45 mm image strongly suggests that it is indeed devoid of small dust particles as well.

The inner panel of Figure 4.2 shows that the brightness temperature increases within 2.5 au at the highest angular resolution. This might be attributed to substructures within the inner disk that become resolved for the first time with the higher angular resolution of our 0.45 mm data.

In the following section, we first discuss the updated modeling of the radial dust properties using all the currently available data of HL Tau. We

then describe the origin of the new features found in the 0.45 mm images, the asymmetry, and the substructure within the inner disk.

4.4 Discussion

4.4.1 Modeling of the dust properties

Several studies have modeled the dust properties in HL Tau using the available data (e.g., Pinte et al. 2016, Liu et al. 2017, Carrasco-González et al. 2019). We used a new modeling procedure that included the new 0.45 mm image we report here, which provides valuable constraints on the dust temperature and enhances the comprehensiveness of our multiwavelength analysis. Thus, this new analysis includes images at 0.45, 0.87, 1.3, 2.1, and 7.0 mm. We created a new 0.45 mm image with a robust parameter of 1.0 using baselines of < 12 $k\lambda$, as previously described for the robust 0.0 image. Then, we convolved it with a 50 mas Gaussian beam and extracted radial profiles in wedges along the major axis within radial beams of approximately 0.01 arcseconds. We also extracted radial profiles at the other wavelengths by applying the same procedure to the images presented in Carrasco-González et al. (2019). Subsequently, each point in the radial profiles was modeled independently. We note that the points in the model are not independent from the neighboring points due to the effects of the beam. Consequently, the contrast of the model parameters between rings and gaps is slightly smoothed in our results. We followed an approach similar to that of (Carrasco-González et al. 2019), that is, at each radius, we fit the spectral energy distribution (SED) in the millimeter wavelength range using a 1D slab model given by

$$I_\nu = B_\nu(T)[(1-\exp(\tau_\nu/\mu)) + \omega_\nu F(\tau_\nu,\omega_\nu)], \tag{4.1}$$

where

$$F(\tau_\nu, \omega_\nu) = \frac{1}{\exp(-\sqrt{3}\epsilon_\nu\tau_\nu)(\epsilon_\nu - 1) - (\epsilon_\nu + 1)} \mathrm{X}$$
$$\left[\frac{1 - \exp(-(\sqrt{3}\epsilon_\nu + 1/\mu)\tau_\nu)}{\sqrt{3}\epsilon_\nu\mu + 1} + \frac{\exp(-\tau_\nu/\mu) - \exp(-\sqrt{3}\epsilon_\nu\tau_\nu)}{\sqrt{3}\epsilon_\nu\mu - 1} \right], \quad (4.2)$$

where $\omega_\nu = \frac{\sigma_\nu}{\kappa_\nu + \sigma_\nu}$ is the albedo, which is defined by the scattering coefficient (σ_ν) and the absorption coefficient (κ_ν), $\tau_\nu = \Sigma_{dust}\chi_\nu$, where $\chi_\nu = \kappa_\nu + \sigma_\nu$, $\mu = cos(i)$ considers the inclination effects by correcting the optical depth by this inclination (i), and $\epsilon_\nu = \sqrt{1 - \omega_\nu}$. This model assumes that most of the dust content is settled in the midplane (see Sierra et al. 2019 and Carrasco-González et al. 2019 for details). While this assumption holds well for the outer HL Tau disk, it is not met within the initial ~ 32 au. A particle size distribution that follows a power-law distribution was also assumed, specifically, $n(a) \propto a^{-p}$. We set the value of the exponent p to 3.5. This value is commonly used for the interstellar medium (ISM) (Mathis et al. 1977).

The dust opacity values were obtained assuming the DSHARP dust composition and following the effective medium approximation (Birnstiel et al. 2018). As usual in the study of protoplanetary disks, we first considered compact solid spherical particles. However, we also performed an analysis by considering spherical porous dust particles with a porosity of 90%. This is motivated by very recent results that strongly suggested that the HL Tau disk contains porous dust particles (Zhang et al. 2023b and Lin et al. 2023a).

The opacity tables for the porous particles were obtained using the same procedure as in (Birnstiel et al. 2018): The grains were assumed to be composed of small monomers within a void matrix. The optical properties of the monomers were first computed using the Bruggeman rule. This same rule was also used for the compact grains. The monomers were then mixed with a void matrix using the Maxwell-Garnett rule. It is well established that the fluxes, and consequently, dust masses significantly

depend on the assumed dust composition, in particular, on the quantity of carbon. For instance, when the opacities presented by Ricci et al. 2010 and Stadler et al. 2022 are used, the fluxes they inferred were higher, which facilitated an explanation of the spectral indices of typical disks. This shows that the composition of the grains plays a crucial role, and the total dust mass derived in the subsequent section should be approached with caution.

We modeled the SED of the disk at each radius independently, and we fit the dust parameters (T_{dust}, a_{max}, and Σ_{dust}). We assumed a flux calibration uncertainty of 10% at 0.45 mm, 0.9 mm, 1.3 mm, and 7 mm, and 5% at 2.1 mm. We computed the posterior probability distribution of our model at each radius using the Markov chain Monte Carlo (MCMC) implementation within `emcee` (Foreman-Mackey et al. 2013). We assumed uniform priors in the dust surface density and maximum grain size. Following Macías et al. 2021, we used a conservative (i.e., wide) prior for the dust temperature based on the expected radial temperature profile for a passively irradiated disk, $T_d = (\phi L_\star / 8\pi r^2 \sigma_{\rm SB})^{0.25}$, assuming $L_{star} = 6 \pm 5\ L_\odot$ (i.e., a very conservative uncertainty on the stellar luminosity) and a range in ϕ (i.e., flaring angle) between 0.005 and 0.3. This prior is wide enough to have no effect on the posterior of the temperature at most radii. It only helps to avoid unphysically high dust temperatures at a few radii within the wide gap between 60 and 90 au, where the emission is optically thin and the dust temperature and dust surface density are highly degenerate.

Figures 4.3 and 4.4 show the dust parameters for the HL Tau disk obtained from the fitting with the solid and porous particles, respectively. Appendix A shows the radial intensity profiles of the model at each wavelength and their uncertainties, obtained from the median, 16th, and 86th percentiles of 500 random SEDs computed from the MCMC chains. As anticipated, the dust temperature is very well constrained for the compact and porous particles. We also note that the surface density is well constrained in both cases. Moreover, our findings reveal that the dust particles in the HL Tau disk are relatively large. Their sizes range from

millimeters to centimeters. These sizes resemble well with models of dust evolution with traps located at different distances (Pinilla et al. 2015).

Our models find a sudden, and likely unphysical, increase in the particle size at the 13 au gap. However, Figures A.1 and A.2 show that our models can't reproduce the observed emission at these radii. The reason probably is our limited angular resolution, paired with the fact that the 13 au gap is highly depleted of large dust particles. The SED at high frequencies is therefore dominated by the small grains in the gap, while at longer wavelengths, the emission mostly comes from the beam smearing of the emission at the 20 au ring. Observations with a higher angular resolution at long wavelengths, which are only feasible with the upcoming ngVLA, are therefore necessary to accurately constrain the dust properties at these radii.

A distinct gap at 70 au, wide and almost without large particles, is evident in 4.3 and 4.4, consistent with prior observations by Carrasco-González et al. 2019. Interestingly, an increase in the dust surface density is then present at the 84 au and 96 au rings, with grain sizes that still remain at a few hundred microns. We note that an infalling streamer has been found to interact with the HL Tau disk at these radii (Garufi et al. 2022). We speculate that the small dust particles of this late-infalling material might ne responsible for the creation of this dust ring, which would explain why the particles at these radii have not yet grown to millimeter/centimeter sizes. More detailed modeling of the interaction between the disk and infalling streamers is required to confirm this scenario.

Furthermore, clear distinctions emerge between the compact and porous particle solutions. In general, the model using compact particles exhibits lower temperatures and dust surface densities across the entire range of radii. The particle sizes predicted by the porous dust composition appear to be slightly smaller, although we note that they have a significantly wide uncertainty range.

Our new 0.45 mm data have allowed us to better constrain the radial dust temperature profile. We can therefore compare the position of the

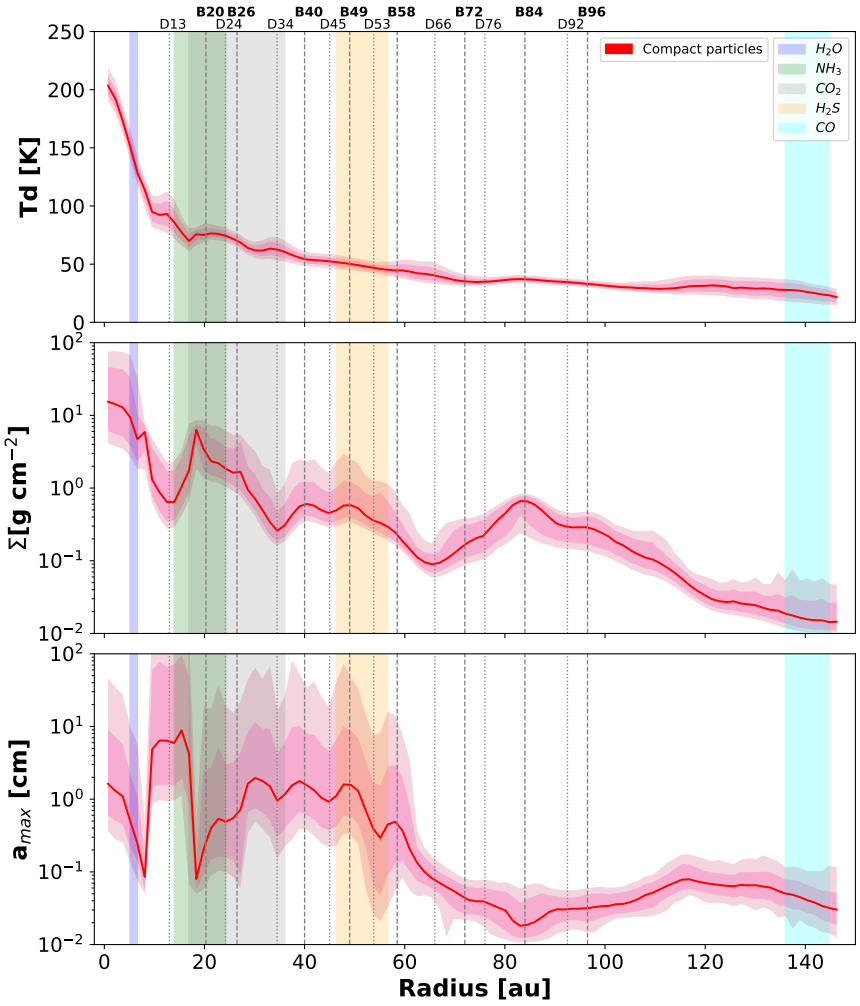


Figure 4.3: Dust parameters at each radius using compact dust particle opacities. The positions of the most common snowlines are plotted in color. The vertical dotted and dashed lines are the positions of the gaps and rings, respectively, as seen from the surface density parameter. *Top panel*: Dust temperature at each radius. *Middle panel*: Dust surface density at each radius. *Bottom panel*: Maximum particle size at each radius. The particle sizes are about 1 mm - 1 cm.

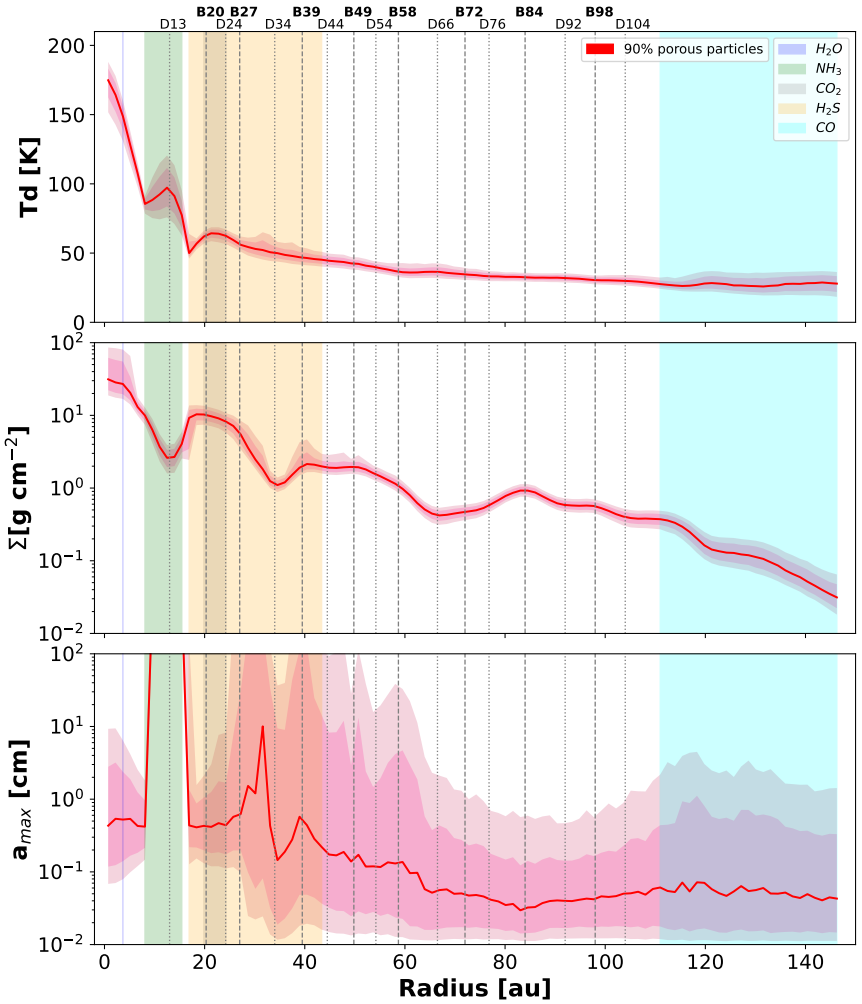


Figure 4.4: Same as Figure 4.3, but using a 90% porosity for the dust particles and for the dust opacities. The dust temperature is lower and the surface density is higher around the gaps, and the maximum particle sizes are similar, but at the 13 au gap, the particle size increases strongly.

rings and gaps in HL Tau with the expected positions of the snowlines of some of the most relevant volatiles in protoplanetary disks more robustly. We plot in Figures 4.3 and 4.4 the expected radii of the snowlines of H_2O, NH_3, CO_2, H_2S, and CO. Except for the H_2O snowline, the uncertainties

in the sublimation temperatures of these volatiles now dominate the uncertainty in their positions. These large uncertainties still make it hard to extract any robust conclusion, despite our improved temperature profile. The abundance of substructures in HL Tau means that these snowlines will always fall close to a ring or gap. This makes it hard to confidently reject the hypothesis that snowlines cause at least a few of the ring substructures in HL Tau, as previously proposed (Zhang et al. 2015b; Carrasco-González et al. 2019). However, many other substructures appear to be far from the expected snowlines, as in other protoplanetary disks (Bae et al. 2023). This mostly applies to the outer substructures, between 65 and 98 au, but also some between 36 to 45 au. We therefore conclude that mechanisms other than snowlines (e.g., MHD effects or planet-disk interactions) must cause most, if not all, the ring substructures in HL Tau.

We infer total dust masses of $2.1^{+1.88}_{-0.84}$ and $6.3^{+1.57}_{-1.04}$ M_J from the compact and porous particles, respectively. The dust masses when porous particles are assumed are thus higher by a factor of ~ 3, as previously reported by Zhang et al. 2023b. Our measurement of the dust mass with compact grains is twice higher than the mass obtained in Carrasco-González et al. 2019 assuming compact particles with the same composition as ours (1.04 M_J). The primary difference between their analysis and ours is that we included Band 9 in our sample. These additional data have allowed us to more robustly constrain the dust temperature, which in turn affects the rest of the modeling. We obtained lower dust temperatures at all radii. The surface density is comparable at the inner radius, but it declines more rapidly than in their study. Additionally, our analysis reveals more pronounced substructures in the surface density. Notably, we observe dust particle sizes that are larger by approximately one order of magnitude within 60 AU, but beyond this point, the particle sizes decrease more significantly compared to the findings in Carrasco-González et al. 2019. These larger particles inside 60 au have lower absorption opacities, which explains that our dust mass is higher than that in Carrasco-González et al. 2019. Additionally, Booth & Ilee 2020 estimated a lower limit for the

total gas mass of the disk of 209.5 M_J. This agrees well with our results of the compact dust particles when we consider a gas-to-dust ratio of 100. However, the elevated mass associated with porous dust particles from our analysis might imply a reduced gas-to-dust ratio of ~ 33 when compared to the total disk mass of 209.5 M_J. This suggests that the total gas mass of the disk might indeed still be higher than 209.5 M_J.

We note that our assumption of a 1D slab model might not be accurate in the inner radius < 32 AU, where the emission at 0.45 mm is so optically thick that it might trace layers of the disk above the midplane (see section 4.4.2). If all wavelengths effectively probe adjacent and close layers in the disk, indicating very little variation in temperature and dust size distribution between them, then the assumption could still be valid. The midplane of protoplanetary disks is generally vertically isothermal. It is, therefore, most likely that, if our observations trace significantly different layers of the disk, this only affects the maximum grain sizes traced at each wavelength. Sierra & Lizano (2020) explored these effects in more detail and found that the high optical depths in the innermost regions of disks could result in an incorrectly measured maximum grain size of a few hundred microns. While we cannot discard the possibility that our modeling is affected by these effects, the fact that we find maximum grain sizes of ~ 5 mm in the inner region instead of the 200-300 microns found by Sierra & Lizano (2020) suggests that our modeling is not severely affected by the high optical depths.

4.4.2 Azimuthally asymmetric emission in the inner disk

As mentioned in Section 3, the first ring, centered at 21 au, shows an azimuthal asymmetry at 0.45 mm that becomes fainter at longer wavelengths. This might be contingent upon the resolution and sensitivity of the observations. This asymmetry appears as an increase in brightness at the northeastern side of the ring, covering almost 180 degrees and centered on the minor axis of the disk (see Fig. 4.1). The position of this

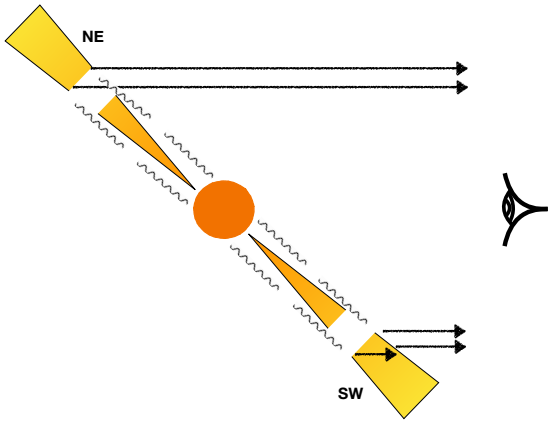


Figure 4.5: Scenario proposed for the origin of the asymmetry seen in HL Tau at 0.45 mm.

asymmetry strongly suggests that it is caused by the combination of the disk inclination and its high optical depth at the observed wavelength (see Fig. 4.5). Specifically, in the NE part of the disk, we directly observe the emission from the internal wall of the first ring, which is directly irradiated by the central star, and this direct irradiation increases its temperature. On the other hand, in the SW part of the disk there is no direct line of sight toward the wall. The wall emission is therefore blocked by the optically thick material in the line of sight (see Figure 4.5).

The HL Tau outflow is blueshifted in the NE and redshifted in the SW (Lumbreras & Zapata 2014). We can therefore infer that the NE corresponds to the far side of the disk and the SW corresponds to the close side of the disk. This explains the position of the asymmetry in that side of the minor axis of the disk.

The asymmetry is in this case fundamentally similar to the asymmetries found in Class 0/I objects (e.g., Guerra-Alvarado et al. 2024,Lin et al. 2023b,Ohashi et al. 2023), where the dust particles did not have time to

settle or are affected by significant turbulence that prevents the grains from falling onto the midplane (larger dust scale height), so that they remain optically thick even at longer wavelengths with ALMA. On the other hand, this asymmetry is fundamentally different from the large-scale asymmetries observed in other disks, where the effects become more pronounced at longer wavelengths (e.g., IRS48 (van der Marel et al. 2015) and HD142527 (Casassus et al. 2015)) which contradicts the observed behavior in HL Tau. These asymmetries are commonly associated with dust traps in which dust can grow to centimeter sizes.

In order to confirm that the asymmetry is caused by a geometric effect, we used a toy model to reproduce the observed asymmetry. We used RADMC-3D (Dullemond et al. 2012) to perform radiative transfer models at 0.45 mm while varying parameters such as the disk dust mass and scale height. We then compared the model emission with the observed data to gain insight into the physical properties and vertical structure of the disk. In this specific radiative modeling, a generic protoplanetary disk model was used within RADMC-3D. The disk dust masses and scale height were adjusted to explore different scenarios and to reproduce the observed asymmetry. The `optool` package (Dominik et al. 2021) was employed to compute the DSHARP dust particle opacities using a_{min} as 0.050 μm and a_{max} as 3mm. For this toy model, we were only interested in the inner regions of the disk. We therefore only considered emission up to a radius of 32 au (the location of the second gap). We assumed that all the grains are at the same height, and we set a small inner radius R_{in}=1 au. A gap between 8 au and 17 au was included in the model to capture the effects of the asymmetry at the outer edge of the gap.

The generic protoplanetary disk model uses a density distribution,

$$\rho(r,z) = \frac{\Sigma(r)}{H_p\sqrt{2\pi}} \exp(-\frac{z^2}{2H_p^2}), \tag{4.3}$$

where r is the distance to the star from the disk, H_p(r) is the dust scale

Table 4.1: Model parameters explored

$M_{Disk}^{<32au}$	1 M_J	3 M_J	5 M_J
H/R	0.01	0.01	0.01
	0.03	0.03	0.03
	0.05	0.05	0.05
	0.08	0.08	0.08
	0.1	0.1	0.1

height of the disk, and $\Sigma(r)$, is the dust surface density, defined as

$$\Sigma(r) = \Sigma_0(\frac{r}{r_{out}})^{-1}. \tag{4.4}$$

The dust scale height in the radiative modeling is defined as a power-law-like dependence, given by

$$H_p(r) = H_{100}(\frac{r}{100AU})^{1+\Psi}, \tag{4.5}$$

where Ψ is the value of the flaring index set by default to 0.14, and H_{100}, is the value of the scale height at a distance of 100 AU from the central star.

Finally, a total stellar mass of 1.7 M$\odot$ (Pinte et al. 2016), a stellar luminosity of 6 $L_\odot$, and an effective temperature of 4395 K (White & Hillenbrand 2004) were assumed. In addition, the inclination angle for HL Tau was set to 46.72°, and the distance was 147 pc.

Several models were run. We varied the dust scale height and the dust disk mass within 32 au ($M_{Disk}^{<32au}$) based on previous studies (Pinte et al. 2016; Liu et al. 2017). We show these parameters and their combination in Table 4.1.

The model images were then convolved using a Gaussian beam with the same beam as for the 0.45 mm image. The final convolved model

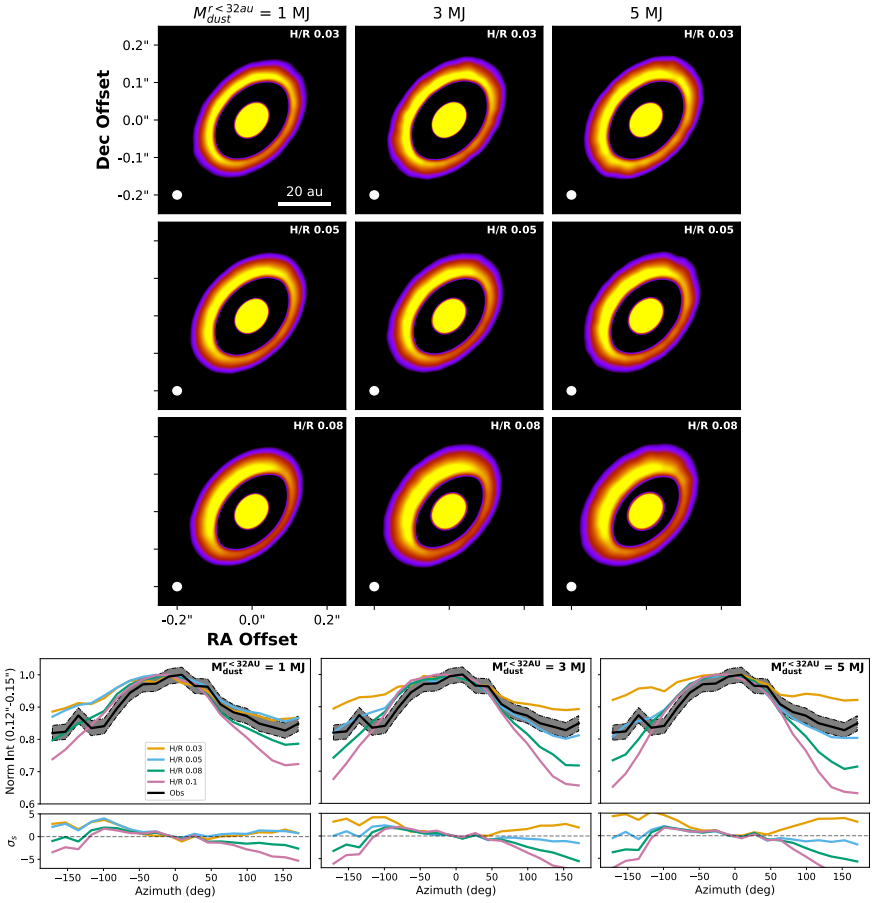


Figure 4.6: RADMC-3D models of the inner HL Tau disk compared with the Band 9 observation. Top panel: Convolved images of the nine different models with RADMC-3D that reproduce the observation better, corresponding to masses of 1 M_J, 3 M_J, and 5 M_J, paired with scale height values of 0.08, 0.05, and 0.03 H_p. The disk mass is defined as the dust mass within 32 au. Bottom panels: Normalized azimuthal profiles considering the emission between 0.12 and 0.15 arcseconds in the HL Tau Band 9 observation and all the RADMC-3D models. The lowest panels depict the difference, measured in sigmas, between the observation and the respective models

images that seem to reproduce the emission of the observation better are shown in Figure 4.6. We also extracted the deprojected emission from each pixel in a ring ranging from 0.12" to 0.15" and around 360° to capture the increased emission in the asymmetry. We show the normalized azimuthal profiles from the observation and all models in Figure 4.6. We note that our goal with this toy models was to show that this type of asymmetry can be obtained at 0.45 mm, and that the dust mass and scale height can be constrained from these images. We therefore did not try to reproduce the exact flux of our observations because that would require a much more detailed modeling in which the disk parameters would need to be varied more strongly. The azimuthal profiles for 1, 3, and 5 Jupiter masses (inner disk mass + ring mass) are also shown in Figure 4.6.

Our modeling shows that an asymmetry such as that observed in HL Tau can be produced by the combined effects of disk orientation, high optical depth, and larger scale heights at 0.45 mm. Figure 4.6 shows that the dust mass plays a significant role in reproducing the observed asymmetry at 0.45 mm. In models in which the scale height is not large enough, the emission no longer produces an asymmetry.

If the asymmetry arises from the scenario we outlined before, we find that a disk dust mass (within 32 au) of approximately 1 M_J, combined with a scale height H/R of 0.08, a disk dust mass of 3 M_J with a scale height H/R of 0.05, or a disk dust mass of 5 M_J with a scale height H/R slightly smaller than 0.05 reproduces the observed asymmetry in the observations best. In other words, the higher the dust mass, the smaller the dust scale height required to reproduce an asymmetry. Because of this, an independent estimate of the dust mass within 32 au would allow for a better constraint on the scale height of the disk. We employed the mass obtained from our multiwavelength analysis in section 4.4.1, acknowledging its known limitations, for an initial approximation of the scale height in this specific region of the disk. From this analysis, we obtained a disk dust mass inside the first 32 au of $0.86^{+1}_{-0.368}$ M_J. If our proposed scenario is the cause of the asymmetry, our derived mass would then imply a scale height ~>= 0.08

H/R in that specific region of the disk. As Figure 4.6 shows, to determine the scale height more effectively, we need a more restrictive constraint on the disk dust mass in subsequent studies, together with a model that reproduces the flux and the actual structure of the HL Tau disk.

We note that the scale height necessary to reproduce the observed asymmetry is significantly larger than the estimates from radiative transfer modeling of the 0.9-3 mm emission, H/R < 0.01 (Pinte et al. 2016). One possible explanation for this inconsistency is that in Pinte et al. 2016, the focus was primarily on gaps and rings in the outer disk, rather than on those within 30 au as constrained in this paper. This result then suggests that the HL Tau disk may exhibit a greater vertical extent (thickness) in the inner regions while maintaining a flatter profile in the outer regions. Radial variations in scale height have indeed been identified for the two rings of HD163296, with the 67au ring being very thick (>4au) and the 100au ring being very flat (<1au) (Doi & Kataoka 2021, Liu et al. 2022).

While there are limited constraints on the radial variation in the scale height, this outcome implies that turbulence in disks might be higher in the inner than in the outer regions. This aligns well with the high accretion rates on some disks that cannot be explained by their current low turbulence values. In this context, the magnetically driven accretion disk models suggested by Delage et al. 2022 could explain the heightened turbulence parameter and increased scale height, leading to the observed asymmetry beyond the dead zone (at 23 AU) and within the MRI-active layer in the HL Tau disk. Additionally, this is consistent with what is expected in the case of vertical shear instability with dust coagulation, where the transition between the thick and thin disk occurs at around 100 au (Pfeil et al. 2023). Finally, it also remains inconclusive whether the streamer observed by Garufi et al. (2022) in HL Tau could have an effect at smaller radii through the flow of material into the inner disk. The findings in Jiang et al. (2024) suggest a potential influence of this streamer on the turbulence at the outer radius (70 au), raising questions about a possible impact on smaller scales. Further analysis is essential to discern

the factors contributing to the increased turbulence, if any, in the HL Tau inner disk and to unravel the specifics of this phenomenon.

4.4.3 Substructure in the inner disk: Possible sign of the traffic-jam effect

As mentioned, our image with the highest angular resolution at 0.45 mm revealed an increase in the brightness temperature within ~2.5 au (see the inset in Figure 4.2). There are several possible explanations for this.

First, we discard the hypothesis that this increase is due to free-free contamination. It is well known that HL Tau drives a powerful jet whose emission has been previously modeled using high angular resolution VLA data at long wavelengths (Carrasco-González et al. 2019). Thus, we know that in the 23-43 GHz frequency range, the expected free-free emission from the radio jet is given by

$$\left[\frac{F_\nu}{\mu Jy\ beam^{-1}}\right] = 175 \times \left[\frac{\nu}{32.5\ GHz}\right]^{0.7}, \tag{4.6}$$

where ν is the frequency of the image at which we wish to calculate the free-free emission. In this frequency range, the free-free emission was found to be partially optically thin, which is reflected in the 0.7 spectral index. Because the optical depth of the free-free emission is proportional to $\nu^{-2.1}$ (e.g., Reynolds 1986), we expect at the frequency of our 0.45 mm image, that is, ~650 GHz, that free-free emission from the jet is optically thin. Thus, there must be a turning point between 50 and 650 GHz. A conservative assumption is that emission from the jet becomes totally optically thin at 100 GHz. Then, using equation 4.6 to estimate the free-free emission at 100 GHz, and extrapolating this with a spectral index of -0.1 to higher frequencies, we obtain that an estimate of the free-free contamination at 650 GHz would be ~300 μJy, which is ~2% of the peak emission at the center of the disk in the 0.45 mm image. The actual contribution at this frequency is probably lower since it is very likely that

the free-free emission would become optically thin at a frequency lower than 100 GHz. Another potential explanation for a significant free-free emission at the central part of the disk is the possibility that it becomes highly optically thick due to photoionization. However, this scenario faces challenges because HL Tau is a K-type star, and these stars typically do not emit sufficient ionizing photons to fully ionize a very dense gas. All of these factors lead us to the conclusion that the elevated emission in the inner region of the disk is unlikely to be primarily caused by free-free contributions.

An interesting explanation for the increased dust emission in the inner part of the disk is the possibility of a dust particle pile-up in that region. Our unprecedented angular resolution allows us to probe the dust emissions down a few au, inside the estimated water snowline at ~ 5 au when we assume $T_{disk} = T_B$ (Zhang et al. 2015b, Figure 4.2). Inside the water snowline, theoretical models predict the appearance of a traffic-jam effect (e.g., Banzatti et al. 2015, Pinilla et al. 2017), as dry silicates are more sensitive to fragmentation than ice-rich grains (Dominik & Tielens 1997; Supulver et al. 1997; Wada et al. 2013; Gundlach & Blum 2014). This leads to lower particle sizes and to a reduced drift speed. The traffic-jam effect offers a favored pathway for the formation of dry planetesimals in the inner disk, but this was recently questioned in the light of new experiments to determine the stickiness of ice-rich grains (e.g., Gundlach et al. 2018; Musiolik & Wurm 2019) and in light of observations that showed the resilience of icy pebbles to sublimation (Houge et al. 2023). Interestingly, Facchini et al. (2024) recently detected water emission at 321 GHz from the inner disk of HL Tau, but their spatial resolution was not enough to robustly measure the position of the water snowline.

Our results could be consistent with the traffic-jam effect because a pile-up of solids like this would increase the dust density and optical depth inside the water snowline (e.g., Banzatti et al. 2015), causing observations to probe higher layers of the disk with more elevated dust temperatures, thereby manifesting a higher brightness temperature, as shown in Figure

4.2 (See Drążkowska & Alibert 2017 and Ros et al. 2019). Moreover, an increase in the population of smaller particles will also result in a decrease in the albedo, which in turn results in an increase in the emission.

A second possibility is that the increase in the brightness temperature is attributed to viscous heating in the inner disk. Overall, the heating mechanisms in protoplanetary disks significantly influence the temperature profile of these. The two dominant heating processes in these disks are stellar radiation and viscous heating (D'Alessio et al. 2005). Throughout most of the disk, stellar radiation contributes most to the thermal structure of the disk. However, in the innermost regions of the disk close to the midplane, where dust surface densities reach notably high values, it is highly likely that viscous heating becomes the primary contributor to the temperature profile of the disk (D'Alessio et al. 2001). More recently, Chambers (2009) found that the midplane temperature may be affected by viscous heating within the radial range of 1 to 40 au in protoplanetary disks. This phenomenon also influences the position of the snowline, which varies depending on the age of the disk. The position where viscous heating takes place, however, depends upon the characteristics of the star and on many other parameters that are hard to constrain.

It is currently challenging to distinguish between the traffic-jam and the viscous heating scenarios. We strongly encourage future works to focus on this aspect, however, given the implications it could have concerning planet formation in the inner disk. For example, observations with a high angular resolution at other wavelengths could help us to constrain the dust emission spectral index and particle size, which would help us to understand the underlying mechanisms that drive the observed changes in brightness temperature.

4.5 Summary and conclusions

We reported new sensitive ALMA images at 0.45 mm of the HL Tau disk with an unprecedentedly high angular resolution of 12 mas or 1.7 au. At this wavelength, the detected emission is known to be highly optically thick. This is evidenced by the shallower substructures that we observed. The extended nature of the disk suggests that we trace smaller dust particles that are more closely coupled to the gas.

By combining the Band 9 image with the images at other wavelengths, we updated the model of the dust properties in the disk. The 0.45 mm image has allowed us to better constrain the dust temperature of the disk, which provided better constraints on the dust density and particle size. The particle sizes are still predicted to be larger than millimeter sizes until ~ 60 au, but there is a significant decrease (to ~ 200 μm) between 60-100 au. These smaller particles coincide with the region in which an accretion shock of infalling material has been found, traced by SO and SO_2. The final derived disk dust masses are 2.1 M_J for compact particles and 6.3 M_J for porous dust particles. These dust masses translate into gas-to-dust ratios ≤ 100.

Our 0.45 mm data clearly show an asymmetry in the emission from the first ring. The emission is considerably more intense in the NE part of the disk than in the SW part. We interpreted this as a combination of very optically thick emission, a moderately inclined disk, and a large dust scale height. In the NE part of the disk, we directly view the emission from the internal wall of the first ring, which is illuminated by the radiation from the central star. This interpretation is supported by our radiative transfer model, which demonstrates the dependence of this asymmetry on the dust mass of the inner regions of the disk and the dust scale height. We propose that this type of asymmetry in other disks can be used to constrain the dust scale height if an independent estimation of the dust mass of the disk has been made. Based on our proposed scenario and the multiwavelength analysis model, we implied the possibility of a dust

scale height H/R ~ >= 0.08 for the HL Tau disk at least in the inner 32 au. This approximation appears to be in strong contrast with the constraints identified by Pinte et al. 2016, who determined H/R < 0.01 in the outer disk. We note that this discrepancy might stem from higher turbulence in the inner regions of HL Tau compared to its outer region, leading to radial variations in the vertical structure of the HL Tau disk. It may be necessary to incorporate the vertical structure in the multiwavelength analysis to determine the disk mass and to employ more quantitative modeling approaches, instead of the qualitative ones in RADMC-3D, to obtain a more realistic scale height of the disk.

We have resolved the innermost part of the HL Tau disk and showed that there is some previously unseen substructure. It is revealed as a steep increase in the brightness temperature very close to the central star, at radii smaller than 5 au. Interestingly, the radius at which this increase starts appears to coincide with the position of the water snowline. Therefore, we discussed the possibility of a pile-up of small particles due to a decrease in the drift velocity of the small grains after they cross the water snowline and are fragmented more efficiently. We also discussed a different possibility in which we resolve the region in which the heating of the disk changes from being dominated by irradiation to being dominated by viscous heating. Previous theoretical models predicted that this change should take place very close to the protostar. To further confirm either of these scenarios, additional modeling and observations at other wavelengths are necessary for the HL Tau disk.

acknowledgements. This paper makes use of the following ALMA data: ADS/JAO.ALMA#2011.0.00005.E and ADS/JAO.ALMA#2017.1.01178.S. ALMA is a partnership of ESO (representing its member states), NSF (USA) and NINS (Japan), together with NRC (Canada), MOST and ASIAA (Taiwan), and KASI (Republic of Korea), in cooperation with the Republic of Chile. The Joint ALMA Observatory is operated by ESO, AUI/NRAO

and NAOJ. C.C.-G. acknowledges support from UNAM DGAPA-PAPIIT grants IG101321 and IG101224 and from CONACyT Ciencia de Frontera project ID 86372. The research of M.V. was supported by an appointment to the NASA Postdoctoral Program at the NASA Jet Propulsion Laboratory, administered by Oak Ridge Associated Universities, under contract with NASA.

Appendix A: Markov chain Monte Carlo model versus observations: VLA fitting

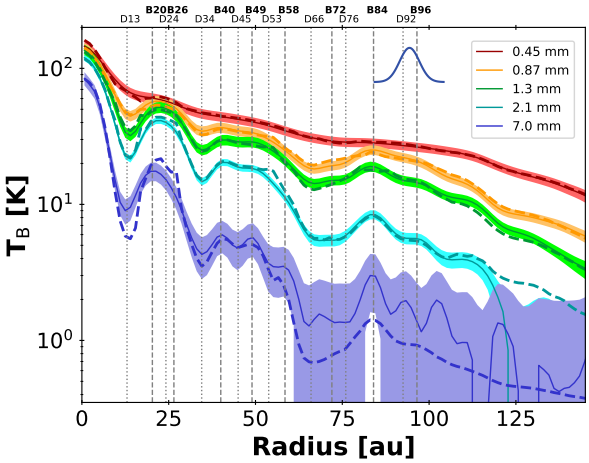


Figure A.1: Comparison of the brightness temperatures of the model (dash lines) with observations (solid lines) at each radius and wavelength. Compact dust particles were used, and the VLA emission is plotted and fit within the MCMC. The vertical lines are the positions of the gaps and bright rings taken from the dust parameters, and the size of the beam is plotted as a Gaussian in the top right corner for the five wavelengths (50 mas).

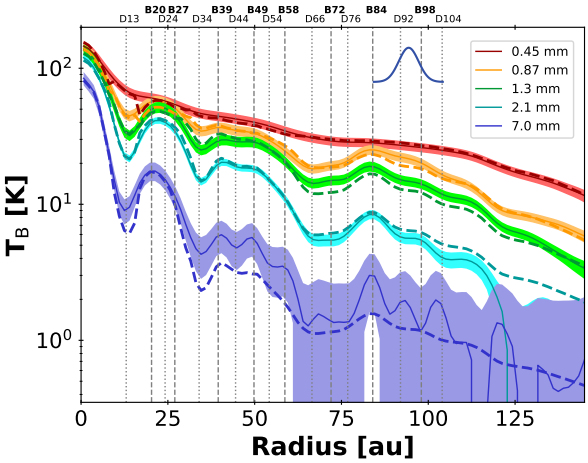


Figure A.2: Same as Figure A.1, but with the porous particle model instead.

A high-resolution survey of protoplanetary disks in Lupus and the nature of compact disks

Osmar M. Guerra-Alvarado, Nienke van der Marel, Jonathan P. Williams, Paola Pinilla, Gijs D. Mulders, Michiel Lambrechts, Mariana Sanchez.

Astronomy & Astrophysics, Volume 696, Article A232, 2025.

Abstract

Aims. Most of the exoplanets discovered in our Galaxy to date orbit low-mass stars, which tend to host small disks in their early stages. To better elucidate the link between planet formation and disk substructures, observational biases should be reduced through observations of these small, faint disks at the highest resolution using the Atacama Large Millimeter Array (ALMA). *Methods.* We present new high-resolution (0.03-0.04") ALMA observations at 1.3 mm of 33 disks located in the Lupus star-forming region that have total dust continuum fluxes of < 25 mJy. Combining archival data and previously published work, we provide a near-complete high-resolution image library of 73 protoplanetary (Class II) disks in the Lupus. This enabled us to measure dust disk radii down to a limit of 0.6 au and analyze intensity profiles using visibility modeling. *Results.* We show that 67% of Lupus protoplanetary dust disks have dust radii smaller than 30 au and characterize the newly discovered substructures in 11 disks with some of the shortest separation gaps. The size-luminosity relation, when accounting for the smallest disks, aligns well with a drift-dominated dust evolution scenario for the Class II Lupus disks. For the most compact disks, with radii of less than 30 au, we compared measured sizes and fluxes with a grid of radiative transfer models to derive millimeter-emitting dust masses, which ranged from 0.3 to 26.3 $M_\oplus$. Assuming that the detected substructures were dynamical effects of planets, we approximated the results of an interpolation to estimate planet masses and found a range of $20 - 2000\,M_\oplus$ with separations between 2 and 74 au. *Conclusions.* Our results indicate that two-thirds of the protoplanetary disks in Lupus are smooth, on scales larger than 4 au, and compact, with substructures being more prominent in the few larger disks. These compact disks are consistent with drift-dominated evolution, with their masses and optical depths suggesting that they may have already experienced some planet formation, with most of the small solids converted into planetesimals and planets. This makes them prime candidates, with optimal conditions, for

explaining the formation and origin of super-Earths.

5.1 Introduction

The field of protoplanetary disks has been revolutionized in the past decade with the sensitivity and spatial resolution of the Atacama Large Millimeter Array (ALMA) telescope. Significant efforts have been dedicated to studying the demographics of protoplanetary disks in recent years with ALMA, providing a broader perspective on disk evolution and enabling direct comparisons and statistical analyses of exoplanets in conjunction with protoplanetary disks (Zhang et al. 2018; Lodato et al. 2019; van der Marel & Mulders 2021). Early ALMA survey programs yielded valuable insights into dust evolution in protoplanetary disks through various disk relations (e.g., Pinilla et al. 2020) despite being taken at relatively low resolutions (~0.25"; Ansdell et al. 2016; Barenfeld et al. 2016; Cieza et al. 2019). Subsequent high-resolution observations (~ 0.04") focused on the brightest disks, which are often large and harbor numerous extended substructures (Andrews et al. 2018a; Cieza et al. 2021), usually associated with pressure bumps halting the radial drift through dust traps (Pinilla et al. 2012c). However, many disks remained unresolved in this initial reconnaissance, preventing a thorough investigation of the entire disk population.

The first discovery of a very small dust disk with high-resolution ALMA observations was XZ Tau B, with a dust disk size of only 3.4 au and potentially an inner cavity, located within a binary system of 39 au separation (Osorio et al. 2016; Ichikawa et al. 2021); this is consistent with predictions from radial drift in binary systems (Zagaria et al. 2021). The first small disk in a single star system studied at high resolution was CX Tau, analyzed by Facchini et al. (2019). They found no substructure but measured a dust disk radius of 14 au, which was five times smaller than the CO extent, indicating efficient radial drift. In subsequent years, several additional studies (Long et al. 2019; Kurtovic et al. 2021; van der Marel et al. 2022; Miley et al. 2024; Shi et al. 2024) identified an increasing number of compact disks, defined as having dust disk radii smaller than 30 au for the purposes

of this paper, which is also the size of Neptune's orbit. We have identified 33 such compact disks in the literature to date, a few of which show centrally cleared cavities. However, the size distribution and structural classification of disks within a single star-forming region remain limited due to the limited number of high-resolution observations and accurate measurements of the disk radii for the smallest disks, which often remain unresolved.

One of the most important yet incomplete relationships for the most compact disks and within single star-forming regions is the size-luminosity relation (SLR). Assuming that the relation is not primordial, meaning that low-mass disks are born small while high-mass disks are born large, current literature identifies three distinct slopes that define the behavior and evolution of disks within this relation. Dust grain growth in disks is limited by two main barriers (Birnstiel et al. 2012): the drift barrier, largely driven by radial drift (Weidenschilling 1977), and the fragmentation barrier, shaped by turbulence which causes grain collisions and destruction (Voelk et al. 1980). These barriers determine how disks evolve along the SLR. Rosotti et al. (2019) studied the SLR in the context of these two primary dust growth barriers, introducing two distinct slopes in this relation. The first is the drift-dominated slope, where a disk's position along the SLR is mainly influenced by its dust mass, which affects both its luminosity and radius. For disks with a smooth density profile, this slope follows $F_{mm} \propto R_{eff}^2$, where F_{mm} is flux and R_{eff} its disk size, which is typically defined as the radius enclosing a specified fraction (often 68% or 90%) of the total flux from the disk. However, in fragmentation-dominated disks, the slope becomes steeper, following $F_{mm} \propto R_{eff}$, as fragmentation increases the mass retained in the disk, increasing the flux for the same radius compared to the drift-dominated scenario, thereby altering the disk's position on the SLR. The third slope, described by Zormpas et al. (2022), is the trap-dominated slope, which implies that disks have strong dust traps. In this case, the SLR behaves differently compared to smooth, non-trap disks. This slope assumes that a disk begins its evolution with

a planet forming within it, which shifts its evolution along the SLR. The relation for these disks follows $F_{mm} \propto R_{eff}^{5/4}$, which is steeper than the drift-dominated slope but less steep than the fragmentation-dominated one. More recently, Delussu et al. (2024) continued this exploration, suggesting that even smooth disks might have hidden substructures. They were able to reproduce the observed $F_{mm} \propto R_{eff}^{2}$ slope by having optically thick high-flux and optically thin low-flux disks with substructures.

Several factors contribute to deviations from the SLR, as noted by Zormpas et al. (2022). Dust properties, such as variations in opacity or porosity, can shift a disk's position along the SLR by affecting its luminosity without changing its size. Additionally, the turbulence parameter α plays a significant role in modifying a disk's location on the SLR. Both factors are essential for the drift and fragmentation barriers, which in turn are key to determining dust evolution and growth. This highlights the importance of studying the SLR in greater detail and at the highest possible resolution, as recent research has done.

Furthermore, constraining disk parameters and extrapolating the SLR to the smallest disks results in disk sizes of only a few au which has significant implications for understanding dust substructures and the comparison with exoplanet populations. Recently, there have been several efforts to directly link exoplanet observations to the properties of their birthplace, the protoplanetary disks. Key parameters have been studied, such as the available bulk mass in protoplanetary disks to form giant and terrestrial exoplanets (Manara et al. 2018; Mulders et al. 2021b), as well as the connection between disk substructures and exoplanet demographics (Lodato et al. 2019; van der Marel & Mulders 2021; Zhang et al. 2023a). Specifically, van der Marel & Mulders (2021) aimed to understand whether disk substructures influence exoplanet formation scenarios or are linked to the observed disk dichotomy. Their work suggests that the majority of close-in rocky exoplanets around M stars likely formed in the more abundant smooth, compact disks in the absence of giant planets at wide orbits, which would have prevented radial drift (Mulders et al.

2021a). These compact disks can form planets, particularly super-Earths through pebble accretion, under the influence of substantial radial drift, concentrating sufficient material in the inner regions (Sanchez et al. 2024) under the assumption that the bulk of the initial dust mass in embedded disks (Class 0/I) decreases rapidly to the mass in the protoplanetary disk stage (Class II) through radial drift (Appelgren et al. subm.). However, due to the relatively low resolution of observations of protoplanetary disks, compared to the regions where most exoplanets are found, the relation between such disks and rocky exoplanets, if any, remains inconclusive.

In this work we present a near-complete high-resolution survey of 73 Class II protoplanetary disks in the young, nearby Lupus star-forming region. The Lupus region, part of the Scorpius-Centaurus association, consists of several subgroups (Lupus 1–9), each associated with distinct molecular clouds. It is a young (1–2 Myr) and nearby (150–200 pc) region, comparable in proximity and age to Taurus (Comerón 2008). This study is based on new ALMA continuum observations as well as ALMA archival data. We measure dust disk radii down to 0.6 au, fit radial profiles to determine substructures and study the relation between the disk flux density and its size. We discuss the observations and data reduction in Sect. 5.2, analyze the continuum visibilities to measure disk sizes and substructure in Sect. 5.3, and discuss the implication of our results and a comparison with a model grid in Sect. 5.4. We summarize our findings in Sect. 5.5.

5.2 Observations

Our data were obtained from Cycle 9 observations with ALMA in Band 6. These observations, with project code 2022.1.00154.S and PI Nienke van der Marel, were carried out in ten execution blocks between August 16, 2023, and September 11, 2023. The total observing time was 8.89 hours, with ~ 7.25 minutes spent on each source. In total, 33 sources were observed: Sz65, Sz66, Sz77, Sz72, Sz74A, Sz74B, J15592523-4235066,

J16002612-4153553, Sz130, Sz131, Sz81A, J16073773-3921388, J16075475-3915446, J16080017-3902595, J16084940-3905393, J16085324-3914401, J16085373-3914367, J16092697-3836269, Sz102, Sz106, Sz108B, Sz110, Sz113, Sz117, Sz88A, Sz88B, Sz90, Sz95, Sz96, Sz97, V1192 Sco, V856 Sco A, and V856 Sco B. The final datasets for each source include six spectral windows with frequencies in the range 219–234 GHz and a total bandwidth of 2 GHz each for the continuum, as well as six spectral windows in the range 220–231 GHz with a total bandwidth of 1.875 GHz dedicated to ^{12}CO and ^{13}CO line emission, all with a maximum recoverable scale between 0.37" and 0.715". Additionally, we incorporated archival ALMA data to complete the sample of Lupus disks at high resolution (project code: 2018.1.01458.S, PI: Yen, Hsi-Wei). These observations were conducted between July 18, 2019, and July 19, 2019, with a total integration time of 1.1 hours and a total of eight sources: Sz71, Sz69, J15450887-3417333, Sz98, Sz123A, Sz100, J16083070-3828268, and Sz73. These observations include six spectral windows to observe line emission, each with a bandwidth of 58.6 MHz, and only one spectral window for the continuum with a total bandwidth of 2 GHz, between 232 and 234 GHz. Finally, a Band 4 dataset was used for EX Lup, as no high-resolution observations were available at any other band (project code: 2017.1.00388.S, PI: Liu, Hauyu Baobab). These observations were conducted on November 11, 2017, covering a frequency range of 145 to 161 GHz, with a total integration time of 5.1 minutes. We searched for line emission to flag but found none, indicating only the presence of the continuum. However, these data were not used for any part of the analysis and served only to provide a high-resolution image of the source.

All datasets were calibrated using the pipeline and scripts provided by the ALMA staff. Version 6.5.4.9 of the Common Astronomy Software Applications (CASA; McMullin et al. 2007) was utilized to analyze and process the data, as well as to clean and create the final images. We separated the line and continuum emission spectral windows for each source and averaged the channels in the continuum spectral windows. Self-calibration

was attempted on the new datasets, but due to the limited observing time per source and the low signal-to-noise ratios (S/Ns), it was not possible to achieve satisfactory results. We used the TCLEAN task in CASA with the Multi-term Multi-Frequency Synthesis (MTMFS) deconvolver (Rau & Cornwell 2011), employing scales of 0, 1, 3, and 5 times the beam size to create the final images of each disk. Several weightings were tested depending on the source, and different weightings were selected from the datasets, as shown in Table A.1. Natural weighting emphasizes short baselines, improving sensitivity but at the cost of resolution. In contrast, uniform weighting gives more weight to longer baselines, maximizing resolution but reducing sensitivity and making the images noisier while Briggs weighting serves as a compromise between natural and uniform, balancing sensitivity and resolution. For each source, we selected the weighting that offered the highest resolution while maintaining sufficient sensitivity to capture and distinguish the entire disk structure effectively. For all sources, pixel sizes between 0.001 and 0.003 arcseconds were used to ensure the pixel size was approximately ten times smaller than the beam size for all images.

To complete the high-resolution Lupus disk sample, we supplemented our data with images obtained from several previous studies. These included Sz103, Sz76, Sz104, Sz112, J16011549-4152351, J16081497-3857145, J16000236-4222145, J16090141-3925119, and J16070384-3911113 from (van der Marel et al. 2022); HT Lup A, B, and C, GW Lup, IM Lup, RU Lup, Sz114, Sz129, and MY Lup from the Disk Substructures at High Angular Resolution Project (DSHARP; Andrews et al. 2018a; Kurtovic et al. 2018); GQ Lup from Wu et al. 2017; and Sz91 in Band 4 from Maucó et al. 2021. Additionally, we used RY Lup data from Francis & van der Marel 2020. For already resolved disks J16070854-3914075, Sz118, Sz84, as well as for two sources without high-resolution observations (J16102955-3922144 and J16000060-4221567), we used images from Ansdell et al. 2018. For V1094 Sco, we used the image presented in van Terwisga et al. 2018, and for Sz111, data from (Rota et al. in prep) (project code 2018.1.00689.S, PI:

Muto, Takayuki). Finally, RXJ1556.1-3655 and Sz133 data were sourced from Bosschaart et al. in prep (project code: 2022.1.01302.S, PI: Mulders, Gijs). The total sample consists of 73 disks in Lupus with all but 5 disks observed at very high angular resolution of $\lesssim$0.05". An overview of the characteristics of the images created in this paper is presented in Table A.1, with all the images of the disks shown in Figure 5.1. The most compact disks with radii < 0.15" are displayed on a smaller scale in Figure 5.2.

5.3 Results

5.3.1 Dust continuum images

In this sample of Class II Lupus disks with continuum images at high angular resolution we find a range of morphologies across all sizes. Although most substructures are detected in the more massive and larger disks, several compact disks also exhibit substructure, such as gaps and inner cavities. Given our resolution, which limits detection to structures as small as approximately 4 au (~ 0.03 arcseconds), we may still miss small inner cavities. With this in mind, the smallest cavity detected in the image plane is in Sz72, with a radius of 4.1 au, right at the edge of our resolution limit. Most disks are well resolved, however, a few remained only marginally resolved. Notably, Sz104, J16075475-3915446, J15592523-4235066, and J16084940-3905393 are very poorly resolved even at 0.03" resolution, which implies a radii of less than 2 au. J16080017-3902595 and J16000060-4221567 are also unresolved at 0.25" but lack the high-resolution data of the bulk of the sample.

In total, we resolved 11 new disks with substructures: 10 cavities (J16083070, Sz100, Sz123A, EXLup, Sz108B, Sz90, Sz72, Sz131, J16092697, and Sz96) and 1 very faint ring and gap (Sz73). We have a total of six resolved binary systems with disk detections and within the field of view of the observations; Sz66 - Sz65, Sz74A - Sz74B, V56ScoA - V856ScoB, Sz81A - Sz81B, J16085324 - 3914401-J16085373-3914367, and the HT-Lup

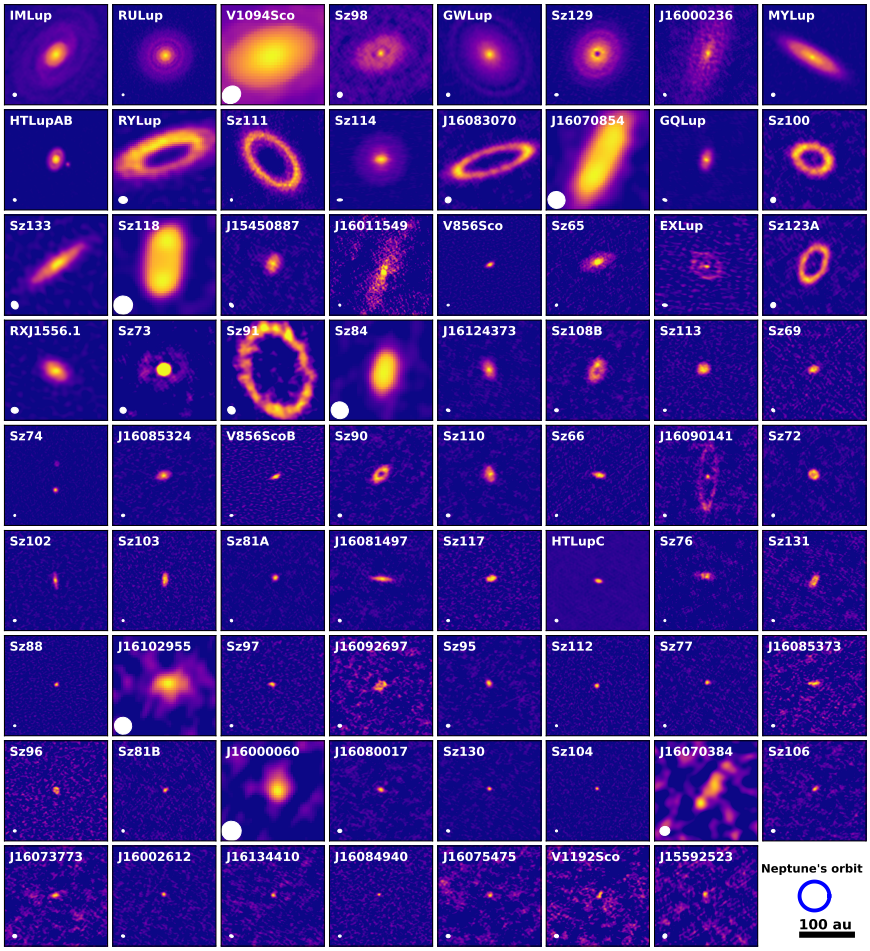


Figure 5.1: All protoplanetary disks in Lupus at high resolution from various projects and observations with ALMA (see Section 2), shown at the same spatial scale. The disks are arranged in descending order based on their total flux. The scale bar and Neptune's orbit in the final panel assumes that each disk is at a distance of 160 pc. Several cavities and substructures are observed, though the smallest disks are barely visible.

triple system. However, no disk detections were found in three additional well-known binaries: Sz88B, Sz108A, and Sz123B-C (Zurlo et al. 2021). The total flux for all targets is determined through aperture photometry, where

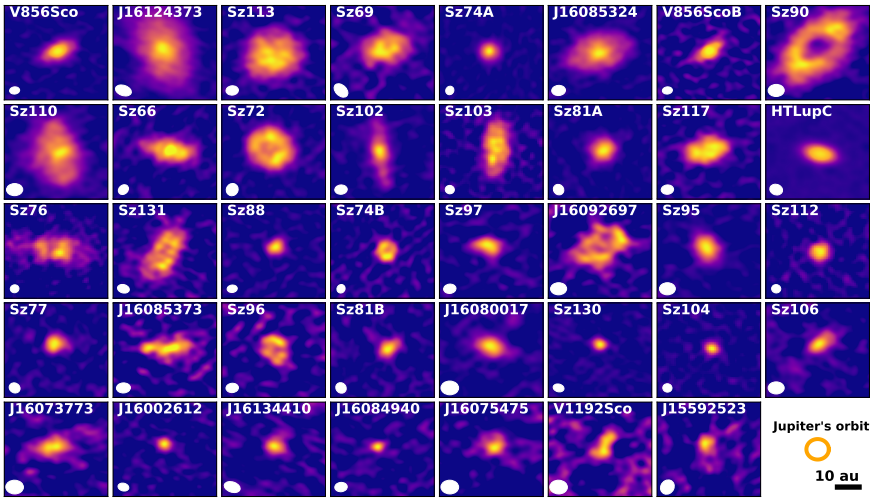


Figure 5.2: Zoomed-in view of the smallest disks in the Lupus molecular cloud. Some of these small disks exhibit substructure, although most appear featureless. The disks are arranged in descending order of their total flux, consistent with the disks shown previously in Fig 5.1. The scale bar and Jupiter's orbit in the final panel assumes that each disk is at a distance of 160 pc.

the aperture is extended until the flux flattens, and inclination corrections are applied. The uncertainty is calculated as the standard deviation inside each aperture. Most flux measurements fall within an 10% uncertainty range compared to those reported at a low resolution by Ansdell et al. 2018. Some discrepancies could arise from the absence of short baselines in our observations, potentially leading to the loss of extended emission flux. Overall, the fluxes appear consistent with previous results, meaning there is no need for a detailed reevaluation and we proceed to the analysis.

5.3.2 Visibility modeling

To analyze the exact orientation and morphologies of these disks, we used the GALARIO code (Tazzari et al. 2018) to model the visibilities of the observations with the best fit possible. We did not fit any features that

were not already visible in the continuum images. For all isolated disks, we computed the visibilities from an axisymmetric brightness profile using different models. For each model, we fitted the visibilities, V_{mod}, following the approach outlined in Tazzari et al. 2018. We explored the parameter space of each model using a Bayesian approach, employing the Markov chain Monte Carlo (MCMC) ensemble sampler provided by emcee (Foreman-Mackey et al. 2013). Each model generates a brightness profile, which is then transformed and compared to the observed visibilities. Posterior distributions are obtained by assuming a Gaussian likelihood. We employed three different models for the isolated disks, choosing the most simple structure we observed for each disk in the continuum images.

The first is a Gaussian like disk,

$$I(R) = I_0 \cdot \exp\left(-\frac{1}{2} \cdot \left(\frac{R}{r_c}\right)^2\right), \tag{5.1}$$

where I_0 is the peak intensity, R the radial distance from the center, and r_c the width of the Gaussian.

The second is a ring with different slopes on each side,

$$\begin{aligned} I(R) = I_0 \left(\left(1 - \Theta(R - r_{\text{ring}})\right) \exp\left(\frac{-(R - r_{\text{ring}})^2}{2(r_w a)^2}\right)\right) \\ + I_0 \left(\Theta(R - r_{\text{ring}}) \exp\left(\frac{-(r - r_{\text{ring}})^2}{2(r_w b)^2}\right)\right) \end{aligned}, \tag{5.2}$$

where I_0 is the peak intensity of the ring, r_{ring} the peak position of the ring, $r_w a$ the width of the ring on the inner side, $r_w b$ the width of the ring on the outer side, and Θ the step function:

$$\Theta(x) = \begin{cases} 1 & \text{if } x \geq 0 \\ 0 & \text{if } x < 0 \end{cases}. \tag{5.3}$$

With the first term active when inside the position of the ring peak, and

the second term when outside the position of the ring peak.

Regarding the third, only one disk, Sz 73, required a two-component model to describe an inner Gaussian and a faint ring. We modeled this disk as follows:

$$I(R) = I_0 \cdot \exp\left(-\frac{1}{2}\cdot\left(\frac{R}{r_c}\right)^2\right) + I_0 b \cdot \exp\left(-\frac{1}{2}\cdot\left(\frac{R-r_{\rm ring}}{r_{\rm width}}\right)^2\right), \tag{5.4}$$

where the left Gaussian describes a ring with $I_0 b$ as the intensity at the peak of the ring, $r_{\rm ring}$ as the radial position of the peak of the ring and $r_{\rm width}$ as the width of the ring.

For the binaries, we sampled a 2D image and computed the corresponding visibilities, rather than using a single radial profile. We adopted a method similar to that of Manara et al. (2019), where the visibilities of the two sources were summed and compared to a Gaussian likelihood to obtain the final visibilities. We used the previously described Gaussian model, where the total visibilities are expressed as the sum of the Fourier transforms of each of the Gaussian models. This is mathematically represented as follows:

$$V_{modT} = V_{modGauss1} + V_{modGauss2}. \tag{5.5}$$

For two of the three binaries in this study, we employed a model consisting of two Gaussian profiles, which were added together in the visibility plane. The model, $V_{modGauss1}$ is a function of the brightness profile parameters and includes an offset relative to the phase center of the image.

V856ScoA was a special case where we see significant flux even on the longest baselines indicating an unresolved point source in addition to a Gaussian disk. To account for this, we defined a combined model as follows:

$$V_{\rm modGauss1} = \mathscr{F}\left(I_0 \cdot \exp\left(-\frac{1}{2}\cdot\left(\frac{R}{r_c}\right)^2\right)\right) + \mathscr{F}\left(\delta(R)\right), \tag{5.6}$$

where $\delta(R)$ is defined as a Gaussian with an extremely small width, effectively approximating a delta function. For all the single disks, we used UVMODELFIT within CASA to obtain the initial parameter estimates. For the MCMC sampling, we employed between 48 and 120 walkers, running the chains for 2,000 to 30,000 steps to ensure convergence, with the binaries requiring more walkers and iterations to achieve satisfactory results. To verify convergence, we discarded the first 1,000 steps (burn-in phase) and examined the corner plots. The final model parameters are represented by the median of the posterior probability distributions for each parameter, while the uncertainties are given by the 16th and 84th percentiles.

Subsequently, we derived the total flux and dust disk radius from the modeled images. The results for the 38 sources modeled are presented in Table B.1 with the corresponding distribution of disk radii shown in Figure 5.4. We excluded Sz65, Sz66, J16083070, and Sz98, from the GALARIO analysis as these have been previously analyzed in Miley et al. (2024), Villenave et al. (2019), and Gasman et al. (2023). The corresponding model images are shown in Figure 5.3 and the visibility plots in Appendix D.

For most disks, the visibility fitting worked very well, but there were a few cases that required specific adjustments. The Gaussian model failed to capture the flux at the shortest baselines for Sz130, Sz77, and J16002612. In the case of Sz130, this resulted in a lower flux (41% lower) compared to the literature values. For Sz77 and J16002612, the model appeared to overestimate the flux by 9,7% and ~3%, respectively. It remains unclear whether these discrepancies are due to the low S/N of the observations or if a more complex emission pattern (potentially with a different orientation) is present that a simple Gaussian model cannot capture. For Sz130, the visibilities suggest the presence of some extended structure or emission that shows below 300 kλ, which we were unable to fit or determine its nature. Nevertheless, we opted to proceed with the model, as it represents only what we could directly observe.

Three disks were unresolved or only marginally resolved, J16075475,

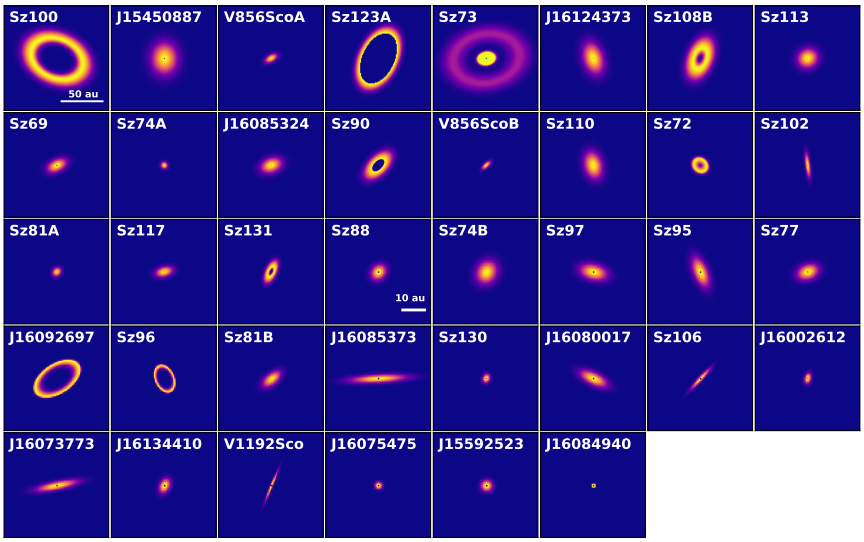


Figure 5.3: Best disk models obtained from the GALARIO visibility fitting. Note that the scale changes from Sz88 onward to better highlight the most compact disks. The disks are arranged in descending order based on their total flux derived from the visibility fitting.

J16084940, and J15592523. These disks exhibit extremely small sizes and very low surface brightness, leading to a low S/N. Consequently, even with visibility fitting, the inclination and position angle (PA) could not be reliably determined. To improve the fitting of other parameters, the inclination and PA were fixed to face-on values. As a result, the radius measurements for these sources should be interpreted with caution. However, the overall fit remained satisfactory, and we retained these results for analysis and discussion in this paper. In the same case, we were unable to fit the PA of J15450887-341733, which best fit was between 0.0 or 180 degrees. To obtain a plausible result, we fixed the PA to 0.0.

The faint ring in Sz73 was not detected during the initial imaging process with CASA, but became apparent when analyzing the visibilities. However, we concluded that this is unlikely for many sources, as nothing was evident in the visibilities. Even the faint ring in Sz73, with surface

brightness between 0.2 and 0.4 mJy, was detected above the 3-σ level. Naturally, this depends on the observation brightness and the rms, but this means that fainter rings below this threshold would remain undetected.

In the Herbig star V856ScoA disk, a point source of strong emission is observed. The origin of this emission remains unknown and further discussion is needed. This emission, was detected at first only in the visibility plots, where the emission at long baselines never approaches zero, but it is observed in the continuum image. A model combining a Gaussian with a very narrow Gaussian successfully reproduced this feature, indicating that the emission is quite intense. Possible explanations include free-free emission from the central star's outflow or wind emission from the disk near the star.

The Sz74 binary system shows a small substructure in the disk around its companion (Sz74B), potentially indicative of a cavity accompanied by a ring or asymmetry. However, due to insufficient resolution, it was impossible to constrain the size of the cavity or determine the disk's PA, complicating the fitting process. To achieve a better fit, we opted to model the system using two Gaussians, as the substructure could also result from binary interactions, such as the formation of a vortex or a dust pile in the disk. While this approach improved the fit for the binary, the asymmetry remained un-modeled, and the PA was still unconstrained, suggesting the source was very unresolved. Similarly, five additional disks (Sz113, Sz69, Sz103, and Sz117) also show signs of cavities but were only fitted with a Gaussian profile since they were facing the same issue as Sz74B. Higher-resolution observations of these systems are necessary to confirm the origin of asymmetries, to better constrain the disk's orientations or the potential presence of a cavity.

5.3.3 Disk size and substructure distribution

The GALARIO visibility fitting allows us to explore the size distribution of disks in the Lupus star-forming region at much smaller scales than previ-

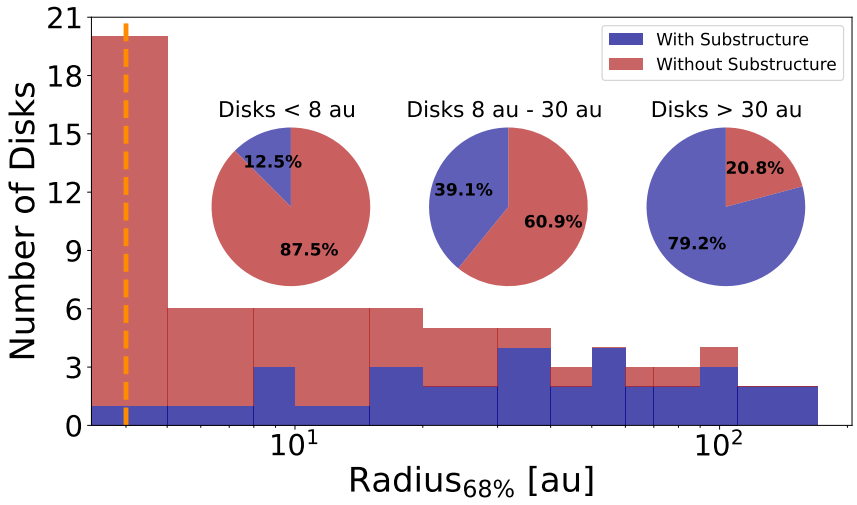


Figure 5.4: Size distribution of the Lupus disks. Disks exhibiting substructures in the continuum images are shown in dark blue, while smooth disks without visible substructures are depicted in red and added on top of the blue histogram. The pie charts inside the plot show the percentages of disks with and without substructures for sizes above and below 30 au. The vertical dashed orange line indicates our resolution limit, which is set at 0.03" (4 au). More than 67% of the sample belongs to the compact disks classification.

ous works. We define disk sizes as the radius where the cumulative flux equals 68% of the total flux (Andrews et al. 2018b; Tripathi et al. 2017). The histogram in Figure 5.4 shows a broad range of disk radii up to ~160 au and a marked increase at sizes smaller than 20 au. We find that two thirds of the disks are compact, with radii < 30 au. On the other hand, the majority of disks with large radii exhibit substructures, specifically at radii ~> 30 au, although they are relatively few in number. However, as we approach the resolution limit (indicated by the dashed orange line in Figure 5.4, the number of smooth disks increases significantly. This is expected, as we would not anticipate resolving any substructures at approximately three times the resolution limit, which is about 12 au. Consequently, while we

can now better measure disk sizes and note an increase in the number of smaller disks, there remains insufficient resolution to discern whether a trend exists that correlates disk size with substructure occurrence. In fact, the better the resolution, the fewer smooth disks appear in observations, which points to a potential bias introduced by resolution wherein very small substructures may remain undetected in the smallest disks. For large disks with $R_{dust} > 30$ au, approximately four-fifths exhibit substructure detectable down to scales of 7 au. Conversely, in the compact disks, at most 72% (5 out of 7) are smooth, with substructures down to scales of 4 au. Considering all disks in the sample, the data suggest that about 3 out of 8 exhibit substructure, regardless of disk size.

We plot the disk radii versus their total flux density (scaled to 160 pc) in Figure 5.5. There is a clear relationship between the two observables and we apply a Bayesian linear regression method implemented in the LINMIX package (Joshua E. Meyers, Kelly 2007),

$$\log_{10}(R_{68}) = \alpha + \beta \log_{10}(F_{\rm mm}). \tag{5.7}$$

The fitted values are an intercept (normalization) $\alpha = 0.66 \pm 0.06$ and slope (power law index) $\beta = 0.61 \pm 0.06$, with an intrinsic dispersion of 0.116 ± 0.02.

This relation can indicate whether dust evolution is dominated by drift or by traps being present in the disk (Rosotti et al. 2019; Zormpas et al. 2022). The observed slope falls between the drift-dominated and the trap- and frag-dominated regimes, which is consistent with previous findings by Andrews et al. (2018b) and Hendler et al. (2020). Notably, a few disks lie significantly below the SLR of Lupus. Most of these disks are in binary systems (star markers in Fig. 5.5), and the interaction between companions likely truncates their radius, as discussed in Rota et al. (2022), affecting their position on the SLR. Another exception is RU Lup (square in Fig. 5.5), one of the most active T Tauri stars, which likely experiences increased flux caused by its strong accretion features (e.g., Gahm et al.

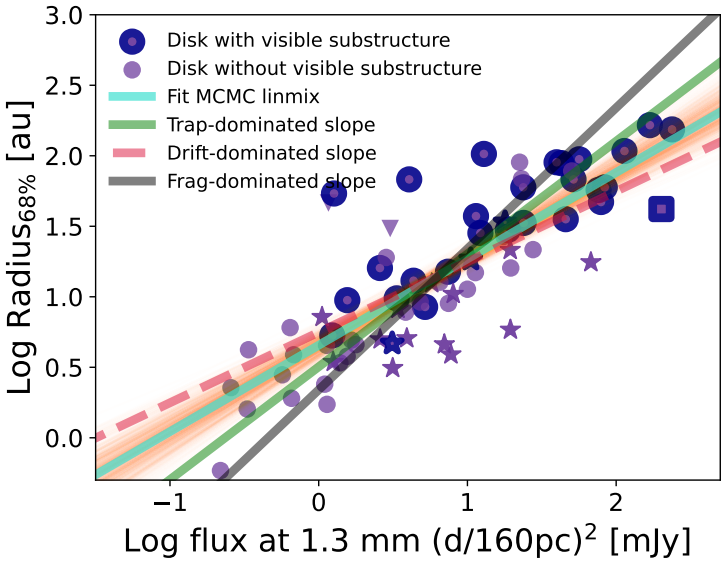


Figure 5.5: SLR for the Lupus star-forming region at high resolution. Disks with substructures are marked by purple circles outlined in dark blue, while smooth disks are represented by solid purple circles without outlines. Unresolved disks are indicated by downward-pointing triangles. Binary disks are marked with star symbols, and RU Lup is identified with a square marker for clarity. The drift-dominated slope, as described by Rosotti et al. (2019), is illustrated by the dashed red line, the trap-dominated slope (Zormpas et al. 2022) in green, and the frag-dominated slope in black. Our fit, using the LINMIX package, is displayed in turquoise. All disks are normalized to a common distance of 160 pc for consistency.

2008; Siwak et al. 2016), placing it below the SLR as well. Of the five disks that appear high above in the SLR, two (J16102955-3922144 and J16000060-4221567) have only been observed at low resolution (Ansdell et al. 2018); therefore, their radius might be overestimated. The other three disks have large cavities and may be more evolved. As mentioned by Zormpas et al. (2022), the presence and location of planets within a disk can alter the SLR by influencing the disk's evolutionary path. Given that the SLR represents only a snapshot of a cluster, with a diverse mix

of stellar masses and angular momenta, it remains challenging to draw definitive conclusions about the outliers.

5.3.4 Radiative transfer modeling

While disk dust masses are usually calculated using a linear relation with the millimeter-flux (e.g., Ansdell et al. 2018), this relation relies on the assumption that the dust continuum emission is optically thin. The existence of very small disks raises questions about how well we can determine their disk masses as the optical depth may be very high. We therefore created a large grid of models to calculate the expected total flux densities for different stellar parameters and disk masses spanning the range of observed radii. We performed radiative transfer at 1.3 mm for the generic protoplanetary disk model in the RADMC-3D software package (Dullemond et al. 2012) with a dust density distribution,

$$\rho(r,z) = \frac{\Sigma(r)}{\sqrt{2\pi}H_p} \exp\left(-\frac{z^2}{2H_p^2}\right), \tag{5.8}$$

where r represents the radial distance from the star, $H_p(r)$ is the disk vertical scale height, and $\Sigma(r)$ is the dust surface density,

$$\Sigma(r) = \Sigma_0 \left(\frac{r}{r_{\rm out}}\right)^{-1}, \tag{5.9}$$

defined out to an outer radius $r_{\rm out}$.

We produced a grid of 1728 models, varying three key parameters: 12 disk dust masses, 12 radius, 12 stellar luminosities ($L_\odot$). These parameters ranged from 4e-6 to 5.1e-3 $M_\odot$, 0.5 to 30 au, 0.0025 to 3 $L_\odot$, with values spaced in a log-uniform manner, respectively. Unsurprisingly, the star's effective temperature has a minimal impact on the flux-derived dust mass of the models as the absorbed stellar radiation is fully reprocessed by the disk to an equilibrium that is determined only by the energy input and dust distribution; therefore, we did not include it in the parameter space.

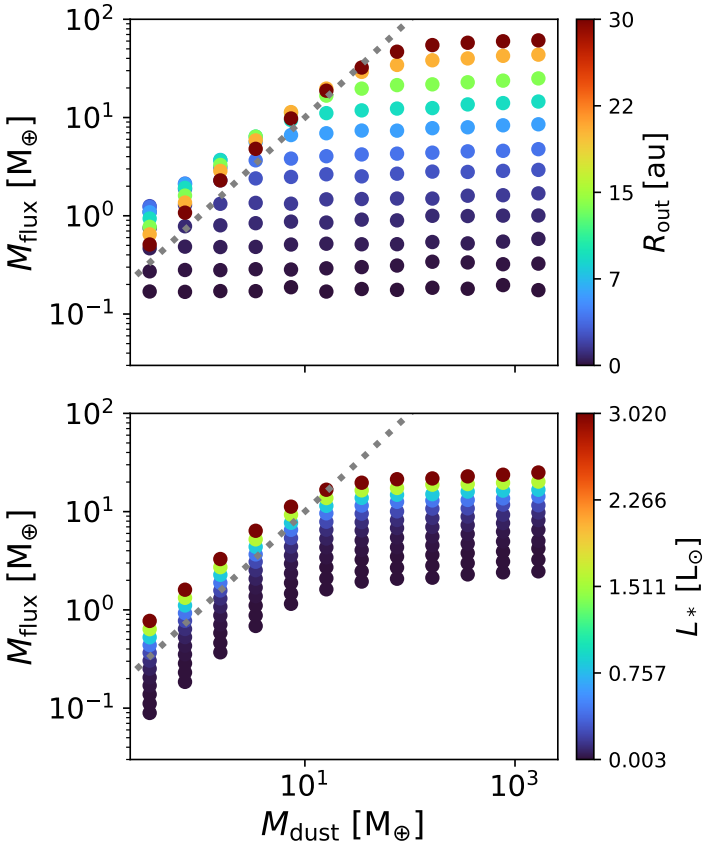


Figure 5.6: Comparison of the disk dust mass from a grid of 1728 models versus the mass derived from flux for the same models. In the top panel, stellar luminosity and effective temperature are fixed, illustrating how disk radius varies with flux and dust mass (see the colorbar with the radius values). The bottom panel shows the effect of changing stellar luminosity while keeping the disk radius and effective temperature constant. The dotted gray line highlights the masses from the flux that equal the disk dust mass introduced in the models.

The parameter limits were based on Alcalá et al. (2017) for Lupus sources, later updated using Gaia DR2 distance corrections as described in Alcalá et al. (2019). The stellar parameters of the Lupus sources, where known,

are provided in Tables C.1 and C.2.

To calculate the dust opacities needed inside RADMC-3D, we utilized the `optool` software (Dominik et al. 2021) with DSHARP opacities (Birnstiel et al. 2018). The dust opacity values were calculated using grain sizes from $a_{\rm min} = 0.050\mu$m to $a_{\rm max} = 3$ mm, incorporating the full scattering matrix.

For each model, we created a ray-traced image assuming a distance of 160 pc and a face-on disk inclination and measured the total flux and R_{68} radius in the same way as for the observations. We first compared the disk masses as derived from the simulated flux, $M_{\rm flux}$, with the model input, $M_{\rm model}$, in Figure 5.6. For the former, we applied the optically thin approximation for dust mass at 1.3 mm simplified in Ansdell et al. (2018),

$$M_{\rm flux} = \frac{F_\nu d^2}{\kappa_\nu B_\nu(T_{\rm dust})} \simeq 0.68 \left(\frac{d}{160{\rm pc}}\right)^2 \left(\frac{F_{1.33{\rm mm}}}{\rm mJy}\right) M_\oplus \tag{5.10}$$

where the dust opacity, $\kappa_\nu = 2.3\,{\rm cm^2\,g^{-1}}$ (Beckwith et al. 1990), B_ν is the Planck function, and we assume a uniform dust temperature, $T_{\rm dust} = 20$ K.

Figure 5.6 primarily highlights the saturation of the disk flux as the emission becomes optically thick, demonstrated by how the models deviate from the dashed gray line, which indicates equality of $M_{\rm flux}$ and $M_{\rm dust}$. Indeed, the flux-derived mass scales in a systematic way with the stellar luminosity for each input mass. Small disks saturate at lower disk masses than larger disks due to their much higher average optical depths.

Motivated by this behavior, we fit power laws to the model grid away from the saturated region, defined through the mean optical depth,

$$\bar{\tau} = \kappa\bar{\Sigma} = \frac{\kappa M_{\rm dust}}{\pi R_{\rm out}^2} \simeq 19.4 \left(\frac{M_{\rm dust}}{M_\oplus}\right)\left(\frac{R_{\rm out}}{\rm au}\right)^{-2}, \tag{5.11}$$

which holds independently of the surface density profile and the normalization is for our mean observing wavelength, 1.33 mm. For very optically

thin emission, $\bar{\tau} < 0.25$,

$$M_{\rm flux} \simeq 7 \left(\frac{R_{\rm out}}{1\,{\rm au}}\right)^{-0.5} \left(\frac{L_*}{1\,L_\odot}\right)^{0.3} M_{\rm dust}, \tag{5.12}$$

to within 10%. As $\bar{\tau}$ increases, the behavior begins to deviate from a linear dependence on $M_{\rm dust}$ and is a more complicated function of radius and luminosity. For optically thick emission, $\bar{\tau} > 1$, the mass dependence is so weak that the flux is no longer a reliable measure of dust mass. This presents a chicken and egg problem because we do not know how accurately we can determine the disk mass without knowing the optical depth and vice versa. However, the SLR provides a way forward.

5.3.5 Dust mass estimates

As shown in Sect. 5.3.3, our survey of compact disks extends the SLR to much lower disk radii than previous work. For a given stellar luminosity, our model grid calculates the flux for a given disk mass and radius. We then invert this relationship to map the disk mass on the flux-radius plane in Figure 5.7, which allows a direct comparison with the two principal observables in our survey.

The locus of the model shifts horizontally with the stellar luminosity but in principle, this allows the disk mass to be estimated from our model. Relatively large, faint disks have low $\bar{\tau}$ and the millimeter flux scales with the mass. However, disks that are relatively bright for their size may be optically thick and very massive. A handful of outliers that lie on or beyond the yellow region of this plot are binaries with relatively low radii for their flux due to tidal truncation and are not well represented by our models. However, most disks lie in the regime of intermediate optical depth, $0.25 < \bar{\tau} < 1$, where radiative transfer modeling is necessary to determine their dust mass.

The observations extend in the same direction as the $\bar{\tau}$ contours. For small optical depths, the flux is proportional to mass so, based on equation 5.11, this is similar to the relation found by Andrews et al. (2018b)

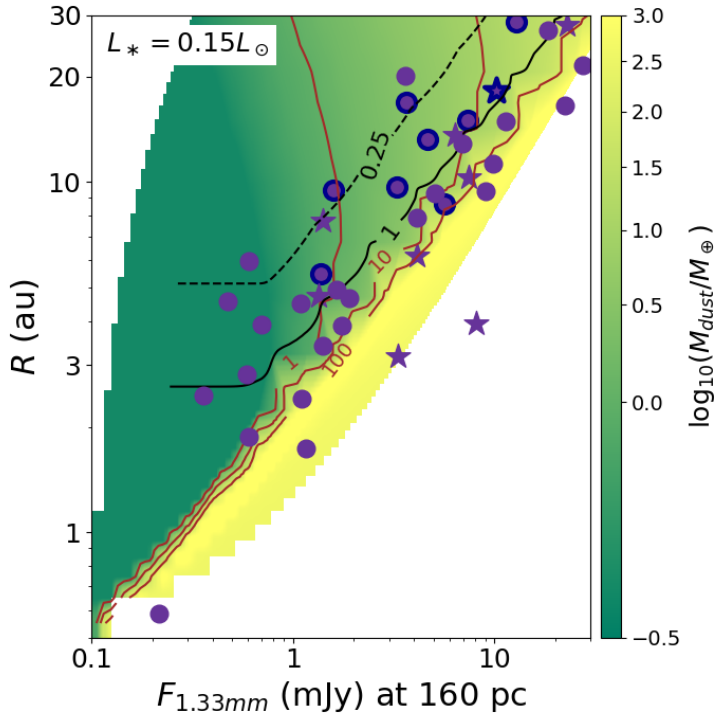


Figure 5.7: Comparison of the model grid with observed disk radii and total flux (normalized to 160 pc). The image represents the model dust mass on a log scale (also in brown contours), and the black contours show the mean optical depth, $\bar{\tau}$, defined in equation 5.11, with values of 0.25 and 1. The dark blue edges indicate a visible substructure in this source and a star-shaped marker distinguishes binary disks.

who found that the millimeter luminosity scales with the disk surface area. They suggested a possible explanation in which the emission comes from optically thick substructures with a filling fraction of ~ 0.3.

Using the stellar luminosities tabulated in Appendix C , we can create a bespoke radius-flux grid for each disk and thereby determine its dust mass. The uncertainties in each observable are readily propagated through. Several disks lie at the edge of their grids (Sz74A, Sz113, Sz102, J16084940-3905393, J15450887-3417333, Sz81A, Sz112, Sz88, Sz69, Sz130, HT LupA,

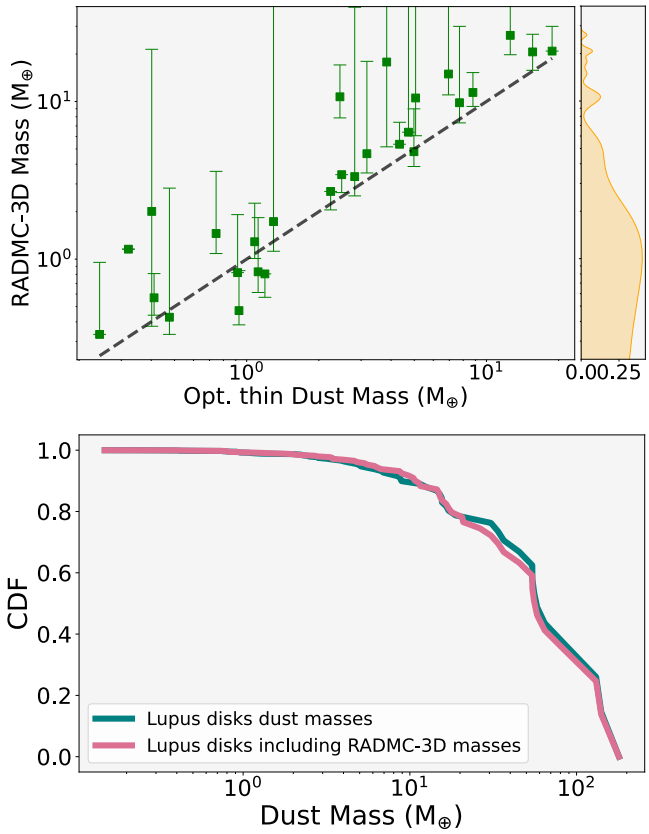


Figure 5.8: Top panel: Masses of the compact disks in Lupus (R < 30 au). These masses were obtained through the RADMC-3D model grid for $\tau < 5$. The dashed black line indicates where the RADMC-3D dust mass equals the optically thin dust mass calculation (see Eq. 10). Top-right panel: Kernel density estimation of the disk dust masses. Bottom panel: Cumulative distribution functions (CDFs) of all the disk masses in Lupus, using two approaches: in teal, all masses are estimated with the optically thin approximation based on flux values (Eq. 10), and in pink, we substitute the masses with values derived from our model grid where available.

Sz104, J16002612-4153553, and J16085373-3914367) due to being part of a binary system, having a poorly constrained luminosity, or being highly

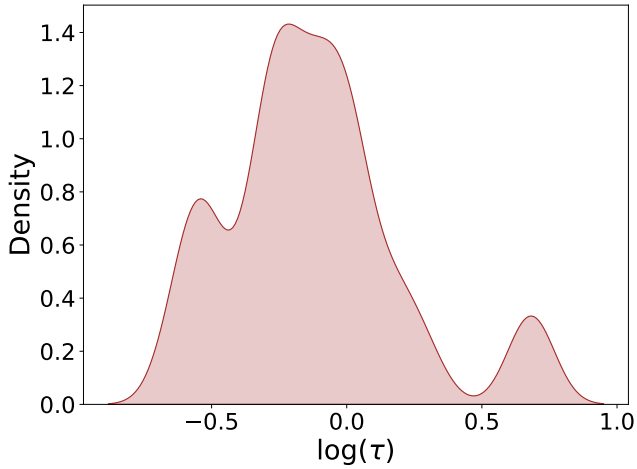


Figure 5.9: Optical depths of the Lupus disks using a kernel density estimation for points with radii < 30 au and obtained through Eq. 5.11 and the grid measurements.

optically thick with $\bar{\tau} \gg 5$, resulting in inferred masses that were either indeterminate or exceptionally large with substantial uncertainties. The distribution of dust masses for the 28 disks with well determined values and known luminosities and the cumulative distribution of all Lupus disks are presented in Figure 5.8 and Table 5.1. Additionally, the τ values are plotted in Figure 5.9.

5.3.6 The exoplanet population in the Lupus substructures

To gain insight into the potential exoplanet population within the Lupus protoplanetary disk sample, we estimated the planetary masses that could dynamically cause each of the observed gaps. We employed DBNets, a deep-learning tool that utilizes convolutional neural networks to analyze observations of dust continuum emission and predict the mass of the gap-opening planets, as developed by Ruzza et al. (2024). DBNets takes several inputs: the continuum emission image of the disk (in the form of a FITS file), the center of the image (in pixels), the disk's orientation

Table 5.1: Dust masses and optical depths for a subsample of 28 Lupus disks.

Source	Dust Mass [$M_\oplus$]	τ
J16124373-3815031	$9.8^{+20.1}_{-2.5}$	0.86
Sz117	$3.3^{+36.3}_{-0.8}$	1.03
Sz110	$6.4^{+92.6}_{-0.0}$	0.75
J16134410-3736462	$2.0^{+19.4}_{-1.6}$	5.00
J16080017-3902595	$1.5^{+2.1}_{-0.4}$	1.40
Sz95	$0.8^{+1.0}_{-0.2}$	0.67
J16073773-3921388	$0.6^{+0.2}_{-0.1}$	0.31
J16085324-3914401	$10.5^{+1030.6}_{-4.5}$	1.93
Sz97	$1.7^{+176.7}_{-0.6}$	1.56
Sz77	$0.8^{+0.0}_{-0.2}$	1.03
Sz106	$0.4^{+2.4}_{-0.1}$	0.54
V1192Sco	$1.2^{+0.0}_{-0.0}$	1.07
Sz81B	$0.8^{+1.1}_{-0.0}$	0.72
J15592523-4235066	$0.3^{+0.6}_{-0.0}$	1.07
Sz108B	$14.9^{+961.3}_{-3.9}$	0.87
J16092697-3836269	$1.3^{+1.0}_{-0.3}$	0.28
Sz72	$17.8^{+47.3}_{-12.6}$	4.63
Sz90	$4.8^{+4.2}_{-0.9}$	0.41
Sz96	$0.5^{+0.4}_{-0.1}$	0.31
Sz131	$2.7^{+0.0}_{-0.6}$	0.55
Sz66	$5.4^{+2.0}_{-0.0}$	0.56
Sz65	$20.6^{+6.1}_{-4.9}$	0.51
Sz76	$3.4^{+0.0}_{-0.8}$	0.23
Sz103	$4.7^{+13.3}_{-1.1}$	0.52
J16081497-3857145	$10.7^{+6.3}_{-2.8}$	0.51
Sz73	$11.4^{+3.8}_{-2.1}$	0.27
GQLup	$20.9^{+9.1}_{-0.0}$	0.87
RXJ1556.1-3655	$26.3^{+15.7}_{-6.5}$	0.69

These disks have radii < 30 au, which fit within our model grid.

Table 5.2: Gap centers and planet mass estimates for the subsample of Lupus disks with substructures.

Source	Gap center [au]	Planet Mass [$M_\oplus$]
*Sz108B	4.03	$66.7^{+130.6}_{-47.6}$
J16092697-3836269	4.78	$38.3^{+22.3}_{-15.8}$
*Sz72	2.04	$200.0^{+370.5}_{-146.8}$
*Sz90	4.57	$520.6^{+581.5}_{-289.5}$
Sz96	2.73	$98.5^{+60.6}_{-41.5}$
Sz123A	16.22	$763.8^{+251.2}_{-181.6}$
Sz100	13.59	$143.5^{+47.8}_{-38.4}$
*Sz131	2.33	$98.5^{+171.2}_{-70.2}$
Sz73	17.3	$237.6^{+139.9}_{-96.3}$
J16083070-3828268	38.5	$2008.3^{+743.8}_{-566.5}$
Sz98	16	$130.3^{+70.1}_{-51.0}$
*Sz98	88	$133.4^{+121.7}_{-67.5}$
*Sz76	2.11	$70.2^{+105.7}_{-46.8}$
RYLup	25	$1306.0^{+854.7}_{-511.6}$
*Sz91	26.3	$897.6^{+3413.6}_{-646.5}$
J16090141-3925119	32	$184.6^{+133.5}_{-79.6}$
Sz111	27.5	$855.4^{+274.0}_{-213.8}$
Sz129	41	$50.4^{+28.7}_{-19.0}$
RULup	29	$92.3^{+50.8}_{-31.8}$
IMLup	117	$66.9^{+51.4}_{-27.0}$
Sz114	24	$19.1^{+12.4}_{-9.1}$
GWLup	74	$44.6^{+35.1}_{-20.0}$

Of these disks, 11 are from our new observations, while 5 were obtained from FITS files of other projects. The final 5 disks have the values taken from Ruzza et al. (2024). * *Due to the high uncertainties exceeding DBNet's rejection threshold, the planet masses for these disks should be interpreted with caution.*

(inclination and PA), the distance to the source, and the position of the planet (in astronomical units), which corresponds to the center of the gap being studied. In total, we analyzed 25 substructures within our sample. For well-studied disks such as RULup, IMLup, Sz129, Sz114, and GWLup, we used the planet masses already estimated in Ruzza et al. (2024).

For the remaining 16 disks and 17 substructures, we ran the code using the continuum FITS files provided in Section 2 (11 from the new images and 5 from other projects). For cavity positions we used $\frac{r_{\rm ring}-r_w a}{2}$ while for the only gap, we used $\frac{r_{\rm ring}-r_{\rm width}+r_c}{2}$. Inclinations and PAs, which were not obtained in Section 3 of this paper, were sourced from previous studies. Specifically, for Sz98, we adopted values from Gasman et al. (2023), for J16083070-3828268 from Villenave et al. (2019), for Sz91 from Maucó et al. (2021), and for Sz76 and J16090141-3925119 from van der Marel et al. (2022). For RYLup and Sz111, we referred to van der Marel et al. (2018). The results, obtained for a range of α-turbulence values between $10^{-2}-10^{-4}$, including predicted planet masses, their radial positions, and whether the uncertainties exceed DBNet's rejection threshold, are summarized in Table 5.2. It is important to note that this rejection threshold defines the significance of the results, meaning these values should be interpreted with caution. Additionally, in Figure 5.10 we show the full population of known exoplanets around M and K stars (sourced from the NASA Exoplanet Archive in November 2024) alongside our predicted exoplanet population in the Lupus star-forming region. Most exoplanets in the archive were discovered via radial velocity (RV), providing minimum mass values (Msini), and transit timing variations, which yield more precise masses when combined with RV data. The disk dust masses obtained in the previous section, where applicable, and the dust masses derived from the flux for the larger disks are plotted at the bottom of Figure 5.11 together with the planet masses for comparison. Moreover, we show the ring peak position beyond each gap and gap widths (this work and the DSHARP disks; Zhang et al. 2018) at the top of Figure 5.11. From Table 5.2 we see that the range of inferred planet masses in Lupus, $\sim 20-2000\,M_\oplus$,

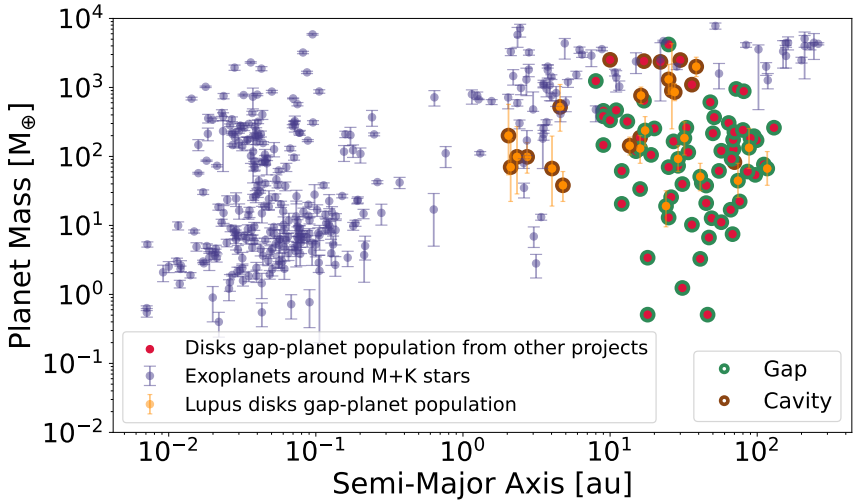


Figure 5.10: Lupus exoplanet masses obtained using DBNets plotted against the semimajor axis, assuming that the gaps are carved by planets. In blue, we show all observed exoplanets around M and K stars from the NASA Exoplanet Archive catalog, while the orange markers represent estimates for the Lupus sample. Brown outlines indicate cavities as the type of substructure, while green outlines denote gaps and rings. Additionally, planet mass estimates from Zhang et al. (2023a), Huang et al. (2024a), and Ruzza et al. (2024) are highlighted in crimson circle markers.

is comparable to similarly derived estimates from observations of disks in Taurus (Zhang et al. 2023a) and the σ Orionis cluster (Huang et al. 2024a). In addition, our high-resolution images reveal gaps at such small radii that the inferred planets overlap with the cluster of RV-detected exoplanets.

5.4 Discussion

5.4.1 New insights into the substructures and origin of compact disks

Our high-resolution compilation of the Lupus disk population shows a large number of compact disks with a relatively small fraction of substruc-

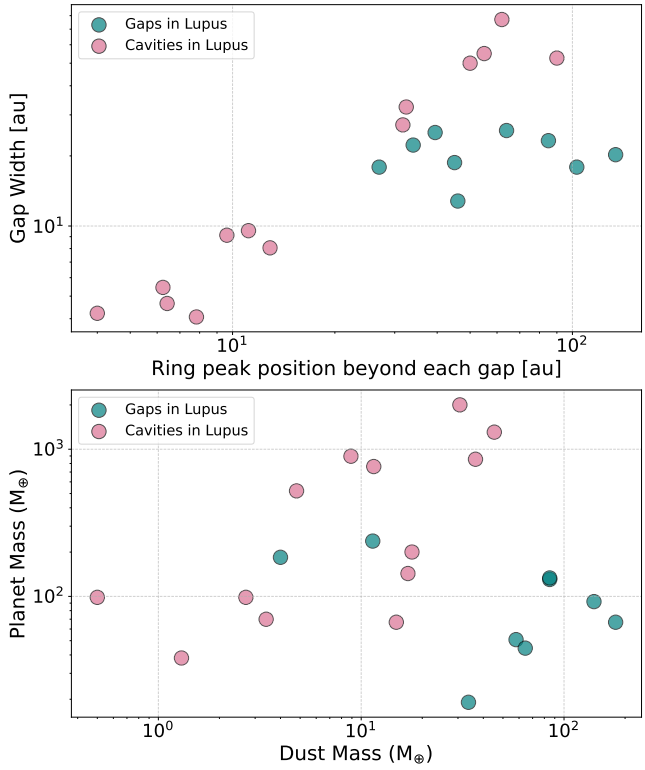


Figure 5.11: Top panel: Gap widths and locations of the ring peaks beyond each gap in our disks, as well as the DSHARP disks (Zhang et al. 2018) in Lupus. Gaps are shown in teal, and cavities in pink. Bottom panel: Disk dust masses versus planet masses from the DBNets analysis, using the same colors to denote the substructure type.

tures, whereas substructures are common in large disks with radii > 30 au, with 79% of them displaying rings or gaps (19 out of 24). However, since the majority of Lupus disks are compact, this fraction may not be representative of the entire disk population. Many previous studies have shown that initially featureless disks reveal greater complexity when the resolution is increased (Long et al. 2019; Kurtovic et al. 2021; Shi et al. 2024; Yamaguchi et al. 2024). Here, we have detected new substructures, mainly cavities down to 4 au in radius, but only in 24% of the compact disks,

excluding those that remain unresolved even in the visibility analysis.

Most of the structured compact disks show cleared cavities rather than rings, with the notable exception of Sz73. At a lower resolution, van der Marel et al. (2018) found that 15%[1] of the Lupus disk population show large cavities of > 20 au radius. Our high-resolution survey increases the resolved transition disk fraction to 24.6% (18 out of 73), including cavities down to 4 au radius.

Sz73 is the sole structured compact disk with a ring. This is faint, between 0.2 and 0.4 mJy, but should be detectable in most of the other disks in the survey. Furthermore, by utilizing GALARIO, we reduced analysis biases and are therefore reasonably confident that there are few, if any, other Sz73-like objects in Lupus.

Our results thus confirm that many of the unresolved disks from Ansdell et al. (2018) are in fact very compact, consistent with the hypothesis from van der Marel & Mulders (2021). They speculate that disks that did not form giant planets early on, and thereby did not halt the pebble drift, will rapidly become compact, following dust evolution models (Pinilla et al. 2020, Appelgren et al. subm.). Subsequently, Sanchez et al. (2024) demonstrated that such drift-dominated disks are capable of producing the close-in Super-Earth population around M dwarfs through pebble accretion.

The observed properties of the compact disks in Lupus are consistent with this scenario. Most of our compact disks (73%) are found around M-type stars, with only 14% around K-type stars (The rest do not have a determined Spectral type). However, this distribution reverses in larger disks: 50% are around M-type stars, but already 41% hosted by K-type stars. Furthermore, Sanchez et al. (2024) showed that the disk dust masses in their models are a few $M_\oplus$ and a few au in size after 1-2 Myr due to the inward drift in combination with inner planet formation through pebble accretion. The observed dust masses are in that case the remnant

[1] This is recalculated (11/73) for the total number of confirmed Lupus members: van der Marel et al. (2018) reported 11% (11/96).

of planet formation and not representative for the solid mass budget for planet formation. A fraction of the formed planets in their simulations reach pebble isolation mass, creating small dust traps, which may be the explanation for some of the observed small cavities in compact disks. While forming wide gaps in the first 10 au of the disk is challenging, Kuwahara et al. (2024) proposed that low-mass planets could carve such gaps in the inner disk (<10 au), with widths as large as their position. For compact disks without observed substructure, either planets have not reached pebble isolation mass or they are located so close in that the dust traps remained unresolved. Predictions of the exact scenarios for individual compact disks will be explored in a follow-up study (Guerra-Alvarado et al. in prep.).

Also, in the sample of large, well-resolved disks in Lupus, there are several disks that do not show substructure (~25% of the disks with radius > 15 au) (e.g., J16011549, J16000236, Sz133, Sz65, RXJ1556.1, GQ Lup, J16081497, J15450887, and HTLupA). Ribas et al. (2023) identified a disk around MP Mus without any substructure at 4 au resolution and proposed that in such evolved systems, large grains should have drifted onto the star unless some mechanism was preventing this. This means that substructures could remain undetected due to high optical depth at 1.3 mm or the substructures could be smaller than the current resolution limits of the observations. This could also be the case for some of the disks in the Lupus sample. An alternative possibility for the lack of substructure could be that the gas surface densities are high enough to drag the millimeter-emitting dust grains along such that there is little radial drift. If this were the case, the total disk masses would be $\sim 10-20\%$ of the stellar mass, near the limit of gravitational stability (Williams et al. 2024) and the mass of millimeter-emitting dust grains is a small fraction, $\sim 5-10\%$, of the total solid mass. Testing this scenario requires more sensitive CO observations to measure the gas disk radius.

For compact disks specifically, Tong & Alexander (2025) found that such disks can form in magnetorotational-instability-active regions be-

yond the dead zone. In these regions, and particularly below ~6 au, dust traps are ineffective, and the optical depth of the dust emission obscures disk substructures.

5.4.2 Size-luminosity relation

The millimeter luminosity in Lupus, which increases with radius as $R_{68}^{1/\beta}$ where β = 0.61+/-0.06, is consistent with the findings of Andrews et al. (2018b) and Tripathi et al. (2017) for a compilation of disks, as well as with Hendler et al. (2020) for Lupus. These results align with the drift-dominated scenario described in Rosotti et al. (2019). This also agrees with the super-Earth formation scenario from Sanchez et al. (2024), which requires significant radial drift. There is no clear distinction in the SLR for disks with or without observed substructures, as their radii and millimeter fluxes appear scattered. When fitted independently, we found that the slope of disks with substructures (β = 0.47+/-0.09) is the same as for disks without substructures (β = 0.55+/-0.08) within the error bars, and the latter group is not favored more than the former for the expected drift-dominated slope.

While our slope aligns with the drift-dominated scenario, there are still some outliers that fall below the drift-dominated slope, which we did not address in section 5.3. Rosotti et al. (2019) predicted a population of fragmentation-dominated disks (lying closer to the fragmentation-dominated slope), which could explain some of the disks outliers. However, various factors may also contribute to these deviations in the SLR (Zormpas et al. 2022). For instance, dust properties, such as variations in opacity or porosity, and changes to the turbulence parameter, α, can shift a disk's position along the SLR and potentially account for some of the observed outliers. Specifically, higher α values increase the luminosity, explaining disks positioned higher on the SLR. Variations in opacity not only affect luminosity but also influence disk size as they evolve. Lastly, extremely high porosity can lead to disks with low luminosity while caus-

ing minimal changes in disk size, which could explain the disks located at the lower end of the SLR.

More recently, for Taurus, Long et al. (2019) and Shi et al. (2024) also found an SLR with a slope consistent with drift-dominated disks by including more high-resolution observations. Nevertheless, they also found two disks, below 5 au, that fall below this slope.

5.4.3 Dust masses and optical depths

We create a grid of radiative transfer models that predict the flux for a range of disk radii, dust masses, and stellar luminosities. Comparing our observations of size and flux, we then estimate disk masses, finding a range from 0.3 to 26.3 $M_{\oplus}$. The average optical depth for these disks shows a narrower variation and clusters around 0.7 for most disks. Most of the masses are consistently higher than those from the optically thin approximation based on flux, but they remain relatively comparable and low. These new masses remain too biased to observe any trends or changes in disk relations, such as M_{dust} - R_{dust} and M_{dust} - M_*. When considering all disks, these relations remain unchanged. Additionally, comparing the optical depths of these disks with other parameters does not reveal any clear trends. This likely indicates that relations like M_{dust} - R_{dust} and M_{dust} - M_* are not significantly impacted by associated optical depth effects. While we might have expected many compact disks to be optically thick, our findings indicate otherwise. A similar pattern was observed in the rings of the DSHARP survey (Dullemond et al. 2018), where optical depths clustered between 0.2 and 0.5, rather than being optically thick. Stammler et al. (2019) showed that if the dust density is regulated by planetesimal formation (small grains turning into large objects), typical millimeter continuum optical depths are ~ 0.5. This means that the dust mass distribution in Lupus is likely not representative for the solid mass budget for planet formation, indicating that the bulk of the pebbles have already been sequestered in larger bodies, perhaps even planets,

especially when considering efficient pebble accretion.

5.4.4 Impact of compact disks in the exoplanet population

Under the assumption that the observed rings and gaps are produced by planets, we estimate their masses using DBNets. We are in agreement with the planet masses found in previous studies, including Zhang et al. (2023a), Huang et al. (2024a), Ruzza et al. (2024), and Kurtovic et al. (2021). However, we extend their findings to include smaller substructures, with gaps as small as 4 au. As previously mentioned, the planet masses and semimajor axes for the smallest disks in our sample align closely with those of exoplanets primarily detected through RV methods and where the occurrence rates of giant exoplanets peak between 1 and 10 au (Fernandes et al. 2019; Fulton et al. 2021). This strengthens the case for planets forming within the observed gaps in several protoplanetary disks. Furthermore, the overlap between these gap radii and the peak in the exoplanet occurrence suggests that at least some exoplanets may form in situ in compact disks rather than migrating to their observed location or that they have already migrated to at the time the compact disks are observed.

In Fig. 5.10, we observe an intriguing lack of planets and/or gap centers in Lupus disks between 5–15 au, this gap remains between 5–8 au even with additional data. Although this needs to be properly quantified, since there is additional uncertainty in the case of cavities because the planet's location can be any value within the cavity and we need more observations of disks at high angular resolution to conclude that this "valley" is significant, we can still speculate about the possible causes if this gap is real. For this to occur, a break in the disk properties is necessary in these two regions. While there is no straightforward explanation at the moment, if the snow lines (H_2O and CO) in Lupus are located around ~5 au and ~15 au, this could give rise to a bimodal population of planets and gaps if planet formation is enhanced at these snow lines.

Alternatively, though less likely, we could be observing a different

regime where the smallest gaps in our sample are caused by internal photoevaporation rather than planet formation (Owen & Clarke 2012). Disks with cavities under 10 au, such as Sz108B, J16092697-3836269, Sz72, Sz90, Sz96, Sz131, and Sz76, have accretion rates of $\log_{10}[M_\odot \cdot yr^{-1}]$ = -9.5, -8.1, -8.6, -8.9, -9.3, -9.1, and -9.1, respectively. Most of these align with the photoevaporation models by Ercolano et al. (2018) and Picogna et al. (2019) and could potentially be explained by this mechanism. However, J16092697-3836269 and Sz72, with larger accretion rates, fall outside the regime predicted by current photoevaporation models, suggesting that other mechanisms, like planets, may be causing these substructures. Generally it is difficult to prove whether cavities are caused by planets, photoevaporation, or a combination of the two (Gárate et al. 2023) without direct observations or limits on the planets itself. Finally, other physical mechanisms, such as dead zones, can also explain the formation of small cavities without invoking planets (Flock et al. 2015; Pinilla et al. 2016; Gárate et al. 2021).

For the remaining planets predicted by DBNets, Fig. 5.10 shows that they occupy a region where only a few exoplanets have been discovered (between 14 - 117 au and 20 - 2008 $M_\oplus$). This could be explained by three possibilities: (1) it is challenging to detect exoplanets in this region due to observation limitations that come with low planet masses or large distances from the star; (2) planets may have formed in these regions but have since migrated inward, closer to their stars, where we now observe them (Kley & Nelson 2012; Lodato et al. 2019); or (3) the gaps observed in protoplanetary disks may not be the result of planet-disk interactions, indicating other formation processes at work, for example snow lines (Zhang et al. 2015a) or zonal flows (Johansen et al. 2009).

In Fig. 5.11 there appears to be a relation between gap widths and the ring peak positions beyond each gap, with gaps and cavities following distinct trends. Additionally, this figure also reveals a lack of substructures (ring peaks) between ~13–27 AU, which is closely related to the cavity gap mentioned before in Fig. 5.10. The absence of substructures, either

cavities or rings, in this region of the disks appears to persist even when considering a more direct observable. There does not appear to be a straightforward relationship between the disk dust mass and the mass of the planet carving the gap. However, the derived planet masses are much larger than the dust masses, even though above 10 $M_{\oplus}$ most of the mass is probably in the gas envelope, this could imply that the millimeter emission we observe is coming from leftover dust particles that have not turned into planetesimals yet, meaning that the Lupus disks could have already finished most of their planet formation. On the other hand, the observed millimeter dust emission could be just a tracer of an unseen, larger population of solids.

Assuming that for other star-forming regions compact disks around M dwarfs are also common (Ansdell et al. 2016; Mulders et al. 2018), understanding the evolutionary paths of these types of disks is crucial for planet formation and dust evolution. The fact that we observe numerous compact disks in the Lupus region, both with and without substructures, aligns with the scenario from van der Marel & Mulders (2021), in which such disks, undergoing significant radial drift, can supply enough dust material to form multiple super-Earths (Sanchez et al. 2024). This offers a potential explanation for the origin of the exoplanet populations observed around M stars. In addition, the fact that we are still observing these disks indicates that another mechanism is hindering dust drift and trapping particles. Instead of forming a single Jupiter or Saturn-mass planet, several super-Earths or smaller planets may be forming in the inner regions of these disks, collectively stopping the drift (Huang et al. 2024b).

5.5 Summary and conclusions

We have analyzed a complete sample of protoplanetary disks in Lupus using the highest-resolution and highest-sensitivity data to date. The key findings of this work are as follows:

- We gathered high-resolution images of Lupus disks and used new

observations of 33 faint disks to complete the Lupus sample of Class II disks at high resolution. Our findings reveal that over 67% of the disks in Lupus have dust radii smaller than approximately 30 au. Additionally, we discovered 11 new disk cavities, including one of the smallest cavities measured to date, with a radius of 4.1 au.

- Through visibility modeling, we measured the dust disk radii of several compact disks, finding sizes as small as 0.6 au.
- The observed properties of the compact disks are consistent with planet formation models which predict efficient formation of close-in super-Earths in drift-dominated disks around M dwarfs (Sanchez et al. 2024).
- We revisited the SLR, finding good agreement with previous works, which found $F_{mm} \propto R_{eff}^2$. This is consistent with drift-dominated disks. We extended the SLR by including the smallest disk sizes.
- By comparing the total flux and radius for each disk with radiative transfer models tailored to the stellar luminosity of each source, we estimated the dust mass and average optical depths of the compact disks. Both are generally low, with median values of $\sim 3.38\,M_\oplus$ and ~ 0.7, respectively. This implies that the observed dust masses in Lupus are not representative of the total solid mass budget for exoplanet formation and that the bulk of the pebbles may have already been converted into boulders or even planets or have already drifted inward and sublimated close to the host star.
- We estimated planet masses for each substructure in our Lupus sample using DBNets. The smaller cavities in our study align well with the population of RV-detected exoplanets, while the larger ones are consistent with previous findings and lie in a region of the parameter space where no exoplanets are currently detected. However, no clear correlation was observed between planet masses and disk dust masses in our sample.

acknowledgements. We thank the anonymous referee for the insightful comments and suggestions, which helped improve the quality of this work. This paper makes use of the following ALMA data: ADS/JAO.ALMA#2022.1.00154.S (PI: van der Marel, Nienke), ADS/JAO.ALMA#2018.1.01458.S (PI: Yen, Hsi-Wei), ADS/JAO.ALMA#2017.1.00388.S (PI: Liu, Hauyu Baobab), ADS/JAO.ALMA#2018.1.00689.S (PI: Muto, Takayuki) and ADS/JAO.ALMA#2022.1.01302.S (PI: Mulders, Gijs). ALMA is a partnership of ESO (representing its member states), NSF (USA) and NINS (Japan), together with NRC (Canada), MOST and ASIAA (Taiwan), and KASI (Republic of Korea), in cooperation with the Republic of Chile. The Joint ALMA Observatory is operated by ESO, AUI/NRAO and NAOJ. This research has made use of the NASA Exoplanet Archive, which is operated by the California Institute of Technology, under contract with the National Aeronautics and Space Administration under the Exoplanet Exploration Program. G.D.M. acknowledges support from FONDECYT project 11221206 and the ANID BASAL project FB210003.

Appendix A: ALMA image characteristics

Table A.1: ALMA image characteristics of the new observations in Lupus.

Source	2MASS Identifier	$F_{1.3mm}$ [mJy]	Weighting	Beam size ["]	Rms [mJy · beam^{-1}]	Peak SNR	Visible Substructure
J16124373-3815031	J16124373-3815031	11.54 ± 0.04	Briggs (2.0)	0.048×0.032	0.04	16.32	No
Sz117	J16094434-3913301	3.79 ± 0.05	Briggs (0.5)	0.036×0.030	0.045	14.4	No
Sz110	J16085157-3903177	6.59 ± 0.04	Briggs (1.0)	0.047×0.038	0.039	18.56	No
J16134410-3736462	J16134410-3736462	0.56 ± 0.04	Briggs (2.0)	0.048×0.032	0.039	11.3	No
J16080017-3902595	J16080017-3902595	1.14 ± 0.04	Natural	0.051×0.044	0.039	15.47	No
Sz69	J15451741-3418283	8.36 ± 0.12	Briggs (0.0)	0.049×0.032	0.128	10.46	No
Sz95	J16075230-3858059	1.63 ± 0.04	Briggs (1.0)	0.046×0.038	0.038	19.0	No
J16085373-3914367	J16085373-3914367	1.4 ± 0.03	Briggs (0.5)	0.041×0.032	0.04	7.74	No
Sz88A	J16070061-3902194	3.11 ± 0.06	Briggs (0.0)	0.029×0.024	0.058	22.8	No
J16073773-3921388	J16073773-3921388	0.73 ± 0.04	Natural	0.051×0.044	0.037	7.58	No
J16002612-4153553	J16002612-4153553	0.61 ± 0.03	Briggs (1.0)	0.032×0.024	0.029	14.35	No
Sz102	J16082972-3903110	5.12 ± 0.04	Briggs (0.5)	0.036×0.030	0.043	18.8	No
Sz113	J16085780-3902227	9.52 ± 0.05	Briggs (0.5)	0.036×0.030	0.04	20.13	No
Sz97	J16082180-3904214	1.74 ± 0.05	Briggs (0.5)	0.036×0.030	0.045	15.09	No
J16085324-3914401	J16085324-3914401	7.56 ± 0.04	Briggs (0.5)	0.040×0.032	0.042	21.74	No
Sz77	J15514695-3556440	1.49 ± 0.04	Briggs (0.5)	0.034×0.030	0.04	16.66	No
Sz130	J16003103-4143369	1.07 ± 0.03	Briggs (1.0)	0.032×0.024	0.031	26.66	No
Sz106	J16083976-3906253	0.75 ± 0.04	Briggs (1.0)	0.046×0.038	0.039	10.35	No
V1192Sco	J16085143-3905304	0.32 ± 0.02	Natural	0.04×0.044	0.038	5.74	No
Sz81A	J15555030-3801329	4.0 ± 0.04	Briggs (0.5)	0.034×0.030	0.042	26.9	No
Sz81B	J15555030-3801329	1.26 ± 0.04	Briggs (0.5)	0.034×0.030	0.042	14.56	No
Sz74A	J15480523-3515526	7.97 ± 0.05	Briggs (0.0)	0.027×0.023	0.054	30.0	No
Sz74B	J15480523-3515526	3.3 ± 0.05	Briggs (0.0)	0.027×0.023	0.054	42.43	Yes
V856ScoB	J16083427-3906181	7.19 ± 0.11	Uniform	0.029×0.023	0.11	17.74	No
V856ScoA	J16083427-3906181	21.74 ± 0.11	Uniform	0.029×0.023	0.11	44.13	No
J15450887-3417333	J15450887-3417333	22.27 ± 0.10	Briggs (0.5)	0.063×0.038	0.091	19.28	No
J16075475-3915446	J16075475-3915446	0.43 ± 0.04	Natural	0.051×0.044	0.038	6.9	No
J16084940-3905393	J16084940-3905393	0.51 ± 0.04	Briggs (0.5)	0.036×0.030	0.041	11.97	No
J15592523-4235066	J15592523-4235066	0.31 ± 0.06	Briggs (2.0)	0.047×0.039	0.035	7.34	No
Sz108B	J160842.9-390615	10.38 ± 0.04	Briggs (1.0)	0.046×0.039	0.039	17.05	Yes (Cavity)
J16092697-3836269	J16092697-3836269	1.72 ± 0.04	Briggs (1.0)	0.47×0.038	0.04	7.35	Yes (Cavity)
Sz72	J15475062-3528353	5.40 ± 0.03	Briggs (1.0)	0.039×0.034	0.039	18.93	Yes (Cavity)
Sz90	J16071007-3911033	6.9 ± 0.04	Briggs (1.0)	0.047×0.038	0.04	15.425	Yes (Cavity)
Sz96	J16081263-3908334	1.41 ± 0.04	Briggs (0.5)	0.048×0.030	0.045	8.12	Yes (Cavity)
Sz123A	J16105158-3853137	18.11 ± 0.07	Briggs (1.0)	0.071×0.063	0.071	16.74	Yes (Cavity)
Sz100	J16082576-3906011	24.86 ± 0.07	Briggs (1.0)	0.071×0.063	0.067	17.5	Yes (Cavity)
Sz131	J16004943-4130038	3.44 ± 0.03	Briggs (1.5)	0.035×0.026	0.03	11.08	Yes (Cavity)
Sz73	J15475693-3514346	3.67 ± 0.06	Briggs (0.0)	0.048×0.033	0.078	35.63	Yes (Gap)
Sz66	J15392828-3446180	6.06 ± 0.04	Briggs (0.5)	0.033×0.027	0.043	17.85	No
Sz65	J15392776-3446171	21.08 ± 0.04	Briggs (0.5)	0.033×0.027	0.043	16.6	No
J16083070-3828268	J16083070-3828268	43.96 ± 0.07	Briggs (2.0)	0.079×0.072	0.07	25.81	Yes (Cavity)
Sz98	J16082249-3904464	119.21 ± 0.06	Briggs (1.0)	0.071×0.063	0.07	18.89	Yes (Gaps)

The images were obtained from the data in projects 2022.1.00154.S and 2018.1.01458.S

Appendix B: GALARIO fitting results

Table B.1: GALARIO visibility fitting results.

Source	$\log I_0$ [Jy sr^{-1}]	r_c ["]	Inc [°]	PA [°]	dRa ["]	dDec ["]	$F_{1.3mm}$ [mJy]	R_{68} [au]	R_{90} [au]
Gaussian Models									
J16124373-3815031	$10.33^{+0.005}_{-0.005}$	$0.07^{+0.0008}_{-0.0008}$	$51.92^{+0.72}_{-0.74}$	$16.26^{+0.9}_{-0.95}$	$0.26^{+0.0005}_{-0.0006}$	$-0.02^{+0.0007}_{-0.0007}$	11.33	14.83	21.84
Sz117	$10.43^{+0.01}_{-0.01}$	$0.041^{+0.0009}_{-0.0009}$	$55.05^{+1.34}_{-1.47}$	$105.22^{+1.52}_{-1.608}$	$0.27^{+0.0007}_{-0.0007}$	$-0.17^{+0.0005}_{-0.0005}$	3.99	7.7	11.56
Sz110	$10.22^{+0.007}_{-0.007}$	$0.064^{+0.0008}_{-0.0008}$	$49.55^{+1.10}_{-1.15}$	$13.10^{+1.45}_{-1.43}$	$-0.002^{+0.0006}_{-0.0007}$	$-0.083^{+0.0008}_{-0.0008}$	6.73	12.69	18.51
J16134410-373646	$10.53^{+0.10}_{-0.089}$	$0.013^{+0.002}_{-0.002}$	$49.40^{+15.71}_{-32.5}$	$155.7^{+13.42}_{-44.2}$	$-0.08^{+0.001}_{-0.001}$	$-0.14^{+0.001}_{-0.001}$	0.58	2.79	3.95
J16080017-3902595	$10.44^{+0.04}_{-0.04}$	$0.02^{+0.002}_{-0.002}$	$65^{+3.28}_{-3.8}$	$64.54^{+3.93}_{-3.93}$	$0.0019^{+0.001}_{-0.001}$	$-0.09^{+0.0009}_{-0.0009}$	1.11	4.52	7
Sz69	$10.6^{+0.013}_{-0.012}$	$0.049^{+0.001}_{-0.001}$	$54.56^{+1.46}_{-1.62}$	$115.87^{+1.85}_{-1.93}$	$-0.02^{+0.0007}_{-0.0008}$	$-0.07^{+0.0006}_{-0.0006}$	8.19	8.98	13.37
Sz95	$10.52^{+0.034}_{-0.032}$	$0.027^{+0.001}_{-0.001}$	$63.30^{+2.64}_{-2.87}$	$21.14^{+2.77}_{-2.81}$	$0.1^{+0.0008}_{-0.0007}$	$-0.27^{+0.0009}_{-0.001}$	1.65	4.93	7.56
J16085373-3914367	$10.38^{+0.178}_{-0.11}$	$0.048^{+0.002}_{-0.004}$	$81.83^{+2.67}_{-3.90}$	$93.04^{+1.4}_{-1.47}$	$0.057^{+0.002}_{-0.002}$	$-0.17^{+0.0008}_{-0.0008}$	1.22	7.18	12
Sz88A	$11.09^{+0.013}_{-0.014}$	$0.014^{+0.0004}_{-0.0005}$	$35.30^{+3.0}_{-4.74}$	$138.94^{+6.48}_{-8.27}$	$-0.15^{+0.0003}_{-0.0003}$	$-0.18^{+0.0002}_{-0.0003}$	3.23	3.12	4.67
J16073773-3921388	$10.20^{+0.209}_{-0.140}$	$0.036^{+0.004}_{-0.004}$	$78.58^{+4.81}_{-5.1}$	$101.20^{+5.05}_{-4.24}$	$0.031^{+0.003}_{-0.003}$	$-0.02^{+0.001}_{-0.001}$	0.62	6.04	9.9
J16002612-4153553	$10.88^{+0.083}_{-0.072}$	$0.009^{+0.0009}_{-0.0008}$	$53.11^{+8.81}_{-13.68}$	$167.56^{+7.59}_{-11.63}$	$-0.008^{+0.0006}_{-0.0006}$	$-0.14^{+0.0007}_{-0.0007}$	0.63	1.90	2.85
Sz102	$10.71^{+0.019}_{-0.018}$	$0.056^{+0.0008}_{-0.0009}$	$78.50^{+0.57}_{-0.58}$	$7.21^{+0.47}_{-0.48}$	$0.20^{+0.0003}_{-0.0004}$	$-0.098^{+0.0007}_{-0.0008}$	4.93	9.18	14.9
Sz113	$10.49^{+0.004}_{-0.004}$	$0.049^{+0.0006}_{-0.0005}$	$26.02^{+1.63}_{-1.96}$	$116.44^{+3.61}_{-4.21}$	$0.032^{+0.0005}_{-0.0005}$	$-0.23^{+0.0004}_{-0.0004}$	9.93	11.30	16.08
Sz97	$10.57^{+0.021}_{-0.021}$	$0.024^{+0.001}_{-0.001}$	$55^{+2.71}_{-2.91}$	$76.13^{+3.49}_{-3.75}$	$0.059^{+0.0009}_{-0.0009}$	$-0.18^{+0.0006}_{-0.0006}$	1.84	4.57	6.68
J16085324-3914401	$10.47^{+0.005}_{-0.005}$	$0.051^{+0.0006}_{-0.0006}$	$48^{+0.96}_{-1.13}$	$110.18^{+1.25}_{-1.15}$	$0.006^{+0.0005}_{-0.0005}$	$-0.15^{+0.0004}_{-0.0004}$	7.73	10.47	15.13
Sz77	$10.63^{+0.025}_{-0.022}$	$0.019^{+0.0009}_{-0.0009}$	$47.37^{+4.54}_{-5.31}$	$110.79^{+5.52}_{-4.79}$	$0.03^{+0.0008}_{-0.0007}$	$-0.21^{+0.0007}_{-0.0005}$	1.65	3.78	5.58
Sz130	$11.18^{+0.041}_{-0.034}$	$0.008^{+0.0004}_{-0.0004}$	$37.73^{+7.4}_{-11.5}$	$158.63^{+11.42}_{-17}$	$0.056^{+0.0003}_{-0.0003}$	$-0.16^{+0.0003}_{-0.0003}$	1.15	1.72	2.48
Sz106	$10.73^{+0.29}_{-0.16}$	$0.024^{+0.002}_{-0.002}$	$81.31^{+4.37}_{-4.33}$	$137.48^{+4.05}_{-4.3}$	$-0.035^{+0.001}_{-0.001}$	$-0.1^{+0.001}_{-0.001}$	0.69	3.87	6.54
V1192Sco	$10.65^{+0.16}_{-0.26}$	$0.028^{+0.004}_{-0.004}$	$85.58^{+2.91}_{-4.43}$	$157.64^{+4.81}_{-105.49}$	$0.095^{+0.002}_{-0.002}$	$-0.14^{+0.004}_{-0.004}$	0.39	4.21	6.79
Binary Gaussian Models									
Sz81A	$10.78^{+0.01}_{-0.01}$	$0.02^{+0.0004}_{-0.0006}$	$34.87^{+2.34}_{-2.34}$	$133.55^{+5.45}_{-7.63}$	$-0.26^{+0.0004}_{-0.0003}$	$-0.87^{+0.0004}_{-0.0004}$	4.0	5.08	7.25
Sz81B	$10.68^{+0.04}_{-0.04}$	$0.02^{+0.001}_{-0.001}$	$59.08^{+4.55}_{-4.71}$	$128.86^{+7.73}_{-37.90}$	$0.38^{+0.0008}_{-0.0007}$	$0.95^{+0.0008}_{-0.0007}$	1.28	3.45	5.17
Sz74A	$11.31^{+0.006}_{-0.006}$	$0.02^{+0.0002}_{-0.0002}$	$14.20^{+6.30}_{-8.12}$	$36.03^{+17.10}_{-10.55}$	$-0.07^{+0.0002}_{-0.0002}$	$-0.43^{+0.0001}_{-0.0002}$	7.94	3.90	5.53
Sz74B	$10.76^{+0.01}_{-0.01}$	$0.02^{+0.0006}_{-0.0006}$	$34.30^{+7.11}_{-10.00}$	$152.61^{+26.93}_{-86.56}$	$-0.09^{+0.0003}_{-0.0004}$	$-0.09^{+0.0004}_{-0.0004}$	3.20	4.67	6.65
V856ScoB	$11.21^{+0.007}_{-0.007}$	$0.03^{+0.0003}_{-0.0003}$	$64.34^{+0.56}_{-0.58}$	$133.66^{+0.66}_{-0.65}$	$1.34^{+0.0002}_{-0.0002}$	$-0.56^{+0.0002}_{-0.0002}$	7.12	4.6	7.1
Binary Gaussian Model + delta function gaussian									
		$\log I_\delta$ [Jy sr^{-1}]							
V856ScoA	$11.40^{+0.004}_{-0.004}$	$0.03^{+0.0002}_{-0.0002}$	$12.84^{+0.008}_{-0.009}$	$57.24^{+0.27}_{-0.28}$	$119.55^{+0.29}_{-0.29}$	$0.005^{+0.00008}_{-0.00007}$	$0.01^{+0.00006}_{-0.00006}$	19.80	5.84	8.73
Gaussian with fix P.A									
J15450887-3417333	$10.49^{+0.005}_{-0.005}$	$0.08^{+0.0007}_{-0.0007}$	$35.81^{+1.17}_{-1.23}$	0.0	$0.008^{+0.0006}_{-0.0006}$	$-0.08^{+0.0006}_{-0.0006}$	20.88	15.99	22.78
Gaussian with fix orientation									
[a] J16075475-3915446	$10.78^{+0.31}_{-0.21}$	$0.006^{+0.002}_{-0.002}$	0.0	0.0	$-0.0002^{+0.002}_{-0.002}$	$0.006^{+0.001}_{-0.001}$	0.33	1.59	2.03
[a] J16084940-3905393	$12.17^{+0.37}_{-0.45}$	$0.002^{+0.001}_{-0.0007}$	0.0	0.0	$-0.03^{+0.0007}_{-0.0007}$	$-0.23^{+0.0006}_{-0.0006}$	0.218	0.58	0.82
[a] J15592523-4235066	$10.33^{+0.29}_{-0.20}$	$0.010^{+0.003}_{-0.003}$	0.0	0.0	$-0.13^{+0.002}_{-0.003}$	$-0.12^{+0.002}_{-0.003}$	0.30	2.26	3.14
Single Ring Models									
		r_{ring} ["]	$r_w a$ ["]	$r_w b$ ["]					
Sz108B	$10.02^{+0.01}_{-0.01}$	$0.08^{+0.005}_{-0.004}$	$0.03^{+0.006}_{-0.005}$	$0.06^{+0.002}_{-0.003}$	$54.87^{+0.60}_{-0.52}$	$-21.04^{+0.66}_{-0.66}$	$0.002^{+0.0008}_{-0.0008}$	$0.02^{+0.0009}_{-0.0010}$	10.36	18.41	25.12
J16092697-3836269	$10.19^{+0.34}_{-0.17}$	$0.07^{+0.005}_{-0.006}$	$0.01^{+0.008}_{-0.01}$	$0.003^{+0.004}_{-0.002}$	$55.21^{+2.25}_{-2.65}$	$-57.28^{+2.63}_{-2.35}$	$0.13^{+0.001}_{-0.001}$	$-0.10^{+0.001}_{-0.001}$	1.57	9.46	10.87
Sz72	$10.33^{+0.01}_{-0.01}$	$0.05^{+0.003}_{-0.003}$	$0.03^{+0.004}_{-0.004}$	$0.01^{+0.002}_{-0.002}$	$31.46^{+1.60}_{-1.70}$	$47.89^{+3.46}_{-3.44}$	$0.007^{+0.0005}_{-0.0005}$	$-0.18^{+0.0005}_{-0.0005}$	5.41	8.477	10.2
Sz90	$10.17^{+0.01}_{-0.01}$	$0.06^{+0.003}_{-0.002}$	$0.002^{+0.003}_{-0.001}$	$0.05^{+0.001}_{-0.002}$	$56.62^{+0.53}_{-0.55}$	$135.87^{+0.75}_{-0.64}$	$0.002^{+0.0006}_{-0.0007}$	$-0.08^{+0.0006}_{-0.0006}$	7.36	15.05	20.31
Sz96	$10.59^{+0.30}_{-0.16}$	$0.04^{+0.004}_{-0.004}$	$0.005^{+0.005}_{-0.004}$	$0.002^{+0.003}_{-0.001}$	$48.90^{+2.72}_{-3.43}$	$23.34^{+3.65}_{-3.87}$	$-0.004^{+0.0010}_{-0.0009}$	$-0.15^{+0.0009}_{-0.0007}$	1.29	5.31	6.06
Sz123A	$10.27^{+0.01}_{-0.01}$	$0.20^{+0.0008}_{-0.0008}$	$0.0002^{+0.0003}_{-0.0001}$	$0.04^{+0.0008}_{-0.001}$	$53.34^{+0.17}_{-0.16}$	$-25.20^{+0.28}_{-0.25}$	$-0.006^{+0.0005}_{-0.0005}$	$-0.12^{+0.0006}_{-0.0006}$	17.43	33.69	38.61
Sz100	$10.03^{+0.008}_{-0.007}$	$0.20^{+0.004}_{-0.002}$	$0.03^{+0.003}_{-0.002}$	$0.05^{+0.001}_{-0.002}$	$44.35^{+0.51}_{-0.23}$	$67.28^{+0.9}_{-0.73}$	$0.07^{+0.0007}_{-0.0008}$	$-0.05^{+0.0007}_{-0.0007}$	24.47	33.39	39.61
Sz131	$10.15^{+0.03}_{-0.03}$	$0.04^{+0.006}_{-0.005}$	$0.01^{+0.008}_{-0.006}$	$0.03^{+0.003}_{-0.003}$	$62.85^{+0.78}_{-0.84}$	$-24.44^{+178.67}_{-2.36}$	$0.003^{+0.0007}_{-0.0008}$	$-0.21^{+0.001}_{-0.001}$	3.31	9.74	13.78
Two gaussians									
		r_c ["]	$\log I_0 b$ [Jy sr^{-1}]	r_{width} ["]	r_{ring} ["]				
Sz73	$11.04^{+0.01}_{-0.01}$	$0.03^{+0.0005}_{-0.0005}$	$9.11^{+0.06}_{-0.03}$	$0.06^{+0.005}_{-0.008}$	$0.25^{+0.005}_{-0.008}$	$42.76^{+1.63}_{-1.59}$	$99.22^{+1.97}_{-4.28}$	$-0.002^{+0.0003}_{-0.0003}$	$-0.08^{+0.0003}_{-0.0003}$	12.56	28.32	41.57

All disks from Table A.1 are included, except for Sz66, Sz65, J16083070-3828268 and sz98. [a] Due to the small sizes and low brightness, the P.A. and inclination are assumed zero for these targets. Therefore, $R_{68\%}$ and $R_{90\%}$ should be interpret with caution.

Appendix C: Lupus stellar parameters

Table C.1: Stellar parameters of the compact disks in Lupus

Source	Spectral Type	T_{eff} [K]	L_* [$L_\odot$]	M_* [$M_\odot$]	log (L_{acc}) [$L_\odot$]	log (M_{acc}) [$M_\odot$ yr^{-1}]	dist [pc]
J16124373-3815031	M1	3720	0.39 ± 0.27	0.47	-2.1	-9.0	159.85
Sz117	M3.5	3300	0.27 ± 0.19	0.23	-2.3	-8.8	156.95
Sz110	M4	3190	0.17 ± 0.13	0.18	-2.2	-8.7	157.49
J16134410-3736462	M5	2980	0.03 ± 0.03	0.09	-2.4	-9.0	158.55
J16080017-3902595	M5.5	2920	0.04 ± 0.03	0.07	-3.8	-10.2	161.13
Sz69	M4.5	3085	0.08 ± 0.14	0.15	-2.7	-9.3	152.56
Sz95	M3	3410	0.26 ± 0.18	0.29	-2.7	-9.3	160.47
J16085373-3914367	M5.5	2920	0.003 ± 0.003	0.068	-3.7	-10.8	148.72
Sz88A	M0	3900	0.3 ± 0.23	0.65	-1.4	-8.5	157.64
J16073773-3921388	M5.5	2920	0.01 ± 0.01	0.67	-3.6	-10.1	162.45
J16002612-4153553	M5.5	2920	0.07 ± 0.04	0.10	-3.2	-9.6	163.17
Sz102	K2	4710	0.009 ± 0.01	-	-2.2	-	158.5
Sz113	M4.5	3085	0.03 ± 0.03	0.13	-2.2	-8.9	160.53
Sz97	M4	3190	0.10 ± 0.08	0.19	-3.1	-9.7	157.34
J16085324-3914401	M3	3410	0.19 ± 0.15	0.3	-3.2	-10	163
Sz77	K7	4020	0.59 ± 0.24	0.67	-1.6	-8.7	155.25
Sz130	M2	3560	0.17 ± 0.07	0.4	-2.1	-9.1	159.18
Sz106	M0.5	3810	0.05 ± 0.04	0.55	-2.6	-10.1	158.71
V1192Sco	M4.5	3197	0.002 ± 0.001	0.17	-4.3	-11.8	147.10
Sz81A	M4.5	3085	0.24 ± 0.11	0.18	-2.4	-8.8	158.23
Sz81B	M5.5	3060	0.11 ± 0.06	0.13	-3.2	-9.6	158.23
Sz74	M3.5	3300	1.15 ± 0.48	0.3	-1.4	-7.8	158.5
V856Sco	–	–	–	–	–	–	–
J15450887-3417333	M5.5	2920	0.06 ± 0.03	0.09	-1.7	-8.1	154.81
J16075475-3915446	–	–	–	–	–	–	–
J16084940-3905393	M4	3190	0.15 ± 0.11	0.19	-3.1	-9.6	160.19
J15592523-4235066	M5	2980	0.02 ± 0.01	0.08	-4.4	-11	147.25
Sz108B	M5	2980	0.1 ± 0.08	0.12	-3.0	-9.5	161.22
J16092697-3836269	M4.5	3085	0.07 ± 0.05	0.15	-1.5	-8.1	159.19
Sz72	M2	3560	0.27 ± 0.12	0.37	-1.7	-8.6	156.71
Sz90	K7	4020	0.42 ± 0.28	0.73	-1.8	-8.9	160.37
Sz96	M1	3720	0.41 ± 0.32	0.46	-2.5	-9.3	155.98
Sz123A	M1	3720	0.13 ± 0.09	0.55	-2	-9.1	162.19
Sz100	M5.5	2920	0.10 ± 0.07	0.13	-3.3	-9.6	158.5
Sz131	M3	3410	0.15 ± 0.06	0.30	-2.3	-9.1	160.62
Sz73	K7	4020	0.46 ± 0.2	0.7	-0.9	-8.0	157.82
Sz66	M3	3410	0.21 ± 0.09	0.2	-1.7	-8.5	155.92
Sz65	K7	4020	0.86 ± 0.3	0.6	-2.5	<-9.4	153.47
Sz76	M4	3190	0.17 ± 0.07	0.18	-2.55	-9.1	156.4
Sz103	M4	3190	0.11 ± 0.09	0.19	-2.6	-9.2	157.15
Sz112	M5	2980	0.11 ± 0.09	0.13	-3.4	-9.8	159.3
Sz104	M5	2980	0.06 ± 0.05	0.10	-3.3	-9.8	159.81
J16081497-3857145	M5.5	2920	0.009 ± 0.005	0.06	-3.6	-10.2	150.83
HTLup	K2	4710	5.69 ± 2.1	1.3	-1.1	<-8.1	158.5
GQLup	K6	4115	1.60 ± 0.6	0.6	-0.6	-7.4	154.1

Table C.2: Stellar parameters of the large disks in Lupus

Source	Spectral Type	T_{eff} [K]	L_* [$L_\odot$]	M_* [$M_\odot$]	log (L_{acc}) [$L_\odot$]	log (M_{acc}) [$M_\odot$ yr^{-1}]	dist [pc]
J16083070-3828268	K2	4710	1.8 ± 1.3	1.2	-2.0	<-9.2	158.5
RYLup	K2	4710	1.84 ± 0.71	1.27	-0.8	-8.0	158.5
Sz98	K7	4020	1.53 ± 1.08	0.5	-0.7	-7.4	156.27
Sz91	M1	3720	0.2 ± 0.14	0.5	-2	-9.0	159.39
J16090141-3925119	M4	3190	0.09 ± 0.07	0.19	-3.1	-9.8	159.2
Sz111	M1	3720	0.21 ± 0.15	0.5	-2.4	-9.4	158.37
Sz129	K7	4020	0.42 ± 0.16	0.73	-1.1	-8.2	160.13
RULup	K7	4020	1.46 ± 0.60	0.55	-0.2	-7	158.5
IMLup	K5	4210	2.51 ± 1.04	0.72	-1	-7.8	155.82
Sz114	M4.8	3022	0.19 ± 0.14	0.16	-2.6	-9.1	156.76
GWLup	M1.5	3640	0.32 ± 0.14	0.414	-2.1	-9.0	155.2
Sz84	M5	2980	0.13 ± 0.06	0.15	-2.6	-9.0	158.5
Sz133	K5	4210	0.07± 0.03	-	-1.7	–	158.5
Sz118	K5	4210	0.69 ± 0.47	0.83	-1.9	-9.1	161.46
V1094 Sco	K6	4115	1.2 ± 0.86	0.64	-1.0	-7.8	158
RXJ1556.1	M1	3705	0.26 ± 0.10	0.5	-0.8	-7.8	158
MYLup	K0	4870	0.86 ± 0.33	1.19	-0.6	-8	158.5
J16102955-3922144	M4.5	3085	0.10 ± 0.07	0.15	-3.38	-9.9	160.44
J16070854-3914075	–	–	–	–	–	–	–
J16070384-3911113	M4.5	3085	–	–	-5.4	–	158.5
J16011549-4152351	–	–	–	–	–	–	–
J16000236-4222145	M4	3190	0.171 ± 0.07	0.19	-2.9	-9.4	160.39
J16000060-4221567	M4.5	3085	0.097 ± 0.04	0.15	-3.0	-9.5	159.43
EXLup	M0	3900	0.73 ± 0.5	0.5	-0.9	-7.8	154.72

Appendix D: Visibility models

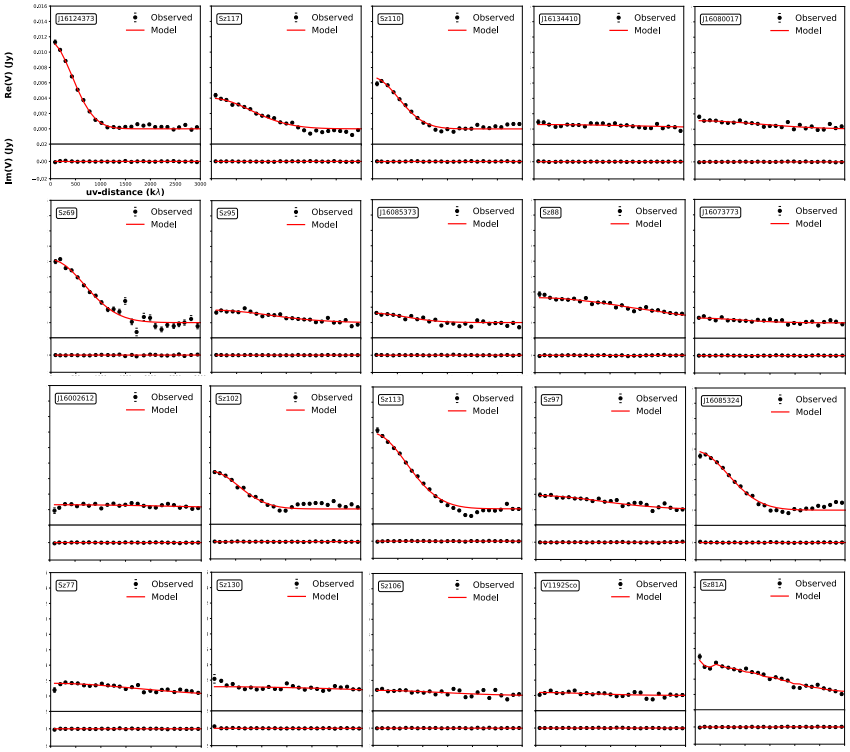


Figure D.1: Visibility plots comparing the observed and modeled visibilities.

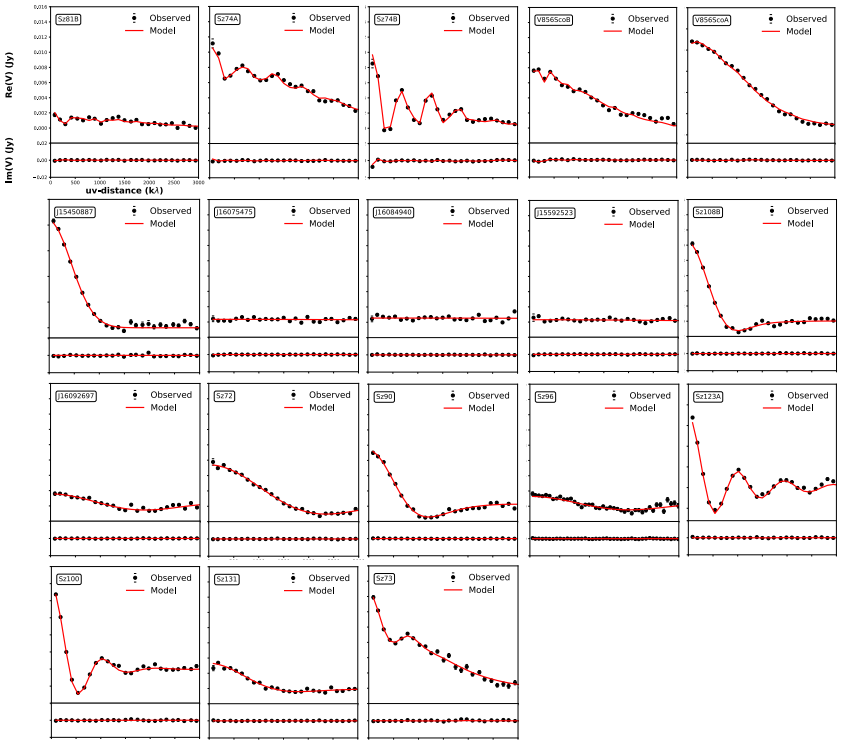


Figure D.1: Continued.

Bibliography

Adachi, I., Hayashi, C., & Nakazawa, K. 1976, Progress of Theoretical Physics, 56, 1756

Aikawa, Y. & Nomura, H. 2006, ApJ, 642, 1152

Alarcón, F., Casassus, S., Lyra, W., Pérez, S., & Cieza, L. 2024, MNRAS, 527, 9655

Alcalá, J. M., Manara, C. F., France, K., et al. 2019, A&A, 629, A108

Alcalá, J. M., Manara, C. F., Natta, A., et al. 2017, A&A, 600, A20

ALMA Partnership, Brogan, C. L., Pérez, L. M., et al. 2015, ApJ, 808, L3

Andre, P., Ward-Thompson, D., & Barsony, M. 1993, ApJ, 406, 122

Andrews, S. M. 2020, ARA&A, 58, 483

Andrews, S. M., Huang, J., Pérez, L. M., et al. 2018a, ApJ, 869, L41

Andrews, S. M., Terrell, M., Tripathi, A., et al. 2018b, ApJ, 865, 157

Andrews, S. M., Wilner, D. J., Zhu, Z., et al. 2016, ApJ, 820, L40

Ansdell, M., Williams, J. P., Manara, C. F., et al. 2017, AJ, 153, 240

Ansdell, M., Williams, J. P., Trapman, L., et al. 2018, ApJ, 859, 21

Ansdell, M., Williams, J. P., van der Marel, N., et al. 2016, ApJ, 828, 46

Artur de la Villarmois, E., Guzmán, V. V., Jørgensen, J. K., et al. 2022, A&A, 667, A20

Artur de la Villarmois, E., Jørgensen, J. K., Kristensen, L. E., et al. 2019a, A&A, 626, A71

Artur de la Villarmois, E., Kristensen, L. E., & Jørgensen, J. K. 2019b, A&A, 627, A37

Asaki, Y., Maud, L. T., Fomalont, E. B., et al. 2020, ApJS, 247, 23

Bae, J., Isella, A., Zhu, Z., et al. 2023, in Astronomical Society of the Pacific Conference Series, Vol. 534, Protostars and Planets VII, ed. S. Inutsuka, Y. Aikawa, T. Muto, K. Tomida, & M. Tamura, 423

Bae, J., Zhu, Z., & Hartmann, L. 2017, ApJ, 850, 201

Baillié, K. & Charnoz, S. 2014, ApJ, 786, 35

Ballesteros-Paredes, J., André, P., Hennebelle, P., et al. 2020, Space Sci. Rev., 216, 76

Ballesteros-Paredes, J., Klessen, R. S., Mac Low, M. M., & Vazquez-Semadeni, E. 2007, in Protostars and Planets V, ed. B. Reipurth, D. Jewitt, & K. Keil, 63

Banzatti, A., Pinilla, P., Ricci, L., et al. 2015, ApJ, 815, L15

Barenfeld, S. A., Carpenter, J. M., Ricci, L., & Isella, A. 2016, ApJ, 827, 142

Barrière-Fouchet, L., Gonzalez, J. F., Murray, J. R., Humble, R. J., & Maddison, S. T. 2005, A&A, 443, 185

Beckwith, S. V. W., Sargent, A. I., Chini, R. S., & Guesten, R. 1990, AJ, 99, 924

Belloche, A., Meshcheryakov, A. A., Garrod, R. T., et al. 2017, A&A, 601, A49

Bianchi, E., López-Sepulcre, A., Ceccarelli, C., et al. 2022, ApJ, 928, L3

Birnstiel, T. 2024, ARA&A, 62, 157

Birnstiel, T., Dullemond, C. P., & Brauer, F. 2010, A&A, 513, A79

Birnstiel, T., Dullemond, C. P., Zhu, Z., et al. 2018, ApJ, 869, L45

Birnstiel, T., Klahr, H., & Ercolano, B. 2012, A&A, 539, A148

Bisschop, S. E., Jørgensen, J. K., van Dishoeck, E. F., & de Wachter, E. B. M. 2007, A&A, 465, 913

Blanco, A., Borghesi, A., Fonti, S., & Orofino, V. 1998, A&A, 330, 505

Bøgelund, E. G., Barr, A. G., Taquet, V., et al. 2019, A&A, 628, A2

Booth, A. S. & Ilee, J. D. 2020, MNRAS, 493, L108

Booth, A. S., Walsh, C., Terwisscha van Scheltinga, J., et al. 2021, Nature Astronomy, 5, 684

Bottinelli, S., Ceccarelli, C., Lefloch, B., et al. 2004, ApJ, 615, 354

Brauer, F., Dullemond, C. P., & Henning, T. 2008, A&A, 480, 859

Brauer, F., Dullemond, C. P., Johansen, A., et al. 2007, A&A, 469, 1169

Brunken, N. G. C., Booth, A. S., Leemker, M., et al. 2022, A&A, 659, A29

Calcutt, H., Viti, S., Codella, C., et al. 2014, MNRAS, 443, 3157

Canta, A., Teague, R., Le Gal, R., & Öberg, K. I. 2021, ApJ, 922, 62

Carrasco-González, C., Henning, T., Chandler, C. J., et al. 2016, ApJ, 821, L16

Carrasco-González, C., Sierra, A., Flock, M., et al. 2019, ApJ, 883, 71

Casassus, S., Maddison, S., Wright, C., Menard, F., & Perez, s. 2013, Planet formation feedback in HD142527, ATNF proposal id.C2094, Semester: April, 2013

Casassus, S., Wright, C. M., Marino, S., et al. 2015, ApJ, 812, 126

Caselli, P. & Ceccarelli, C. 2012, A&A Rev., 20, 56

Cassen, P. & Moosman, A. 1981, Icarus, 48, 353

Cazzoletti, P., van Dishoeck, E. F., Pinilla, P., et al. 2018, A&A, 619, A161

Ceccarelli, C. 2004, in Astronomical Society of the Pacific Conference Series, Vol. 323, Star Formation in the Interstellar Medium: In Honor of David Hollenbach, ed. D. Johnstone, F. C. Adams, D. N. C. Lin, D. A. Neufeeld, & E. C. Ostriker, 195

Ceccarelli, C. 2023, in European Conference on Laboratory Astrophysics ECLA2020. The Interplay of Dust, 3–16

Cernicharo, J., Kisiel, Z., Tercero, B., et al. 2016, A&A, 587, L4

Chahine, L., Ceccarelli, C., De Simone, M., et al. 2024, MNRAS, 531, 2653

Chambers, J. E. 2009, ApJ, 705, 1206

Chiang, E. I., Joung, M. K., Creech-Eakman, M. J., et al. 2001, ApJ, 547, 1077

Ching, T.-C., Lai, S.-P., Zhang, Q., et al. 2016, ApJ, 819, 159

Chuang, C.-Y., Aso, Y., Hirano, N., Hirano, S., & Machida, M. N. 2021, ApJ, 916, 82

Ciesla, F. J. & Cuzzi, J. N. 2006, Icarus, 181, 178

Cieza, L. A., González-Ruilova, C., Hales, A. S., et al. 2021, MNRAS, 501, 2934

Cieza, L. A., Ruíz-Rodríguez, D., Hales, A., et al. 2019, MNRAS, 482, 698

Comerón, F. 2008, in Handbook of Star Forming Regions, Volume II, ed. B. Reipurth, Vol. 5, 295

Comrie, A., Wang, K.-S., Hwang, Y.-H., et al. 2018, CARTA: The Cube Analysis and Rendering Tool for Astronomy

Cox, E. G., Harris, R. J., Looney, L. W., et al. 2015, ApJ, 814, L28

Csengeri, T., Belloche, A., Bontemps, S., et al. 2019, A&A, 632, A57

Csengeri, T., Bontemps, S., Wyrowski, F., et al. 2018, A&A, 617, A89

Cuzzi, J. N., Hogan, R. C., Paque, J. M., & Dobrovolskis, A. R. 2001, ApJ, 546, 496

Cyr, K. E., Sears, W. D., & Lunine, J. I. 1998, Icarus, 135, 537

D'Alessio, P., Calvet, N., & Hartmann, L. 2001, ApJ, 553, 321

D'Alessio, P., Calvet, N., & Woolum, D. S. 2005, in Astronomical Society of the Pacific Conference Series, Vol. 341, Chondrites and the Protoplanetary Disk, ed. A. N. Krot, E. R. D. Scott, & B. Reipurth, 353

Dauphas, N. & Chaussidon, M. 2011, Annual Review of Earth and Planetary Sciences, 39, 351

de Juan Ovelar, M., Min, M., Dominik, C., et al. 2013, A&A, 560, A111

De Simone, M., Ceccarelli, C., Codella, C., et al. 2020, ApJ, 896, L3

De Simone, M., Codella, C., Testi, L., et al. 2017, A&A, 599, A121

De Simone, M., Podio, L., Chahine, L., et al. 2024, A&A, 686, L13

Delage, T. N., Okuzumi, S., Flock, M., Pinilla, P., & Dzyurkevich, N. 2022, A&A, 658, A97

Delussu, L., Birnstiel, T., Miotello, A., et al. 2024, A&A, 688, A81

Di Francesco, J., Myers, P. C., Wilner, D. J., Ohashi, N., & Mardones, D. 2001, ApJ, 562, 770

Dipierro, G., Laibe, G., Price, D. J., & Lodato, G. 2016, MNRAS, 459, L1

Doi, K. & Kataoka, A. 2021, ApJ, 912, 164

Dominik, C., Min, M., & Tazaki, R. 2021, Astrophysics Source Code Library, ascl:2104.010

Dominik, C. & Tielens, A. G. G. M. 1997, ApJ, 480, 647

Dong, R., Najita, J. R., & Brittain, S. 2018, ApJ, 862, 103

Dong, R., Zhu, Z., & Whitney, B. 2015, ApJ, 809, 93

Draine, B. T. 2003, ARA&A, 41, 241

Drążkowska, J. & Alibert, Y. 2017, A&A, 608, A92

Drążkowska, J., Bitsch, B., Lambrechts, M., et al. 2023, in Astronomical Society of the Pacific Conference Series, Vol. 534, Protostars and Planets VII, ed. S. Inutsuka, Y. Aikawa, T. Muto, K. Tomida, & M. Tamura, 717

Dubrulle, B., Morfill, G., & Sterzik, M. 1995, Icarus, 114, 237

Dullemond, C. P., Birnstiel, T., Huang, J., et al. 2018, ApJ, 869, L46

Dullemond, C. P. & Dominik, C. 2004, A&A, 421, 1075

Dullemond, C. P., Isella, A., Andrews, S. M., Skobleva, I., & Dzyurkevich, N. 2020, A&A, 633, A137

Dullemond, C. P., Juhasz, A., Pohl, A., et al. 2012, RADMC-3D: A multi-purpose radiative transfer tool, Astrophysics Source Code Library, record ascl:1202.015

Ercolano, B., Weber, M. L., & Owen, J. E. 2018, MNRAS, 473, L64

Evans, II, N. J., Dunham, M. M., Jørgensen, J. K., et al. 2009, ApJS, 181, 321

Facchini, S., Testi, L., Humphreys, E., et al. 2024, Nature Astronomy

Facchini, S., van Dishoeck, E. F., Manara, C. F., et al. 2019, A&A, 626, L2

Fedele, D., van den Ancker, M. E., Henning, T., Jayawardhana, R., & Oliveira, J. M. 2010, A&A, 510, A72

Fernandes, R. B., Mulders, G. D., Pascucci, I., Mordasini, C., & Emsenhuber, A. 2019, ApJ, 874, 81

Fiorellino, E., Tychoniec, Ł., Cruz-Sáenz de Miera, F., et al. 2023, ApJ, 944, 135

Flock, M., Ruge, J. P., Dzyurkevich, N., et al. 2015, A&A, 574, A68

Foreman-Mackey, D., Hogg, D. W., Lang, D., & Goodman, J. 2013, PASP, 125, 306

Francis, L. & van der Marel, N. 2020, ApJ, 892, 111

Frediani, J., De Simone, M., Testi, L., et al. 2025, arXiv e-prints, arXiv:2501.19188

Fulton, B. J., Rosenthal, L. J., Hirsch, L. A., et al. 2021, ApJS, 255, 14

Furlan, E., McClure, M., Calvet, N., et al. 2008, ApJS, 176, 184

Gahm, G. F., Walter, F. M., Stempels, H. C., Petrov, P. P., & Herczeg, G. J. 2008, A&A, 482, L35

Galametz, M., Maury, A. J., Valdivia, V., et al. 2019, A&A, 632, A5

Galli, P. A. B., Bouy, H., Olivares, J., et al. 2020, A&A, 643, A148

Galli, P. A. B., Loinard, L., Ortiz-Léon, G. N., et al. 2018, ApJ, 859, 33

Galván-Madrid, R., Liu, H. B., Izquierdo, A. F., et al. 2018, ApJ, 868, 39

Gárate, M., Birnstiel, T., Pinilla, P., et al. 2023, A&A, 679, A15

Gárate, M., Delage, T. N., Stadler, J., et al. 2021, A&A, 655, A18

Garrod, R. T. & Herbst, E. 2006, A&A, 457, 927

Garufi, A., Podio, L., Codella, C., et al. 2022, A&A, 658, A104

Gasman, D., van Dishoeck, E. F., Grant, S. L., et al. 2023, A&A, 679, A117

Glover, S. C. O. & Mac Low, M.-M. 2007, ApJ, 659, 1317

Goldreich, P. & Ward, W. R. 1973, ApJ, 183, 1051

Gorti, U. & Hollenbach, D. 2009, ApJ, 690, 1539

Guerra-Alvarado, O. M., van der Marel, N., Di Francesco, J., et al. 2024, A&A, 681, A82

Guidi, G. 2019, in ALMA2019: Science Results and Cross-Facility Synergies, 88

Guidi, G., Isella, A., Testi, L., et al. 2022, A&A, 664, A137

Gundlach, B. & Blum, J. 2014, in Asteroids, Comets, Meteors 2014, ed. K. Muinonen, A. Penttilä, M. Granvik, A. Virkki, G. Fedorets, O. Wilkman, & T. Kohout, 191

Gundlach, B. & Blum, J. 2015, ApJ, 798, 34

Gundlach, B., Schmidt, K. P., Kreuzig, C., et al. 2018, MNRAS, 479, 1273

Harsono, D., Bjerkeli, P., van der Wiel, M. H. D., et al. 2018, Nature Astronomy, 2, 646

Harsono, D., Jørgensen, J. K., van Dishoeck, E. F., et al. 2014, A&A, 562, A77

Harsono, D., van der Wiel, M. H. D., Bjerkeli, P., et al. 2021, A&A, 646, A72

Hashimoto, J., Liu, H. B., Dong, R., et al. 2023, AJ, 166, 186

Hayashi, C. 1981, Progress of Theoretical Physics Supplement, 70, 35

Hendler, N., Pascucci, I., Pinilla, P., et al. 2020, ApJ, 895, 126

Herbst, E. & van Dishoeck, E. F. 2009, ARA&A, 47, 427

Houge, A., Macías, E., & Krijt, S. 2023, arXiv e-prints, arXiv:2312.01856

Howard, A. W., Marcy, G. W., Bryson, S. T., et al. 2012, ApJS, 201, 15

Howard, A. W., Marcy, G. W., Johnson, J. A., et al. 2010, Science, 330, 653

Hsieh, C.-H., Arce, H. G., Maureira, M. J., et al. 2024, ApJ, 973, 138

Huang, J., Andrews, S. M., Cleeves, L. I., et al. 2018a, ApJ, 852, 122

Huang, J., Andrews, S. M., Pérez, L. M., et al. 2018b, ApJ, 869, L43

Huang, J., Ansdell, M., Birnstiel, T., et al. 2024a, ApJ, 976, 132

Huang, S., van der Marel, N., & Portegies Zwart, S. 2024b, A&A, 691, A155

Ichikawa, T., Kido, M., Takaishi, D., et al. 2021, ApJ, 919, 55

Isella, A., Guidi, G., Testi, L., et al. 2016, Phys. Rev. Lett., 117, 251101

Ishimaru, A. 1978, Journal of the Optical Society of America (1917-1983), 68, 1368

Jacobsen, S. K., Jørgensen, J. K., Di Francesco, J., et al. 2019, A&A, 629, A29

Jiang, H., Macías, E., Guerra-Alvarado, O. M., & Carrasco-González, C. 2024, A&A, 682, A32

Jin, S., Li, S., Isella, A., Li, H., & Ji, J. 2016, ApJ, 818, 76

Johansen, A., Youdin, A., & Klahr, H. 2009, ApJ, 697, 1269

Johnson, J. A., Aller, K. M., Howard, A. W., & Crepp, J. R. 2010, PASP, 122, 905

Jonkheid, B., Faas, F. G. A., van Zadelhoff, G. J., & van Dishoeck, E. F. 2004, A&A, 428, 511

Jørgensen, J. K., Belloche, A., & Garrod, R. T. 2020, ARA&A, 58, 727

Jørgensen, J. K., Bourke, T. L., Myers, P. C., et al. 2007, ApJ, 659, 479

Jørgensen, J. K., van der Wiel, M. H. D., Coutens, A., et al. 2016, A&A, 595, A117

Jørgensen, J. K., van Dishoeck, E. F., Visser, R., et al. 2009, A&A, 507, 861

Kataoka, A., Tsukagoshi, T., Pohl, A., et al. 2017, ApJ, 844, L5

Kelly, B. C. 2007, ApJ, 665, 1489

Kemper, F., Jäger, C., Waters, L. B. F. M., et al. 2002, Nature, 415, 295

Kley, W. & Nelson, R. P. 2012, ARA&A, 50, 211

Krijt, S., Ciesla, F. J., & Bergin, E. A. 2016, ApJ, 833, 285

Krijt, S., Kama, M., McClure, M., et al. 2023, in Astronomical Society of the Pacific Conference Series, Vol. 534, Protostars and Planets VII, ed. S. Inutsuka, Y. Aikawa, T. Muto, K. Tomida, & M. Tamura, 1031

Kurtovic, N. T., Pérez, L. M., Benisty, M., et al. 2018, ApJ, 869, L44

Kurtovic, N. T., Pinilla, P., Long, F., et al. 2021, A&A, 645, A139

Kuwahara, A., Lambrechts, M., Kurokawa, H., Okuzumi, S., & Tanigawa, T. 2024, A&A, 692, A45

Kwon, W., Looney, L. W., Mundy, L. G., Chiang, H., & Kemball, A. J. 2009, in American Astronomical Society Meeting Abstracts, Vol. 213, American Astronomical Society Meeting Abstracts #213, 413.18

Lada, C. J. 1987, in IAU Symposium, Vol. 115, Star Forming Regions, ed. M. Peimbert & J. Jugaku, 1

Laibe, G., Gonzalez, J.-F., Maddison, S. T., & Crespe, E. 2014, MNRAS, 437, 3055

Lee, C.-F., Codella, C., Ceccarelli, C., & López-Sepulcre, A. 2022, ApJ, 937, 10

Lee, C.-F., Li, Z.-Y., Ho, P. T. P., et al. 2017, ApJ, 843, 27

Lee, C.-F., Li, Z.-Y., Yang, H., et al. 2021, ApJ, 910, 75

Lee, J.-E., Lee, S., Baek, G., et al. 2019, Nature Astronomy, 3, 314

Li, A. & Draine, B. T. 2002, ApJ, 564, 803

Li, J., Quan, D., Wang, J., et al. 2024, PASJ, 76, 54

Lin, Z.-Y. D., Li, Z.-Y., Stephens, I. W., et al. 2023a, arXiv e-prints, arXiv:2309.10055

Lin, Z.-Y. D., Li, Z.-Y., Tobin, J. J., et al. 2023b, ApJ, 951, 9

Liu, H. B. 2019, ApJ, 877, L22

Liu, Y., Bertrang, G. H. M., Flock, M., et al. 2022, Science China Physics, Mechanics, and Astronomy, 65, 129511

Liu, Y., Henning, T., Carrasco-González, C., et al. 2017, A&A, 607, A74

Lodato, G., Dipierro, G., Ragusa, E., et al. 2019, MNRAS, 486, 453

Lombardi, M., Lada, C. J., & Alves, J. 2008, A&A, 480, 785

Long, F., Herczeg, G. J., Harsono, D., et al. 2019, ApJ, 882, 49

Long, F., Pinilla, P., Herczeg, G. J., et al. 2020, ApJ, 898, 36

Long, F., Pinilla, P., Herczeg, G. J., et al. 2018, ApJ, 869, 17

López-Sepulcre, A., Sakai, N., Neri, R., et al. 2017, A&A, 606, A121

Lumbreras, A. M. & Zapata, L. A. 2014, AJ, 147, 72

Macías, E., Guerra-Alvarado, O., Carrasco-González, C., et al. 2021, A&A, 648, A33

Manara, C. F., Morbidelli, A., & Guillot, T. 2018, A&A, 618, L3

Manara, C. F., Tazzari, M., Long, F., et al. 2019, A&A, 628, A95

Mathis, J. S., Rumpl, W., & Nordsieck, K. H. 1977, ApJ, 217, 425

Maucó, K., Carrasco-González, C., Schreiber, M. R., et al. 2021, ApJ, 923, 128

Maureira, M. J., Gong, M., Pineda, J. E., et al. 2022, ApJ, 941, L23

Maury, A. J., André, P., Testi, L., et al. 2019, A&A, 621, A76

McGuire, B. A. 2022, ApJS, 259, 30

McMullin, J. P., Waters, B., Schiebel, D., Young, W., & Golap, K. 2007, in Astronomical Society of the Pacific Conference Series, Vol. 376, Astronomical Data Analysis Software and Systems XVI, ed. R. A. Shaw, F. Hill, & D. J. Bell, 127

Michel, A., Sadavoy, S. I., Sheehan, P. D., Looney, L. W., & Cox, E. G. 2022, ApJ, 937, 104

Michel, A., van der Marel, N., & Matthews, B. C. 2021, ApJ, 921, 72

Miley, J. M., Carpenter, J., Booth, R., et al. 2024, A&A, 682, A55

Miyake, K. & Nakagawa, Y. 1993, Icarus, 106, 20

Mulders, G. D. 2018, Planet Populations as a Function of Stellar Properties (Springer), 153

Mulders, G. D., Drążkowska, J., van der Marel, N., Ciesla, F. J., & Pascucci, I. 2021a, ApJ, 920, L1

Mulders, G. D., Pascucci, I., Apai, D., & Ciesla, F. J. 2018, AJ, 156, 24

Mulders, G. D., Pascucci, I., Ciesla, F. J., & Fernandes, R. B. 2021b, ApJ, 920, 66

Müller, H. S. P., Thorwirth, S., Roth, D. A., & Winnewisser, G. 2001, A&A, 370, L49

Murillo, N. M., Lai, S.-P., Bruderer, S., Harsono, D., & van Dishoeck, E. F. 2013, A&A, 560, A103

Musiolik, G. & Wurm, G. 2019, ApJ, 873, 58

Nakagawa, Y., Sekiya, M., & Hayashi, C. 1986, Icarus, 67, 375

Natta, A. 1993, ApJ, 412, 761

Nazari, P., Meijerhof, J. D., van Gelder, M. L., et al. 2022, A&A, 668, A109

Nazari, P., Sellek, A. D., & Rosotti, G. P. 2025, A&A, 697, A84

Nazari, P., Tabone, B., Ahmadi, A., et al. 2024, A&A, 686, A201

Neufeld, D. A. & Hollenbach, D. J. 1994, ApJ, 428, 170

Öberg, K. I., Facchini, S., & Anderson, D. E. 2023, ARA&A, 61, 287

Öberg, K. I., Furuya, K., Loomis, R., et al. 2015, ApJ, 810, 112

Öberg, K. I., Murray-Clay, R., & Bergin, E. A. 2011, ApJ, 743, L16

Ohashi, N., Tobin, J. J., Jørgensen, J. K., et al. 2023, ApJ, 951, 8

Ohashi, S., Codella, C., Sakai, N., et al. 2022, ApJ, 927, 54

Ohashi, S., Kataoka, A., van der Marel, N., et al. 2020, ApJ, 900, 81

Okoda, Y., Oya, Y., Imai, M., et al. 2022, ApJ, 935, 136

Okuzumi, S., Momose, M., Sirono, S.-i., Kobayashi, H., & Tanaka, H. 2016, ApJ, 821, 82

Osorio, M., Macías, E., Anglada, G., et al. 2016, ApJ, 825, L10

Owen, J. E. & Clarke, C. J. 2012, MNRAS, 426, L96

Paneque-Carreño, T., Miotello, A., van Dishoeck, E. F., et al. 2023, A&A, 669, A126

Pérez, L. M., Carpenter, J. M., Andrews, S. M., et al. 2016, Science, 353, 1519

Persson, M. V., Jørgensen, J. K., & van Dishoeck, E. F. 2012, A&A, 541, A39

Pfeil, T., Birnstiel, T., & Klahr, H. 2023, arXiv e-prints, arXiv:2310.07332

Phuong, N. T., Dutrey, A., Chapillon, E., et al. 2021, A&A, 653, L5

Pickett, H. M., Poynter, R. L., Cohen, E. A., et al. 1998, J. Quant. Spectr. Rad. Transf., 60, 883

Picogna, G., Ercolano, B., Owen, J. E., & Weber, M. L. 2019, MNRAS, 487, 691

Pinilla, P., Benisty, M., & Birnstiel, T. 2012a, A&A, 545, A81

Pinilla, P., Birnstiel, T., Ricci, L., et al. 2012b, A&A, 538, A114

Pinilla, P., Birnstiel, T., Ricci, L., et al. 2012c, A&A, 538, A114

Pinilla, P., de Juan Ovelar, M., Ataiee, S., et al. 2015, A&A, 573, A9

Pinilla, P., Flock, M., Ovelar, M. d. J., & Birnstiel, T. 2016, A&A, 596, A81

Pinilla, P., Lenz, C. T., & Stammler, S. M. 2021, A&A, 645, A70

Pinilla, P., Pascucci, I., & Marino, S. 2020, A&A, 635, A105

Pinilla, P., Pohl, A., Stammler, S. M., & Birnstiel, T. 2017, ApJ, 845, 68

Pinte, C., Dent, W. R. F., Ménard, F., et al. 2016, ApJ, 816, 25

Pizzati, E., Rosotti, G. P., & Tabone, B. 2023, MNRAS, 524, 3184

Podio, L., Tabone, B., Codella, C., et al. 2021, A&A, 648, A45

Rau, U. & Cornwell, T. J. 2011, A&A, 532, A71

Reynolds, S. P. 1986, ApJ, 304, 713

Ribas, Á., Macías, E., Weber, P., et al. 2023, A&A, 673, A77

Ricci, L., Testi, L., Natta, A., et al. 2010, A&A, 512, A15

Ros, K., Johansen, A., Riipinen, I., & Schlesinger, D. 2019, A&A, 629, A65

Rosotti, G. P., Booth, R. A., Tazzari, M., et al. 2019, MNRAS, 486, L63

Rota, A. A., Manara, C. F., Miotello, A., et al. 2022, A&A, 662, A121

Ruzza, A., Lodato, G., & Rosotti, G. P. 2024, A&A, 685, A65

Rybicki, G. B. & Lightman, A. P. 1979, Radiative processes in astrophysics

Sakai, N., Sakai, T., Hirota, T., et al. 2014, Nature, 507, 78

Sanchez, M., van der Marel, N., Lambrechts, M., Mulders, G. D., & Guerra-Alvarado, O. M. 2024, A&A, 689, A236

Sánchez-Monge, Á., Schilke, P., Ginsburg, A., Cesaroni, R., & Schmiedeke, A. 2018, A&A, 609, A101

Santangelo, G., Codella, C., Cabrit, S., et al. 2015, A&A, 584, A126

Segura-Cox, D. M., Schmiedeke, A., Pineda, J. E., et al. 2020, Nature, 586, 228

Sheehan, P. 2020, Nature, 586, 205

Sheehan, P. D., Tobin, J. J., Li, Z.-Y., et al. 2022, ApJ, 934, 95

Shi, Y., Long, F., Herczeg, G. J., et al. 2024, ApJ, 966, 59

Sierra, A. & Lizano, S. 2020, ApJ, 892, 136

Sierra, A., Lizano, S., Macías, E., et al. 2019, ApJ, 876, 7

Sierra, A., Pérez, L. M., Zhang, K., et al. 2021, ApJS, 257, 14

Siwak, M., Ogloza, W., Rucinski, S. M., et al. 2016, MNRAS, 456, 3972

Stadler, J., Gárate, M., Pinilla, P., et al. 2022, A&A, 668, A104

Stammler, S. M., Birnstiel, T., Panić, O., Dullemond, C. P., & Dominik, C. 2017, A&A, 600, A140

Stammler, S. M., Drążkowska, J., Birnstiel, T., et al. 2019, ApJ, 884, L5

Supulver, K. D., Bridges, F. G., Tiscareno, S., Lievore, J., & Lin, D. N. C. 1997, Icarus, 129, 539

Suzuki, T., Ohishi, M., Saito, M., et al. 2018, ApJS, 237, 3

Tabone, B., Cabrit, S., Bianchi, E., et al. 2017, A&A, 607, L6

Takahashi, S. Z. & Muto, T. 2018, ApJ, 865, 102

Taniguchi, K., Saito, M., Majumdar, L., et al. 2018, ApJ, 866, 150

Taquet, V., Codella, C., De Simone, M., et al. 2020, A&A, 637, A63

Taquet, V., López-Sepulcre, A., Ceccarelli, C., et al. 2015, ApJ, 804, 81

Tazzari, M., Beaujean, F., & Testi, L. 2018, MNRAS, 476, 4527

Tazzari, M., Testi, L., Natta, A., et al. 2021, MNRAS, 506, 5117

Teague, R. & Foreman-Mackey, D. 2018, Research Notes of the American Astronomical Society, 2, 173

Testi, L., Birnstiel, T., Ricci, L., et al. 2014, in Protostars and Planets VI, ed. H. Beuther, R. S. Klessen, C. P. Dullemond, & T. Henning, 339–361

Tobin, J. J., Bourke, T. L., Mader, S., et al. 2019, ApJ, 870, 81

Tobin, J. J., Hartmann, L., Chiang, H.-F., et al. 2012, Nature, 492, 83

Tobin, J. J., Looney, L. W., Li, Z.-Y., et al. 2016, ApJ, 818, 73

Tobin, J. J., Looney, L. W., Li, Z.-Y., et al. 2018, ApJ, 867, 43

Tobin, J. J., Sheehan, P. D., Megeath, S. T., et al. 2020, ApJ, 890, 130

Tong, S. & Alexander, R. 2025, MNRAS, 537, 3525

Treffers, R. & Cohen, M. 1974, ApJ, 188, 545

Tripathi, A., Andrews, S. M., Birnstiel, T., & Wilner, D. J. 2017, ApJ, 845, 44

Tychoniec, Ł., Manara, C. F., Rosotti, G. P., et al. 2020, A&A, 640, A19

Tychoniec, Ł., van Dishoeck, E. F., van't Hoff, M. L. R., et al. 2021, A&A, 655, A65

Valdivia, V., Hennebelle, P., Gérin, M., & Lesaffre, P. 2016, A&A, 587, A76

van der Marel, N. & Mulders, G. D. 2021, AJ, 162, 28

van der Marel, N., Pinilla, P., Tobin, J., et al. 2015, ApJ, 810, L7

van der Marel, N., van Dishoeck, E. F., Bruderer, S., et al. 2013, Science, 340, 1199

van der Marel, N., Williams, J. P., Ansdell, M., et al. 2018, ApJ, 854, 177

van der Marel, N., Williams, J. P., Picogna, G., et al. 2022, arXiv e-prints, arXiv:2204.08225

van Gelder, M. L., Tabone, B., van Dishoeck, E. F., & Godard, B. 2021, A&A, 653, A159

van 't Hoff, M. L. R., van Dishoeck, E. F., Jørgensen, J. K., & Calcutt, H. 2020, A&A, 633, A7

van Terwisga, S. E., van Dishoeck, E. F., Ansdell, M., et al. 2018, A&A, 616, A88

van't Hoff, M. L. R., Harsono, D., Tobin, J. J., et al. 2020, ApJ, 901, 166

Vastel, C., Bottinelli, S., Caux, E., Glorian, J. M., & Boiziot, M. 2015, in SF2A-2015: Proceedings of the Annual meeting of the French Society of Astronomy and Astrophysics, 313–316

Villenave, M., Benisty, M., Dent, W. R. F., et al. 2019, A&A, 624, A7

Villenave, M., Ménard, F., Dent, W. R. F., et al. 2020, A&A, 642, A164

Villenave, M., Podio, L., Duchêne, G., et al. 2023, ApJ, 946, 70

Villenave, M., Stapelfeldt, K. R., Duchêne, G., et al. 2022, ApJ, 930, 11

Visser, R., van Dishoeck, E. F., Doty, S. D., & Dullemond, C. P. 2009, A&A, 495, 881

Voelk, H. J., Jones, F. C., Morfill, G. E., & Roeser, S. 1980, A&A, 85, 316

Wada, K., Tanaka, H., Okuzumi, S., et al. 2013, A&A, 559, A62

Weidenschilling, S. J. 1977, MNRAS, 180, 57

Weidenschilling, S. J. 1980, Icarus, 44, 172

Whipple, F. L. 1972, in From Plasma to Planet, ed. A. Elvius, 211

White, R. J. & Hillenbrand, L. A. 2004, ApJ, 616, 998

Whittet, D. C. B., Duley, W. W., & Martin, P. G. 1990, MNRAS, 244, 427

Williams, J. P., Painter, C., Anderson, A. R., & Ribas, A. 2024, ApJ, 976, 50

Wilson, T. L. & Rood, R. 1994, ARA&A, 32, 191

Windmark, F., Birnstiel, T., Ormel, C. W., & Dullemond, C. P. 2012, A&A, 544, L16

Woitke, P., Kamp, I., & Thi, W. F. 2009, A&A, 501, 383

Wu, Y.-L., Sheehan, P. D., Males, J. R., et al. 2017, ApJ, 836, 223

Wurster, J., Price, D. J., & Bate, M. R. 2016, MNRAS, 457, 1037

Yamaguchi, M., Muto, T., Tsukagoshi, T., et al. 2024, PASJ, 76, 437

Yamato, Y., Notsu, S., Aikawa, Y., et al. 2024, AJ, 167, 66

Yang, Y.-L., Evans, Neal J., I., Green, J. D., Dunham, M. M., & Jørgensen, J. K. 2017, ApJ, 835, 259

Yen, H.-W., Koch, P. M., Takakuwa, S., et al. 2015a, ApJ, 799, 193

Yen, H.-W., Koch, P. M., Takakuwa, S., et al. 2017, ApJ, 834, 178

Yen, H.-W., Takakuwa, S., Koch, P. M., et al. 2015b, ApJ, 812, 129

Youdin, A. N. & Shu, F. H. 2002, ApJ, 580, 494

Zagaria, F., Rosotti, G. P., & Lodato, G. 2021, MNRAS, 504, 2235

Zamponi, J., Maureira, M. J., Zhao, B., et al. 2021, MNRAS, 508, 2583

Zapata, L. A., Loinard, L., Rodríguez, L. F., et al. 2013, ApJ, 764, L14

Zhang, K. 2024, Reviews in Mineralogy and Geochemistry, 90, 27

Zhang, K., Blake, G., & Bergin, E. 2015a, in IAU General Assembly, Vol. 29, 2256118

Zhang, K., Blake, G. A., & Bergin, E. A. 2015b, ApJ, 806, L7

Zhang, S., Kalscheur, M., Long, F., et al. 2023a, ApJ, 952, 108

Zhang, S., Zhu, Z., Huang, J., et al. 2018, ApJ, 869, L47

Zhang, S., Zhu, Z., Ueda, T., et al. 2023b, ApJ, 953, 96

Zhao, B., Caselli, P., Li, Z.-Y., et al. 2020a, MNRAS, 492, 3375

Zhao, B., Tomida, K., Hennebelle, P., et al. 2020b, Space Sci. Rev., 216, 43

Zhu, Z., Stone, J. M., Rafikov, R. R., & Bai, X.-n. 2014, ApJ, 785, 122

Zhu, Z., Zhang, S., Jiang, Y.-F., et al. 2019, ApJ, 877, L18

Zormpas, A., Birnstiel, T., Rosotti, G. P., & Andrews, S. M. 2022, A&A, 661, A66

Zsom, A., Ormel, C. W., Güttler, C., Blum, J., & Dullemond, C. P. 2010, A&A, 513, A57

Zucker, C., Schlafly, E. F., Speagle, J. S., et al. 2018, ApJ, 869, 83

Zurlo, A., Cieza, L. A., Ansdell, M., et al. 2021, MNRAS, 501, 2305

Nederlandse Samenvattig

We leven in een klein hoekje van ons melkwegstelsel, de Melkweg, in een planetair systeem dat we het Zonnestelsel noemen. Lange tijd geloofden we dat ons systeem het centrum van het universum was, of beter gezegd, dat de mens het centrum van het universum was, een overtuiging waarvan we nu weten dat die onjuist is. Als we hier geboren zijn en zijn opgegroeid, is het niet onredelijk om voor te stellen dat iets vergelijkbaars ook rondom andere sterren in onze Melkweg of in verre sterrenstelsels kan zijn gebeurd.

Interessant genoeg is de Zon niet eens een typische ster binnen de Melkweg, laat staan in het universum. Sterker nog, recent bewijs suggereert dat de vorming van ons Zonnestelsel mogelijk een nogal ongebruikelijk pad heeft gevolgd vergeleken met de meeste andere planetaire systemen. Toch blijft het intrigerend dat we weten dat er andere mogelijkheden bestaan, en dat leven elders kan ontstaan. De vraag blijft dan: wat leidde tot de vorming van dit specifieke planetaire systeem rond een ster met een zonnemassa, dat uiteindelijk het ontstaan van leven mogelijk maakte?

Om daar een antwoord op te vinden, moeten we teruggaan naar het allereerste begin: de geboorte van sterren en planeten, in de uitgestrekte leegte van het heelal waar gas en koud stof samenkomen, het interstellaire medium (ISM).

Ster- en planeetvorming in het ISM

In ons universum bestaan enorme gebieden van gas en stof, de zogeheten moleculaire wolken, die deel uitmaken van het ISM. Dit zijn de gebieden waar sterren en planeten worden geboren. Moleculaire wolken bestaan voornamelijk uit waterstof en helium, met sporen van zwaardere elementen zoals zuurstof, stikstof en koolstof. Wanneer delen van deze wolken voldoende dicht en zwaar worden, veroorzaakt de zwaartekracht hun ineenstorting, waardoor een protoster ontstaat. Het ineenstortende materiaal, zowel gas als stof, begint op te warmen en af te vlakken tot een roterende structuur terwijl de protoster materie blijft verzamelen. Het overgebleven materiaal rond de jonge ster vormt wat we een protoplanetaire schijf noemen.

Binnen deze schijf beginnen stofdeeltjes aan elkaar te kleven, en vormen zo steeds grotere klonten. Na verloop van tijd groeien deze uit tot objecten van kilometers groot, de zogenaamde planetesimalen, die vervolgens meer materiaal blijven aantrekken en uiteindelijk uitgroeien tot planeten. Naarmate de protoster evolueert, start de kernfusiereactie in zijn centrum. Op dat moment begint de intense straling van de ster het omringende materiaal weg te blazen, waardoor alleen de planeten en planetesimalen overblijven, nu onderdeel van een nieuw gevormd sterrensysteem. Zo'n systeem kan miljoenen of zelfs miljarden jaren stabiel blijven, totdat de ster zijn nucleaire brandstof uitgeput heeft. Afhankelijk van zijn massa kan de ster dan exploderen als een supernova of uitzetten en eindigen als een witte dwerg. In beide gevallen keert het resterende materiaal terug naar het interstellaire medium, waarmee de cyclus van ster- en planeetvorming opnieuw begint. Dit proces wordt geïllustreerd in Figuur 1.

Hoewel we via meteorieten en geologische gegevens diep in het verleden van de aarde kunnen kijken, is de beste manier om het ontstaan van planeten en mogelijk leven elders te bestuderen het observeren van andere protoplanetaire schijven, systemen die zich nog in de vroege stadia

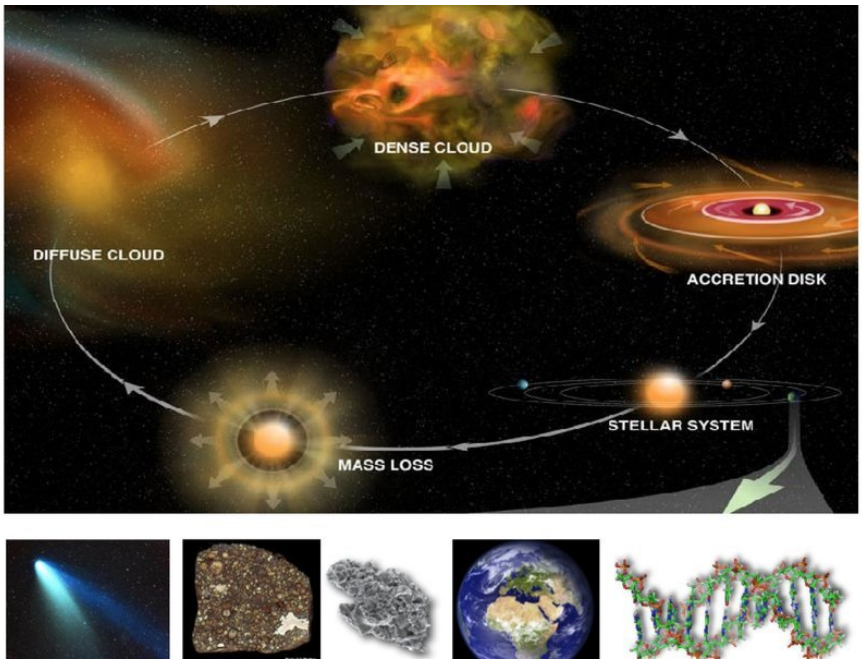


Figure 1: Deze afbeelding illustreert het volledige proces van stervorming, samen met de vroege stadia van planeetvorming. Alles begint met een moleculaire wolk, een koude en dichte regio van gas en stof in het interstellaire medium. Na verloop van tijd storten delen van deze wolk in onder invloed van de zwaartekracht, waardoor een protoster ontstaat met een accretieschijf van materiaal eromheen. Terwijl de protoster zich ontwikkelt, wordt de omringende protoplanetaire schijf de geboorteplaats van planeten. Binnen deze schijf botsen kleine deeltjes en klonteren samen, wat uiteindelijk leidt tot de vorming van stofdeeltjes en planeten. Na verloop van tijd wordt een groot deel van het materiaal in de schijf weggeblazen, en blijft een planetair systeem over met complexe organische moleculen, atomen en reststof, overblijfselen zoals planetesimalen van de oorspronkelijke schijf. Afbeelding: B. Saxton, NRAO/AUI/NSF

van planeetvorming bevinden. Deze systemen bevinden zich in nabijgelegen moleculaire wolken en bieden een uniek venster op het ontstaan van planeten zoals de onze. Om ze te onderzoeken, gebruiken we krachtige telescopen die het licht opvangen dat wordt uitgezonden door stofdeeltjes

of atomen en moleculen in deze schijven. In het bijzonder maken interferometrische telescopen het mogelijk om hun structuur in opmerkelijk detail te bestuderen, zodat we de omgevingen kunnen begrijpen waarin planeten, en mogelijk ook leven, worden geboren.

Overzicht van de thesis

In deze thesis heb ik met behulp van de modernste telescopen de eigenschappen van stof in nabijgelegen protosterren en stervormingsgebieden bestudeerd, die doorgaans lijken op de structuur weergegeven in Figuur 2. Mijn onderzoek richtte zich voornamelijk op de evolutie en groei van stof, een essentiële stap richting planeetvorming. Daarnaast heb ik onderzocht hoe moleculen, met name complexe organische moleculen, kunnen bijdragen aan het beantwoorden van fundamentele vragen over het ontstaan van planetaire systemen.

De thesis is opgebouwd uit vijf hoofdstukken. Hoofdstuk 1 geeft een inleiding tot stervorming, protoplanetaire schijven, de rol van stof en gas in deze schijven, de aanwezigheid van complexe organische moleculen, en substructuren in protoplanetaire schijf. De daaropvolgende hoofdstukken bevatten gedetailleerde analyses van stofevolutie, stofgroei en de chemie van complexe organische moleculen in verschillende stervormingsregio's.

Hoofdstuk 2: In dit hoofdstuk onderzoek ik de hoge-resolutie stofemissie van het binair systeem NGC 1333 IRAS4A, een protostellaire regio die een van de vroegste stadia van stervorming vertegenwoordigt. De studie van zulke jonge systemen is essentieel om te begrijpen wanneer en hoe planeetvorming begint. Dit werk onderzoekt of vroege aanwijzingen zoals korrelgroei of substructuurvorming al zichtbaar zijn in dit stadium, of pas later in de evolutie van de protoplanetaire schijf. De analyse toont aan dat het stof in IRAS4A1 al eigenschappen vertoont, zoals korrelgrootte en dichtheid, die gunstig zijn voor het ontstaan van planetesimalen of

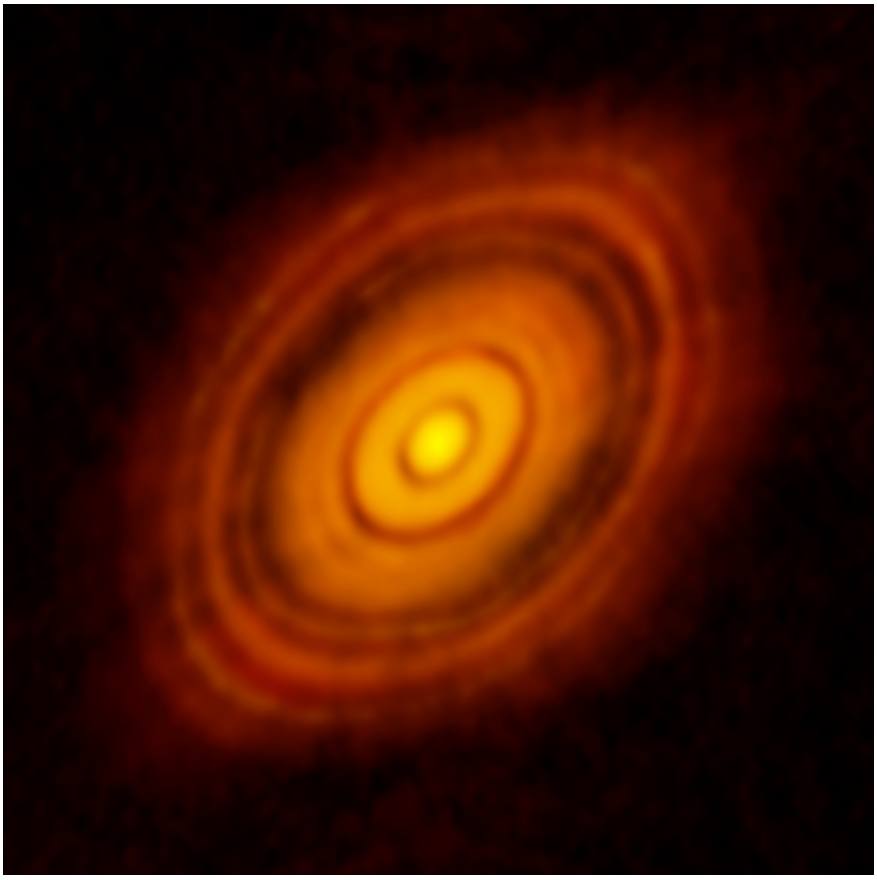


Figure 2: Deze afbeelding toont hoe een protoster met een protoplanetaire schijf eruitziet wanneer die wordt waargenomen met een telescoop zoals de Atacama Large Millimeter/submillimeter Array (ALMA) op submillimetergolflengten. De schijf laat verschillende kenmerken zien, waaronder ringen en gaten, de zogenaamde substructuren, die mogelijk het resultaat zijn van planeetvorming of andere dynamische processen in de schijf. Afbeelding: ALMA(ESO/NAOJ/NRAO); C. Brogan, B. Saxton (NRAO/AUI/NSF)

substructuren. Stralingstransportmodellen suggereren dat substructuren mogelijk al bestaan maar nog verborgen zijn onder dichte lagen gas en stof.

Hoofdstuk 3: In dit hoofdstuk richt ik me op de complexe organische moleculen rond IRAS4A2. Ik analyseer hun ruimtelijke distributie en verband met de verdeling van stofdeeltjes. De resultaten tonen aan dat de radiële en azimutale verdeling van deze moleculen veel complexer is dan eerder werd gedacht. Dit wijst op een snelle stofevolutie in IRAS4A2, in contrast met zijn binaire metgezel IRAS4A1, waar de moleculaire emissie grotendeels verborgen blijft.

Hoofdstuk 4: Hier bestuderen we de protoplanetaire schijf HL Tau met behulp van multi-golflengteanalyses. Met modelering van het stralingstransport konden we de waargenomen emissie reproduceren en stofeigenschappen afleiden zoals korrelgrootte, dichtheid en temperatuur. Observaties met ALMA Band 9 onthullen een andere structuur en geven aanwijzingen over kleinere stofdeeltjes, grotere schijfgroottes en mogelijk een ander verticale uitgestrektheid van de schijf. We ontdekten ook een nieuwe binnenste substructuur en een opvallende asymmetrie.

Hoofdstuk 5: Hoofdstuk 5 richt zich op alle bekende schijven in de Lupus-regio. Met behulp van hoge resolutie konden we vaststellen dat meer dan 67% van deze schijven zeer compact zijn (straal < 30 au). Daarnaast vonden we nieuwe substructuren. Deze bevindingen wijzen erop dat de meeste schijven al de voorwaarden bezitten voor de vorming van een veelvoorkomend type exoplaneet: de super-aarde. Zo ontstaat een brug tussen waarnemingen van schijven en de uiteindelijke planetaire systemen.

Op basis van alle hoofdstukken concluderen we dat er meer aandacht moet worden besteed aan zowel de radiële als de verticale structuur van protoplanetaire schijven. Deze systemen zijn complexer dan eerder gedacht, met variërende geometrieën en afmetingen. Radiële variaties in de verticale structuur kunnen inzicht bieden in de initiële omstandighe-

den van planeetvorming, het ontstaan van substructuren en de triggers voor dit proces. Begrijpen of compacte of grote schijven vaker voorkomen, helpt bij het beantwoorden van een fundamentele vraag: is ons Zonnestelsel een uitzondering? Als dat zo is, zou leven wel eens zeldzamer en moeilijker te vormen kunnen zijn dan we altijd dachten.

Spanish summary

Vivimos en un pequeño rincón de nuestra galaxia, la Vía Láctea, dentro de un sistema planetario que llamamos el Sistema Solar. Durante mucho tiempo se creyó que nuestro sistema, o más concretamente la humanidad, era el centro del universo, una creencia que hoy sabemos que está lejos de la realidad. Si nacimos y crecimos aquí, no era descabellado imaginar que algo similar pudo haber ocurrido alrededor de otras estrellas en nuestra galaxia o incluso en galaxias distantes.

Curiosamente, el Sol ni siquiera es una estrella típica dentro de la Vía Láctea, y mucho menos en el universo. De hecho, evidencia reciente sugiere que la formación de nuestro Sistema Solar podría haber seguido un camino bastante inusual en comparación con la mayoría de otros sistemas planetarios. Aun así, el simple hecho de que sepamos de otras posibilidades y que la vida pueda surgir en otros lugares sigue siendo algo que nos intriga profundamente. Entonces: ¿qué llevó a la formación de este sistema planetario alrededor de una estrella como el Sol, que eventualmente permitió el surgimiento de la vida?

Para responder a esta pregunta, debemos retroceder hasta el nacimiento de estrellas, en las regiones más frías y oscuras del universo, donde el gas y el polvo interestelar se acumulan, el medio interestelar.

Formación de Estrellas y Planetas en el Medio Interestelar

En nuestro universo existen vastas regiones de gas y polvo conocidas como nubes moleculares, que constituyen una parte fundamental del

medio interestelar. Estas regiones son los lugares donde nacen las estrellas. Las nubes moleculares están compuestas principalmente por hidrógeno y helio, aunque también contienen pequeñas cantidades de elementos más pesados como oxígeno, nitrógeno y carbono. Cuando ciertas zonas de estas nubes alcanzan suficiente densidad y masa, la gravedad provoca su colapso, lo que da lugar a la formación de una protoestrella. El material colapsado comienza a calentarse y a aplanarse en una estructura giratoria. Este material aplanado que queda alrededor de la joven estrella forma lo que se conoce como un disco protoplanetario.

Dentro de este disco, las partículas de polvo comienzan a adherirse entre sí, formando cúmulos de partículas cada vez más grandes. Con el tiempo, estos cúmulos se convierten en cuerpos de varios kilómetros de tamaño, conocidos como planetesimales, que continúan creciendo hasta dar origen a planetas. Este proceso continúa hasta que se activan las reacciones nucleares en la protoestrella. La radiación que emite se vuelve tan intensa que empieza a dispersar el material restante del disco, dejando atrás únicamente los objetos más masivos: los planetas, planetesimales y, en definitiva, un sistema planetario completamente formado.

Este sistema puede permanecer estable durante millones o incluso miles de millones de años, hasta que la estrella agota su combustible nuclear. Dependiendo de su masa, la estrella puede explotar como una supernova o expandirse y terminar su vida como una enana blanca. En cualquiera de los casos, el material remanente es devuelto al medio interestelar, reiniciando así el ciclo de formación estelar. Este proceso se ilustra en la Figura 1.

Mientras que desde la Tierra podemos estudiar el pasado del sistema solar mediante meteoritos y registros geológicos, la mejor forma de comprender el origen de los planetas y la posibilidad de vida en otros lugares es observar discos protoplanetarios en formación. Estos sistemas se encuentran en nubes moleculares cercanas y nos ofrecen una ventana única a los inicios de la formación planetaria. Para estudiarlos, utilizamos telescopios potentes capaces de detectar la luz proveniente de las partículas

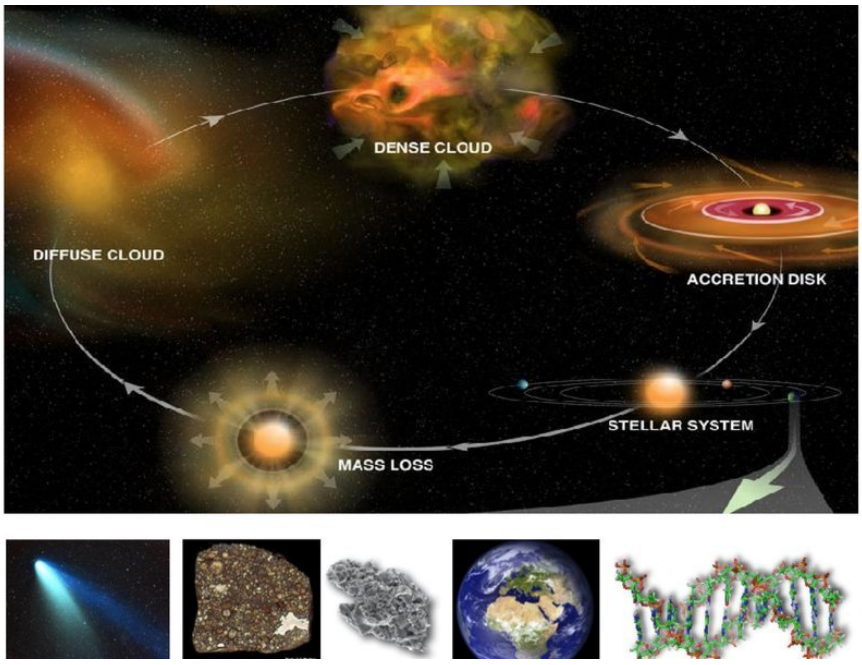


Figure 1: Esta imagen ilustra el proceso completo de formación estelar, junto con las primeras etapas de la formación planetaria. Todo comienza con una nube molecular, una región fría y densa de gas y polvo en el medio interestelar. Con el tiempo, partes de esta nube colapsan por efecto de la gravedad, formando una protoestrella rodeada por un disco de material en acreción. A medida que la protoestrella evoluciona, el disco protoplanetario circundante se convierte en el lugar de nacimiento de los planetas. Dentro de este disco, pequeñas partículas colisionan y se adhieren, formando granos de polvo y, eventualmente, planetas. Con el tiempo, gran parte del material del disco se disipa, dejando atrás un sistema planetario con moléculas orgánicas complejas, átomos y polvo residual. Crédito de la imagen: B. Saxton, NRAO/AUI/NSF

de polvo, átomos y moléculas en estos discos. En particular, los telescopios interferométricos nos permiten resolver su estructura con gran detalle, ayudándonos a entender los entornos donde nacen los planetas y posiblemente se origine la vida como la conocemos hoy.

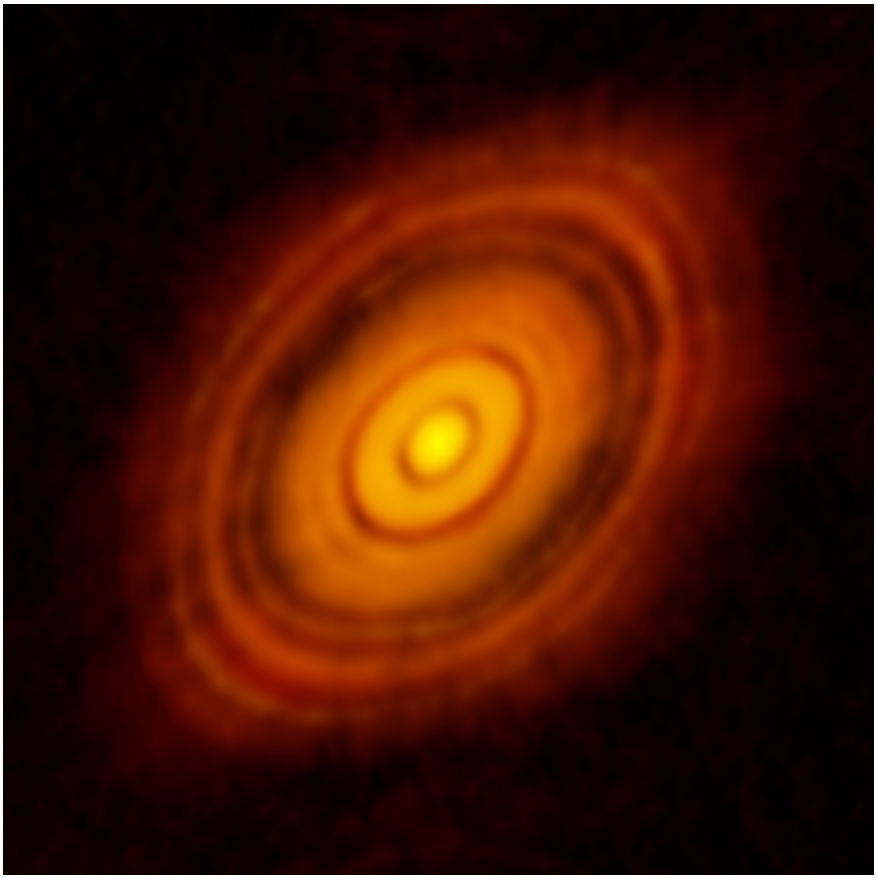


Figure 2: Esta imagen muestra cómo se ve una protoestrella con un disco protoplanetario cuando se observa con un telescopio como el Atacama Large Millimeter/submillimeter Array (ALMA) en longitudes de onda submilimétricas. El disco revela diversas características, incluidas anillos y huecos, a las que nos referimos como subestructuras. Estas pueden ser el resultado de la formación de planetas u otros procesos dinámicos dentro del disco. Crédito de la imagen: ALMA (ESO/NAOJ/NRAO); C. Brogan, B. Saxton (NRAO/AUI/NSF)

Esta Tesis

En esta tesis, utilizando los telescopios más modernos de nuestra era, he estudiado las propiedades del polvo en protoestrellas y regiones de

formación estelar cercanas, que típicamente se asemejan a la estructura mostrada en la Figura 2. Mi investigación se ha enfocado principalmente en cómo evoluciona y crece el polvo, un paso fundamental hacia la formación planetaria, pero también he explorado cómo las moléculas, especialmente las moléculas orgánicas complejas, pueden ayudarnos a responder preguntas fundamentales sobre los orígenes de los sistemas planetarios.

La tesis está estructurada en cinco capítulos. El Capítulo 1 ofrece una introducción a la formación estelar, los discos protoplanetarios, el papel del polvo y el gas en estos discos, la presencia de moléculas orgánicas complejas y las subestructuras observadas en discos aislados. Los capítulos siguientes presentan análisis detallados sobre la evolución y crecimiento del polvo en discos, así como la química de las moléculas orgánicas complejas en diferentes regiones de formación estelar.

Capítulo 2: En este capítulo investigo la emisión de polvo a alta resolución del sistema binario NGC 1333 IRAS4A, una región protoestelar, que representa una de las fases más tempranas de formación estelar. Los resultados muestran que el polvo en IRAS4A1 ya ha alcanzado condiciones necesarias, como el tamaño y la densidad de los granos, para permitir la formación de planetesimales o subestructuras, regiones donde se cree que comienzan a formarse los planetas. Además, el modelado de transferencia radiativa sugiere que podrían existir subestructuras ya formadas, pero ocultas bajo capas densas de gas y polvo, lo que implica que la formación planetaria podría comenzar mucho antes de lo que se pensaba.

Capítulo 3: En este capítulo continúo el estudio del sistema NGC 1333 IRAS4A, esta vez centrado en las moléculas orgánicas complejas alrededor de la binaria IRAS4A2. Analizo su distribución espacial y su relación con los granos de polvo en el sistema. Los resultados revelan una distribución radial y azimutal más compleja de lo esperado, lo que indica una fuerte conexión entre la emisión molecular y cómo el polvo se acumula y se

asienta en regiones específicas. Este hallazgo sugiere una evolución del polvo muy rápida en IRAS4A2, especialmente en comparación con su compañera binaria IRAS4A1, donde la mayor parte de la emisión molecular parece estar oculta bajo el polvo.

Capítulo 4: Este capítulo se enfoca en HL Tau, un disco protoplanetario ligeramente más evolucionado. Usando imágenes de alta resolución a diferentes longitudes de onda, aplicamos modelos de transferencia radiativa para ajustar la emisión observada y derivar propiedades clave del polvo como el tamaño, la densidad y la temperatura. Particularmente, nuestras observaciones en la Banda 9 del telescopio ALMA revelan una estructura diferente, posiblemente asociada con granos más pequeños, una mayor extensión del disco y una nueva subestructura interna, visible solo en estas longitudes de onda más cortas.

Capítulo 5: En este capítulo analizo todos los discos protoplanetarios en una sola región de formación estelar, en la región de formación estelar, Lupus. Examinamos todos los radios y otros parámetros físicos de los discos y descubrimos que más del 67% de estos son muy compactos (radio < 30 au). Resaltamos que en estos discos también se detectaron subestructuras. Estos resultados sugieren que la mayoría de los discos ya tienen las condiciones para formar supertierras, uno de los tipos de exoplanetas más comunes descubiertos hoy en día, ofreciendo una conexión directa entre las propiedades iniciales de los discos y la población actual de exoplanetas.

A partir de los resultados presentados, concluimos que se debe prestar mayor atención a las estructuras radiales y verticales de los discos protoplanetarios. Estos discos no son simplemente estructuras planas y extensas, sino que presentan geometrías complejas y una gran variedad de radios. En particular, las variaciones en la estructura vertical a diferentes radios ofrecen pistas valiosas sobre las condiciones iniciales para la

formación de planetas y de las subestructuras.

Además, comprender si los discos son en su mayoría compactos o radialmente extensos nos puede ayudar a responder una pregunta fundamental: ¿es el Sistema Solar una excepción? Para formarlo se requieren discos de al menos 100 au, que permiten la formación de gigantes gaseosos, sin embargo, si la mayoría de los discos son compactos, el origen de la vida tal como la conocemos sería un proceso poco frecuente y, por ello, su hallazgo resultaría aún más desafiante.

English summary

We live in a small corner of our galaxy in the universe, the Milky Way, in a planetary system we call the Solar System. For a long time, we believed our system was the center of the universe, or more correctly, that humans were the center of the universe, a belief we now know is far from true. If we were born and raised here, it's not unreasonable to imagine that something similar could have happened around other stars in our galaxy or in distant galaxies.

Interestingly, the Sun is not even a typical star within the Milky Way, let alone the universe. In fact, recent evidence suggests that the formation of our Solar System might have followed a rather unusual path compared to most other planetary systems. Still, the mere fact that we know about these other possibilities, and that life may form elsewhere, continues to intrigue us. Then the question remains: What led to the formation of this specific planetary system around a solar-mass star that eventually enabled life to evolve? To find an answer to this, we must go back to the very beginnings, to the birth of stars and planets, in the vast void of the universe where gas and cold dust gather, the interstellar medium (ISM).

Star and Planet Formation in the ISM

In our universe, there are vast regions of gas and dust called molecular clouds that form the ISM. These are the places where stars and planets are born. Molecular clouds consist primarily of hydrogen and helium, with trace amounts of heavier elements like oxygen, nitrogen, and carbon.

When parts of these clouds become dense and massive enough, gravity causes them to collapse, forming a protostar. The collapsing material, both gas and dust, begins to heat up and flatten into a rotating structure as the protostar accretes. This leftover material, around the young protostar, forms what we call a protoplanetary disk.

Within this disk, dust particles begin to stick together, forming larger and larger clumps. Over time, these clumps become as large as kilometer-sized objects, planetesimals, which then continue to accrete more material and grow into planets. As the protostar evolves, nuclear fusion eventually ignites in its core. At that point, the surrounding disk starts to clear due to the strong radiation coming from the star and what remains are the planets and planetesimals, now part of a newly formed stellar system. This system can remain stable for millions or even billions of years, until the star exhausts its nuclear fuel. Depending on its mass, the star may then explode as a supernova or expand and leave behind a white dwarf. In either case, its remaining material is returned to the interstellar medium, restarting the cycle of star and planet formation. This is the star formation process, shown also in Figure 1. While we can look deep into Earth's past through meteorites and geological records, the best way to study planetary origins and the potential for life elsewhere is by observing other protoplanetary disks, systems still in the very early stages of planet formation. These systems exist within nearby molecular clouds and offer us a unique window into the beginning of planets like our own. To explore them, we rely on powerful telescopes capable of detecting the light emitted from either the dust particles or the atoms and molecules in these disks. In particular, interferometric telescopes, which allow us to resolve their structure in remarkable detail, helping us understand the environments where planets, and perhaps life, are born.

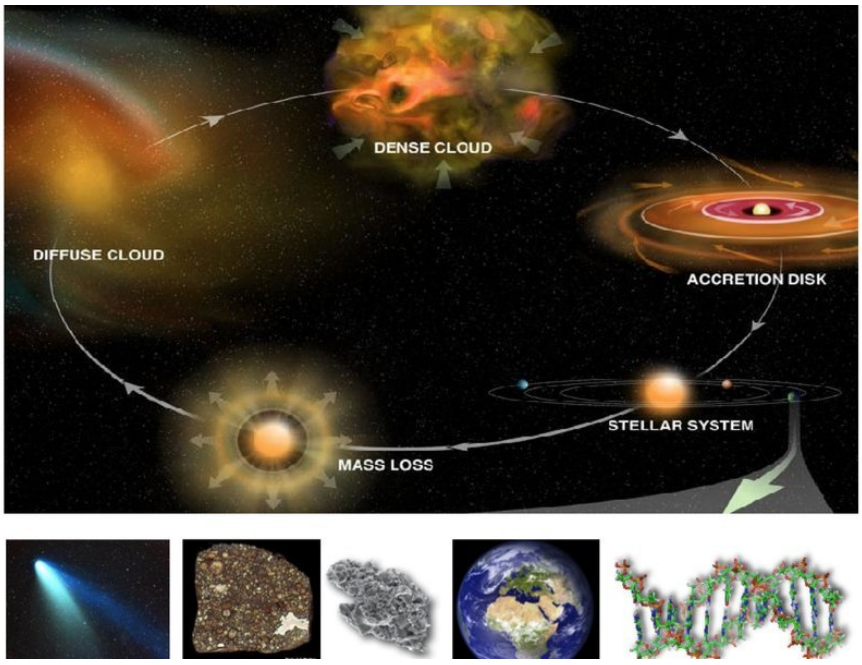


Figure 1: This image illustrates the full star formation process, together with the early stages of planet formation. It all begins with a molecular cloud, a cold and dense region of gas and dust in the interstellar medium. Over time, parts of this cloud collapse under gravity, forming a protostar surrounded by an accreting disk of material. As the protostar evolves, the surrounding protoplanetary disk becomes the birthplace of planets. Within this disk, small particles collide and stick together, forming dust grains and eventually planets. Over time, much of the disk material is cleared away, leaving behind a planetary system with complex organic molecules, atoms, and residual dust—remnants like planetesimals of the original disk. Image credit: B. Saxton, NRAO/AUI/NSF

Thesis overview

In this thesis, using the most modern telescopes, I have studied and investigated the properties of dust in nearby protostars and star-forming regions, which typically resemble the structure shown in Figure 2. My research has primarily focused on how dust evolves and grows, an essential

step toward planet formation, but I have also explored how molecules, particularly complex organic ones, can contribute to answering fundamental questions about the origins of planetary systems.

The thesis is structured into five chapters. Chapter 1 provides an introduction to star formation, protoplanetary disks, the role of dust and gas in these disks, the presence of complex organic molecules, and substructures in (isolated) disks. The subsequent chapters present detailed analyses of dust evolution, dust growth and the chemistry of complex organic molecules across different star-forming regions.

Chapter 2: In this chapter, I investigate the high-resolution dust emission from the binary system NGC 1333 IRAS4A, a deeply embedded protostellar region, which represents one of the earliest stages of star formation. Studying such young systems is essential to understanding when and how planet formation begins. Specifically, this work explores whether the initial steps toward planet formation, such as grain growth or substructure formation, can already be detected at this early stage, or whether they occur much later in the protoplanetary disk evolution. The analysis of dust properties in IRAS4A1 reveals that the dust has already reached the necessary conditions, such as grain size and density, to support the formation of planetesimals or substructures, the latter being the regions where we believe planets begin to form. Furthermore, radiative transfer modeling suggests that substructures may already exist within the system, but remain hidden beneath dense layers of gas and dust. This finding implies that planet formation might begin much earlier than previously thought.

Chapter 3: In this chapter, I continue the investigation of the NGC 1333 IRAS4A system, this time focusing on the complex organic molecules (COMs) surrounding IRAS4A2, rather than the dust. I analyzed the spatial distribution of these molecules and explored their relationship with the dust grain distribution in the system. The results reveal that the radial and

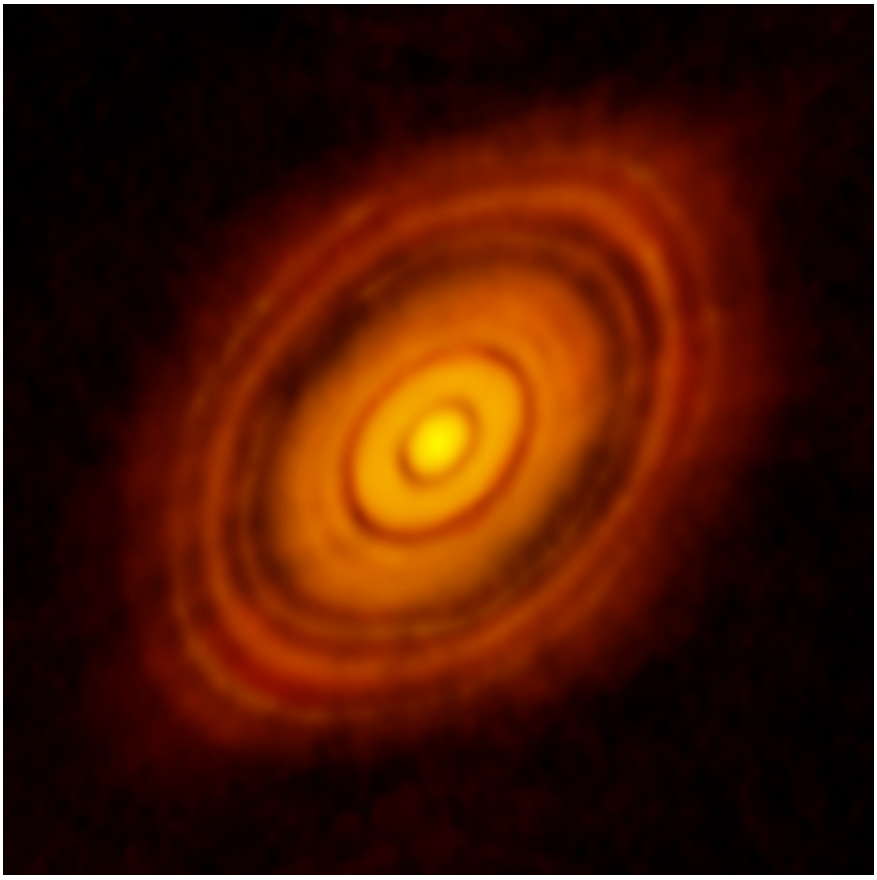


Figure 2: This image shows what a protostar with a protoplanetary disk looks like when observed with a telescope such as the Atacama Large Millimeter/submillimeter Array (ALMA) at submillimeter wavelengths. The disk reveals various features, including rings and gaps, which we refer to as substructures, these may be the result of planet formation or other dynamic processes within the disk. Image credit: ALMA(ESO/NAOJ/NRAO); C. Brogan, B. Saxton (NRAO/AUI/NSF)

azimuthal distribution of the complex organic molecules is significantly more intricate than previously expected. This complexity suggests a deeper connection between the molecular emission and the way dust is accumulating and beginning to settle in specific regions of the system.

These findings point toward a rapid dust evolution process in IRAS4A2, especially when compared to its primary binary companion, IRAS4A1, where most of the molecular emission appears to remain obscured beneath a thick layer of dust.

Chapter 4: In this chapter, we study a slightly more evolved protoplanetary disk: HL Tau. Using a multi-wavelength analysis approach, we analyzed high-resolution images of the disk taken at several different frequencies. By applying radiative transfer modeling, we were able to fit the observed emission and derive key dust properties, including dust grain size, dust density, and dust temperature. In particular, we utilized Band 9 observations from the ALMA telescope, which probe optically thick wavelengths. This allowed us to study the disk from a different perspective, revealing a structure distinct from that observed at longer wavelengths. The data likely trace smaller grains measurable at millimeter wavelengths and reveal a larger disk radius, denser substructures, and possibly a different vertical extent of the disk compared to previous observations. Additionally, we identified a previously undetected inner substructure visible only at these shorter wavelengths, along with a notable asymmetry in the disk.

Chapter 5: Chapter 5 focuses on understanding protoplanetary disks across an entire star-forming region. In this work, we studied and analyzed all known (isolated) disks in the Lupus region, examining their radii and other physical properties. Investigating a complete sample of protoplanetary disks offers valuable insights into dust evolution and its connection to planet formation. However, many previous studies have been limited by low-resolution observations, mainly due to telescope constraints. In contrast, our higher-resolution analysis revealed that over 67% of the disks in Lupus are very compact, with radial extents smaller than 30 au. Additionally, we discovered new substructures within several of these disks. These results suggest that the majority of protoplanetary

disks already possess the conditions necessary to form one of the most common types of exoplanets: super-Earths. This connection between early disk properties and the observed exoplanet population provides important clues about the typical pathways of planet formation, helping bridge the gap between disk observations and planetary system outcomes.

Based on the individual results of all the chapters, we conclude that greater attention should be given to both the radial and vertical structures of protoplanetary disks. These disks are far more complex than previously thought, not simply large, flat structures, but systems with intricate geometries and a wide range of radial extents.

In particular, radial variations in the vertical structure of protoplanetary disks offer important insights into the initial conditions of planet formation, how this process is triggered, and how substructures, which may eventually give rise to planets, form within disks. Moreover, understanding whether compact or large protoplanetary disks are more common can help answer a key question: Is our Solar System the exception rather than the rule? If it is, then life might be rarer and harder to form than we've often assumed.

List of Publications

Refereed publications

IRAS4A1: Multiwavelength continuum analysis of a very flared Class 0 disk
Osmar M. Guerra-Alvarado, N. van der Marel, J. Di Francesco, L. W. Looney, J. J. Tobin, E. G. Cox, P. D. Sheehan, D. J. Wilner, E. Macías, and C. Carrasco-González, 2024, Astronomy & Astrophysics, 681, A82.

Into the thick of it: ALMA 0.45 mm observations of HL Tau at a resolution of 2 au
Osmar M. Guerra-Alvarado, Carlos Carrasco-González, Enrique Macías, Nienke van der Marel, Adrien Houge, Luke T. Maud, Paola Pinilla, Marion Villenave, Yoshiharu Asaki, and Elizabeth Humphreys, 2024, Astronomy & Astrophysics, 686, A298.

A high-resolution survey of protoplanetary disks in Lupus and the nature of compact disks
Osmar M. Guerra-Alvarado, Nienke van der Marel, Jonathan P. Williams, Paola Pinilla, Gijs D. Mulders, Michiel Lambrechts, and Mariana Sanchez, 2025, Astronomy & Astrophysics, 696, A232.

Rocky planet formation in compact disks around M dwarfs
M. Sanchez, N. van der Marel, M. Lambrechts, G. D. Mulders, and **O. M. Guerra-Alvarado**, 2025, Astronomy & Astrophysics, 689, A236.

Grain-size measurements in protoplanetary disks indicate fragile pebbles and low turbulence
Haochang Jiang, Enrique Macías, **Osmar M. Guerra-Alvarado**, and Carlos Carrasco-González, 2024, Astronomy & Astrophysics, 682, A32.

Multiple Shells Driven by Disk Winds: ALMA Observations in the HH 30 Outflow
J. A. López-Vázquez, Chin-Fei Lee, M. Fernández-López, Fabien Louvet, **O. Guerra-Alvarado**, and Luis A. Zapata, 2024, The Astrophysical Journal, 962, 28.

Submitted publications

From large-scale outflows to compact line emission in IRAS4A2
Osmar M. Guerra-Alvarado, N. van der Marel, P. Nazari, J. Di Francesco, Ł. Tychoniec, L. W. Looney, E. G. Cox, D. J. Wilner, and M. R. Hogerheijde, Submitted to Astronomy & Astrophysics.

Gaps and Rings: A Near-Universal Trait of Extended Protoplanetary Discs
Q. Bosschaart, **O. M. Guerra-Alvarado**, N. van der Marel, and G. D. Mulders, Submitted to Astronomy & Astrophysics.

Multi-Wavelength Dust Characterization of the HL Tau Disk and Implications for Planet Formation
Takahiro Ueda, Sean M. Andrews, Carlos Carrasco-González, **Osmar M. Guerra-Alvarado**, Satoshi Okuzumi, Ryo Tazaki, and Akimasa Kataoka, Accepted for publication in the Astrophysical Journal.

Curriculum Vitae

I was born in Colorado Springs, United States, on July 13th, 1994. As my father used to tell me, it was a very luxurious birth, since he was helping build a house for a well-known doctor. I have no real recollection, however, of those early days.

As far as I'm concerned, I grew up in a town called Morelia, west of Mexico City, where I spent most of my early school years. Back then, I didn't have a clear idea of what I wanted to become; I was, after all, still a child, but I always considered myself good at studying and eager to solve mysteries. In middle school, a few things changed. I started focusing more on my friends, and I realized I wasn't particularly good at pure mathematics, which, looking back, really comes as a surprise. I was, however, drawn to problem-solving courses and history, though the latter path never materialized.

In high school at Liceo Michoacano, I was expected to begin thinking about my future career. I probably should have paid more attention to that decision, but I was too busy focusing on other things. I don't regret at all how I spent those years.

From 2012 to 2017, I studied Electronic Engineering at Instituto Tecnológico de Morelia. I completed a major in biomedical instrumentation, but I realized midway that I wanted to pursue something else. Regardless, I graduated by starting a project on non-invasive glucose monitoring using NIR spectroscopy under the supervision of Dr. Adriana del Carmen Téllez Anguiano, together with my friend and colleague, Ing. Kevin Raúl

Hernández Franco.

After graduation, I decided not to pursue a career in engineering anymore and instead applied for a master's in a field I found more fulfilling. I was fortunate to be accepted into the Master's program in Astrophysics at UNAM, under the supervision of Dr. Carlos Carrasco González. I've always been fascinated by planets and the search for life beyond Earth, so it felt like a natural fit. From 2018 to 2021, I caught up with relevant courses needed as an astrophysicist, worked on and wrote my thesis, and graduated with honors.

Still not ready to leave research behind, I applied for PhD positions in several countries. It was a long and challenging process, but eventually, I landed a position at Leiden University. My friend Kevin, who also helped me graduate and who was living in the Netherlands at the time, encouraged me to apply to Leiden. However, I wasn't sure if anyone there was working on what I did for my master's. Nevertheless, I applied, and to my surprise, Dr. Nienke van der Marel offered me a PhD position in her planet formation group starting on September 13th, 2021.

Though it was difficult to leave my life in Mexico, my PhD has taken me to incredible places, Japan, Belgium, France, and even back to Morelia to present my work. These four years have challenged me and helped me grow in ways I never expected, and I now realize how valuable that growth has been. After completing my PhD, I look forward to a new challenge outside academia, where I can continue to grow and apply everything I've learned, especially during these past four years.

Acknowledgments

This PhD marks a wonderful chapter in my life, full of change, challenge, and growth. I could never have done it alone, so there are many people I want to thank.

First of all, I want to thank my family. To my parents, Elizabeth and Manuel, thank you for always supporting me and letting me choose my own path, no matter where it led. I know you always care and worry about me, and I'm deeply grateful for that. To my sister Thalia, thank you for always being there for me. You're the best sister I could have asked for.

To my supervisors, Nienke and Michiel, thank you for your patience, guidance, and all your support throughout the PhD. Thank you for allowing me to grow, both professionally and personally. I've learned so much from working with you. I also want to thank my former supervisors, Carlos and Enrique. Without you, I probably would never have studied protoplanetary disks or discovered how fascinating these systems are.

To my fellow PhD and dear friend Alessia, thank you for all the talks that kept me sane, and for all the meetings and office hours that were much more fun with you. To all the protoplanetary disk folks and the Allegro team, thank you for your help with my data and your endless patience with my questions about planet formation: Marianna, Margot, Lucas, Milou, Andres, Andrew, Luna, Marissa, Logan, and Sam.

I'd also like to thank many people from the institute: the secretariat staff for their continuous help and support, and the IT team for always solving my technical problems. Special thanks to the social events com-

mittee for the fun moments, like the BBQ and the Sinterklaas celebration, and to all the borrel committees (including mine) for making Fridays a day to look for.

To all the PhDs I met during this journey, thank you for the coffees, dinners, and gatherings. You made the university a genuinely enjoyable place to work: Pranjal, Nico, Josh, Silvia, Marta, Christian, Elia, Kirstie, Dilovan, Dario, Ciaran, Chloe, Vanesa, Roi, Willeke, Jessica, Will, Orestis, Timo, Joey, Ivana, Fraser, Sill, Amy, Christiaan, Rob, Roland, Thomas, Veronica, Manuel, Thijs, Lucy, and Martje.

To the people in Leiden who made these years so memorable, I'm thankful to share so many happy moments with you. Kevin, amigo, there's probably not much I can put into words, but without you, I probably wouldn't even be in the Netherlands. Thank you for everything. To my first friend and colleague here, Jurgen, thank you for helping me adjust to life in the Netherlands. Alfred, days at the office were never the same without you, amigo, no more gossip, no more fun breaks. To my friends Mira, Andrés, and Javier, thank you for all the unforgettable weekends, the wild raves and parties, but most importantly, for always being there. To my bromigo, Andrew, thank you for all the gym and darts sessions. To Nina, thank you for standing by me during the toughest year of my PhD, I love you.

To my family back in Mexico, thank you for your unconditional love and support. And to my friends in Morelia, thank you for helping shape the person I am today: Manuel, Diego, Pepe, Alex, Haydee, Karen, Beto, Lalo, Rasu, Paola, Anahí, Karla, Andu, Aura, y por supuesto, Carlos (Kike), donde quiera que estés, nos vemos pronto.